Dissertation

submitted to the
Combined Faculty of Natural Sciences and Mathematics
of Heidelberg University, Germany
for the degree of
Doctor of Natural Sciences

put forward by
Jan Hendrik Willibald Becher
Born in: Limburg a.d. Lahn
Oral examination: 13.05.2020

Characterizing Few-Fermion Systems with Momentum Correlations

Supervisors:
Prof. Dr. Selim Jochim
Prof. Dr. Francesca Ferlaino
Referees:
Prof. Dr. Selim Jochim
JProf. Dr. Fred Jendrzejewski

Abstract

In this thesis I report on the experimental study of fermionic systems in two complementary experimental settings, i.e. large ensembles of dipolar erbium atoms and few-particle systems of fermionic lithium trapped in optical tweezers.
Compared to alkali atoms, dipolar quantum gases offer new avenues to explore due to their long-range anisotropic interactions and a rich internal structure. Such richness comes at the cost of complexity and therefore requires precise investigations of the atomic properties as well as the development of new experimental methods. In the first part of this thesis we present measurements of the anisotropic light shift of erbium atoms and compare the results to semiempirical electronic-structure calculations. Measurements of scalar and tensor polarizabilies of the ground and one excited state show good agreement with calculated values. We furthermore present the first experimental realization of a two-component strongly-interacting Fermi gas with dipolar interactions. We identify several intra and interspin Feshbach resonances at low magnetic field and precisely map out the scattering length across one broad resonance.
The second part of this thesis is dedicated to the characterization of small fermionic systems with momentum correlation measurements. Starting with systems of two or three indistinguishable fermions, we detect and discuss second and third-order momentum correlations that arise from quantum statistics alone. We then extend the study of correlation functions to interacting systems and develop a scheme to constrain large parts of the density matrix. Based on these constraints we reconstruct physical density matrices via Bayesian inference. We finally use the reconstructed states to address the influence of exchange symmetry on particle-particle entanglement in systems of identical fermions. Using the simple notion of an *Antisymmetric Negativity* we are able to separate entanglement from antisymmetrization from entanglement induced by interaction.

Zusammenfassung

In dieser Arbeit berichte ich von der experimentellen Untersuchung fermionischer Systeme in zwei komplementären Umgebungen: große Ensembles dipolarer Erbiumatome und Wenigteilchensysteme aus fermionischem Lithium.
Im Gegensatz zu Alkaliatomen ist die Wechselwirkung zwischen Erbiumatomen langreichweitig und anisotrop, was zusammen mit ihrer reichhaltigen inneren Struktur neue Möglichkeiten bietet, interessante Vielteilchenphänomene experimentell zu untersuchen. Dazu ist jedoch eine genaue Kenntnis über die atomare Struktur von Erbium und die Entwicklung neuer experimenteller Methoden nötig. Im ersten Teil dieser Arbeit stellen wir Messungen der anisotropen Stark-Verschiebung von Erbiumatomen vor und vergleichen die Ergebnisse mit semiempirischen Atomstruktur-Berechnungen. Messungen der Skalar- und Tensorpolarisierbarkeit des Grundzustands und eines ausgewählten angeregten Zustands stimmen gut mit berechneten Werten überein. Des Weiteren präsentieren wir die erste experimentelle Realisierung eines stark wechselwirkenden zweikomponentigen Fermigases mit dipolarer Wechselwirkung. Wir identifizieren mehrere intra- und interspin Feshbach-Resonanzen bei niedrigem Magnetfeld und bestimmen präsize die Streulänge in der Nähe einer ausgewählten Resonanz.
Der zweite Teil dieser Arbeit befasst sich mit der Charakterisierung kleiner fermionischer Systeme durch Impulskorrelationsmessungen. Ausgehend von Systemen aus zwei oder drei ununterscheidbaren Fermionen messen und diskutieren wir Impulskorrelationen zweiter und dritter Ordnung, die sich allein aus der Quantenstatistik ergeben. Anschließend erweitern wir die Studie der Korrelationsfunktionen auf wechselwirkende Systeme und entwickeln ein Schema, um den Großteil der Dichtematrix einzuschränken. Basierend auf diesen Bedingungen rekonstruieren wir physikalische Dichtematrizen durch Bayes'sche Inferenz. Schließlich verwenden wir die rekonstruierten Zustände, um den Einfluss der Austauschsymmetrie auf Teilchen-Teilchen-Verschränkung in Systemen identischer Fermionen zu untersuchen. Unter Benutzung einer *antisymmetrischen Negativität* können wir Verschränkung von Antisymmetrisierung von Verschränkung trennen, die durch Wechselwirkung induziert wird.

Danksagung

Es gibt viele Menschen, die zum Gelingen dieser Arbeit beigetragen haben. An dieser Stelle möchte ich mich bei jedem dafür bedanken.
Besonderer Dank gilt *Francesca Ferlaino* und *Selim Jochim* für die gute Betreuung während meiner gesamten Promotion und für die Möglichkeit, das erste Jahr meiner Doktorarbeit in Innsbruck zu verbringen.
Des Weiteren bedanke ich mich recht herzlich bei JProf. *Fred Jendrzejewski* für die Übernahme der Zweitkorrektur sowie bei Prof. *Björn Malte Schäfer* und Prof. *Jörg Evers* für die Bereitschaft, Teil meines Prüfungskommitees zu sein.
Diese Arbeit wäre natürlich nicht ohne Arbeitskollegen möglich, die mir im Labor jederzeit tatkräftig unter die Arme gegriffen haben. Danke an das ERBIUM Team: *Simon, Dani, Gabriele, Giulia, Lauriane, Manfred* und mittlerweile auch *Alex* und an das RARE Team: *Max, Philipp, Claudia, Arno* und *Gianmaria*. Vielen Dank an die gesamte Gruppe in Heidelberg: *Luca, Marvin, Keerthan, Lukas, Ram-Janik, Laurin*, sowie *Philipp L* und an alle früheren Doktoranden, mit denen ich noch im Labor zusammenarbeiten durfte. Ganz besonderer Dank gilt *Ralf* und *Philipp P.* für die viele Unterstützung, die Geduld beim Diskutieren und die letzten zwei gemeinsamen Jahre im Labor. Ein besonderes Dankeschön nochmal an *Ralf*, *Philipp L.*, *Laurin* und *Luca* für das Korrekturlesen meiner Arbeit und die vielen hilfreichen Kommentare.
Ich bedanke mich ebenfalls bei allen Koautoren, mit denen ich direkt zusammenarbeiten konnte und ohne die sämtliche Publikationen so nicht möglich gewesen wären. Besonderer Dank gilt den Koautoren *Maxence Lepers, Enrico Sindici* und *Andrew Daley*.
Zu guter Letzt bedanke ich mich bei all meinen Freunden für die schöne und unvergessliche Zeit in Heidelberg und meiner gesamten Familie für den Rückhalt und die bedingungslose Unterstützung während meines gesamten Studiums.

Contents

Preamble

The work presented in this thesis was conducted in two different ultracold-atom laboratories. I spent the first year of my graduation at Innsbruck University, where I worked in the erbium laboratory under the supervision of Prof. Dr. Francesca Ferlaino. During this time, we pursued two major projects. The first project was the investigation of effects of the anisotropic polarizability of erbium atoms and its potential application for state-dependent manipulation or trapping of an atomic sample. The second project focused on preparing a spin mixture of fermionic erbium in an optical lattice and to map out the scattering length across an s-wave Feshbach resonance, which might enable future studies of BEC-BCS crossover physics with ultracold dipolar atoms. After the first year in Innsbruck, I continued to work at Heidelberg University under the supervision of Prof. Dr. Selim Jochim. During that time we developed new methods to investigate and characterize few-fermion systems of fermionic lithium trapped in an array of optical tweezers. By analyzing single-particle resolved momentum-density correlation functions, we are able to reconstruct physical density matrices of systems containing two or three mobile, interacting fermions via Bayesian inference. We apply this scheme to a range of different experimental states and use the reconstructed density matrices to investigate entanglement properties of fermionic identical-particle states.
Due to the very different kind of experiments in Innsbruck and Heidelberg, they will be presented in separate parts in this thesis. The thesis is therefore divided into three major parts. The first part gives a general introduction to the field of ultracold atoms. The second part presents the results obtained during my first year in Innsbruck and finally the last part presents results from my time in Heidelberg.

Outline of this Thesis

Introductory Part: This part provides an introduction to the field of ultracold atoms and embeds the presented experiments within the respective research field. We briefly introduce the main aspects and tools that make ultracold atoms a versatile platform to investigate a range of different physics. We discuss how to trap and cool an ensemble of atoms and how laser light can be used to create optical potentials for neutral atoms. We also comment on how interactions between neutral atoms can be tuned in the laboratory. While most concepts presented in this part apply to both species, erbium and lithium, this part is also used to briefly compare properties, where they are distinctly different.

Erbium Part: This part presents the work done in Innsbruck. We start by giving an overview on the main atomic properties of erbium, including the discussion of the structure of energy levels, available optical transitions and magnetic properties. This sets the stage to present the main results from my first year. We start by discussing the concept of anisotropic light shifts and present measurements of the anisotropic polarizability of erbium both in the ground and in one excited state. We compare the measurements to electronic structure calculations and find very good agreement despite the complicated structure of electronic energy levels. The following chapter presents our work on the realization of a strongly interacting two-component Fermi gas of dipolar atoms. We make use of a lattice projection technique to suppress inelastic collisions during the initialization of the spin-mixture and map out an s-wave Feshbach resonance at around 680 mG via modulation spectroscopy in an optical lattice. This measurement presents the first realization of a dipolar Fermi gas with tunable s-wave interactions.

Lithium Part: This part presents the work done in Heidelberg. We start with a brief chapter on the main properties of lithium and the tools that we have available in the laboratory to initialize and characterize few-particle Fermi systems. In the experiment we can measure single-particle and spin resolved momentum distributions of systems containing few mobile, interacting particles in arrays of optical tweezers. This technique enables the measurement of momentum-density correlation functions, which we use to characterize the system. We start by investigating momentum-density correlations in systems involving two or three non-interacting indistinguishable atoms, where we measure and discuss strong second and third-order correlations induced by exchange statistics. In the following chapter we develop a method to analyze measured momentum-density correlation functions of states consisting of mobile, interacting particles and to construct physical density matrices via Bayesian inference. We apply this scheme to a range of different states and finally use the reconstructed density matrices to investigate particle-particle entanglement in systems with identical particles. To this end we employ the notion of an *Antisymmetric Negativity* to remedy conceptual problems that arise when individual particles are treated as subsystems for entanglement characterization.

List of Publications

This thesis is based on the work published in the four publications:

- **Measurement of Identical Particle Entanglement and the Influence of Antisymmetrisation**, *arXiv:2002.11207*
  J.H. Becher, E. Sindici, R. Klemt, S. Jochim, A.J. Daley, and P.M. Preiss

- **High-Contrast Interference of Ultracold Fermions**, Phys. Rev. Lett. **122**, 143602 (2019)
  P.M. Preiss, J.H. Becher, R. Klemt, V. Klinkhamer, A. Bergschneider, N. Defenu, and S. Jochim

- **Realization of a Strongly Interacting Fermi Gas of Dipolar Atoms**, Phys. Rev. Lett. **121**, 093602 (2018)
  S. Baier, D. Petter, J.H. Becher, A. Patscheider, G. Natale, L. Chomaz, M.J. Mark, and F. Ferlaino

- **Anisotropic polarizability of erbium atoms**, Phys. Rev. A **97**, 012509 (2018)
  J.H. Becher, S. Baier, K. Aikawa, M. Lepers, J.-F. Wyart, O. Dulieu, and F. Ferlaino

Further publications, not covered within this thesis:

- **Density Oscillations Induced by Individual Ultracold Two-Body Collisions**, Phys. Rev. Lett. **122**, 083401 (2019)
  Q. Guan, V. Klinkhamer, R. Klemt, J.H. Becher, A. Bergschneider, P.M. Preiss, S. Jochim, and D. Blume

- **Experimental characterization of two-particle entanglement through position and momentum correlations**, *Nature Phys.* 15, 640–644 (2019) A. Bergschneider, V.M. Klinkhamer, J.H. Becher, R. Klemt, L. Palm, G. Zürn, S. Jochim, and P.M. Preiss

- **Spin-resolved single-atom imaging of ^{6}Li in free space**, Phys. Rev. **A** 97, 063613, (2018)
  A. Bergschneider, V.M. Klinkhamer, J.H. Becher, R. Klemt, G. Zürn, P.M. Preiss, and S. Jochim

- **Observation of roton mode population in a dipolar quantum gas**, *Nature Phys.* 14, 442–446 (2018)
  L. Chomaz, R. M. W. van Bijnen, D. Petter, G. Faraoni, S. Baier, J.H. Becher, M. J. Mark, F. Wächtler, L. Santos and F. Ferlaino

Part I

Ultracold Quantum Gases A Playground for Quantum Physicists

Chapter 1

Introduction

About one and a half centuries ago, a series of peculiar experimental observations such as the spectrum of hydrogen and the discovery of the Balmer series [1], the discovery of the photoelectric effect by Heinrich Hertz [2] or the Zeeman-splitting effect by Pieter Zeeman [3] required physicists to question the validity of classical physics on microscopic scales. The seminal work of many physicists, including Einstein, Planck, Born or Pauli, ultimately led to the development of quantum mechanics in the early 20th century, which revolutionized our understanding of the microscopic world. The key ideas were to quantize the energy of states, to ascribe both a wave and a particle character to quantum mechanical objects and to allow superposition states. Although being heavily debated at that time, already from the very beginning, quantum mechanics was able to explain most experimental observations such as blackbody radiation or the famous Stern-Gerlach experiment, it enabled the development of the Bohr model for the atom, and facilitated the understanding of the periodic table of elements. Due to the rapid understanding of quantum mechanics, it only took a few decades until it caused the first technological breakthroughs, for example the development of the first photomultipliers in the 1930s [4], the understanding and development of semiconductor devices like the transistor in 1948 [5] or the realization of the Maser and the Laser in the 1950s and 1960s [6]. Quantum mechanics therefore was crucial for the technological development of today's world. Until the end of the 20th century quantum mechanical concepts have become essential for many core technologies in everyday life and can be found in many devices, ranging from medical applications like MRI or cancer treatment to industrial applications such as telecommunication, cutting metal, sensing and robotics or designing and fabricating modern computers and smartphones.

While those technological breakthroughs rely on single-particle effects, there is a range of intriguing quantum phenomena that involve many strongly correlated electrons or atoms. In fact, in the regime where the (deBroglie) wavelengths of individual constituents of a system becomes comparable to the spacing between them, quantum effects become dominant. One of the most prominent examples of the peculiar behavior of quantum-mechanical many-body systems was the discovery of superconductivity in 1911, a phenomenon which was baffling theorist for a long time [7]. While being

extensively studied in condensed matter systems, phenomenological theories could capture the basic physics of superconductors and superfluids, but still today, the quantum-mechanical description of systems containing only a few strongly correlated atoms is a challenging task for theory. For instance the exact diagonalization of a system of N atoms with two internal degrees of freedom requires the diagonalization of a $2^N \times 2^N$ matrix, which already exceeds available computational power for about 20-30 atoms.

Initially inspired by the idea of Richard Feynman [8], experimental physicists pursued the road of *quantum simulation*: Instead of trying to simulate a quantum mechanical system on a classical computer, it might be much more efficient to realize a system in the laboratory that evolves under the same Hamiltonian as the system of interest. One hence *simulates* a quantum system with another quantum system, that is more accessible in the laboratory. There are many different possible platforms for quantum simulation, such as ensembles of neutral atoms [9], photonic [10] or ionic systems [11]. The idea of engineering a quantum system has led to the development of a huge research field, including experiments on ultra-precise optical clocks [12], the development of nuclear clocks [13], the realization of a quantum computer with e.g. superconducting qubits [14], or the study of hybrid systems such as exciton-polaritons condensates [15], levitated microspheres as ultra-precise force sensors [16] or optomechanical systems [17]. Research interests do no longer only include quantum simulation. Instead, the unprecedented control and precision that can today be achieved in the laboratory enables fundamental tests of physics including loophole free Bell tests [18], the search for the electron electric-dipole moment [19] or for exotic forces beyond the standard model [20], the variation of fundamental constants, the detection of gravitational waves [20] or the realization of measurement devices beyond the standard quantum limit [21].

The cornerstone for quantum simulation with neutral atoms was laid by the first realization of a Bose-Einstein condensate (BEC) in 1995 [22, 23] and the first degenerate Fermi gas in 1999 [24]. Followed by many succeeding ground-breaking experiments, neutral atoms, trapped in optical traps, have proven to be a promising candidate for quantum simulation [9, 25] and for the search of exotic phases of matter. Over the years, many powerful theoretical and experimental tools have been developed both to describe and to manipulate ensembles of interacting atoms or molecules. Many different species, including both fermionic and bosonic isotopes are routinely cooled to quantum degeneracy and trapped in arbitrary optical potentials such as quasi-crystalline optical lattices [26] or arbitrary three-dimensional arrays of optical tweezers [27]. Using (orbital) Feshbach resonances [28, 29], interactions can be tuned over a wide range, enabling the realization of strongly interacting and strongly correlated systems. Recent experimental advances made it possible to engineer systems with single-particle control and readout [30], which opened up a new era for cold quantum gases: Large genuinely entangled systems can be readily created in the laboratory [31], advancing concepts for quantum computing and quantum information processing. Low-entropy states in optical lattices serve as toy models to simulate the doped Hubbard model [32]. The ability to bring electronically more complex atomic species (such as Dy, Er, Yb, Sr) or molecules to quantum degeneracy enables the study of

exotic phases with no equivalent in *natural* matter and recently led to the observation of supersolidity in a gas of magnetic atoms [33–35]. Arrays of optical tweezers might lead to a new generation of atomic clocks and new applications in metrology [36].

Despite enormous progress in the field of ultracold atoms, there are still many challenges, of which we address two within this thesis. Experimental progress of laser cooling and trapping made it possible to cool molecules [10] or atoms with a complicated electronic structure to quantum degeneracy, which offers new avenues to explore, due to properties including long-range anisotropic interactions, state-dependent light shifts, ultra-narrow optical transitions or a rich internal structure. However, in such systems much more care has to be taken to initialize interesting states. A precise understanding of the atomic structure and magnetic properties is therefore inevitable in such systems. In the first part of the thesis we measure the ac stark shift of erbium atoms at different wavelengths to verify the validity of electronic-structure calculations and we develop methods to map out the interaction in a two-component Fermi gas of magnetic erbium atoms without being affected from inelastic dipolar collisions. In contrast, the preparation of interesting states is well under control in quantum gas experiments with alkaline atoms. However, a major challenge in such experiments is the experimental characterization of the final state due to the lack of proper many-body observables. Currently many new ways to characterize strongly correlated systems are proposed and tested both theoretically and experimentally. In the last part of this thesis, we develop and explore a new method to fully characterize systems consisting of few mobile and interacting fermions, trapped in an array of optical tweezers. This method is complemetary to traditional tomography methods and presents an alternative approach to characterizing strongly correlated, fermionic systems in the laboratory.

The following two sections elaborate on the state of the art in the two respective research areas and embeds the studies presented in this thesis within the two fields of magnetic quantum gases and state characterization in Hubbard systems.

1.1 Magnetic Quantum Gases

From the first observation of Bose-Einstein condensation until 2005, all species that had been Bose-Einstein condensed interacted predominantly via short-range isotropic potentials. The first BEC of Chromium atoms in 2005 [37] allowed to study effects of the long-range, anisotropic dipole-dipole interaction on the behaviour of ultracold quantum gases. This led to the observation of many dipolar effects in BECs, including the suppression of the inversion of ellipticity during expansion [38], the observation of a d-wave collapse [39] or the spontaneous demagnetization of a dipolar gas at low magnetic fields [40]. The successful realization of a Bose-Einstein condensate of the most magnetic element Dysprosium in 2011 [41] and shortly after the first BEC of Erbium atoms in 2012 [42] opened a new frontier to study the interplay between short-range isotropic and long-range anisotropic interactions in systems of ultracold bosonic atoms.

One of the most prominent examples for the impact of dipolar interactions on the

behaviour of ultracold atoms was the observation of the formation of droplets [43], stabilized by quantum fluctuations [44, 45]. This manifestation of a beyond mean-field effect was followed by the observation of a roton mode in a dipolar BEC [46] and ultimately led to the observation of supersolididy, a state of matter that features both superfluid properties and a crystalline structure [33–35].
While bosonic dipolar quantum gases experienced a lot of attention, it took until 2012 until the first realization of a dipolar degenerate Fermi gas with Dysprosium [47], followed by Erbium in 2014 [48] and Chromium in 2015 [49]. Dipolar Fermi gases raise prospects for studying many different physical phenomena such as liquid crystal phases [50], p-wave, topological or anisotropic superfluid phases [51–53] or unconventional magnetism [54]. Due to their large quantum numbers in the electronic ground state, magnetic atoms possess a very rich internal structure and are therefore interesting candidates to study spinor physics with long-range dipolar interaction, to use the internal states as synthetic dimensions [55, 56] or to investigate the influence of dipole-dipole interaction on BEC-BCS crossover physics [57] or the BKT transition in two dimensional systems [58].
The results that we present in this thesis report on the measurement of the anisotropic light shift of erbium atoms and the first realization of a two-component Fermi gas with tunable interaction. The measurements on the anisotropic light shift agree very well with electronic-structure calculations and show that despite the complex electronic structure of erbium, it is well understood in terms of its atomic properties. Such understanding facilitates the application of state-dependent manipulation and trapping. We furthermore realize the first two-component strongly interacting dipolar Fermi-gas with tunable s-wave interaction, which paves the way to exploring many interesting areas in dipolar Fermi systems.

1.2 Characterization of Fermi-Hubbard-like States

With the advent of experiments operating on the single-particle level [30, 59–63], the field of ultracold quantum gases entered a new era of control. Experimentalists can readily initialize strongly correlated systems in the laboratory and probe them with spin and single-particle resolution [30, 64–67]. To fully characterize a prepared state in the laboratory however, the reconstruction of the full many-body density matrix is necessary. Unfortunately the number of entries of the density matrix scales quadratically with the number of available states and therefore scales exponentially with the system size. Traditional tomography of a many-body state thus also requires exponentially many measurements. A straightforward application to larger systems hence quickly becomes impractical. Despite considerable effort and progress in developing new techniques for the characterization of many-body states [68–71], the efficient characterization of Fermi-Hubbard like states, involving mobile, interacting particles, is still very demanding. The required protocols are technically challenging to realize for large systems since they require a large number of unitary operations on neighboring lattice sites. That's why throughout the community many new, complementary approaches are proposed to characterize a many-body state, including the

measurement of correlation functions [72, 73], the study of entanglement properties [74, 75], the application of random unitary operations [76, 77] or the use of machine learning [32, 78] or neural networks [79] to classify experimental data.
In this thesis we explore a new scheme for characterizing small Fermi-Hubbard like systems via the measurement of single-particle and spin resolved momentum-density correlation functions. We develop a scheme that allows us to reconstruct physical density matrices of small systems based on experimental results by employing a Bayesian quantum state estimation. In particular, our measurement protocol does not depend on the system size and only involves two complementary measurements, one in real space and one in momentum space. This is fundamentally different to other tomography protocols, where the number of operations scales with the system size [68]. We successfully apply our scheme to systems consisting of two or three mobile, interacting particles in an array of optical tweezers. As a first application, we reconstruct density matrices of a range of different states and discuss entanglement properties of fermionic identical-particle states. Furthermore we believe that the experimental methods developed within this thesis are not restricted to Fermi-Hubbard like states but will also find applications for the characterization of strongly correlated mesoscopic continuous systems.

Chapter 2

Realizing Ultracold Quantum Gases

Quantum mechanical effects become dominant at low temperatures, where the thermal deBroglie wavelength exceeds the interparticle spacing. Studying quantum mechanical effects in dilute samples of neutral atoms hence requires to cool down the system into the quantum degenerate regime, where the temperature becomes smaller than characteristic energy scales in the system. For Fermi systems, this characteristic energy scale is given by the Fermi temperature T_F. While the Fermi temperature for metallic superconductors is on the order of 10^5 K, a typical ensemble of fermionic atoms in an optical dipole trap has a Fermi temperature of only about 1 μK, due to the very low densities on the order of $10^{13}\,\mathrm{cm}^{-3}$ [80]. In order to realize such systems in the laboratory, atoms have to be trapped and cooled down from room temperature to the nK regime. As will be explained in this chapter, this is commonly achieved with magneto-optical traps and evaporative cooling in optical dipole traps. Once the route to quantum degeneracy is established, an important tool to tune interactions are Feshbach resonances, which we will also briefly introduce in this chapter.

2.1 Cooling and Trapping of Neutral Atoms

In this section we briefly present the main tools that are used in our experiments to cool a hot beam of atoms down to quantum degeneracy. Experimental details have been discussed in detail in previous works, see e.g. [81, 82] for the erbium machine and [83–85] for the lithium machine.

2.1.1 Vaccum Chamber

Experiments with ultracold gases absolutely require ultra-high vacuum on the order of 10^{-11} mbar since otherwise collisions with the background gas might limit the lifetime of the cold sample. Figure 2.1 shows a schematic of both vacuum chambers, the erbium machine in Innsbruck and the lithium machine in Heidelberg. Both experiments have a very similar design. The experiment starts with a high-temperature oven,

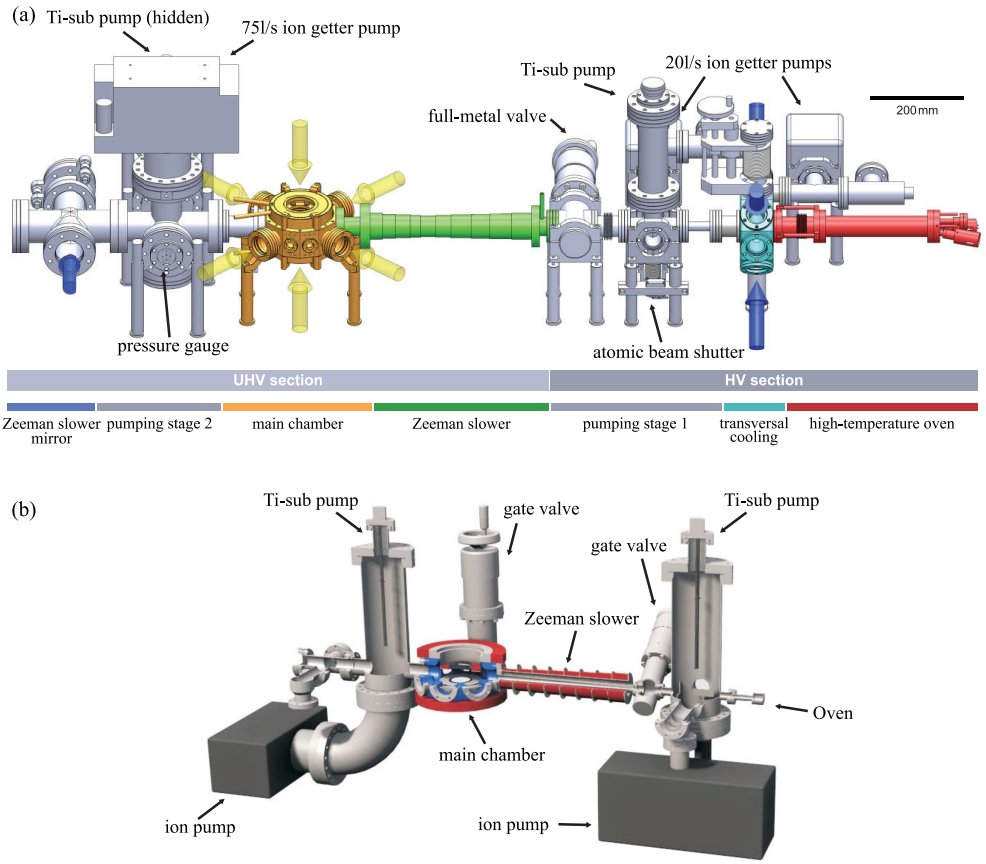

Figure 2.1: Vacuum chamber. (a) Vacuum chamber of the erbium machine. (b) Vacuum chamber of the lithium machine. Both experiments have a similar design, including oven, Zeeman slower and main chamber. Vacuum is maintained on the 10^{-11} mbar level by a differential pumping stage with two titanium sublimation pumps and two ion pumps. The main conceptual difference between the two machines is the additional transversal cooling stage in the erbium experiment. (a) taken and adapted from [81], (b) taken and adapted from [83].

where the respective species is heated up to approximately its melting temperature. At that temperature atoms start to evaporate from the surface, which leads to an increase of the vapor pressure and creates a hot gas of atoms. This gas is first of all precollimated with an initial transversal cooling stage in the erbium machine and only a simple tube in the lithium machine. The oven connects to the Zeeman slower and finally to the main chamber, where the experiments take place. Optical access to the science chamber is possible via eight (erbium) or six (lithium) viewports from the sides and two larger viewports from the top and the bottom, which are reentrant in the lithium machine, allowing a high numerical aperture of up to $NA = 0.65$. In both experiments two titanium sublimators and two ion pumps are used to reach and maintain the ultra-high vacuum at a pressure on the order of 10^{-11} mbar.

2.1.2 Dissipative Cooling

The atoms that exit the high-temperature oven are collimated to form an atomic beam towards the main chamber. At that stage of the experiment, atoms typically have velocities of around $500 - 1000\,\mathrm{m/s}$. The first two cooling steps employ near resonant laser light to create a dissipative force on the atoms, which first slows them down in the Zeeman slower and enables trapping them in a magneto-optical trap (MOT).

Zeeman-Slower:

The atomic beam is guided through the Zeeman-Slower, a tube surrounded by magnetic field coils, which create a spatially varying magnetic offset field along the path of the atoms (spin-flip configuration in the erbium experiment, decreasing field configuration in the lithium experiment). A near-resonant, circularly polarized laser beam is colinearly aligned with the counter propagating atomic beam. Fast atoms, which are initially Doppler shifted from the bare atomic resonance, become resonant to the laser beam via the Zeeman-shift in the spatially varying magnetic field such that they absorb photons with a directed momentum "$-k_{\mathrm{ph}}$" along the atomic beam direction. The excited atom spontaneously emits a photon in a random direction so that after one cycle the atom lost on average one photon momentum. The lower Doppler shift of the slowed atom is compensated by the varying magnetic field along the beam path. Atoms are kept resonant throughout the whole Zeeman slower and arrive in the science chamber with velocities of on average only a few meters per second. The lithium Zeeman-slower uses the $D2$ line with a natural linewidth of $\Gamma = 2\pi \times 5.8724\,\mathrm{MHz}$ [86]. The erbium Zeeman slower is operated on the broadest line at $\lambda_Z = 401\,\mathrm{nm}$ with a natural linewidth of $\Gamma = 2\pi \times 29.7\,\mathrm{MHz}$ [81]. After the atoms are slowed down, they can be captured in a magneto-optical trap (MOT).

Magneto-Optical Trap:

A MOT consists of six laser beams, typically realized by three retro-reflected, red-detuned laser beams with circular polarizaion, and a magnetic gradient field, produced by two coils close to anti-Helmholtz configuration. In fact in the erbium experiment, the MOT only requires five beams; due to its high mass, the top beam is not necessary for efficient operation of the MOT [87]. The laser beams cause a velocity-dependent radiation pressure on the atoms and the magnetic field gradients prevents the atoms to diffuse out of the trap by inducing a position dependent restoring force on the atoms. In the lithium experiment we have to add an additional repumper-frequency due to the decay of atoms into the $F = 3/2$ manifold in the ground state. A repumper is not necessary in the erbium experiment, where the five-beam, narrow-line MOT automatically spin-polarizes the atoms in the lowest state.
Due to the repeated process of scattering photons from the MOT beams, the temperature of the MOT is intrinsically limited by the natural linewidth of the transition, it is operated on. This so-called *Doppler temperature*, i.e. the lowest temperature that

can be achieved in the MOT, is given by [88]

$$T_D = \frac{\hbar\Gamma}{2k_B} \tag{2.1}$$

with $\hbar$ being the reduced planck constant, Γ the scattering rate and k_B the Boltzmann constant. The lithium MOT is operated on the $D2$ line with a natural linewidth of $\Gamma = 2\pi \times 5.8724\,\mathrm{MHz}$, which yields a Doppler temperature of $T_D = 141\mu K$. The erbium MOT profits from the electronically more complex structure of erbium and employs a relatively narrow line at $\lambda_M = 583\,\mathrm{nm}$ with a natural linewidth of $\Gamma \approx 2\pi \times 190\,\mathrm{kHz}$, achieving a Doppler temperature of $T_D \approx 5\,\mu\mathrm{K}$ [81, 89].

2.1.3 Conservative Potentials and Evaporative Cooling

In order to enter the quantum degenerate regime, the temperature has to be further reduced. To this end, the atoms are transferred from the MOT into a crossed-beam optical dipole trap (ODT) and then evaporatively cooled to quantum degeneracy. Optical dipole traps rely on the polarizability of an atom and are one of the workhorses of cold-atom experiments. Far detuned laser beams are not only used for evaporative cooling of atoms but also for the generation of external potentials and to confine atoms e.g. in optical lattices, optical tweezers or to reduced dimensions. A brief summary on the optical setup for the generation of optical potentials for both erbium and lithium will be given in Part II and Part III, respectively.

Far-Off-Resonant Traps

In order to generate a conservative potential for trapping the atomic sample, far-off-resonant laser beams are used. Depending on the sign of the detuning with respect to the optical resonance, such laser beams either create a repulsive or an attractive potential for neutral atoms.
When a neutral atom is placed into an oscillating electric field $\vec{E}(\vec{r}, t)$, the atom gets polarized with its induced dipole moment $\vec{p}$ given by

$$\vec{p} = \alpha\vec{E}. \tag{2.2}$$

α is called the ac-polarizability and generally is a 3×3 tensor, taking into account the anisotropy of the induced dipole moment. However, anisotropic effects vanish for far-detuned laser beams and we therefore neglect them in this part of the thesis. We elaborate on anisotropic light shifts in Chapter 4 for the case of erbium atoms. In the isotropic case, the induced dipole moment $\vec{p}$ is parallel and proportional to the amplitude of the electric field and α is a complex number. The energy of the induced dipole moment $\vec{p}$ in the electric field of a laser beam is then given by [90]

$$U_{\mathrm{dip}}(\vec{r}) = -\frac{1}{2}\langle\vec{p}\vec{E}(\vec{r})\rangle = -\frac{1}{2\epsilon_0 c}\Re(\alpha)I(\vec{r}), \tag{2.3}$$

with the real part of the polarizability $\Re(\alpha)$ and the intensity of the laser beam $I = \frac{1}{\epsilon_0 c}|E_0|^2$. Note that the imaginary part of the polarizability is related to the

off-resonant scattering of photons

$$\Gamma_{sc} = -\frac{1}{\hbar\epsilon_0 c}\Im(\alpha)I. \tag{2.4}$$

Considering the atom as a classical oscillator within Lorentz's model [90], the polarizability can be calculated for a two-level atom by

$$\alpha = 6\pi\epsilon_o c^3 \frac{\Gamma}{\omega_0^2(\omega_0^2-\omega^2) - i\omega^3\Gamma}, \tag{2.5}$$

with the laser frequency ω and the resonance frequency ω_0. Γ is the on-resonance scattering rate and can be calculated using the dipole transition element between the ground state $|g\rangle$ and the excited state $|e\rangle$

$$\Gamma = \frac{\omega_0^3}{3\pi\epsilon_0\hbar c^3}\left|\langle e|\,\mu\,|g\rangle\right|^2. \tag{2.6}$$

Using Eq. (2.5), we can directly calculate the real and imaginary part of α and can write down explicit equations for the dipole potential U_{dip} and the scattering rate Γ_{sc},

$$\begin{aligned} U_{\mathrm{dip}}(\vec{r}) &= -\frac{3\pi^2\Gamma}{2\omega_0^3}\left(\frac{1}{\omega_0-\omega}+\frac{1}{\omega_0+\omega}\right)I(\vec{r}) \\ \Gamma_{\mathrm{sc}}(\vec{r}) &= \frac{3\pi^2\Gamma^2}{2\hbar\omega_0^3}\left(\frac{\omega}{\omega_0}\right)^3\left(\frac{1}{\omega_0-\omega}+\frac{1}{\omega_0+\omega}\right)^2 I(\vec{r}). \end{aligned} \tag{2.7}$$

The potential experienced by the atom is hence proportional to the intensity of the laser beam, while the sign is given by the detuning $\delta = \omega_0 - \omega$. For red detuned laser beams ($\delta > 0$) the atoms experience an attractive potential and can be trapped in regions of maximum intensity. For blue detuned traps ($\delta < 0$), atoms experience a repulsive potential and get expelled from high-intensity regions. Since the scattering rate Γ_{sc} scales with $1/\delta^2$, the detuning is typically chosen very large. This in turn requires the application of high-power lasers to realize deep optical traps with very low number of photon-scattering events.

The concept of optical trapping can be exploited to create complex spatial potentials by shaping the form of the laser beam. Prominent examples are interfering laser beams to create optical lattices (as we use in the erbium machine), or optical tweezers (as we use in the lithium machine). However, in principle arbitrary optical potentials can be created by using either liquid crystal spatial light modulators or digital micro mirror devices to control either the phase or the amplitude of a light field.

Note that the given formulas are valid only for two-level systems. For real atoms, the dipole potential is given by a sum over all optical transitions, weighted by the coupling strength of each line (cf. Chapter 4). Typically in alkali atoms at infrared wavelengths, the ground-state polarizability is almost entirely given by the $D1$ and the $D2$ line [91]. As we will discuss in Chapter 4, this is different in erbium atoms, where the accurate calculation of the polarizability is hindered by a lack of spectroscopic data.

Evaporative cooling

Once atoms are trapped in the optical dipole trap, they can be evaporatively cooled to quantum degeneracy. Evaporative cooling [88, 92] relies on continuously removing the highly energetic atoms from the trap by lowering the optical potential. At the same time, interactions between the atoms in the trap lead to fast rethermalization. Hence energy is constantly removed from the atomic sample at the cost of decreasing the atom number. Evaporative cooling became a standard technique to cool atomic samples to quantum degeneracy. Since interactions between ultracold atoms usually are only of s-wave character, identical fermions do not interact and hence evaporatively cooling an alkaline Fermi gas requires a second internal state [80]. In the lithium machine this is achieved by cooling a balanced mixture of two of the three lowest hyperfine states. For fermionic erbium, this is not necessary due to universal dipolar scattering [48] as we will briefly discuss in the next section.
Typical experimental atom numbers at the end of the evaporation are about 40.000 atoms per spin state at a temperature of 0.1 T_F in the lithium machine and 40.000 spin-polarized atoms in the lowest state at temperatures of about 0.2 T_F in the erbium machine.

2.2 Interaction between Neutral Atoms

Collisions between two neutral atoms are governed by two different kinds of interactions. Atoms with a spherically symmetric electronic configuration, such as alkali atoms, only interact via the short-range van-der-Waals (vdW) interaction; an attractive potential, that drops with the sixth power of the distance r between the two atoms, r^{-6}. In addition, atoms with a permanent magnetic dipole moment also interact via the anisotropic magnetic dipole-dipole interaction [81],

$$U(\vec{r}) = U_{\mathrm{vdW}}(\vec{r}) + U_{\mathrm{dd}}(\vec{r}) \tag{2.8}$$

$$U_{\mathrm{vdW}}(\vec{r}) \rightarrow \frac{C_6}{r^{-6}} \text{ , for } r \rightarrow \infty \tag{2.9}$$

$$U_{\mathrm{dd}}(\vec{r}) = \frac{C_{\mathrm{dd}}}{4\pi} \frac{(\vec{e}_1 \cdot \vec{e}_2) r^2 - 3(\vec{e}_1 \cdot \vec{r})(\vec{e}_2 \cdot \vec{r})}{r^5}. \tag{2.10}$$

Here, C_6 is the vdW C_6 coefficient, $C_{\mathrm{dd}} = \mu_0 \mu_1 \mu_2$ is the dipolar coupling constant with the vacuum permeability μ_0 and the magnetic moments of the two colliding atoms $\mu_i = m_J g_J \mu_B$ with magnetic quantum number m_J, Landé factor g_J and the Bohr magneton μ_B. $\vec{e}_i$ is the orientation of the magnetic moment of each atom, as illustrated in Fig. 2.2 (a).

Short-Range Interaction

The vdW interaction arises due to the interaction between the electrons of the two atoms and is characterized by the vdW length $\beta_6 = \left(\frac{2\mu C_6}{\hbar^2}\right)^{1/4}$ [93] with the reduced mass μ of the two interacting atoms. This length is typically on the order of a few hundreds of picometers and therefore much shorter than the typical interparticle distance in the atomic sample. For describing the scattering physics of ultracold gases,

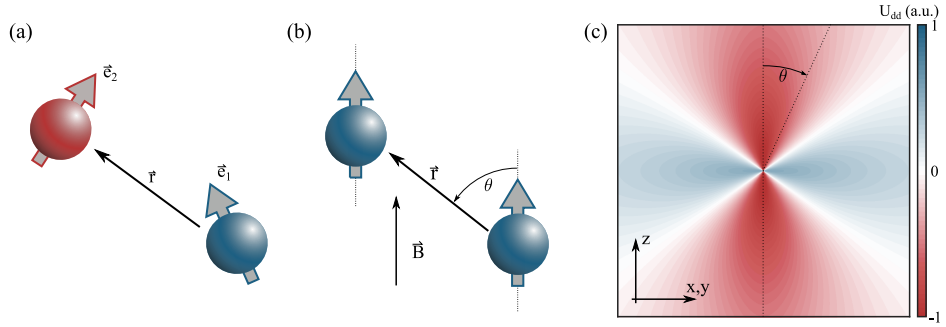

Figure 2.2: Dipolar interaction. (a) Geometry of dipolar interaction between two randomly aligned dipoles. (b) Interaction between two dipoles that are polarized by an external magnetic field. (c) Angle dependence of dipolar interaction U_{dd} between two polarized dipoles. The interaction vanishes at the magic angle of $\theta_m \approx 54.7°$. It is attractive for a head-to-tail alignment ($\theta < \theta_m$) and repulsive for a side-by-side configuration ($\theta > \theta_m$).

one typically expands the relative wave function of the two colliding atoms where at ultralow temperatures only the lowest partial wave contributes. U_{vdW} can then be replaced by a contact-like delta-function interaction (for derivations see e.g. [93, 94])

$$U_{\mathrm{vdW}}(r) = g_0 \delta(r) \frac{d}{dr} r, \tag{2.11}$$

with the interaction strength $g_0 = \frac{4\pi\hbar^2}{m} a_s$. Here a_s is the s-wave scattering length, which is defined via the phase shift an atom experiences in the interaction potential upon scattering. a_s is strictly zero for identical fermions due to their relative wave function being zero at $r = 0$ because of the Pauli-exclusion principle.
It is important to note that the vdW interaction is isotropic for atoms with a spherically symmetric electronic configuration, as it is the case for lithium. However, in the case of atoms with large permanent dipole moments, interactions show anisotropic effects [95, 96]. In particular, two colliding bosonic erbium atoms (with total angular momenta $J_1 = J_2 = 6$) have 49 non-degenerate molecular Born-Oppenheimer potentials and hence 49 different C_6 coefficients for 12 different collisional channels $\Omega = m_{J_1}^{\mathrm{in}} + m_{J_2}^{\mathrm{in}} = m_{J_1}^{\mathrm{out}} + m_{J_2}^{\mathrm{out}}$ (for more information, see [81]), giving rise to chaotic scattering physics, which was observed both in dysprosium and erbium. [97, 98].

Long-Range Dipolar Interaction

The magnetic dipolar interaction between two atoms decays with r^{-3} and is fundamentally different from the vdW interaction, both because of its range and its anisotropic character. In the experiment, the atoms are typically polarized by an external magnetic field, so that Eq. (2.12) simplifies to

$$U_{\mathrm{dd}} = \frac{\mu_0 \mu^2}{4\pi} \frac{1 - 3\cos^2\theta}{r^3}, \tag{2.12}$$

with θ being the angle between the vector $\vec{r}$ between the two atoms and their polarization axis, see Fig. 2.2 (b). As illustrated in (c) in the same figure, the interaction between two dipoles can be either attractive ($\theta \in [0°, 54.7°]$) or repulsive

($\theta \in [54.7°, 90°]$), and vanishes at the magic angle of $\theta_m = 54.7°$. This anisotropic interaction is the main difference between alkali or alkali-earth atoms and strongly magnetic lanthanide atoms such as Er or Dy. It is responsible for many peculiar effects that were not observed with alkali atoms before, such as a d-wave collapse [39], chaotic scattering [97], and beyond mean-field effects like the formation of droplets [43, 99], the observation of a roton mode [46] and supersolidity [33–35].

Scattering Cross Sections - Alkali vs. Dipolar

As already mentioned in the discussion around Eq. (2.11), our experiments are typically conducted in regimes where only the s-wave scattering length a_s is relevant for the short-range physics. This implies that identical fermions do not interact via the short-range vdW interaction potential at ultracold temperatures. In contrast, identical fermions can interact via the long-range dipolar interaction. In fact it turns out that at ultralow temperatures the scattering cross section of dipolar collisions approaches a universal value [81, 100, 101]. The scattering cross sections both for alkali and and magnetic atoms can be summarized as

$$\sigma_{\text{alkali}} = \begin{cases} 0 & \text{id. fermions} \\ 4\pi a_s & \text{otherwise} \end{cases} \tag{2.13}$$

$$\sigma_{\text{dipole}} = \begin{cases} \frac{32\pi}{15} a_D^2 & \text{id. fermions} \\ \frac{16\pi}{15} a_D^2 + 4\pi a_s & \text{otherwise} \end{cases}. \tag{2.14}$$

In the case of erbium, this allows even identical fermions to scatter and to thermalize and hence it is possible to evaporatively cool a single-component Fermi-gas of erbium atoms to quantum degeneracy [48] whereas for alkali atoms two spin states are necessary for efficient evaporative cooling.

Tuning the Interaction: Feshbach Resonances

One very helpful tool, which makes ultracold quantum gas experiments a versatile platform to study a range of different physical phenomena, is the ability to tune s-wave interactions over a wide range via Feshbach resonances (FRs). A particularly interesting regime is the regime of a diverging scattering length. In this so called unitary regime, the scattering length dominates over all other length scales in the system and therefore solely dictates the behavior of the atomic ensemble [103]. Extensive literature on FR in ultracold atomic gases is available [28] and will not be discussed here. The effect relies on the coupling of colliding atoms to molecular states and therefore strongly depends on the molecular structure of the colliding atoms. While ^{6}Li features a very broad s-wave FR between each two of the three different spin states (see upper panel in Fig. 2.3), erbium shows hundreds of FRs with higher partial wave character [98, 104] and only very sparse knowledge about the scattering lengths in erbium (and also in dysprosium) is available. Recently, we were able to map out one specific s-wave FR between the two lowest hyperfine states of fermionic ^{167}Er via modulation spectroscopy in an optical lattice [102], see lower panel in Fig. 2.3. Both resonances,

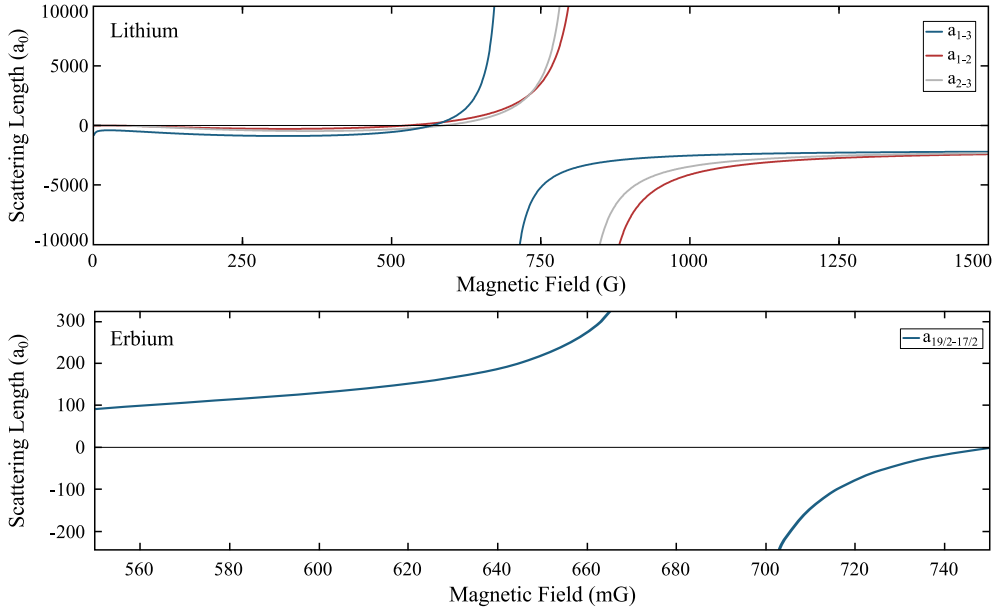

Figure 2.3: Feshbach Resonances. The upper plot shows the scattering lengths between each two of the three lowest spin states of ^{6}Li. Each combination shows one Feshbach resonance with a diverging scattering length. The lower plot shows one example of an s-wave Feshbach resonance for ^{167}Er [102] between its two lowest spin states (note the different scaling of the x-axis).

in lithium and erbium, show qualitatively different behaviour. While lithium features a single FR, that spans over hundreds of Gauss, the shown FR of ^{167}Er has a width of only a few mG and additionally many further close overlapping FRs (not shown in the plot, refer to [102] or Chapter 5). However, the required relative magnetic field stability for a precise tuning of the scattering length in both systems is similar, paving the route to the study of BEC-BCS crossover physics also in dipolar quantum gases.

Tuning Dipolar Interaction

In the erbium machine we furthermore have the ability to also tune the magnetic dipole-dipole interaction. To this end we employ a set of three coils around the experimental table to freely rotate the magnetic field axis [81]. In an elongated dipole trap, this enables to tune the mean interaction energy in the atomic cloud from positive (dipoles mainly aligned *head-to-tail*) to negative (dipoles mainly aligned *side-by-side*). In an optical lattice this can be used to switch off the dipolar interaction along one particular axis by rotating the magnetic field such that the angle to the lattice axis is $\theta_m = 54.7\,^\circ$.

Part II

Interacting Dipolar Fermi Gases

Chapter 3

Properties of Erbium

The rare-earth atom erbium is mostly known from its application in optical amplifiers in the telecommunication regime [105]. In an erbium-doped fiber amplifier, the trivalent cation Er^{3+} is optically pumped at around 980 nm or 1440 nm and radiates at around 1530 nm via stimulated emission. Moreover, recent experiments have shown that Erbium might also play an important role in the development of integrated photonic devices [106, 107].
For ultracold-atom experiments however, erbium is particularly interesting because of its large magnetic moment of $7\mu_{\mathrm{Bohr}}$, which comes along with strong dipolar interaction (see Sec. 2.2), but also because of its very rich and complex electronic level structure, offering hundreds of optical transitions with linewidths ranging from tens of Megahertz down to linewidths of only a few Hertz. Such richness of course comes with the disadvantage of complexity, which sometimes also aggravates the development of new methods in the laboratory. First experiments on laser cooling erbium were already done in 2006 [108] but it took until 2012 to produce the first Bose-Einstein condensate of erbium [42] and until 2014 to cool a fermionic isotope to quantum degeneracy [48].
In this chapter we present the main atomic properties of erbium and give a brief overview of the optical setup that we have available in the laboratory.

3.1 Atomic Properties of Erbium

Erbium has an atomic number of $Z = 68$ and features six stable isotopes with natural abundances as shown in Fig. 3.1 (a). In the experiment we can readily switch between the four most abundant isotopes, three bosonic isotopes ^{166}Er, ^{168}Er, ^{170}Er and one fermionic isotope ^{167}Er. Erbium is located in the lanthanide block of the periodic table and therefore has a rather complicated electronic structure: the $6s$ shell gets filled with 2 valence electrons before the $4f$ shell starts to get populated with the remaining 12 electrons. There are hence two vacancies in the $4f$ shell, resulting in a so called *submerged* shell structure. The electronic configuration of the ground state is typically written as

$$[\mathrm{Xe}]4\mathrm{f}^{12}6\mathrm{s}^2,$$

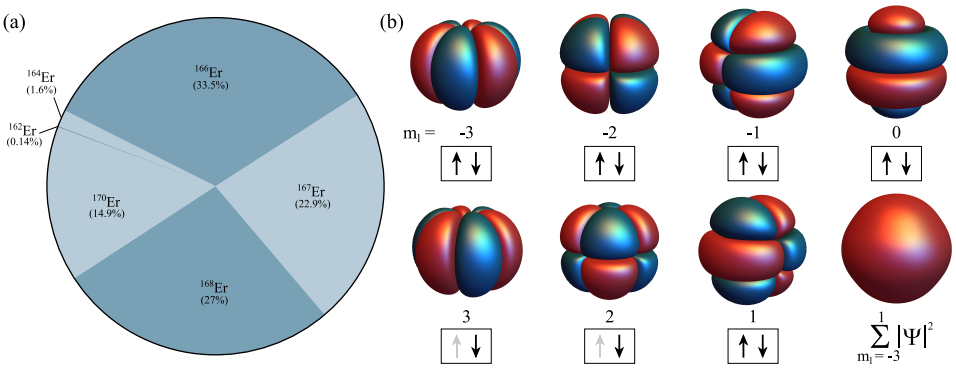

Figure 3.1: Properties of erbium. (a) Natural abundances of stable isotopes of erbium. In the experiment, we can readily switch between four most abundant isotopes: ^{166}Er, ^{168}Er, ^{170}Er (bosonic) and ^{167}Er (fermionic). (b) Isosurface plots of the electron wave functions (red = positive, blue = negative) of the 4f orbitals for different m_l quantum numbers (general set) and the anisotropic electron density of erbium $\sum_{m_l=-3}^{1} |\Psi_{m_l}|^2$.

where [Xe] represents the electronic configuration of the ground state of Xenon. The contour plots in Fig. 3.1 (b) illustrate the electronic $4f$ wave functions, of which the $m_l = 3$ and $m_l = 2$ states are only occupied with a single electron. These two electron vacancies are responsible for an anisotropic electronic wave function around the core (see bottom right panel in Fig. 3.1 (b)). In contrast to alkali and earth-alkali atoms that are commonly used in cold-atom experiments, erbium offers very large quantum numbers in its ground state, $L = 5$, $S = 1$ and $J = 6$. All bosonic isotopes have a nuclear spin of $I = 0$, and therefore no hyperfine structure, while the fermionic isotope ^{167}Er has a nuclear spin of $I = 7/2$, and hence a total angular momentum ranging from $F = J + I = 19/2$ to $F = J - I = 5/2$ in the ground-state manifold, which we illustrate in Fig. 3.2 (b). The anisotropic nature of the electronic configuration and the large quantum numbers in the ground state are responsible for the main atomic properties that make erbium interesting for cold-atom experiments.

3.2 Energy Spectrum and Optical Setup

Currently, the NIST database reports 674 energy levels for neutral Erbium with total angular momenta quantum numbers ranging from $J = 1$ to $J = 12$ [109] and 232 observed spectral lines [110] between 877 nm to 336 nm. Recent theoretical work predicts many further energy levels and dipole allowed transitions [111], that have not yet been observed experimentally. A significant attribute of the spectrum is the very broad transition at 401 nm with a linewidth of around $2\pi \times 30$ MHz [81] but also a plurality of narrow lines in the kHz or even Hz-regime. Neutral erbium has an ionization threshold of 49262 cm^{-1}, corresponding to a wavelength of 203 nm. Fig. 3.2 (a) shows the spectrum of energy levels of erbium as a function of the total angular momentum and indicates all laser frequencies that are used in our experiment. For ground-state erbium, only the transitions starting from the $J = 6$ ground state

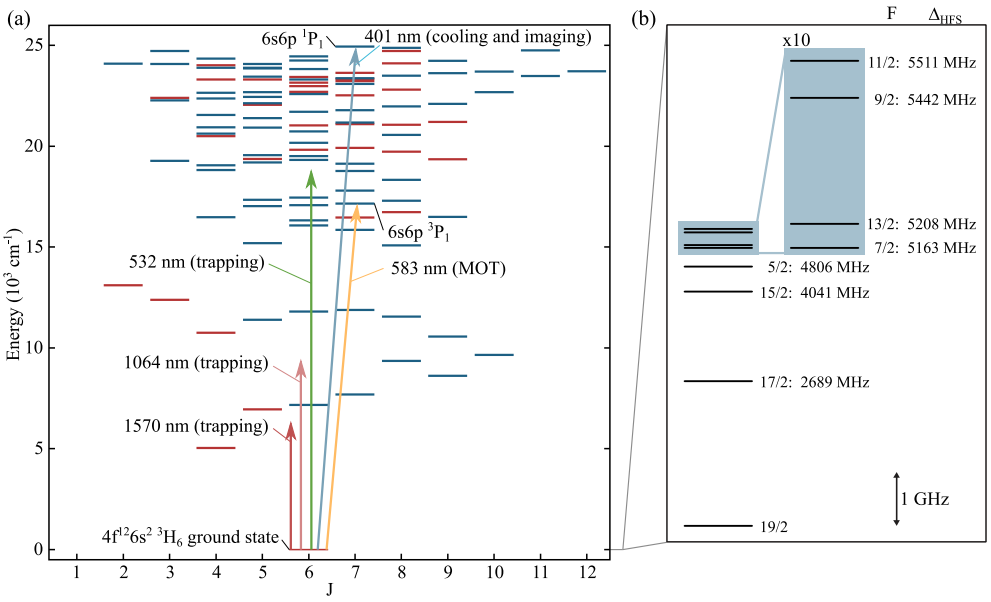

Figure 3.2: Energy spectrum of erbium. (a) Level scheme of erbium in the experimentally relevant region for all angular-momentum states $J \in [1, 12]$. Blue and red levels indicate different level parity. The arrows represent all laser frequencies that we use in the experiment. There are two resonant lasers, one for Zeeman-slower, transversal cooling and imaging (401 nm) and the other for the MOT (583 nm). The three off-resonant lasers are used for optical dipole traps (1064 nm and 1570 nm) and the optical lattice (532 nm). (b) Zoom-in on the fermionic ground state with hyperfine splitting and 8 different sublevels $F \in \{19/2...5/2\}$. Figure taken and adapted from [82].

are relevant. There is a variety of different optical transitions to choose from but besides the linewidth also branching ratios to metastable states and the availability of laser sources is important for the usefulness in the experiment. Suitable transitions for an efficient cooling of erbium have been discussed in the literature [112, 113] and a few lines have been already experimentally characterized [114, 115].

As already mentioned before, we use the broadest transition at $\lambda = 401\,\text{nm}$ with a linewidth of $\Gamma \approx 2\pi \times 30\,\text{MHz}$ for the Zeeman slower, the transversal cooling and for imaging of the atomic sample. The laser light is derived from a Toptica TA-SHG laser module and locked on the spectroscopic signal of a hollow cathode lamp. The MOT profits from the relatively narrow line at $\lambda = 583\,\text{nm}$ with a linewidth of $\Gamma \approx 2\pi \times 190\,\text{kHz}$. The light is generated by a Radiant Dyes Dye laser, which is locked onto a ULE cavity. We are furthermore using three off-resonant lasers for creating optical dipole traps and for our optical lattice. We employ two crossed-beam optical dipole traps, one at $\lambda = 1064\,\text{nm}$ (Mephisto MOPA, Coherent), which we primarily use for the bosonic isotopes, and the other at $\lambda = 1570\,\text{nm}$ (NKT Photonics), which is used for the fermionic isotope (cf. [81, 82, 116]). As described in [82, 117] we realize a three-dimensional optical lattice with a cuboid unit cell with lattice constants $(a_x, a_y, a_z) = (266\,\text{nm}, 266\,\text{nm}, 532\,\text{nm})$. To this end we interfere two laser beams at a wavelength of 532 nm with their retroreflected beams in the horizontal plane, which yields the lattice spacing $a_x, a_y = \lambda/2 = 266\,\text{nm}$ and similar with a laser beam at a

wavelength of 1064 nm along the z-axis.

3.3 Magnetic Properties of Erbium

As already mentioned before, due to the submerged $4f$ shell, most lanthanide atoms possess very large quantum numbers in their electronic ground state. Compared to alkali atoms this causes substantially larger dipolar effects. The magnetic moment μ of an atomic state with magnetic quantum number m_F can be calculated as

$$\mu = m_F g_F \mu_B \tag{3.1}$$

with μ_B being the Bohr magneton and g_F the Landé-factor for the given state. g_F is given by

$$g_F = g_J \frac{F(F+1) - I(I+1) + J(J+1)}{2J(J+1)}, \tag{3.2}$$

with g_J given by

$$g_J = 1 + (g_S - 1)\frac{J(J+1) - L(L+1) + S(S+1)}{2J(J+1)}. \tag{3.3}$$

Here g_S is the electronic Landé-factor $g_S \approx 2.0023$. Note that in the case of bosonic erbium without hyperfine structure ($I = 0$) the above equations evaluate to $g_F = g_J$. For the ground state of erbium we find the theoretic values $g_J = 1.16705$ and $g_F = 0.63157 \times g_J = 0.73503$ for the fermionic isotope, respectively. The experimentally reported value is slightly smaller, $g_J = 1.163801(1)$ [118]. For the state with maximal m_F, this hence results in a magnetic moment of

$$\mu_{\mathrm{Er}} = 6.982606(6)\mu_B. \tag{3.4}$$

As a comparison, lithium in its electronic ground state (at low magnetic field) features a magnetic moment of $\mu_{\mathrm{Li}} = 2/3\mu_B$ and hence the dipole-dipole interaction between two erbium atoms is a factor of $(\mu_{\mathrm{Er}}/\mu_{\mathrm{Li}})^2 \approx 110$ stronger than the dipolar interaction between two lithium atoms, see Eq. (2.12). Note that the magnetic moment depends on the magnetic sublevel m_F, of which there are 20 in the ground state, ranging from $-19/2$ up to $+19/2$. Furthermore g_J depends on the quantum number of the respective state and is different in excited states.

3.3.1 Erbium in an External Magnetic Field

When an atom in subjected to an external magnetic field B, energy levels with different magnetic moments split up due to the Zeeman-effect. In the case of bosonic erbium with zero nuclear spin I, the total angular momentum reads as $F = J = L+S$ and hence no hyperfine splitting occurs. As a consequence, in fields relevant for the experiments (i.e. 0-100 G, far below the Paschen-Back regime), the energy splitting is linear since the magnetic energy shift is much weaker than the spin-orbit coupling.

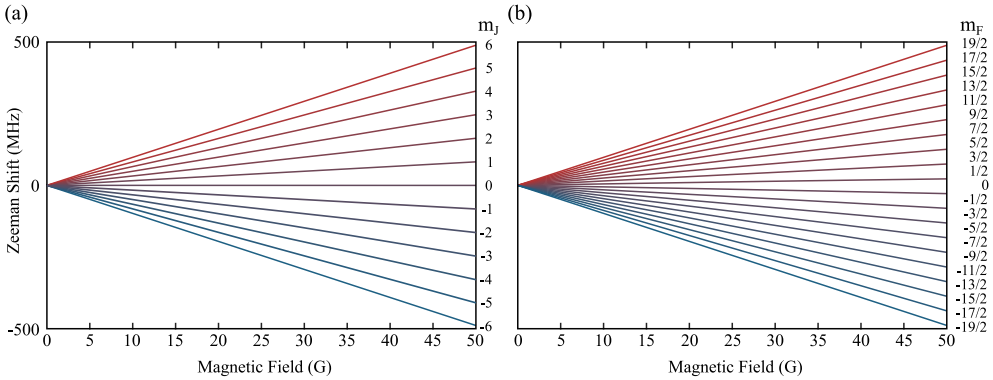

Figure 3.3: Zeeman splitting. (a) The bosonic isotopes has $F = 0$ and splits linearly into 13 levels $m_J \in \{-6...6\}$. (b) The fermionic isotope with $F = 7/2$ features 20 Zeeman sublevels $m_F \in \{-19/2...19/2\}$. Although the splitting looks perfectly linear in the graph, there is a small quadratic correction, as explained in the main text.

The energy levels split up according to

$$E_Z^{\mathrm{Bo}} = \mu B = m_J g_J \mu_B B. \tag{3.5}$$

Fig. 3.3 (a) shows a plot of the splitting of the ground state of bosonic erbium. The 13 magnetic sublevels $m_J \in \{-6, ..., 6\}$ are degenerate at zero magnetic field and split linearly in an external magnetic field without any quadratic contribution to the energy shift. The energy spacing between two adjacent levels is independent of the magnetic quantum number m_J,

$$\Delta E_Z^{\mathrm{Bo}} = g_J \mu_J B = 1.628879\,\mathrm{MHz/G} \times hB \tag{3.6}$$

with the Planck constant h. This comes with some complications when it comes to the investigation of spin-mixtures of bosonic erbium, since the coupling of two adjacent levels e.g. with a radio-frequency pulse always couples all 13 magnetic levels.
The scenario slightly changes for fermionic erbium where the hyperfine splitting comes into play. Also here, all 20 magnetic sublevels are degenerate at zero magnetic field and split linearly in small magnetic fields. However, when the magnetic energy is on the same order as the hyperfine coupling, the total angular momentum quantum number F ceases to be a good quantum number since the nuclear spin I and the electronic angular momentum J start to decouple. This leads to a deviation of the energy shift from its linear behavior. We plot the Zeeman-shift for all 20 sublevels in Fig. 3.3 (b). The quadratic correction to the linear shift is so small, that it cannot be seen in the figure (it will be discussed again and plotted in Chapter 5). In the experimentally relevant regime, this correction can be sufficiently captured by adding a quadratic term to Eq. (3.5),

$$E_Z^{\mathrm{Fe}} = m_F g_F \mu_B B + z(F^2 - m_F^2)B^2. \tag{3.7}$$

The quadratic correction vanishes for the two stretched states $m_F = \pm 19/2$ and is maximal for the $m_F = 0$ state. The linear term can directly be calculated as $g_F \mu_B = h \times 1.0287\,\mathrm{MHz/G}$, whereas the coefficient z is determined with a fit to the energy spectrum at low magnetic field [82] to be

$$z = -h \times 12.76(1)\,\mathrm{Hz/G^2}. \tag{3.8}$$

Although this quadratic correction is very weak, it causes the energy difference of two adjacent magnetic sublevels to be no longer degenerate. Instead it is given by

$$\Delta E_Z^{\mathrm{Fe}} = E_Z^{\mathrm{Fe}}(m_F) - E_Z^{\mathrm{Fe}}(m_F + 1) = g_F \mu_B B + z(m_F + 1)B^2. \tag{3.9}$$

Hence at sufficiently large magnetic fields, two adjacent levels can be coupled without coupling to other m_F state. This will become relevant in Chapter 5 for the initialization of spin mixtures.

Chapter 4

Anisotropic Polarizability of Erbium

Optical trapping of ultracold atoms relies on the ability of an atom to be polarized by the oscillating field of a laser beam. The basics of optical trapping were already presented in Section 2.1 and can be understood from a simple oscillator model [119]: The closer the wavelength of the laser is to the wavelength of an optical transition, the larger is its polarizability. The polarizability diverges on resonance and its sign depends on the detuning of the laser with respect to the optical transition.
The common approach to calculate the polarizability of an atom at a given laser frequency ω is hence to sum over all optical transitions, weighted by the detuning of the laser to the optical transition and by the strength of the optical transition, i.e. the dipole matrix element. In the case of alkali atoms, where the ground-state polarizability is almost completely determined by the $D1$ and $D2$ transitions, the good spectroscopic knowledge of those transitions enables an accurate calculation of the ground-state polarizability [91]. In contrast, for electronically more complex elements, such as erbium or dysprosium, there are hundreds of optical transitions from the ground state with linewidths ranging from many MHz down to only a few Hz. Moreover, reliable spectroscopic data is only available for very few of those transitions, aggravating a direct calculation of the polarizability.
To tackle this problem, electronic-structure calculations [120] are used to model electronic properties of the atom and to extract all parameters of optical transitions so that the polarizability can again be calculated with a *sum-over-state* formula [96, 111, 121]. Hence an experimental investigation of the atomic polarizability presents an excellent testbed to verify the validity of such electronic-structure calculations and in the best case even to feed back important information that improve their predictive power.
Furthermore there is also an increasing experimental interest of gaining a better understanding of the atomic polarizability, in particular for atoms, where the polarizability can exhibit a significant anisotropic character. This is typically the case for atoms with an anisotropic electronic configuration around the core as it is the case for lanthanide atoms with a *submerged* 4f shell. Applications where a precise knowledge

of the polarizability is required are e.g the determination of magic wavelengths for clock transitions [122, 123], the use of tuneout wavelengths in cold-atom experiments [124–127] or the realization of state-dependent potentials [128–132].

This chapter presents an experimental investigation of the anisotropic polarizability of erbium atoms and compares the measured values to calculations based on semiempirical electronic-structure calculations [111]. We briefly introduce the concept of anisotropic polarizability and the main formulas that are used for our calculations. We then present measurements of the scalar and the tensor contribution of both the ground-state and the 583 nm excited-state polarizability for three different wavelengths, that are particularly relevant for optical trapping. We also theoretically explore the usability of near-resonant light shifts for a precise tuning of optical potentials via vector and tensor polarizabilities. The content of this chapter was published in [133].

4.1 Anisotropic Polarizability

An isotropic medium subjected to an electric field $\vec{E}$ gets polarized parallel (or antiparallel) to the applied electric field. The response of the medium to the field is described by the polarizability α and the induced dipole moment $\vec{p}_\parallel$ reads as

$$\vec{p}_\parallel = \alpha \vec{E}. \tag{4.1}$$

For an isotropic medium such as an alkali atom in its electronic ground state, α is a complex scalar. However, in the case of multi-electron lanthanide atoms with a submerged-shell structure, the atomic polarizability can exhibit a tensorial structure, due to the anisotropic electronic configuration. In that case an electric field might also induce a dipole moment $\vec{p}_\perp$ with a component perpendicular to the electric field. To better understand those two contributions, it is instructive to consider the total energy shift experienced by the atom in an electric field,

$$U = \frac{1}{2}\vec{E}^\dagger \mathcal{P} \vec{E}. \tag{4.2}$$

Here $\mathcal{P}$ is the 3×3 polarizability tensor, whose diagonal entries describe the scalar response of the atom ($\vec{p}_\parallel$) and whose off-diagonal entries can induce anisotropic effects ($\vec{p}_\perp$). We can decompose the polarizability tensor $\mathcal{P}$ into the scalar polarizability tensor $\mathcal{A}_s$, containing only the diagonal entries, the vector polarizability tensor $\mathcal{A}_v$, which is the antisymmetric part of $\mathcal{P}$ and the tensor polarizability tensor $\mathcal{A}_t$, the symmetric part of the off-diagonal entries. With this decomposition, we identify the three following contributions to the total light shift

$$\begin{aligned} U_{\text{tot}} &= U_s + U_v + U_t \\ &= \frac{1}{2}\vec{E}^\dagger [\mathcal{A}_s + \mathcal{A}_v + \mathcal{A}_t] \vec{E}, \end{aligned} \tag{4.3}$$

that we call the scalar, vector, and tensor light shift, U_s, U_v, and U_t, respectively.

Let us now consider the case of an atom with angular momentum J and magnetic quantum number m_J, placed in a laser field of intensity $I(\vec{r}) = \frac{\epsilon_0 c}{2}|\vec{E}(\vec{r})|^2$, polarization vector $\mathbf{u}$ and frequency $\omega = 2\pi\frac{c}{\lambda}$. ϵ_0 is the vacuum permitivity, λ the wavelength of the laser and c the speed of light. Following the derivations in Refs. [111, 134] the above expression can be developed and an explicit equation for the three terms can be written down as

$$\begin{aligned} U(\vec{r},\omega) &= U_s + U_v + U_t \\ &= -\frac{1}{2\epsilon_0 c} I(\vec{r})\Big[\alpha_s(\omega) + |\mathbf{u}^* \times \mathbf{u}| \cos\theta_k \frac{m_J}{2J}\alpha_v(\omega) \\ &\quad + \frac{3m_J^2 - J(J+1)}{J(2J-1)} \times \frac{3\cos^2\theta_p - 1}{2}\alpha_t(\omega)\Big] \\ &=: -\frac{1}{2\epsilon_0 c} I(\vec{r})\alpha_{\mathrm{tot}}(\omega). \end{aligned} \tag{4.4}$$

We call α_{tot} the total polarizability, i.e. the sum over the scalar, the vector (linear in m_J) and the tensor (quadratic in m_J) contribution to the total light shift. While the scalar term only depends on ω and the spectral properties of the atomic species, the latter two also depend on the internal state of the atom $|J, m_j\rangle$ and also the polarization and propagation axis of the laser field. As illustrated in the inset of Fig. 4.1, θ_k (θ_p) is the angle between the propagation (polarization) axis and the quantization axis, set by the external magnetic field. More precisely, θ_k is the angle between the vector $\vec{v} = \mathbf{u}^* \times \mathbf{u}$ and the quantization axis. The three polarizability coefficients $\{\alpha_s, \alpha_v, \alpha_t\}$ can be expressed in terms of the so called coupled polarizability $\alpha_J^{(K)}$ as

$$\begin{aligned} \alpha_s(\omega) &= -\frac{1}{\sqrt{3(2J+1)}}\alpha_J^{(0)}(\omega) \\ \alpha_v(\omega) &= \sqrt{\frac{2J}{(J+1)(2J+1)}}\,\alpha_J^{(1)}(\omega) \\ \alpha_t(\omega) &= \sqrt{\frac{2J(2J-1)}{3(J+1)(2J+1)(2J+3)}}\,\alpha_J^{(2)}(\omega), \end{aligned} \tag{4.5}$$

where $\alpha_J^{(K)}$ can be calculated with a sum-over-state formula [135] and in constant-sign convention is given by

$$\begin{aligned} \alpha_J^{(K)}(\omega) &= \sqrt{2K+1} \times \sum_{(J')} (-1)^{J+J'} \\ &\quad \begin{Bmatrix} 1 & K & 1 \\ J & J' & J \end{Bmatrix} |\langle J'||\mathbf{d}||J\rangle|^2 \times \\ &\quad \frac{1}{\hbar}\Re\underbrace{\left[\frac{1}{\Delta^-_{J'J} - i\gamma_{J'}/2} + \frac{(-1)^K}{\Delta^+_{J'J} - i\gamma_{J'}/2}\right]}_{=:A}. \end{aligned} \tag{4.6}$$

with $K \in \{0, 1, 2\}$. The sum runs over all excited states, whereas the dipole selection rules are incorporated into the Wigner $6j$ symbol (in curly brackets). $|\langle J'||\mathbf{d}||J\rangle|^2$ is the reduced dipole transition element, $\gamma_{J'}$ the natural lifetime of the excited state and $\Delta^{\pm}_{J'J} = \omega_{J'J} \pm \omega$ is either the difference or the sum of the transition frequency $\omega_{J'J}$ to the excited state and the laser frequency ω. Under the assumption that $\gamma_{J'}/2 << \Delta^{\pm}_{J'J}$, i.e. that the laser in far detuned to the optical transition, we can express the real part of the last line in Eq. (4.6) as

$$\Re[A] = \frac{2\omega_{J'J}}{\omega^2_{J'J} - \omega^2}. \tag{4.7}$$

Once all intrinsic atomic properties are know, the calculation of the polarizability hence boils down to the threefold evaluation of the sum in Eq. (4.6) and can be done at any wavelength ω. The imaginary part of the above expression is directly related to the off-resonant photon-scattering rate, it reads as

$$\Im[A] = \gamma_{J'} \frac{\omega^2_{J'J} + \omega^2}{\left(\omega^2_{J'J} - \omega^2\right)^2}. \tag{4.8}$$

From an experimental point of view, a good understanding of the photon scattering rate is crucial to realize dipole traps with low heating rates and low atom loss. Scattering rates can be calculated in a similar way by employing a slightly modified *sum-over-state* formula (cf. [111]).

From Eq. (4.6), a few interesting cases can be discussed. First of all, the Wigner $6j$ symbol $\begin{Bmatrix} j_1 & j_2 & j_3 \\ J_1 & J_2 & J_3 \end{Bmatrix}$ is invariant under permutation of any two columns and under exchanging the entries within any column [136]. Furthermore, the conservation of angular momentum is guaranteed by the constraint that all triples $\{(k_1, k_2, k_3), k \in \{j, J\}\}$ have to fulfill triangle rules, $|k_2 - k_3| \leq k_1 \leq k_2 + k_3$ and have to sum up to an integer. Together with the explicit formulas for the total light shift we find the following special cases:

1. **Alkali Atoms:** Alkali atoms have $J = 1/2$ in their electronic ground state. Hence $\alpha_t = 0$ and the tensor light shift U_t is zero. As a consequence, alkali atoms do not have a quadratic light shift in their electronic ground state and a state-dependent light shift can only be induced via the vector light shift U_v or by a detuning of the laser light that is comparable to the hyperfine splitting [137].

$$\boxed{U_t = 0}$$

2. **Linear Polarization:** For linear polarization of the laser beam, the polarization vector $\mathbf{u}$ is real and therefore $\mathbf{u}^* = \mathbf{u}$. The cross product $\mathbf{u}^* \times \mathbf{u}$ evaluates to zero and the vector light shift U_v vanishes.

$$\boxed{U_v = 0}$$

3. **Perpendicular Propagation:** For the case where the angle between the prop-

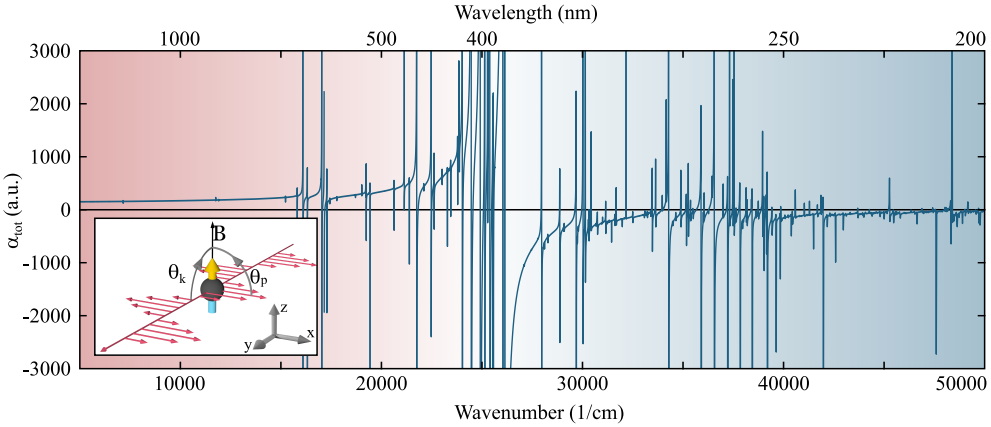

Figure 4.1: Calculated atomic polarizability. The plot shows the total polarizability for an erbium atom in its lowest Zeeman sublevel ($m_J = -6$) with $\theta_p = \theta_k = 90°$ as a function of wavenumber and wavelength of the light field. With the shown configuration (inset), U_v vanishes and U_t is maximally 'negative'. Each divergence of the total polarizability indicates an optical transition (finite amplitude of peaks are due to finite number of calculated points). There is a mostly blue-detuned region towards shorter wavelengths and a red-detuned region towards longer wavelengths as indicated by the back ground color.

agation axis of the laser beam and the quantization axis (magnetic field) is $\theta_k = 90°$, we have $\cos(\theta_k) = 0$ and the vector light shift vanishes.

$$\boxed{U_v = 0}$$

4. **Magic Angle:** If the angle between the polarization vector and the quantization axis is such that $\cos(\theta_p) = 1/\sqrt{3}$, i.e. $\theta_p \approx 54.7°$, the tensor light shift vanishes even though $\alpha_t \neq 0$.

$$\boxed{U_t = 0}$$

5. **Dependence on m_J:** For finite vector and tensor polarizability, the total light shift is state dependent and depends quadratically on m_J. This enables almost arbitrary tuning of the relative light shift between adjacent hyperfine states. If not explicitly stated otherwise, all shown calculations are performed for the $m_J = -6$ state.

4.2 AC-Polarizability of Erbium

As mentioned above, the calculation of the polarizability requires a good knowledge of the electronic spectrum and lifetimes of optical transitions. While the NIST database [138] only lists 232 observed optical transitions for neutral erbium, of which only a few contain the relevant information for the calculation of the polarizability, we base our calculations on a more detailed list from semiempirical electronic-structure calculations [111, 133]. The full list of states that was used for the calculations of the ground-state polarizability can be found as supplemental information of Ref. [133].

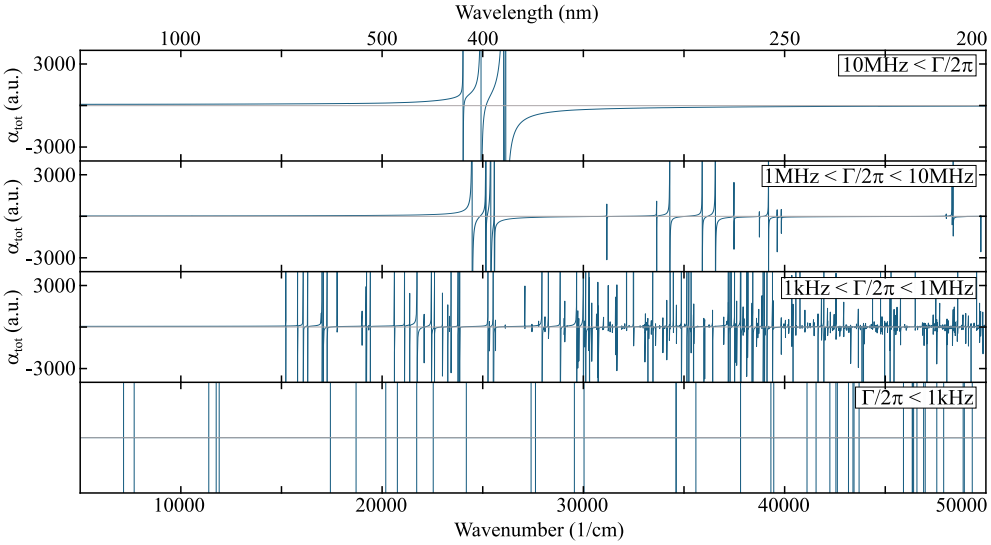

Figure 4.2: Different contributions to the total light shift. The four plots show the calculated polarizability for the same setting as in the previous figure but for each plot only lines with the indicated strength are taken into account. The lower plot does not show calculations of the polarizability but only indicates the narrow transitions with vertical lines.

For the calculations shown within this thesis, we replace the 401 nm and 583 nm lines with experimentally measured values from Ref. [81]. In the whole chapter, the results are given in atomic units (a.u.). The conversion to SI units is given by

$$\alpha[\mathrm{Hz/Wmm^2}] = \frac{1.6488 \times 10^{-35}}{2h\epsilon_o c}\alpha[\mathrm{a.u.}]. \tag{4.9}$$

Figure 4.1 shows the calculation of the total polarizability α_{tot} for an atom in the lowest state $m_J = -6$ as a function of the light's wavenumber and wavelength for the scenario depicted in the inset of the same figure, i.e. for linearly polarized light with $\theta_k = \theta_p = 90°$. As argued above, in this configuration the vector light shift U_v vanishes completely and the prefactor to the tensor light shift is maximally negative,

$$\alpha_{\mathrm{tot}}(\theta_p = 90°, \theta_k = 90°) = \alpha_s - \frac{1}{2}\alpha_t. \tag{4.10}$$

Each divergence of the polarizability indicates an optical transition. The finite height of some peaks is caused by a limited number of calculated data points. The main contribution to the total polarizability comes from the broadest optical transition ($2\pi \times 29.7\,\mathrm{MHz}$ [81]) at around 401 nm. Together with a few further relatively strong lines in the same region, it determines the main shape of the polarizability. In the region towards longer wavelengths the polarizability is predominantly positive, enabling the generation of attractive optical potentials, whereas in the region towards shorter wavelengths the polarizability is mainly negative, giving rise to repulsive optical potentials. On top of the broad transitions, there are hundreds of further transitions with linewidths ranging from the MHz down to the Hz-regime.
To better visualize this complex spectrum and in order to separate the contribution of

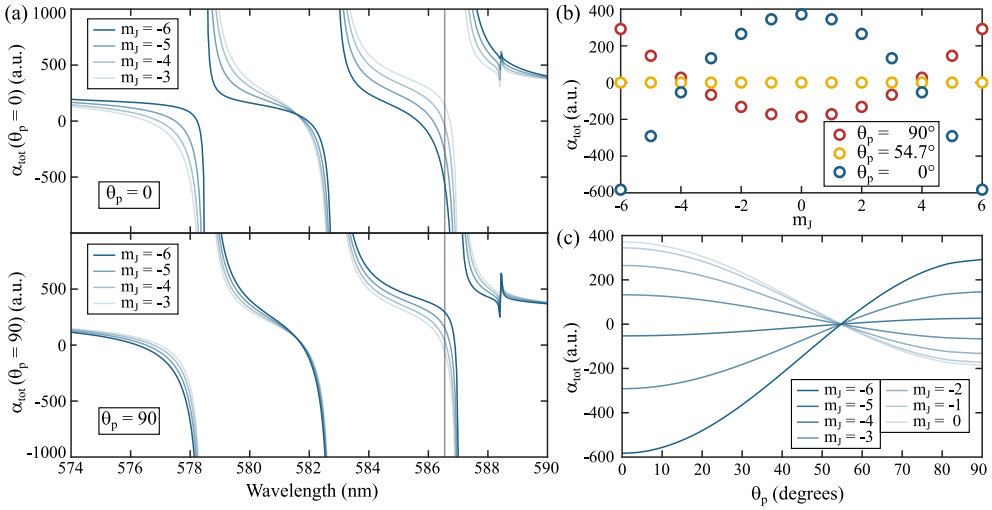

Figure 4.3: State dependent light shift. (a) Total polarizability in the proximity of the MOT transition for the four lowest hyperfine states $m_J \in \{-6, -5, -4, -3\}$ for two different polarization angles $\theta_p = 0°$ (top) and $\theta_p = 90°$ (bottom). (b) Total polarizability at 586.56 nm for all hyperfine states and three different polarization angles. (c) Total polarizability as a function of θ_p for the 7 lowest hyperfine states at 586.56 nm.

broad and narrow lines, Fig. 4.2 shows 4 plots with the same calculation as for Fig. 4.1 but for each plot only transitions within a certain linewidth region were taken into account. The upper plot shows that there are 4 optical transitions with linewidths above 10 MHz. All those transitions are located around 400 nm. The second panel shows that there are a few lines in the range of 1 MHz to 10 MHz, primarily located in the ultra-violet region. As shown in the third panel, by far the most transitions have a linewidth in the range of 1 kHz to 1 MHz. Some of them are in the visible region but also here the biggest part is located in the ultra-violet regime. Narrow transitions below 1 kHz are sparsely distributed over the whole plotted range as shown in the lowest panel. Note that this panel only indicates the positions of the narrow transitions and does not show the calculated polarizability.

As shown e.g. with Dy [125, 139] or Sr [140], narrow lines are particularly promising candidates for state-dependent trapping and manipulation of cold atoms due to large tensorial and vectorial light shifts. To show how the anisotropic light shift can be exploited for generating state-dependent potentials, we discuss possible applications of near-resonant laser light in a region with overlapping resonances. We choose the transition on which we operate our magneto-optical trap with $\lambda = 582.84$ nm, $J' = 7$, and a measured linewidth of $\Gamma = 186$ kHz [81]. Figure 4.3 (a) shows the calculation of α_{tot} for $\theta_k = 90°$ for two polarization angles $\theta_p = 0°$ (top) and $\theta_p = 90°$ (bottom) for 4 different spin states, $m_J \in \{-6, -5, -4, -3\}$. The two resonances at $\lambda_1 = 578.5$ nm and $\lambda_2 = 587$ nm have total angular momentum of $J_1' = 5$ and $J_2' = 6$, which explains the asymmetric behavior around the MOT transition (e.g. the presence of the magic wavelength below the MOT transition but not above). However, a change of the polarization angle by 90 degrees has an enormous effect on the total light shift. This

behavior is summarized in (b) and (c) at the example wavelength $\lambda^* = 586.56\,\mathrm{nm}$, which is indicated by the grey line in (a). For each angle θ_p the total polarizability depends quadratically on the magnetic quantum number m_J. This quadratic behavior disappears at the magic angle of $\theta_{p0} \approx 54.7°$, where the tensor light shift U_t vanishes (see Eq. (4.9)). For the particular wavelength λ^*, the light shift for each spin state even flips its sign at the magic angle. This becomes even clearer in the plot in (c), where we plot the total polarizabilities for 7 different hyperfine states as a function of the polarization angle θ_p. The state dependency of the polarizability vanishes at θ_{p0} and the different hyperfine levels even flip their energetic order. In fact the wavelength λ^* was chosen such that $\alpha_s = 0$ and hence the total light shift vanishes at the magic angle. By using also the vector light shift or the magnetic field dependence of the coupling to excited states with different g-factors g_J, one can almost arbitrarily tune the relative light shift [141].

4.2.1 Measurement of Ground-State Polarizability

We experimentally access the polarizability of the ground state by measuring the depth of the optical potential, which is induced by an off-resonant laser beam. To this end we measure trap frequencies and relate them to the total polarizability α_{tot}. For a laser beam propagating along the x-axis with total power P and Gaussian radial intensity profile $I(y,z) = I_0 \exp(-\frac{2y^2}{\sigma_y^2} - \frac{2z^2}{\sigma_z^2})$ with beam waists $\sigma_{y/z}$ along the two orthogonal directions perpendicular to the propagation axis and $I_0 = \frac{2P}{\pi\sigma_y\sigma_z}$, the depth of the induced optical potential is given by

$$U_0 = -\frac{P}{\epsilon_0 c\pi\sigma_y\sigma_z}\alpha_{\mathrm{tot}}. \tag{4.11}$$

In harmonic approximation the depth U_0 can be related to the trap frequencies ω_i, $i \in \{z, y\}$ via

$$\omega_i = \sqrt{\frac{-4U_0}{\sigma_i^2 m}}, \tag{4.12}$$

with the atomic mass m. Combining the two above equations yields the expression

$$\alpha_{\mathrm{tot}} = \omega_i^2 \epsilon_0 c\pi m \frac{\sigma_y\sigma_z\sigma_i^2}{4P}. \tag{4.13}$$

Hence to deduce the total polarizability from trap frequency measurements, a precise characterization of the trapping beam is necessary. In particular the beam waists σ have to be measured as precise as possible, because of the σ^4 scaling of α_{tot}. We measure the power in the beam with a power meter and stabilize the light power with a PID loop onto a photo diode to avoid power drifts in the course of the measurement. The most reliable measurement of the beam waists was done using the knife edge method [142] or using a beam profiler camera mounted on a piezo-controlled translation stage. This allows us to measure the beam waist at multiple points along the beam propagation axis. Figure 4.4 shows a typical such measurement from which we extract the beam waist σ_i, $i \in \{y, z\}$, by fitting the data with $\sigma(z) = \sigma_i\sqrt{1 + (z/z_R)^2}$,

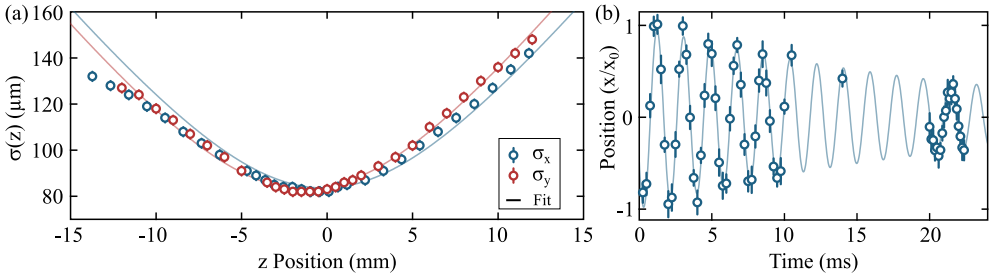

Figure 4.4: Trapping-beam characterization. (a) Typical beam waist measurement of trapping beam. We plot the radial size of the beam along the propagation axis and fit the data to extract the beam waists σ_i along both axes. (b) Typical trap frequency measurement with damped sine fit.

with the Rayleigh range $z_R = \pi\sigma_i^2/\lambda$. To reduce deviations between the trapping beam and the beam for the measurement of the waist to a minimum, we implement a mirror directly in front of our vacuum chamber and reflect the trapping beam in order to perform the beam-waist measurement as close to the atomic position as possible.

Despite a careful characterization of the beam waist, we assume a systematic uncertainty of 2 μm due to aberrations and a finite ellipticity of the beam. Because of the σ^4 scaling this is the major contribution to the uncertainty of the polarizability. Trap frequencies are measured by exciting a center-of-mass oscillation of the atomic cloud in the optical trap and monitoring the position of the atoms over time. For the measurement of the total ground-state polarizability we choose $\theta_k = \theta_p = 90°$, such that the vector light shift vanishes ($U_v = 0$) and the tensor contribution is maximally negative. In that case, the total polarizability is given by Eq. (4.10). Figure 4.4 shows a typical trap frequency measurement in a single-beam optical dipole trap of wavelength $\lambda = 1064.5\,\text{nm}$. We extract the trap frequency by fitting a damped sine function.
From the measurements of the beam waists and the trap frequencies we compute the total light shift and deduce the total polarizability for three different wavelengths, 532.26 nm, 1064.5 nm, and 1570.0 nm. The following table summarizes the experimental results and gives the calculations for the same wavelengths for $\theta_k = \theta_p = 90°$.

λ (nm)	$\alpha_{\text{tot}}^{\text{exp}}$	$\alpha_{\text{tot}}^{\text{theo}}$
532.26	$430 \pm 8_{\text{st}} \pm 80_{\text{sys}}$	317
1064.5	$166 \pm 3_{\text{st}} \pm 61_{\text{sys}}$	176
1570.0	$163 \pm 9_{\text{st}} \pm 36_{\text{sys}}$	162

As mentioned above, the large systematic uncertainty is caused by the uncertainty of the beam waist. We find a good overall agreement between the measured and calculated polarizabilty, in particular the measurement of the two wavelengths in the infrared region match very nicely with the theoretical predictions. As can be seen in Fig. 4.2 the light shift at those wavelengths is not significantly affected by many optical transitions and mainly determined by the broad optical transitions around 400 nm so that a reliable prediction can be made. However the polarizability at

532.26 nm significantly deviates from the theoretical value even beyond the systematic uncertainty. We attribute this to the presence of many strong and narrow transitions in the proximity of that wavelengths and small uncertainties of their parameters can have a large effect on the calculated polarizability. Nevertheless, the overall agreement is very satisfying.

4.2.2 Anisotropic Ground-State Polarizability

Although the above measurements showed a good overall agreement between measurement and theory for the total light shift, they do not tell anything about different contributions to the light shift. With the vector light shift being zero for $\theta_k = 90°$, we perform an additional measurement to isolate the scalar and the tensorial contributions to the total light shift. To this end we measure trap frequencies for different angles θ_p by either rotating the magnetic field or the linear polarization of the trapping beam with a waveplate, while keeping $\theta_k = 90°$. In order to eliminate systematic uncertainties that may arise from the beam waist measurement, we investigate the relative change of the total light shift and quantify this change via the parameter $\kappa(\theta_p)$ with

$$\begin{aligned} \kappa(\theta_p) &= \frac{U - U_s}{U_s} = \frac{U_t}{U_s} = \frac{\omega(\theta_p)^2 - \omega(\theta_{p0})^2}{\omega(\theta_{p0})^2} \\ &= \frac{3m_J^2 - J(J+1)}{J(2J-1)} \times \frac{3\cos^2\theta_p - 1}{2}\frac{\alpha_t}{\alpha_s}. \\ &\overset{J=6,m_J=-6}{=} \frac{3\cos^2(\theta_p) - 1}{2}\frac{\alpha_t}{\alpha_s}. \end{aligned} \tag{4.14}$$

Here θ_{p0} is such that $\cos(\theta_{p0}) = 1/\sqrt{3}$, i.e. the angle where the tensor light shift vanishes, $U_t(\theta_{p0}) = 0$. Note that for the maximally polarized state, $m_J = \pm J$, the prefactor in the second line evaluates to 1 so that the peak-to-peak variation of κ is given by $\kappa_0 = 1.5 \times \frac{\alpha_t}{\alpha_s}$, from which also an absolute value for the tensor polarizability can be deduced. Figure 4.5 summarizes the measurements for the two wavelengths 532.26 nm and 1064.5 nm. For both wavelengths there is a sinusoidal dependence of the total light shift on the polarization angle θ_p. We fit the data with Eq. (4.14) to extract κ_0 and use κ_0 and the measured scalar polarizabilities to calculate α_t. The dotted lines in the plot are the expected curves for $\kappa(\theta_p)$ using the calculated scalar and tensor polarizability, α_s and α_t respectively. From the fit we find the following values for κ_0 and for α_t.

λ (nm)	$\kappa_0^{\mathrm{exp}}(\%)$	$\kappa_0^{\mathrm{th}}(\%)$	α_t^{exp}	α_t^{th}
532.26	-5.3 ± 1	-9.2	$-15 \pm 3_{\mathrm{st}} \pm 6_{\mathrm{sys}}$	-19
1064.5	-1.8 ± 0.8	-4.7	$-1.9 \pm 0.8_{\mathrm{st}} \pm 1.2_{\mathrm{sys}}$	-5.4

For both wavelengths we measure slightly smaller tensorial effects than predicted by the calculations, but the agreement is still satisfying. The deviations might be due to the very small changes in trap frequencies, which might be affected by additional systematic effects in the measurements.
As a comparison, the erbium tensor polarizability for 1064.5 nm is similar but slightly

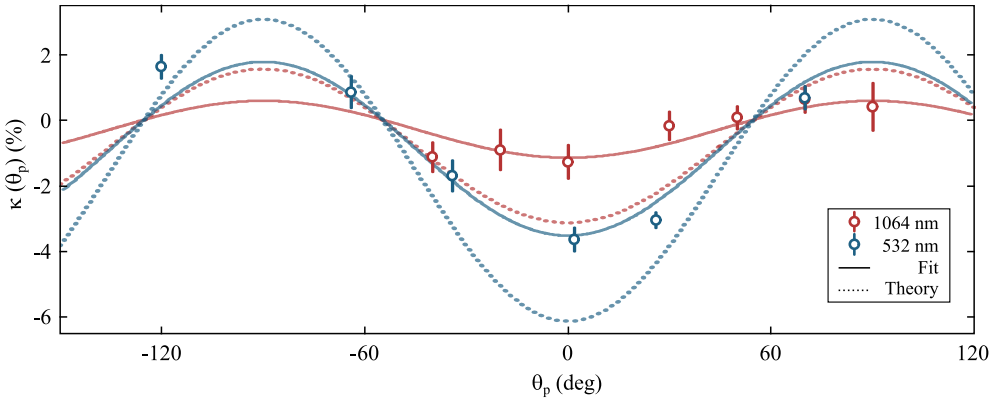

Figure 4.5: Anisotropic ground-state polarizability. The plot shows the anisotropy parameter of the light shift κ for 532.26 nm (blue) and 1064.5 nm (red). The measured values show a sinusoidal dependence on the polarization angle θ_p. Solid lines are fits to the data, dotted lines are theory curves. For both wavelengths the measured anisotropy is slightly smaller than expected from theory.

larger than the dysprosium tensor polarizability, which was recently measured to be $\{\alpha_s, \alpha_t\} = \{184.4(2.4), 1.7(6)\}$ [143]. Given the complexity of the erbium atomic spectrum, the overall agreement between theoretical predictions and the experimental values for all investigated wavelengths is remarkable.
However, we further test the electronic-structure calculations and finally investigate the 583 nm excited-state polarizability, where anisotropic effects are expected to be larger than in the ground state.

4.2.3 Excited-State Polarizability

Anisotropic effects are expected to be stronger in excited states due to the even more anisotropic electronic wave function. We therefore investigate the light shift of the 583 nm excited state (MOT transition, 17157 cm^{-1}, $J' = 7$) to further test the calculated spectrum of erbium. For the chosen state we cannot perform trap frequency measurements due to its short lifetime. We therefore extract the light shift by measuring the shift of the bare atomic resonance frequency. Experimentally this is done by applying a short laser pulse of circularly polarized 583 nm light to the atomic sample in the optical dipole trap. This polarization couples the $|J = 6, m_F = -6\rangle$ ground state to the $|J = 7, m_F = -7\rangle$ excited state. As shown in Fig. 4.6 (a) the trap induces a different light shift in the ground and the excited state and therefore shifts the resonance frequency. By scanning the laser frequency around the atomic resonance we find a resonant atom loss whenever the laser frequency matches the sum of the atomic transition, the ground-state light shift and the excited-state light shift. To calculate the ground-state light shift we use the measured ground-state polarizability and neglect its angle dependence since the anisotropic effects are two orders of magnitude smaller than in the excited state. Figure 4.6 (b) shows the measured light shift of the excited state for $\theta_k = 90°$ as a function of θ_p for the two wavelengths $\lambda = 1064.5$ nm and $\lambda = 1570$ nm. The scalar polarizabilities of both wavelengths have opposite sign and therefore cause a repulsive potential for $\lambda = 1064.5$ nm and an attractive po-

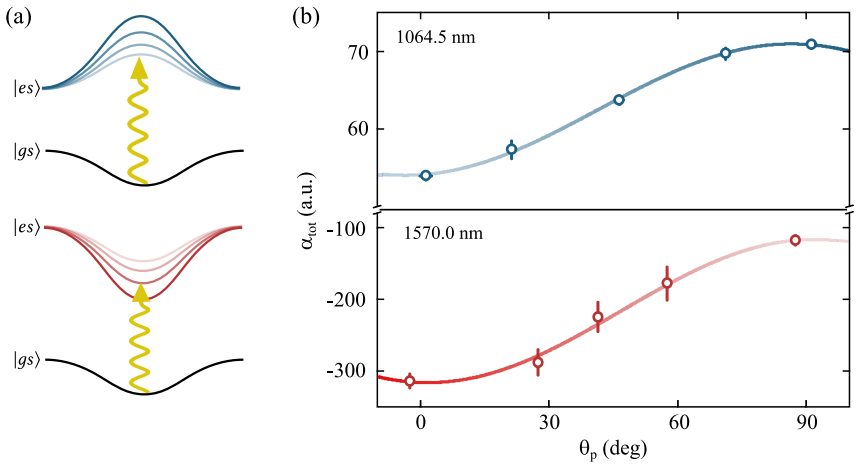

Figure 4.6: Measurement of excited-state polarizability. (a) Instead of performing trap frequency measurements, we measure the shift of the bare transition frequency from the ground to the excited state, induced by the optical dipole trap. The light shift of the excited state can either be repulsive (upper panel) or attractive (lower panel) and depends on the angle θ_p as indicated by the different shades of the excited state. (b) Measurement of total polarizability as a function of θ_p for the two wavelengths 1064.5 nm (top) and 1570.0 nm (bottom). Solid lines are a fit to the data. Color gradient of solid lines correspond to color shades in (a).

tential for $\lambda = 1570\,\text{nm}$. However, the tensor polarizability have the same sign, so that they tune equally with θ_p. The total light shift shows a strong dependence on θ_p, which is much stronger than the measured anisotropies in the ground state. The tensor polarizability α_t is even on the same order as α_s, so that the total light shift can be substantially changed by changing the angle θ_p. We fit the data with Eq. (4.4) and extract the scalar and tensor polarizability. For the two wavelengths we find the following results.

λ (nm)	α_s^{exp} (a.u.)	α_s^{th}(a.u.)	α_t^{exp} (a.u.)	α_t^{th} (a.u.)
1064.5	$66.6 \pm 0.5_{\text{st}} \pm 28_{\text{sys}}$	91	$-11.3 \pm 0.5_{\text{st}} \pm 2_{\text{sys}}$	-18
1570.0	$-203 \pm 9_{\text{st}} \pm 50_{\text{sys}}$	-254	$-141 \pm 9_{\text{st}} \pm 19_{\text{sys}}$	-68.5

Again, the large systematic uncertainties are caused by the systematic errors of the ground state polarizability, that in turn are caused by the uncertainty of the beam-waist measurements. Nevertheless, considering the complex electronic structure of erbium, the agreement between the measured and calculated values is surprisingly good. In particular, as we show in Fig. 4.7, the two investigated wavelengths are surrounded by many broad and narrow optical transitions. This is different in the ground state, where there are only very few transitions in the infrared.

All in all we find good agreement between calculated and measured values of the polarizability for all investigated wavelengths both for the ground and the excited state. In particular the measurement of the ground-state scalar polarizability of the infrared wavelengths agrees excellently with the predicted values. We measure a small but finite anisotropic effect in the ground state and showed that the 583 nm excited

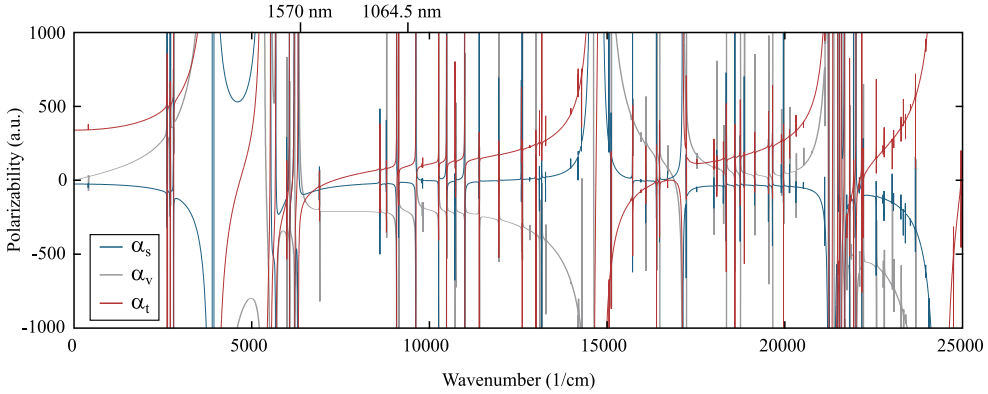

Figure 4.7: Calculated excited-state polarizability. The plot shows the scalar (blue), vector (grey) and tensor (red) polarizability of the 583 nm excited state. There are many optical transitions in the proximity of the two experimentally investigated wavelengths of 1064.5 nm and 1570 nm. Given this complex structure, the agreement between measured and calculated polarizabilities is surprisingly good. The shown calculations for the excited state polarizability were done by M. Lepers.

state exhibits much stronger anisotropic light shifts, which are caused by the many optical transition in the proximity of the investigated wavelengths. Although there are still large uncertainties on the measured values, the results prove a good understanding of the level structure of erbium. Our results do not only test semiempirical electronic-structure calculations [111] but might also enable the use of near resonant light in order to exploit large vector and tensor light shifts for generating m_J-dependent optical potentials, to control the energy landscape on the different hyperfine levels [141] and to use the quadratic light shift to initialize and control spin dynamics [144].

Chapter 5

A Strongly Interacting Fermi Gas of Dipolar Atoms

Despite the significant number of machines with utracold dipolar gases [37, 41, 42, 47, 48, 145–147], only very few experiments with fermionic species were conducted [139, 148–150]. In particular, those experiments only investigated spin-polarized Fermi-systems and did not exploit the spin degree of freedom. In fact, dipolar atoms, such as Er or Dy, posses large quantum numbers in their ground state and therefore offer a huge number of spin states. For instance, fermionic ^{167}Er has a total angular momentum of $F = 19/2$ and hence 20 hyperfine states. Such a system offers the possibility to explore spin physics with many different internal states and to study the effect of dipolar interaction in spinor systems.
At least in the case of erbium atoms, the reason for the lack of experiments on fermionic spinor gases is threefold. On the one hand the investigation of fermionic systems with strong dipolar interaction is hindered by complex scattering dynamics [98] and the presence of many higher-order Feshbach resonances even between identical spin states. For spin mixtures, the number of Feshbach resonances is expected to be even higher [139], eventually leading to Ericson fluctuations [151] at high magnetic field, which makes it even harder to find a magnetic field region with a long lifetime and high collisional stability. A further complication is the spontaneous relaxation of the atomic spin since the dipole-dipole interaction only conserves the total angular momentum, but not the spin [148, 152]. Finally, in the case of fermionic erbium, the *weak* hyperfine coupling further aggravates the deterministic preparation of multi-component spin systems. In the magnetic-field region at around 1 G, where our experiments are conducted, the *quadratic* Zeeman splitting is almost negligible and hence a standard spin initialization via radio-frequency (rf) coupling cannot be straightforwardly applied. For negligible quadratic Zeeman splitting, rf coupling of neighboring spin states would immediately couple to all further spin states due to the fact that all adjacent levels are equally spaced in energy (see Fig 5.1 (a)).

This chapter presents the first steps towards solving the described problems and studying spinor physics with fermionic erbium atoms. To this end we make use of

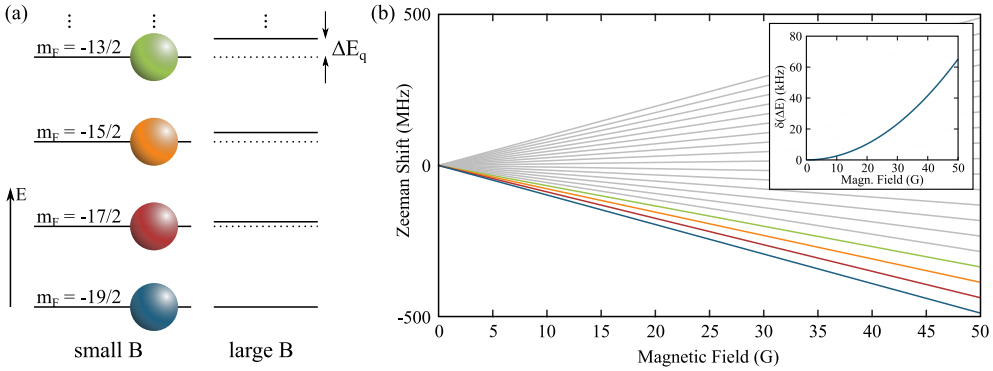

Figure 5.1: Quadratic Zeeman effect. (a) Schematic of erbium level scheme at low and large magnetic field. (b) Zeeman shift for all 20 magnetic sublevels of fermionic ^{167}Er. The plot in the inset shows the relative splitting between two lowest adjacent pairs of states, $\delta(\Delta E) = (E_{17/2} - E_{15/2}) - (E_{19/2} - E_{17/2})$. Note the different y-axis for main plot and the inset.

a new method to initialize a long-lived two-component spin mixture and perform Feshbach spectroscopy by employing a lattice-projection technique. We identify and carefully map out a comparatively broad Feshbach resonance between the two lowest hyperfine states of ^{167}Er. The results may enable the study of strongly interacting fermions with dipole-dipole interaction and the investigation of the BEC-BCS crossover in a dipolar quantum gas. The results of this chapter are published in [102].

5.1 Preparing a Spin Mixture of ^{167}Er

As already mentioned and presented in Sec. 3.1, fermionic ^{167}Er has a nuclear spin of $I = 7/2$ and hence a total angular momentum quantum number of $F = 19/2$ with 20 magnetic sublevels $m_F \in \{-19/2...19/2\}$. In an external magnetic field, these sublevels split up due to the Zeeman effect. In contrast to the bosonic isotopes of erbium with $I = 0$, the hyperfine coupling induces a quadratic Zeeman splitting in the fermionic isotope ^{167}Er according to Eq. (3.7). However, in the magnetic field region, where most experiments with erbium are conducted (i.e. around one to a few Gauss), the quadratic splitting is typically smaller than magnetic-field noise such that it cannot be resolved by radio-frequency coupling of adjacent states. It can therefore not easily be exploited for a deterministic initialization of a spin mixture. Similiar ideas such as the coupling of two next-to-nearest spin states via a Raman scheme also suffer from the small quadratic Zeeman shift. It is hence unavoidable to perform the spin preparation at high magnetic field, where the quadratic correction to the Zeeman shift is large enough to be able to exclusively couple two neighboring spin states. This requires that the relative energy splitting between the states, $\delta(\Delta E) = (E_{17/2} - E_{15/2}) - (E_{19/2} - E_{17/2})$ is much larger than the magnetic field noise and the Fourier limit of the applied rf pulse. For instance, as shown in Fig. 5.1 (b), in order to get a relative splitting on the order of 50 kHz, a magnetic field of around 40 G is needed. Unfortunately an evaporation in the low-field region (around 600 mG) implies

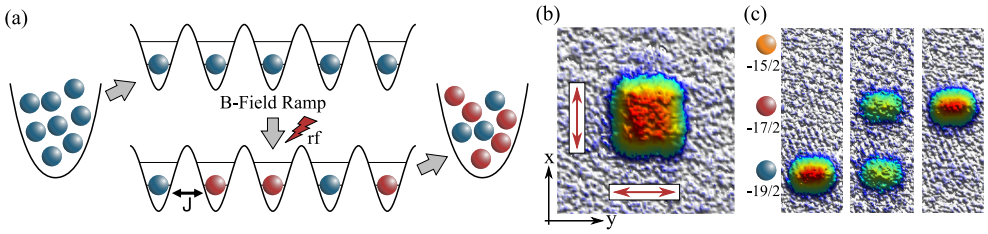

Figure 5.2: Spin preparation and band mapping. (a) In order to prevent heating and atom loss during the ramp to high magnetic field before the spin preparation, we initialize a spin-polarized band insulator. We then ramp to high magnetic fields and apply a resonant rf-pulse to induce spin mixing. (b) Band mapping in the horizontal plane. Red arrows indicate the calculated size of the Brillouin zone. (c) Three examples of different spin mixtures of the lowest two hyperfine states, without populating higher spin states. Shown examples have $\delta_s \in \{1, 0.02, -0.94\}$ (from left to right).

that we have to ramp the magnetic field across hundreds of Feshbach resonances[1] in order to start the spin-preparation. Furthermore, once the spin-mixture is initialized, we need to ramp the magnetic field back to low values across even more Feshbach resonances. This procedure will cause heating of the atomic sample and significant atom loss and hinders the preparation of a cold spin mixture in our setup.

In order prevent heating of the atomic sample during the preparation, we employ a lattice-projection technique that suppresses atomic collisions. As illustrated in Fig. 5.2, we start by evaporatively cooling a spin-polarized gas in the lowest hyperfine state in our optical dipole trap to a temperature of about $0.15T_F$. We then adiabatically ramp up a deep three-dimensional optical lattice [117] with lattice spacings $(a_x, a_y, a_z) = (266, 266, 532)\,\mathrm{nm}$ and prepare a band insulator by populating only the lowest band. This effectively freezes out any collisions between atoms. We verify the preparation of a band insulator by band mapping, see Fig. 5.2 (b), a standard technique that is commonly used in cold-atom experiments [153]. By comparing absorption images to expected profiles computed from the first Brillouin zone, we estimate the populations in higher bands to be $< 5\%$ along the z-axis and even smaller in the xy plane, as it is below our detection limit. With this system we ramp the magnetic field to 40.51 G, where the quadratic splitting between the three lowest states is $\delta(\Delta E) = 42.6\,\mathrm{kHz}$. During this ramp we do not see significant atom loss or heating. In principle the high quadratic splitting enables the initialization of any arbitrary spin mixture [144], but we only consider scattering properties of mixtures of the two lowest hyperfine states $|m_F = -19/2\rangle$ and $|m_F = -17/2\rangle$ in this work. We initialize the spin-mixture by applying a resonant rf pulse and realize different spin compositions by varying the duration of the pulse. As shown in Fig. 5.2 (c), this procedure solely couples the two lowest spin states and does not populate any higher spin states. We quantify the spin composition with the parameter $\delta_s = \frac{N_{-19/2} - N_{-17/2}}{N_{\mathrm{tot}}}$, ranging from $\delta_s = 1$ (fully polarized in the $m_F = -19/2$ state) to $\delta_s = -1$ (fully polarized in the $m_F = -17/2$ state). Fig. 5.2 (c) shows three examples for $\delta_s \in \{1, 0.02, -0.94\}$.

While the atomic gas is stable in the lowest hyperfine state $m_F = -19/2$, there

[1] See Extended Data Figure 1 in Ref [98]

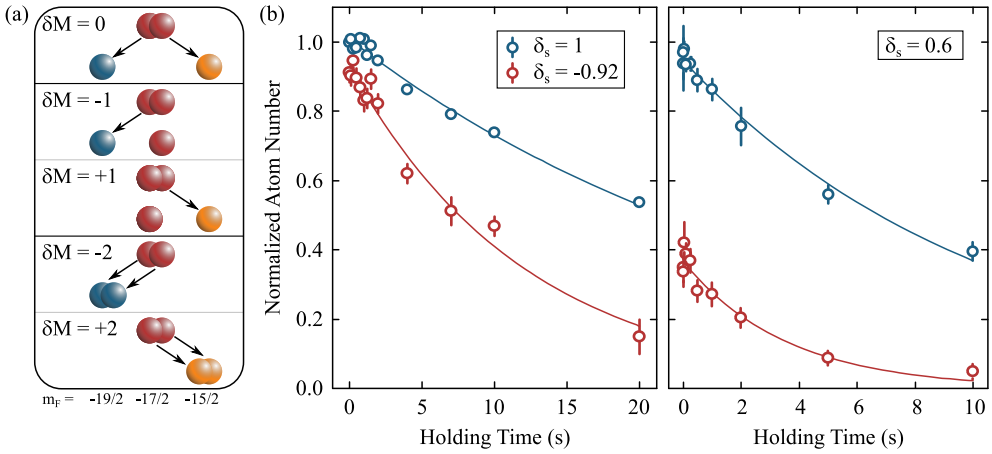

Figure 5.3: Collisional stability of erbium spin mixtures. (a) There are five possible scattering processes driven by dipolar interaction that can occur between two identical particles. They can be both spin conserving ($\delta M = 0$) or spin non-conserving ($\delta M = \pm 1, \pm 2$). Spin non-conserving processes are usually strongly suppressed by energy conservation. (b) Lifetime measurements of three different spin mixtures in a deep optical lattice. $\delta_s = 1$ and $\delta_s = -0.92$ in the left plot, $\delta_s = 0.6$ in the right plot. Blue (red) data points correspond to $m_F = 19/2$ (17/2). Solid lines are exponential fits to the data.

are different types of collisions for higher hyperfine states, that might influence the lifetime of the atomic sample. In principle there are 5 different scattering processes that can happen between two identical dipolar atoms [40, 144]. As illustrated in Fig. 5.3 (a), both magnetization-conserving ($\delta M = 0$) and magnetization-non-conserving ($\delta M \neq 0$) collisions are allowed. Since these processes are driven by the long-range DDI, they can even occur between 2 atoms on neighboring sites. However, collisions that do not conserve magnetization are typically strongly suppressed in a magnetic field because of the energy mismatch of the initial and final state due to the Zeeman shift. However, energy conversation can in principle be guaranteed e.g. by scattering with a third particle. Eventhough this process should be strongly suppressed in the lattice we experimentally test the collisional stability of a spin mixture of the two spin states, $m_F = -19/2$ and $m_F = -17/2$. We perform this measurement in a region without a Feshbach resonance, at a magnetic offset field of $B = 3.99\,\mathrm{G}$. Figure 5.3 (b) shows the decay of the atom number over time for three different spin compositions with $\delta_s \in \{1, 0.6, -0.92\}$. We fit an exponential decay to the data and extract surprisingly long lifetimes of $\tau_{19/2} = -31(3)\,\mathrm{s}$ and $\tau_{-17/2} = 12.2(7)\,\mathrm{s}$. In particular we find no strong dependence of the lifetime on the initial spin mixture. However, we always observe a shorter lifetime for the $m_F = -17/2$ state. Since we do not measure an increase of atom number in the $m_F = -15/2$ state, we conclude that no magnetization-conserving scattering processes ($\delta M = 0$) occur. We instead attribute the reduced lifetime of the $m_F = -17/2$ state to a small but continuous transfer of atoms into higher bands via intensity noise on the optical lattice. Two atoms in the $m_F = -17/2$ state on the same lattice site can then decay via spin-relaxation ($\delta M = -2$), where the released Zeeman energy is large enough to escape from the lattice. This process is not possible for the $m_F = -19/2$ state.

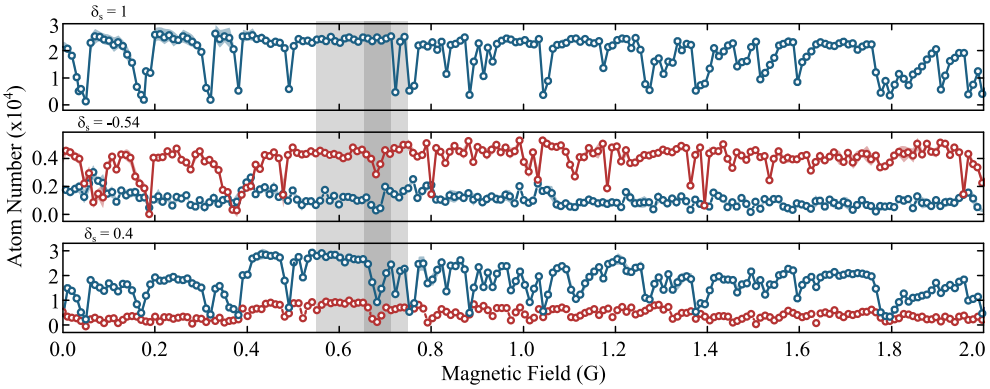

Figure 5.4: Large Feshbach scan. The three plots show a Feshbach scan for three different spin mixtures, $\delta_s = 1$ (top), $\delta_s = -0.54$ (middle) and $\delta_s = 0.4$ (bottom). The dark grey shaded region illustrates the broadest loss feature that occurs in both spin states. We therefore perform a finer Feshbach scan in the light grey shaded region, which is presented in Fig. 5.5.

The results of this section show that we can initialize the system in arbitrary spin compositions with lifetimes of several seconds. This systems provides a good starting point for the investigation of scattering physics between spin states. The next section presents our measurements on Feshbach loss spectroscopy in an ODT and modulation spectroscopy in a deep optical lattice.

5.2 Feshbach Spectroscopy

With the ability to prepare arbitrary spin mixtures, we can investigate scattering properties both between identical fermions in the $m_F = -17/2$ state but also between the two lowest hyperfine states. To this end we make use of our lattice-projection technique to ramp the magnetic field through the dense Feshbach spectrum. As described above, we initialize the spin mixture in the optical lattice at high magnetic field. We then ramp the magnetic field to the value that we want to probe and wait for the magnetic field to stabilize. We then release the atomic sample back into the dipole trap and hold the spin mixture for $t_h = 500\,\mathrm{ms}$ before measuring the spin-resolved atom number. At a Feshbach resonance, the scattering length diverges, three-body recombination rates increase substantially and hence the lifetime of the sample decreases, causing a dip in the atom number during the Feshbach scan [28]. Figure 5.4 shows a Feshbach scan in the region from zero to two Gauss for three different spin mixtures, $\delta_s \in \{1, -0.54, 0.4\}$. The different spin combinations enable the assignment of occurring loss features to the spin states. The upper pot ($\delta_s = 1$) only indicates Feshbach resonances between identical atoms with $m_F = -19/2$. Those are resonances of higher partial wave character, depending on temperature and optical confinement [154]. With the two further plots ($\delta_s = -0.54$ and $\delta_s = 0.4$), we can identify Feshbach resonances between two identical atoms in the $|m_F = -17/2\rangle$ state, such as the narrow feature at around 0.8 G or the very broad feature around 0.35 G or identify interspin resonances e.g. at 1.1 G. The light-grey shaded sector shows a broad region without loss feature, close to a relatively broad loss feature in both

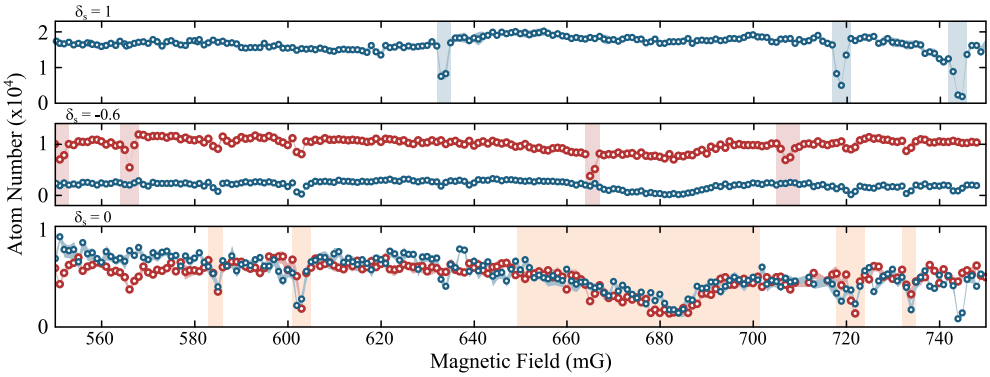

Figure 5.5: High-resolution Feshbach scan. The three plots show a high resolution Feshbach scan for different spin mixtures of the two lowest hyperfine states, $|m_F = -19/2\rangle$ (blue) and $|m_F = -17/2\rangle$ (red) with $\delta_s = 1$ (top), $\delta_s = -0.6$ (middle), and $\delta_s = 0$ (bottom). The shaded regions indicate loss features that only appear in the respective spin (red and blue) or in both spin states (orange).

spin components, highlighted by the dark-grey shaded region. This points towards a promising candidate of a broad interspin Feshbach resonance, which we further investigate by performing a second Feshbach scan with higher resolution within the light-grey shaded region. This scan is presented in Figure 5.5, again for three different spin combinations, $\delta_s = 1$ (top), $\delta_s = -0.6$ (middle), and $\delta_s = 0$ (bottom). Thanks to the employed lattice-projection technique, the loss features do not suffer from magnetic field ramps at all and do not show any artificial broadening. We are therefore also sensitive to very narrow resonances on the order of a milligauss. The measurement reveals 7 further narrow intra-spin resonances (blue and red-shaded regions in top and middle plot) and 5 inter-spin resonances (orange-shaded regions in bottom plot), from which the one at 680 mG stands out because of its much larger width of about 50 mG. We choose that resonance for further investigation and perform modulation spectroscopy in our optical lattice to extract the inter-spin scattering length.

We start by preparing a balanced spin mixture ($\delta_s = 0$) in the optical lattice. As illustrated in Fig. 5.6 (a) we sinusoidally modulate the depth of the optical potential at frequency ν_{mod}. If the modulation frequency is resonant to the onsite interaction of two atoms, i.e. $h\nu_{\mathrm{mod}} = U_{\mathrm{o}}$, the system is resonantly excited and doubly occupied lattice sites are created. Those doublons have a shorter lifetime and get lost faster from the optical lattice than singly occupied sites. After modulation of the lattice depth we therefore hold the sample in the lattice and wait for the doublons to decay. After this hold time we detect the atom number via spin-resolved absorption imaging after Stern-Gerlach separation of the two spin states and find a resonant loss whenever the above resonance condition is met.

For dipolar gases there are two contributions to the onsite interaction [117], the

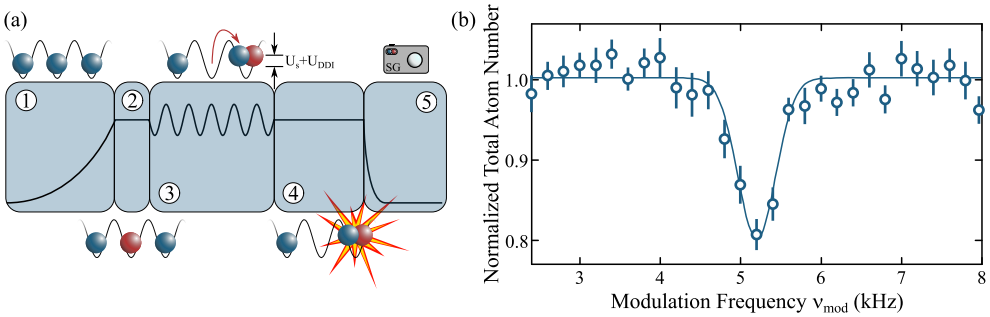

Figure 5.6: Modulation spectroscopy in the optical lattice. (a) We load a band insulator into a 3D optical lattice and prepare a balanced spin mixture with $\delta_s = 0$. Modulation of the lattice depth creates double occupancies if the resonance condition is met. Double occupancies have a shorter lifetime and can be detected as a loss of atoms. (b) Exemplary scan of the modulation frequency ν_{mod}. The dip in the total atom number indicates atom losses due to the resonant creation of doubly occupied sites. Solid line is a Gaussian fit to the data.

contact interaction U_c, and the dipole-dipole interaction, U_{dd}, with

$$\begin{aligned} U_{\mathrm{o}} &= U_c + U_{\mathrm{dd}} \\ U_c &= \frac{4\pi\hbar a}{m_{\mathrm{Er}}} \int d\vec{r}\, |\phi(\vec{r})|^4 \,, \\ U_{\mathrm{dd}} &= \frac{\mu_0 \mu_1 \mu_2}{4\pi} \int d\vec{r} \int d\vec{r}'\, |\phi(\vec{r})|^2 \, \frac{1 - 3\cos^2(\theta_{\vec{r}-\vec{r}'})}{|\vec{r} - \vec{r}'|^3} \, |\phi(\vec{r}')|^2 \,. \end{aligned} \tag{5.1}$$

Here a is the inter-spin s-wave scattering length, that we want to determine from the measurement. m_{Er} is the mass of erbium, $\phi(\vec{r})$ is the onsite Wannier wave function, μ_0 is the vacuum permeability, μ_1 and μ_2 the magnetic moment of the first and second atom, respectively, and $\theta_{\vec{r}-\vec{r}'}$ is the angle between the alignment axis of the dipole with respect to their interparticle axis (see Sec. 2.2 on dipolar interaction). Both sign and strength of U_{dd} depend on the shape of the Wannier wave function. Following [117] we define the aspect ratio as $AR = l_z/l_{xy}$, with $l_i = d_i/(\pi s_i^{1/4})$, where d_i is the harmonic oscillator length and s_i the lattice depth in units of the photon recoil energy E_i/E_{rec}. Due to our lattice geometry and available laser powers in the laboratory, the Wannier function has a prolate shape ($AR > 1$). As illustrated in Fig. 5.7 (a), for dipoles aligned along the z-axis, the dipoles mainly experience a *head-to-tail* configuration, in which they interact attractively. This causes the dipole-dipole onsite interaction energy to be negative, $U_{\mathrm{dd}}^z < 0$. By rotating the magnetic field into the xy plane, the dipoles mainly align *side by side* and interact repulsively, which leads to a positive dipole-dipole onsite energy $U_{\mathrm{dd}}^z > 0$. By performing modulation spectroscopy for those two configurations, we get the equalities $|U_{\mathrm{o}}^{xy}| = |U_{\mathrm{c}} + U_{\mathrm{dd}}^{xy}|$ and $|U_{\mathrm{o}}^z| = |U_{\mathrm{c}} + U_{\mathrm{dd}}^z|$, where U_{dd}^{xy} and U_{dd}^z contribute to the total energy with different signs. By comparing those two energies we can directly extract the amplitude and the sign of U_{dd} and use the result to determine the shape of the Wannier wave function, with which we finally extract the scattering length a_s. Figure 5.7 shows the experimentally obtained values for the scattering length in the proximity of the observed loss feature. We fit a simple

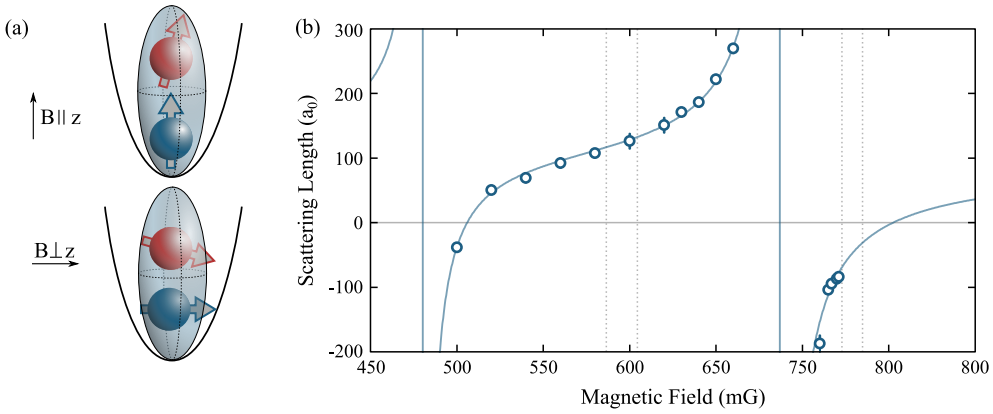

Figure 5.7: Feshbach resonance in ^{167}Er. (a) The dipole interaction energy U_{dd} depends on the aspect ratio (AR) and the alignment of the dipoles. For a fixed AR $\neq 1$, the magnitude and sign of U_{dd} can be changed, which allows us to extract the sign of the scattering length a by comparing interaction energies for two angles. (b) Scattering length as a function of magnetic field. The solid line is a single-channel fit to the experimental data (see main text). Dashed grey vertical lines indicate further narrow resonances (cf. Fig. 5.5).

single-channel model to the data [28, 155], taking into account a second resonance around 480 mG (cf. Fig. 5.4),

$$a(B) = a_{\mathrm{bg}} \left(1 - \frac{\Delta}{B - B_0} - \frac{\Delta'}{B - B_0'}\right), \tag{5.2}$$

with the background scattering length a_{bg}, the widths Δ and Δ', and the resonance positions B_0 and B_0'. We find a background scattering length of $a_{\mathrm{bg}} = 93(9)a_0$, where a_0 is the Bohr radius. The lower resonance is located at $B_0 = 480(4)$ mG with a width of $\Delta = 33(6)$ mG. For the other resonance we extract a position of $B_0' = 687(1)$ mG, and a slightly broader width of $\Delta' = 57(6)$ mG, consistent with the loss feature in the Feshbach scan in Fig. 5.4. The grey dashed vertical lines in Fig. 5.7 (b) indicate the four further narrow resonances, which we observed in Fig. 5.5 and which we do not take into account for the fit. Assuming a differential magnetic moment of $\delta\mu = 3\mu_0$ (as was measured in bosonic Er_2 [156]), we can estimate the order of the effective range to be $r^* = \hbar/m_{\mathrm{Er}} a_{\mathrm{bg}} \delta\mu\Delta \approx 600\,\mathrm{a_0}$ for the resonance at 480 mG and $r^* \approx 1000\,\mathrm{a_0}$ for the resonance at 687 mG. This value of the effective range yields an intermediate dimensionless parameter of $\gamma^* = \frac{8}{\pi}\frac{1}{k_F r^*} \gtrsim 1$ [157].

In a final measurement we investigate the lifetime of the atomic sample across the resonance at 687 mG. Figure 5.8 (a) shows the decay of the atom number over time for positive scattering lengths of $a = 880(140)\,\mathrm{a_0}$ at a magnetic offset field of 680 mG and for negative scattering length $a = -1500(500)\,\mathrm{a_0}$ at a magnetic offset field of 690 mG. We fit the data with an exponential decay and extract $1/e$-lifetimes of $\tau_+ = 150$ ms and $\tau_- = 1200$ ms, respectively. The longer lifetime on the repulsive site of the resonance ($a < 0$) is a direct consequence of the Pauli principle, which suppresses three-body losses in a two-component Fermi gas [158]. On the attractive (BEC) site, the existence of a weakly bound molecular state supports three-body

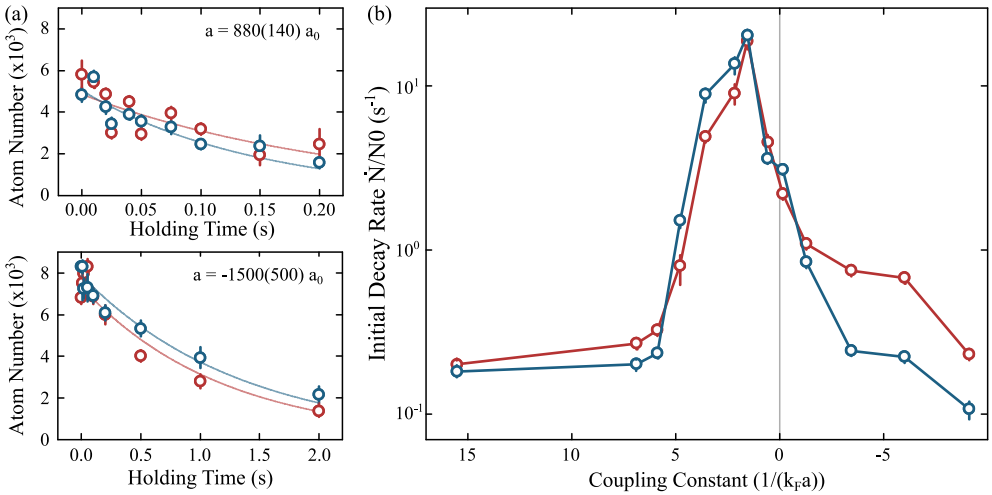

Figure 5.8: Collisional stability across the resonance. (a) Two exemplary lifetime measurements below (top) and above (bottom) the resonance for a 50-50 mixture of the $m_F = -19/2$ (blue) and $m_F = -17/2$ (red) spin state. Solid lines are exponential fits to the data. (b) Initial decay rate across the 687 mG Feshbach resonance as a function of the dimensionless coupling constant $1/(k_F a)$. Solid line only serves as guide to the eye.

recombination and leads to a faster decay of the atom number. This behavior can also be seen in Figure 5.8 (b), where we plot the initial decay rate $\dot{N}/N_0$ as a function of the dimensionless coupling constant $1/(k_F a)$. We extract the initial decay rate with a linear fit to the initial decay of the atom number. We find a large collisional stability on the repulsive site, where the lifetime can reach a few seconds. On the attractive site, the initial decay is more than one order of magnitude larger. This asymmetry is an essential feature for the BEC-BCS crossover and hence the investigated resonance might be a promising candidate to study such physics in systems with anisotropic long-range interaction.

In this chapter we presented the first realization of a two-component Fermi gas with dipolar and tunable s-wave interaction. Our preparation scheme does not suffer from inelastic dipolar scattering and can easily be extended to prepare arbitrary spin compositions [144]. Even though the measured resonances are only of intermediate strength and much more narrow than typical Feshbach resonances in systems with alkali atoms (in terms of the magnetic field), the presented resonance can be used to freely tune the interaction between the two lowest hyperfine states in ^{167}Er, $|m_F = -17/2\rangle$ and $|m_F = -19/2\rangle$. With a magnetic field stability of below 1 mG in the experiment, we can precisely tune the scattering length to the desired value. Our results therefore enable the investigation of BEC-BEC crossover physics in dipolar quantum gases but also motivates the search for further broad resonances at higher magnetic fields, or between further combinations of spin states. Furthermore such measurements could facilitate the understanding of complex spin dynamics [144] and enable the study of rich magnetic behaviors in systems with long-range interaction and the search for exotic phases of matter by exploiting the many spin states as

synthetic dimensions [159].

Chapter 6

Conclusion and Outlook

This part of the thesis presented the results that were obtained within my first year in Innsbruck at the erbium experiment.
The first project was the investigation of the anisotropic light shift of erbium atoms. We presented measurements on the anisotropic ac-polarizability of the ground state and the 583 nm excited state of erbium and compare the experimental results to semiempirical electronic-structure calculations. Despite the complicated electronic configuration in erbium and a huge number of optical transitions in the proximity of the investigated wavelengths we find good agreement between theory and experiment. There are few investigations in dysprosium experiments [125, 143], however, a similar direct comparison of experiment and theory is still pending. Our results prove a good understanding of the erbium level structure and a good knowledge of existing optical transitions beyond the NIST database. Such an understanding facilitates the design of new experimental schemes and raises prospects for realizing state-dependent optical potentials via the application of near-resonant laser light. It also enables state-selective manipulation by using narrow lines for spin-orbit coupling [139] or to realize synthetic dimensions with the large number of internal spin states[55].
The second project investigated the preparation of a strongly interacting dipolar Fermi gas. We presented a scheme for the deterministic preparation of two-component spin-mixtures in a Fermi gas of erbium atoms. Despite spin non-conserving processes we measure a high collisional stability and find that the lifetime is independent of the initial spin-composition. We performed Feshbach loss spectroscopy in the region from $0 - 2\,\mathrm{G}$, where we detect a range of inter and intra-spin Feshbach resonances. We map out and characterize one particularly broad inter-spin Feshbach resonance around 680 mG via modulation spectroscopy in an optical lattice. Our measurement constitutes the first realization of a two-component dipolar Fermi gas with tunable interaction and enables the future study of strongly interacting dipolar Fermi gases.

Outlook

The results obtained within this thesis directly enable a range of interesting experiments with dipolar Fermi gases. As shown in a recent experiment in our group [144],

state-dependent light shifts can be used to quickly control dipolar exchange dynamics by compensating the quadratic Zeeman shift with a quadratic light shift. This paves the way to the study of rich magnetic behaviors in dipolar Fermi gases involving a huge number of internal degrees of freedom.
A further interesting topic is the study of transport properties in optical lattices and the influence of dipolar interaction [160]. Based on energy conservation, a system interacting via nearest-neighbor dipolar interaction is expected to form dynamically-bound nearest-neighbor dimers, which decrease or even completely suppress expansion and transport in a dipolar system. Fermi gases are particularly promising candidates to study such effects [161] since optical lattices with unity filling can be readily realized.
Furthermore the ability to tune the short-range interaction and to realize a strongly interacting Fermi gas allows to investigate the effect of dipolar interactions on fermionic pairing and the BEC-BCS crossover. In particular, similar as was done in bosonic dipolar gases, the study of systems where the interaction can be tuned from purely dipolar to a regime where it is dominated by s-wave interaction might reveal interesting new phases or dynamics caused by the interplay of short-range isotropic and long-range anisotropic interactions.

Part III

Characterizing Fermi Systems via Momentum-Correlation Measurements

Chapter 7

Experimental Tools in the Laboratory

With our setup in the Heidelberg experiment we have the ability to deterministically prepare mesoscopic Fermi-Hubbard-like systems by trapping few atoms in an array of few optical tweezers [94, 162, 163]. By using a single-atom and spin sensitive fluorescence imaging scheme, which we developed in our group over the past few years [67, 85], we can investigate those few-fermion systems both in real space and in momentum space. By investigating the system in two conjugate basis (i.e. position and momentum) we have direct access to coherence properties of the prepared state and can therefore extract information that is not accessible when only looking in real space. As we will discuss in the following chapters, we can use this information to characterize few-fermion systems and to constrain large parts of their density matrix. Based on these constraints, we can reconstruct physical density matrices of systems containing two or three mobile, interacting atoms by performing a Bayesian quantum state estimation. In this first chapter we present the basic tools that we have available in the laboratory. We start by introducing the main properties of lithium and briefly discuss how we deterministically prepare few-particle systems in the laboratory. We then briefly discuss which states we can prepare in the laboratory and how we investigate them using our single-atom sensitive imaging scheme.

7.1 ^{6}Li - Atomic Properties

Lithium is the lightest alkali atom with atomic number $Z = 3$. It has a single valence electron and compared to the previously discussed erbium a simple electronic structure in the ground state. There are two stable isotopes which are both commonly used in cold atom experiments: bosonic ^{7}Li with a natural abundance of 92.4% and a nuclear spin of $I = 3/2$ and fermionic ^{6}Li with a natural abundance of 7.6% [164] and a nuclear spin of $I = 1$. In our experiment we use the fermionic isotope ^{6}Li.
Figure 7.1 (a) shows the level structure and the hyperfine splitting of ^{6}Li in the ground and the first excited state. The electronic ground state ($2^2S_{1/2}$) splits into two submanifolds ($F = 1/2$ and $F = 3/2$) with a splitting of $\Delta = h\times 228.2\,\mathrm{MHz}$. The ^2P excited

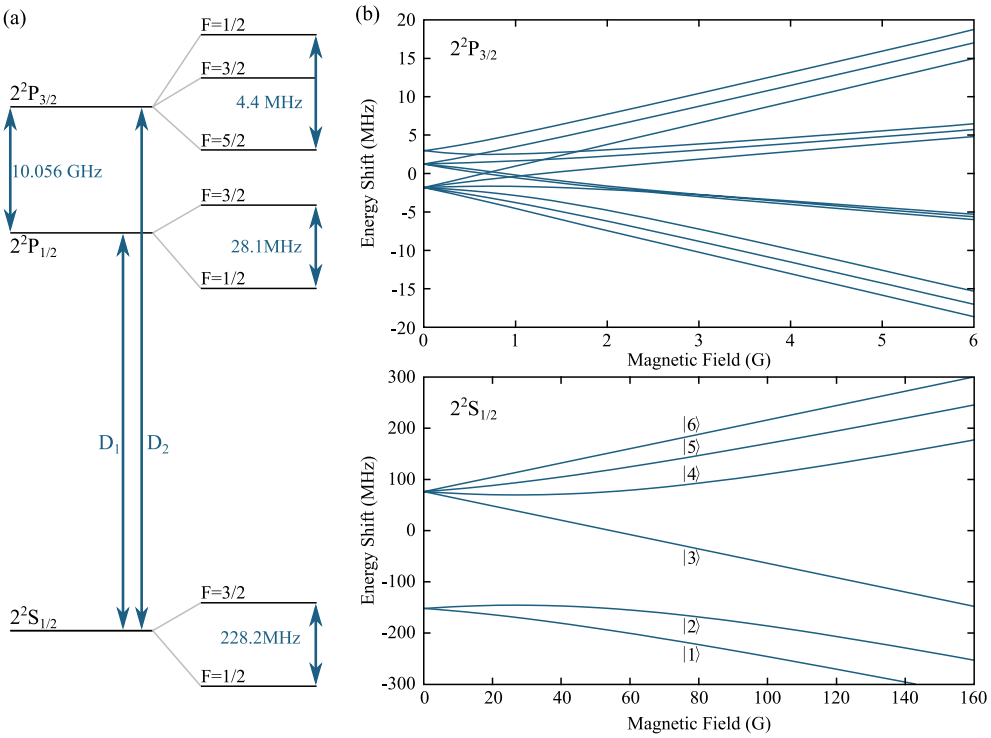

Figure 7.1: Lithium level structure. (a) Level structure and hyperfine splitting of ^{6}Li at zero magnetic field (not to scale). (b) Zeeman splitting of the different m_F states for the two experimentally relevant states, i.e. the ground state $2^2S_{1/2}$ and the upper excited state $2^2P_{3/2}$. Note the different x-axes in the top and bottom plot. Figure taken and adapted from [86].

state splits into the two manifolds $^2P_{1/2}$ and $^2P_{3/2}$ with a fine structure splitting of around $\Delta_{FS} = h \times 10.056\,\text{GHz}$, which in turn split up into five sub-manifolds with different total angular momenta F. The D_1 and D_2 lines have wavelengths of $\lambda_1 = 670.992421\,\text{nm}$ and $\lambda_2 = 670.977338\,\text{nm}$, respectively, with a natural linewidth of $\Gamma = 5.8724\,\text{MHz}$ [86]. In our experiments however, we only drive transitions within the D_2 line, i.e. to the $2^2P_{3/2}$ excited state. At zero magnetic field, the hyperfine splitting of that state is smaller than the D_2 linewidths and can hence not be resolved. It is interesting to note that compared to other alkali atoms the fine structure splitting of $\Delta_{FS} = 10.056\,\text{GHz}$ of the excited state is very small. Even though this can have technical advantages, e.g. for the implementation of grey-molasses cooling [165], it might also complicate the application of strong Raman couplings within the ground state [166].

When lithium is subjected to an external magnetic field, the different m_F sublevels of each F-manifold split up due to the Zeeman effect. Generally this splitting is linear at small magnetic fields, but once the magnetic interaction energy becomes comparable to the hyperfine interaction energy, F ceases to be a good quantum number and the states rearrange in groups according to their m_J value (see Fig.7.1 (b) or [85, 86] for a more detailed description of the different levels). For the $2^2P_{3/2}$ excited state this already happens at very low magnetic field (around 1 Gauss) due to the small hyperfine constant of the excited state of $A_{2^2P_{3/2}} = -1.155\,\text{MHz}$ [167]. In contrast,

for the ground state much larger magnetic fields are necessary to decouple the nuclear moment from the electronic angular momentum. As described in [67, 85, 168], this has important consequences for our free-space momentum imaging scheme, due to small but finite branching rations for the decay from the excited state into the three highest states (labeled $|4\rangle$, $|5\rangle$, $|6\rangle$ in Fig. 7.1 (b)) of the ground state.
For our experiments, we use two of the three lowest hyperfine states of the ground state, labeled $|1\rangle$, $|2\rangle$ and $|3\rangle$, according to their energy at high magnetic field. At high magnetic field, the splitting between two adjacent states is on the order of 80 MHz so that they can be individually addressed via the D_2-line. Experiments presented in this thesis are all done with a $|1\rangle$-$|3\rangle$ mixture, because (i) state $|3\rangle$ is the only state that features a completely closed optical transition [168], which is beneficial for imaging, and (ii) to maximize the energy difference between the two states in order to suppress off-resonant scattering during the imaging process.

7.2 Deterministic Preparation of Few-Fermion Systems

In order to deterministically prepare few-fermion systems it is essential to prepare atomic samples with very low temperature and entropy. This section outlines the main steps of the experimental procedure. A more detailed description of the experimental setup and procedure can be found e.g. in [84, 85, 94, 169]. For the setup of the vacuum chamber, see Chapter 2 or given references.

Optical Setup

As described in the first part of the thesis, cooling an atomic sample requires both resonant and off-resonant laser light. For dissipative cooling in the Zeeman slower and the MOT we derive near-resonant laser light at $\lambda_{\text{res}} = 671\,\text{nm}$ from a Toptica tapered amplifier. We employ two further Toptica DL100 external cavity diode lasers at the same wavelength for absorption and fluorescence imaging. All visible lasers are beat-offset locked to a reference laser which in turn is locked to the D_2 line (to the $F = 3/2 \rightarrow 2^2P_{3/2}$ transition) via modulation transfer spectroscopy. Fast frequency jumps during the imaging process (e.g. for state-resolved imaging) are achieved by controlling the DC modulation input of the DL100 with a Red Pitaya [94].
For experiments in this thesis, we use two kinds of dipole traps. Evaporation is performed in a crossed-beam optical dipole trap. Laser light for this trap is derived from a 1064 nm, 100 W Yb-doped fiber amplifier, YLR-200-LP-WC, IPG Photonics. The deterministic preparation (see below for details) is done with optical tweezers, for which we use light from a 1064 nm, 1 W Innolight Mephisto laser. The tweezer array is realized with an acousto optical deflector (AOD) [170], operated at low radio-frequency (rf) powers to keep nonlinearities in the crystal as small as possible. Generation of multiple tweezers is achieved by sending multiple rf tones to the AOD. We focus the tweezer light through our high-resolution objective [171], sitting in the reentrant viewport on top of our main chamber. The objective has a design numerical aperture

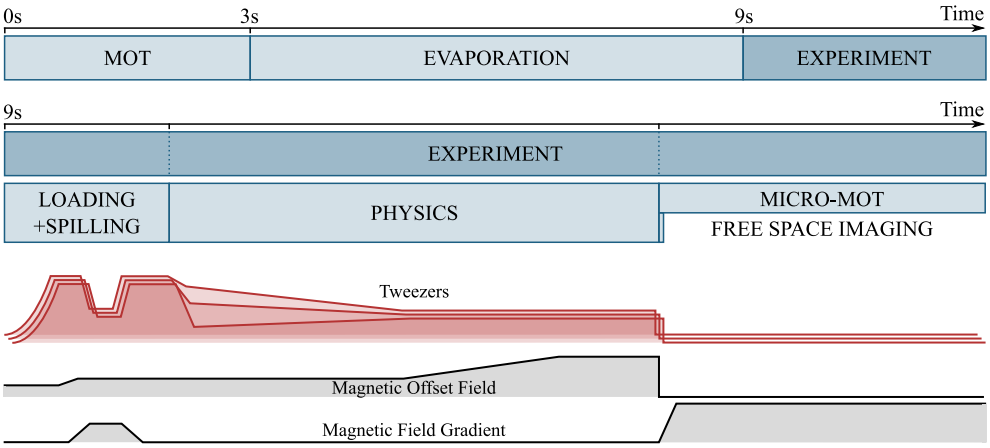

Figure 7.2: Experimental sequence for deterministic preparation of few-fermion systems. The top row shows the different blocks of the full experimental sequence, including the initial MOT phase, followed by the evaporation and the experimental part. Below the top row there is a zoom-in on the preparation, manipulation and imaging sections. We also schematically illustrate the sequence for the tweezers, the magnetic offset field and the magnetic field gradient during the experimental part.

of $NA = 0.6$ with an an effective focal length of 20.3 mm. We use the same objective for fluorescence imaging as will be described in Sec. 7.4.

Experimental Sequence

The experiment is controlled by an ADwin Pro II from Jäger Messtechnik, using 2×32 DIO channels, 16 analog out and 8 analog input channels. Digital channels can be set with 0.5 μs time steps, analog channels have an update rate of 400 kHz, which is fast enough for the implementation of real-time PIDs for active stabilization of experimental parameters. Figure 7.2 shows a schematic of the experimental sequence. The experiment starts with the loading of a magneto-optical trap (MOT), in which typically 10^7 atoms are captured. At the end of the MOT phase, all atoms get pumped into the $F = 1/2$ state. We then compress the MOT and transfer it into a crossed-beam optical dipole trap (ODT), where the ramping on of the offset magnetic field produces a spin-imbalanced mixture of atoms in states $|1\rangle$ and $|2\rangle$. Spin balance is established by a high-power radio-frequency pulse. Atoms are eventually transferred from state $|2\rangle$ to $|3\rangle$ by an adiabatic Landau-Zener passage. After a short phase of plain evaporation, the power of the ODT is lowered to force evaporation either at low (300 G) or high (685 G for $|1\rangle - |3\rangle$) magnetic field (refer to Sec. 2.2 for scattering lengths). At the end of the evaporation we typically have 40.000 atoms per spin state at temperatures of below 0.5 T_F. We then ramp on one or, depending on the experiment, multiple tweezers at the same time, that can be individually controlled by controlling the radio-frequency tones that are sent into the AOD. As illustrated in Fig. 7.3, once the tweezer is filled with atoms, we first switch off the crossed-beam ODT and only retain a completely filled tweezer. At that stage there are only a few hundreds of atoms left. We deterministically reduce the atom number to a few atoms by applying a magnetic

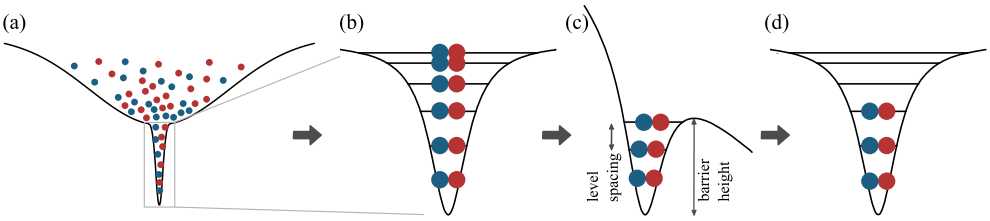

Figure 7.3: Deterministic preparation of few fermions. (a) After the evaporation in our large crossed-beam optical dipole trap, we transfer the atoms into a dimple trap, created by a tightly focussed laser beam. (b) We switch off the large reservoir trap and retain a few hundred atoms in the dimple trap. (c) We lower the optical potential and apply a magnetic field gradient to deterministically spill atoms above a certain trap level out of the trap. (d) We obtain a deterministic atom number and achieve fidelities on the order of 96% per atom.

field gradient along the longitudinal axis of the tweezer and by subsequently lowering the optical potential. As indicated in the figure this procedure spills out all atoms above a certain trap level [162]. The preparation of single atoms works with a fidelity of about 96 %. Depending on the experiment, we either separately prepare multiple tweezers with single atoms or prepare a fixed number of atoms in the first tweezer and initialize the final system with an adiabatic passage to the total ground state (see e.g. [163]). After the final state has been prepared, we eventually induce interactions by tuning the magnetic field across the Feshbach resonance. We finally investigate the state by two different means: fluorescence imaging in a microMOT (only atom-number resolved) or free-space single-atom and spin resolved imaging.

MicroMOT

A first and very robust method to investigate a few-atom state is the microMOT. In order to count the total atom number after the experimental sequence, we recapture the atoms from the tweezers into our MOT and collect the fluorescence signal on a CCD camera for one second [162]. To get a good signal-to-noise ratio on the camera, we compress the MOT as much as possible by using a much higher magnetic field gradient and less detuning than we use in the initial MOT, hence the name *micro*MOT. With this method we can count the total atom number up to about 15 atoms with very high fidelity. In combination with the above described spilling technique, the microMOT is well suited to perform spectroscopic measurements [172–174]. While the microMOT cannot provide any information about the momenta of the atoms it can in principle be applied to extract information beyond the total atom number. We can e.g. measure the spin and site-resolved populations by removing all atoms of one spin state and switching off all wells except one prior to imaging. However, such sequences can get very tedious so that we developed a complementary imaging scheme that gives access to both real and momentum-space spin-resolved single-particle positions.

Free-Space Imaging

In order to extract more information from the state than just the total atom number, we employ a single-atom and spin-resolved free-space imaging scheme [67, 85]. Briefly explained, we illuminate atoms with resonant laser light for 20 μs and collect on average around 20 fluorescence photons per atom with our high-NA objective onto an EMCCD camera. Successively taking two images of different spin states also provides spin-resolution. In particular, this imaging scheme works without any confining potentials so that also the momenta of single atoms can be accessed. The results presented later in the thesis were obtained with this imaging scheme. We will therefor give a more detailed description in Sec. 7.4. However, for all technical details, please refer to [67, 85, 168].

7.3 Fermi-Hubbard Model

A system consisting of few fermions trapped in an array of optical tweezers can be described by the Fermi-Hubbard model [163]. This model was initially used to describe interacting fermions in flat energy bands [175] but is readily applied to ultracold atoms in optical lattices [176, 177]. Despite its simplicity, the Fermi-Hubbard (FH) model still raises open questions and is seen as a promising candidate to explore physics related to high-T_C superconductivity [178]. This section discusses the basic aspects of the FH model, that are relevant for our experiments and discusses the states that we can realize in the laboratory.

The Hubbard model is a simple model to describe a system in a periodic potential with nearest-neighbor hopping and onsite interaction. It only considers the lowest energy band and furthermore assumes that different spatial modes are orthogonal to each other. For a two-component Fermi gas in a periodic potential, we can write the Fermi-Hubbard Hamiltonian as

$$\hat{H}_{FH} = \underbrace{-J \sum_{\langle i,j\rangle,\sigma} \left(\hat{c}^\dagger_{i\sigma}\hat{c}_{j\sigma} + \hat{c}^\dagger_{j\sigma}\hat{c}_{i\sigma}\right)}_{H_{\mathrm{kin}}} + \underbrace{U \sum_i \hat{n}_{i\uparrow}\hat{n}_{i\downarrow}}_{H_{\mathrm{int}}} + \underbrace{\sum_i \mu_i \left(n_{i\uparrow} + n_{i\downarrow}\right)}_{H_{\mathrm{ext}}}, \tag{7.1}$$

with fermionic annihilation (creation) operators $c^{(\dagger)}_{i\sigma}$ on site i with spin σ and number operators $\hat{n}_{i\sigma} = c^\dagger_{i\sigma}c_{i\sigma}$. Figure 7.4 (a) schematically illustrates the different terms of this Hamiltonian. The kinetic term $\hat{H}_{\mathrm{kin}}$ describes hopping of fermions between neighboring sites $\langle i,j\rangle$ with hopping element J. The interaction term $\hat{H}_{\mathrm{int}}$ describes the interaction of two fermions with opposite spin on the same lattice site, contributing the onsite interaction energy U. Finally the last term takes into account and external confinement or an energy offset μ_i on individual sites of the lattice, as illustrated in Fig. 7.4 (b) for the case of a double-well potential. In the illustrated case of a detuned double well, we have $\mu_1 = -\mu_2 = \mu$ and a doubly-occupied left well, where the repulsive interaction between the two opposite spins contributes the energy U to the total energy of the system.

For small systems, it is instructive to explicitly write out the FH Hamiltonian. For

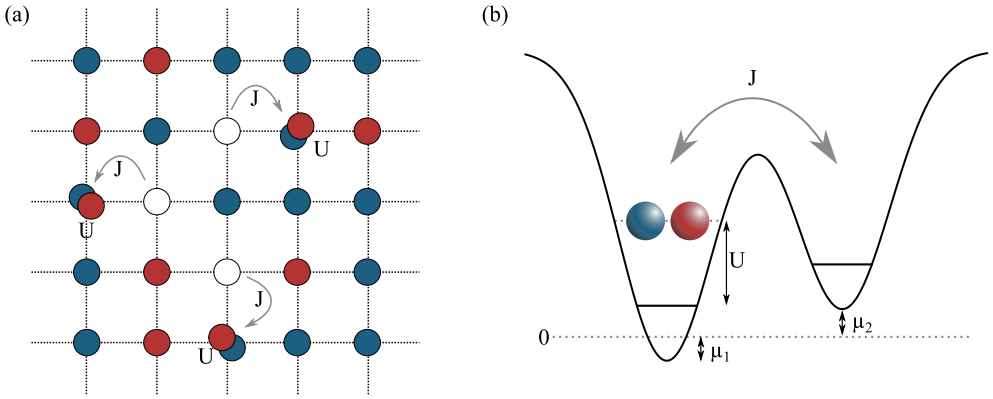

Figure 7.4: Fermi-Hubbard model. (a) Illustration of the FH model for a two-component Fermi gas on a two-dimensional optical lattice. The evolution of the system is governed by only two parameters, the tunnelling element J and the onsite interaction U. (b) Two interacting atoms in an imbalanced double-well potential with $\mu_1 = -\mu_2$.

later purposes we discuss the cases of two atoms in a double well and three atoms in a triple well.

2 Atoms in a Double Well

For the case of two identical atoms, i.e. if the two atoms have the same spin, there is only one possible state within the Fermi-Hubbard model. In the notation $|\cdot,\cdot\rangle$, where the first entry is the spin population in the left well and the second entry the spin population in the right well, the state of two identical atoms reads as $|\uparrow,\uparrow\rangle$. In that state there is exactly one fermion per site since the two atoms cannot occupy the same well due to the Pauli-exclusion principle. Hence, the Hamiltonian is simply $\hat{H} = 1$, since tunneling is forbidden ($J = 0$) and there is no onsite interaction U.
The case of two interacting atoms with different spin (labeled $|\uparrow\rangle$ and $|\downarrow\rangle$) is illustrated in Fig. 7.4 (b). With the same notation as above, we can identify four basis states as

$$|\Psi\rangle \quad \in \quad \{|\uparrow\downarrow,\cdot\rangle\,;|\uparrow,\downarrow\rangle\,;|\downarrow,\uparrow\rangle\,;|\cdot,\uparrow\downarrow\rangle\}\,. \tag{7.2}$$

An alternative and useful representation of the same states (that we will use later) is what we will call the *particle representation*. Instead of giving the population of the first or second well, the first or the second entry in $|\cdot,\cdot\rangle$ indicate the well in which the spin-up, or the spin-down particle are located, respectively. In this representation we can rewrite the above states as

$$|\Psi\rangle \quad \in \quad \{|LL\rangle\,;|LR\rangle\,;|RL\rangle\,;|RR\rangle\}\,. \tag{7.3}$$

The first and the last state are doubly occupied sites and therefore come along with an energy penalty of U. The occupation of those states is hence favored (suppressed) for attractive (repulsive) interaction. There is no energy penalty associated with the two other states, but they are connected to the doubly occupied states via a single tunnelling event J. We can write the Hamiltonian in its matrix representation, using

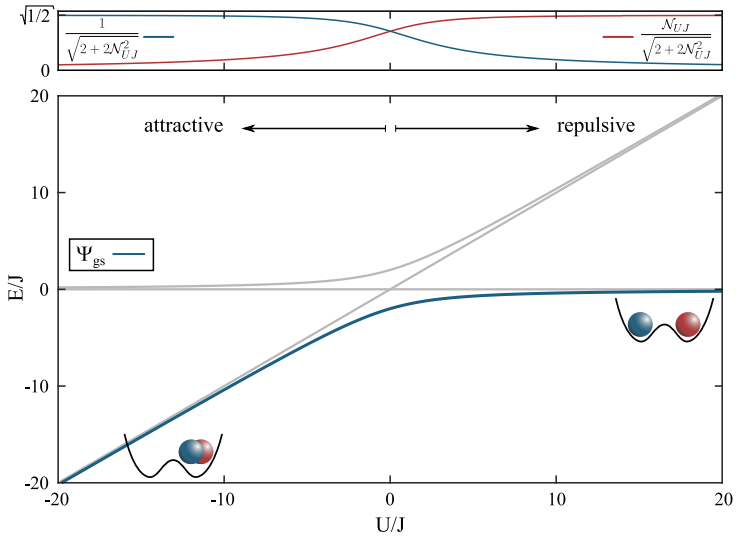

Figure 7.5: Spectrum of balanced double well. The top panel shows the coefficients of the four basis states in the ground state, see Eq. (7.5). The lower plot shows the four eigenenergies of the balanced double well as function of the interaction U/J. The attractively interacting ground state (blue solid line) approaches the state with the superposition of two doubly occupied sites. On the repulsive site, each atom becomes localized on an individual site.

$H_{ij} = \langle \Psi_i | \hat{H} | \Psi_j \rangle$, as

$$\hat{H}_{\mathrm{DW}} = \begin{pmatrix} U + 2\mu_1 & -J & -J & 0 \\ -J & 0 & 0 & -J \\ -J & 0 & 0 & -J \\ 0 & -J & -J & U + 2\mu_2 \end{pmatrix}. \tag{7.4}$$

We can analytically diagonalize this Hamiltonian to find the four eigenstates and the associated eigenenergies, which we plot in Fig. 7.5 for the balanced double well, i.e. for $\mu_i = 0$. In our experiments we are primarily interested in the ground state $|\Psi_{\mathrm{gs}}\rangle$, which is highlighted in the figure.

The ground state $|\Psi_{\mathrm{gs}}\rangle$ is explicitly given by

$$|\Psi_{\mathrm{gs}}\rangle = \frac{1}{\sqrt{2 + 2\mathcal{N}_{UJ}^2}} \left(|LL\rangle + |RR\rangle + \mathcal{N}_{UJ}(|LR\rangle + |RL\rangle) \right) \tag{7.5}$$

$$\text{with} \qquad \mathcal{N}_{UJ} = \frac{U}{4J} + \sqrt{1 + \left(\frac{U}{4J}\right)^2}. \tag{7.6}$$

The prefactors of both the doubly and singly occupied states are plotted in the upper panel of Fig. 7.5. The population of doubly occupied sites is favored (suppressed) for attractive (repulsive) interaction and the coefficients already saturate at an interaction of $U/J \approx \pm 8$. To gain some understanding of the states, let's take a look at the three limiting cases of $U = 0$, $U/J \to \infty$, and $U/J \to -\infty$. In those cases, the state from

Eq. (7.5) takes the form

$$\begin{aligned} |\Psi_0\rangle &= \frac{1}{2}\left(|LL\rangle + |RR\rangle + |LR\rangle + |RL\rangle\right) \\ &= \frac{1}{\sqrt{2}}\left(|L\rangle + |R\rangle\right) \otimes \frac{1}{\sqrt{2}}\left(|L\rangle + |R\rangle\right) \qquad (7.7) \\ |\Psi_\infty\rangle &\rightarrow \frac{1}{\sqrt{2}}\left(|LR\rangle + |RL\rangle\right) \qquad (7.8) \\ |\Psi_{-\infty}\rangle &\rightarrow \frac{1}{\sqrt{2}}\left(|LL\rangle + |RR\rangle\right). \qquad (7.9) \end{aligned}$$

At $U = 0$ the state factorizes into a product of the two single-particle states, whereas the strongly interacting states are maximally entangled Bell states. For later purposes we explicitely write out the density matrices of the three states, which can be calculated by $\rho = |\Psi\rangle\langle\Psi|$. In the basis from Eq. (7.3) the density matrices are given by

$$\rho^{-\infty} = \frac{1}{2}\begin{pmatrix} 1 & 0 & 0 & 1 \\ 0 & 0 & 0 & 0 \\ 0 & 0 & 0 & 0 \\ 1 & 0 & 0 & 1 \end{pmatrix}, \rho^{0} = \frac{1}{4}\begin{pmatrix} 1 & 1 & 1 & 1 \\ 1 & 1 & 1 & 1 \\ 1 & 1 & 1 & 1 \\ 1 & 1 & 1 & 1 \end{pmatrix}, \rho^{\infty} = \frac{1}{2}\begin{pmatrix} 0 & 0 & 0 & 0 \\ 0 & 1 & 1 & 0 \\ 0 & 1 & 1 & 0 \\ 0 & 0 & 0 & 0 \end{pmatrix}. \qquad (7.10)$$

3 Atoms in a Triple Well

In the trivial case of three identical atoms, there is again only a single state available, $|\uparrow,\uparrow,\uparrow\rangle$. We therefore consider the configuration with two spin-up and one spin-down atom (or vice versa). In that case, we identify the 9 following states as basis states,

$$\begin{aligned} |\Psi\rangle \in \{&|\uparrow,\uparrow,\downarrow\rangle; |\uparrow,\downarrow,\uparrow\rangle; |\downarrow,\uparrow,\uparrow\rangle; \\ &|\uparrow\downarrow,\uparrow,\cdot\rangle; |\uparrow\downarrow,\cdot,\uparrow\rangle; \\ &|\uparrow,\uparrow\downarrow,\cdot\rangle; |\cdot,\uparrow\downarrow,\uparrow\rangle; \\ &|\uparrow,\cdot,\uparrow\downarrow\rangle; |\cdot,\uparrow,\uparrow\downarrow\rangle\}, \end{aligned} \qquad (7.11)$$

where similar to the double well, $|\cdot,\cdot,\cdot\rangle$ describes the occupation of the first, the second and the third well, respectively. Alternatively, we can again write these states in the particle representation as

$$\begin{aligned} |\Psi\rangle \in \{&|L,C,R\rangle; |L,R,C\rangle; |C,R,L\rangle; \\ &|L,C,L\rangle; |L,R,C\rangle; \\ &|L,C,C\rangle; |C,R,C\rangle; \\ &|L,R,R\rangle; |C,R,R\rangle\}, \end{aligned} \qquad (7.12)$$

where the first two entries describe the spatial mode (left (L), center (C) and right (R) well) of the two spin-up particles and the third entry the spatial mode of the spin-down

particle. Note that this representation identifies individual particles as subsystems of the state and is therefore not unique, since e.g. the state $|L,C,R\rangle$ describes the same spin-configuration as the state $|C,L,R\rangle$. Due to the indistinguishability of the two spin-up atoms special care must be taken to ensure a proper antisymmetrization of the state. The subtleties of treating individual particles as systems rather than spatial modes will be discussed in Chapter 10.
In the above basis, the Hamiltonian of the balanced triple well (i.e. $\mu_i = 0$) in its matrix representation takes the form

$$\hat{H}_{\mathrm{TW}} = \begin{pmatrix} 0 & 0 & 0 & 0 & 0 & -J_{23} & 0 & -J_{23} & 0 \\ & 0 & 0 & 0 & -J_{12} & -J_{23} & -J_{12} & -J_{23} & 0 \\ & & 0 & 0 & -J_{12} & 0 & -J_{12} & 0 & 0 \\ & & & U & -J_{23} & -J_{12} & 0 & 0 & 0 \\ & & & & U & 0 & 0 & 0 & 0 \\ & & & & & U & 0 & 0 & 0 \\ & & & & & & U & 0 & -J_{23} \\ & h.c. & & & & & & U & -J_{12} \\ & & & & & & & & U \end{pmatrix}, \tag{7.13}$$

where J_{12} is the tunnel coupling between the left and the center well and J_{23} the tunnel coupling between the center and the right well.
Figure 7.6 shows the nine eigenenergies of this Hamiltonian for the homogeneous triple well ($J_{12} = J_{23} = J$) as a function of the interaction strength U/J. On the repulsive site, $U > 0$, the three lowest states are only separated by an energy on the order of the super-exchange energy $4J^2/U$, which vanishes for strong interactions. This energy scale will become important in Chap. 9 when we discuss the experimentally reconstructed density matrix of the ground state of the homogeneous triple well.
Also for the triple well we are primarily interested in the ground state, since we will discuss its entanglement properties in Chap. 10. Similar to the double well, doubly occupied sites are favored for attractive interaction, whereas they are suppressed in the strongly repulsively interacting ground state. However, on the attractive (repulsive) site, the spin-down particle (the doublon) delocalizes across the triple well, so that for $U/J \to \pm\infty$ the ground state takes the following form,

$$|\Psi_{\infty}\rangle = \frac{1}{\sqrt{6}}|\uparrow,\uparrow,\downarrow\rangle + \frac{2}{\sqrt{6}}|\uparrow,\downarrow,\uparrow\rangle + \frac{1}{\sqrt{6}}|\downarrow,\uparrow,\uparrow\rangle \tag{7.14}$$

$$|\Psi_{-\infty}\rangle = \frac{1}{2}|\uparrow\downarrow,\uparrow,\cdot\rangle + \frac{1}{\sqrt{8}}|\uparrow\downarrow,\cdot,\uparrow\rangle + \frac{1}{\sqrt{8}}|\uparrow,\uparrow\downarrow,\cdot\rangle + \frac{1}{\sqrt{8}}|\cdot,\uparrow\downarrow,\uparrow\rangle + \frac{1}{\sqrt{8}}|\uparrow,\cdot,\uparrow\downarrow\rangle + \frac{1}{2}|\cdot,\uparrow,\uparrow\downarrow\rangle\,. \tag{7.15}$$

Using the experimental techniques that we discussed above, we can deterministically initialize such FH-like states. To verify the successful preparation of those states, it is necessary to fully characterize their quantum state. Since experimentally realized states usually suffer from technical noise, it is particularly relevant to access

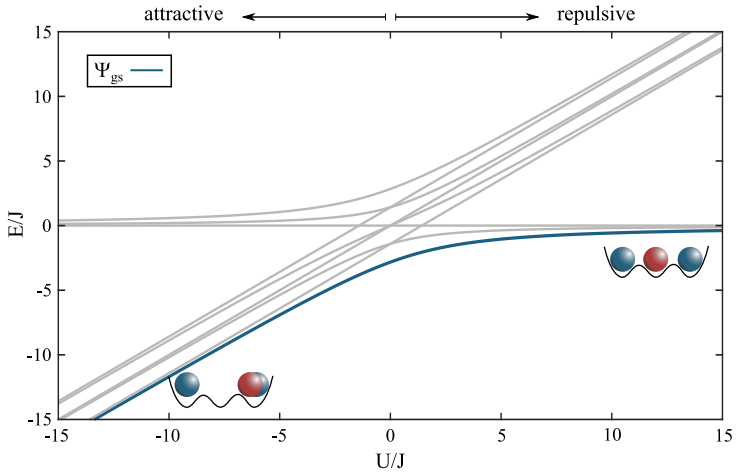

Figure 7.6: Spectrum of homogeneous triple well. The plot shows the nine eigenenergies of the homogeneous triple well ($J_{12} = J_{23} = J$) as a function of the interaction strength U/J. The blue solid line is the energy of the ground state, which favors doubly occupied sites on the attractive site and suppresses them on the repulsive site.

coherence properties of the state. As mentioned before, coherences can be accessed by investigating the system in two conjugate bases, such as in real and in momentum space. In our experiment this is achieved with our spin-resolved free-space, single atom imaging, which will be presented in the next section.

7.4 Spin-resolved single-atom imaging

Apart from the deterministic preparation of small systems in an array of optical tweezers, the key feature of our experiment is the possibility to image single atoms in a spin-resolved way. In particular, there is no need for confining potentials during the imaging process and we can readily apply the scheme after time-of-flight to detect the momenta of single particles. Our imaging technique hence provides access to both the single-atom resolved in-situ and momentum distribution of the system. This gives access to coherence properties by sampling the momentum wave-function of individual particles or by calculating momentum correlation functions of few-fermion systems. In this section the working principle of our imaging scheme is described and the measurement of single-particle coherences is presented to exemplify the usefulness of accessing single particle momenta. A detailed characterization of the performance of the imaging scheme can be found in [67, 85, 168].

To image a single atom, we apply two counter-propagating, horizontally polarized, resonant laser beams in an alternating scheme, see Fig. 7.7 (a). The alternating scheme is chosen to avoid interference between the two imaging beams. We pulse each beam with a periodicity of 200 ns and a duty cycle of 40 % for a total imaging time of 20 μs and focus the scattered light onto an Electron Multiplying CCD-camera (EMCCD, ANDOR iXon DV887, back illuminated). At an intensity of $s_0 = I/I_{\text{sat}} \approx 8.5$

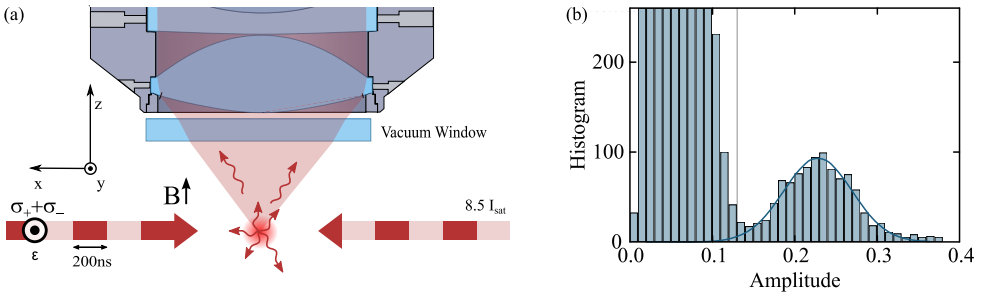

Figure 7.7: Single-atom imaging. (a) Resonant pulses of laser light are successively applied to the atom from both sides in an alternating scheme and the scattered photons are collected with our high-NA objective. Driving σ_+ transitions and making use of the dipolar radiation pattern, we focus on average 20-30 photon per atom on an EMCCD camera. (b) Histogram of single-atom fluorescence signal (see text). The grey vertical line indicates the cutoff above which we identify an event as an atom.

and a natural linewidth of $\gamma = 2\pi \times 5.8724\,\mathrm{MHz}$, the atomic scattering rate on resonance is $\Gamma_{\mathrm{sc}} = (1 + s_0^{-1})^{-1}\gamma/2 = 0.45\gamma$. Hence an atom scatters in total around 330 photons during an illumination time of $20\,\mu$s. The horizontally polarized imaging light is polarized perpendicular to the magnetic field and can therefore only drive σ_+ or σ_- transitions. Tuning the laser to resonance we selectively drive the σ_+ transition into the lowest branch of the excited state ($m_J = -3/2$) to suppress radiative decay from the excited state into other hyperfine states of the ground state [168]. With this scheme, state $|3\rangle$ features a completely closed optical trantision. In order to close the optical transitions of states $|1\rangle$ and $|2\rangle$ we add a second laser frequency to the imaging light (see [67, 85] for exact transitions). Taking advantage of the anisotropic dipolar radiation pattern for σ-transitions, we estimate that about 10% of the scattered photons get detected by the camera. On average we hence only detect around 20-30 photons per atom. In this low photon regime it is essential to use an EMCCD-camera, operated in photon-counting mode. In this mode (EM mode), a single electron on the camera sensor gets stochastically amplified in an extra gain register before being read out. This causes the signal from a single electron to be well above the electronic read noise, enabling the detection of single photons. However, this stochastic amplification process makes it impossible to clearly distinguish a single photon from multiple photons on the same pixel [94]. This is why the magnification of the imaging system has to be chosen such that the signal from a single atom gets distributed over several pixels.

We process the images with three simple steps. The individual steps are exemplarily illustrated in Fig. 7.8. First of all, to get rid of electronic noise, the raw image that we get from the camera is binarized, i.e. we introduce a cutoff, above which we identify the count on a single pixel as an electron (see [85, 94]) and convert the raw image into an image containing only zeros (no electron) or ones (at least one electron). These electrons can be caused both by light or electronic noise. We apply a Gaussian low-pass filter (LP) to the binary image to filter out background noise, which appears with lower spatial frequencies than the actual atomic signal. We then search for local maxima in the lowpass-filtered images and plot the distribution of the

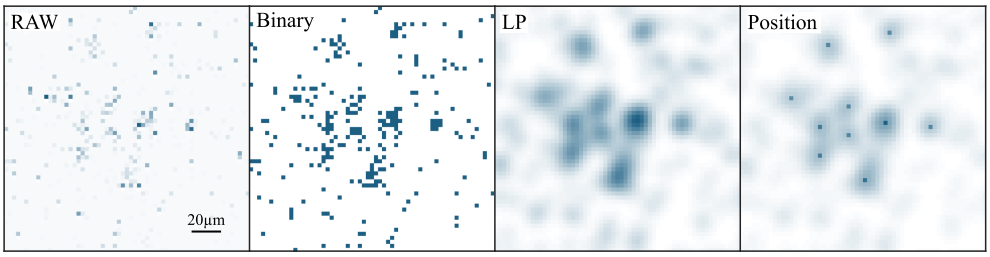

Figure 7.8: Image processing. In EM mode the camera introduces counting noise due to the stochastic amplification of electrons on the sensor. We therefore need to process the images with three simple steps. The raw image from the camera (RAW) is first binarized using a threshold value above which a pixel is identified with at least one electron (Binary). A Gaussian lowpass filter (LP) smoothes the background noise which appears with a different spatial frequency than the atomic signal. Local maxima above a threshold are identified as positions of single atoms (10 atoms in the shown example).

local maxima in a histogram. An example of such a histogram is shown in Fig. 7.7 (b). This histogram shows a clear bimodal distribution with a peak at very low amplitude, corresponding to the maxima in the background noise, and a distinct peak at higher amplitude, caused by the atomic signal. Based on that histrogram we define a cutoff above which we identify a single atom, see grey line in Fig. 7.7 (b). We choose this cutoff such that the amount of false positive and false negative events are identical. Obviously the identification of a single atom depends on the chosen size of the region in which one searches for an atom, since the number of false positive events scales linearly with the size of the region of interest (ROI). For very small ROIs, e.g. imaging a single atom in a well localized optical tweezer, the identification of a single atom works with a fidelity of over 99 % [67]. For larger ROIs, e.g. after expansion of the atoms in a wave guide potential, we hence have to increase the cutoff for identifying an atom at the cost of detection efficiency.

The performance of our imaging scheme is mainly limited by the two following things:

- Spurious charges (such as residual background light or clock-induced charges (CICs)) on the sensor set a lower bound on the signal above which an atom can be identified. Reducing the number of CICs is therefore absolutely crucial to improve the imaging performance. We currently plan to do this by replacing the current Andor EMCCD camera with a Nuvu camera, which has proven to have significantly lower CICs at similar read-out settings [179].

- Diffusive motion of the atoms during the imaging process due to scattering of photons limits the spatial resolution. This effect is particularly bad for lithium because of its small mass and limits our resolution to about 30 μm. Note that this is substantially larger than our in-situ well spacing, which is typically on the order of a few μm so that we have to employ a small trick to measure the single-particle resolved insitu population, as we explain below. However, the large resolution typically does not matter for imaging after time-of-flight, since

we typically expand the atoms in our dipole trap by several hundreds of μm. The diffusive motion is expected to be almost fully suppressed for heavier atoms such as rubidium or erbium.

Spin Resolution

Spin resolution is implemented by successively taking two images of the two different spin states. To this end we make use of the fast-kinetics mode of our camera, which allows us to take two images within a few μs. For the experiments with the double and triple well, where we expand the atoms in our ODT, the fast kinetics mode shifts the first image by 40 pixels within 20 μs so that the atomic signal gets shifted out of the imaging region. At the same time, we quickly ramp the laser frequency of the imaging laser to be resonant to the second spin component and briefly wait for the laser frequency to settle. We subsequently image the second spin state and then read out the whole camera chip. The time between the beginning of the first and the beginning of the second image is hence only 50 μs and therefore negligible on the time scale of a few milliseconds, during which we expand the atoms in the ODT.

In-Situ Imaging

As already mentioned above, the diffusive motion of the atoms during the imaging process effectively enlarges the point spread function of the imaging system to around 30 μm. Since this is much larger than typical distances between adjacent tweezers, we have to employ a small trick to resolve the site-resolved insitu density. As we illustrate in Fig. 7.9 (a) we first project the prepared state by instantly increasing the depth of the individual tweezers and thus abruptly switching off the tunnel coupling between the wells. We then map each well to a distinct momentum by a sudden displacement of each tweezer and a evolution in the respective tweezer by a quarter of the trap period, $T_{\text{tweezer}}/4$. During the evolution in the displaced tweezer, an atom in well i is mapped onto the momentum k_i. We switch off the optical tweezers and let the atoms evolve freely in our crossed-beam ODT, acting as a one-dimensional waveguide. We then detect the atoms after time-of-flight. Fig. 7.9 (b) shows the sampled in-situ distribution in the triple well with exactly this scheme: we map the two outer wells to $\pm k$ and keep the center well switched on during imaging. The figure shows the averaged signal after about 1000 realizations. The scheme can in principle also be applied to larger systems by mapping different wells to different momenta

Momentum-Space Imaging

Following the ideas of [180], we access the single-particle momentum distribution by expanding the system in our crossed-beam optical dipole trap (ODT) for a quarter of the trap frequency $T_{\text{ODT}}/4$. Our tweezers are aligned along the long axis of the ODT with a small residual angle that we estimate to be on the order of 1 °. After the evolution in the ODT, the initial momentum of the atoms is mapped onto the position and vice versa. Longitudinal trap frequencies of the ODT are typically on the order of 40 Hz so that a typical evolution before detection is on the order of 6 ms. Note that the expansion in the ODT only provides the 1D momentum along the long

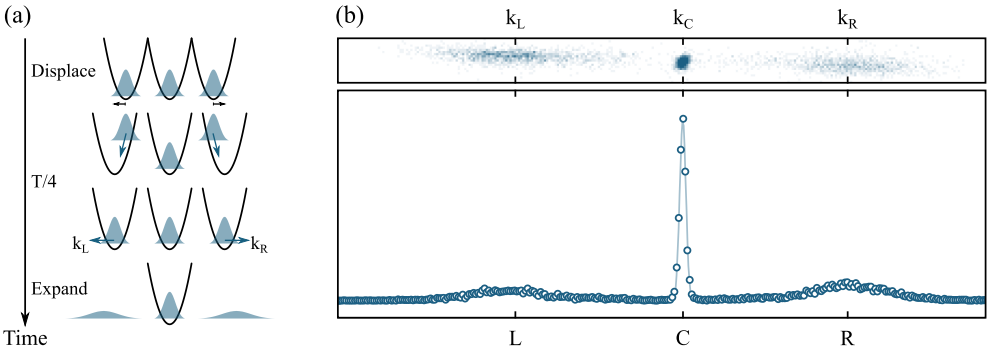

Figure 7.9: In-situ imaging. (a) To measure the in-situ distribution in an array of tweezers we have to project each tweezer onto a distinct momentum and subsequently apply our momentum imaging technique. We do this mapping by instantly displacing each tweezer, followed by the in-trap evolution of the atomic wavefunction for a quarter of the trap period $T/4$. We then let the atoms expand in a wave guide potential and detect them after time-of-flight. (b) The plot shows the sampled in-situ distribution of a triple-well potential, averaged over around 1000 repetitions.

axis of the ODT. For the measurement of a 2D momentum, an expansion in a 2D confining potential is necessary.

To illustrate the usefulness of our imaging scheme, let's discuss the example of a single atom in the ground state of a double-well potential. By sampling the single-atom momentum distribution we can measure the coherence of the single-particle wave function.

7.4.1 Single-Particle Coherences

Examining a quantum state only in one basis does not give access to its coherence properties. Accessing off-diagonal entries of the density matrix requires a complementary measurement in second basis. By investigating the system in real and momentum space, we have access to off-diagonal entries of the density matrix. We illustrate this by detecting the coherence of a single-particle superposition state.
Suppose we have created a single atom in a coherent superposition state, such as the single-particle ground state of a balanced double-well potential, where the atom is in the superposition of being either in the left or the right well,

$$|\Psi\rangle = \frac{1}{\sqrt{2}}\left(|L\rangle + |R\rangle\right). \tag{7.16}$$

Repeatedly measuring the in-situ density results in finding the atom in $|L\rangle$ for 50% of the measurements and in $|R\rangle$ for the remaining 50% of the measurements. An incoherent mixture of an atom in $|L\rangle$ or $|R\rangle$ would yield exactly the same result. Based on the in-situ measurement it is hence impossible to decide, whether the atom is in a coherent superposition-state of the two spatial modes, ρ^c, or in the fully mixed state, ρ^m. We can therefore not distinguish between the two states described by the

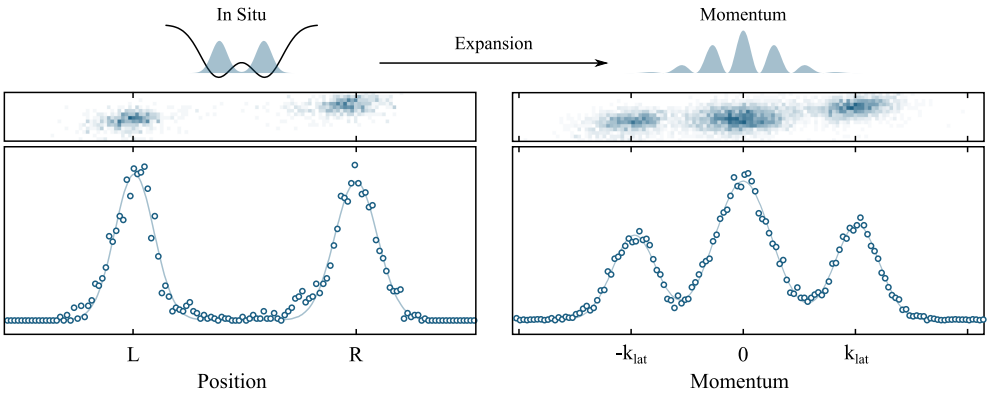

Figure 7.10: Single-particle coherences. Measurements in a conjugate basis provide additional information about the coherence of the quantum state. The plots show sampled real and momentum space densities of a single atom, initially prepared in the ground state of a balanced double-well potential. The contrast of the interference fringes in the momentum density is directly related to the purity of the initial state.

density matrices

$$\rho^c = \begin{pmatrix} 1/2 & 1/2 \\ 1/2 & 1/2 \end{pmatrix} \text{ or } \rho^m = \begin{pmatrix} 1/2 & 0 \\ 0 & 1/2 \end{pmatrix}, \tag{7.17}$$

or between any state between those, $\rho = r\rho^c + (1-r)\rho^m$ with $r \in [0,1]$. Having also access to the momentum of the atom allows to investigate the system in the conjugate basis and to directly measure the off-diagonal entries of the density matrix. As explained above, we switch off the double-well potential at $t = 0$ and let the atom freely evolve in our crossed-beam ODT. After a quarter of the trap period $t = T_{\mathrm{ODT}}/4$ the initial momentum of the atom is mapped onto its position [180]. During this evolution the two components of the coherent superposition state start to overlap and interfere, showing density modulations in the far field (in analogy to Young's double slit experiment). The contrast of these interference fringes is directly related to the coherence and hence the purity of the initial state. If the initial state was the incoherent mixture ρ^m, no interference fringes in the momentum density would form, whereas the coherent superposition state ρ^c shows full-contrast modulations.
Figure 7.10 shows the measurement of the real space and momentum space density of a single atom prepared in the ground state of a double-well potential, a superposition state as given by Eq. (7.16). The state was repeatedly initialized and either probed in real or momentum space. The in-situ measurement shows that the atom is detected in the left and right well with equal probability. The sampled momentum distribution shows strong modulations, a signature of the coherent nature of the state. The periodicity of the momentum-space modulation is given by the real space distance a between the two wells, $k_{\mathrm{lat}} = \pi/a$

7.5 Momentum Correlation Functions

In the previous section we discussed how we can use our imaging scheme to extract coherence properties of a single-particle state, which allows us to fully determine the single-particle density matrix. However, the full characterization of a many-body quantum state necessarily also involves the analysis of many-particle observables. Obviously the atomic real or momentum space densities $\langle n_x \rangle$ or $\langle n_k \rangle$, respectively, are single-particle observables and therefore do not contain any information beyond the single-particle level. In order to gain information about the many-body nature of a state, one possible approach is to look at correlation functions. A lot of pioneering work has already been done in this direction such as the characterization of the superfluid to Mott-insulator transition [181] or the observation of pair-correlated fermions [182] via noise correlations in the atomic density or the description of the system via higher-order correlation functions [72, 73, 183, 184].
The tools that we have in our laboratory are ideal to study possible prospects for the characterization of such systems via the measurement of correlation functions both in real and in momentum space. Having access to the single-particle resolved real-space and momentum-space density gives us the possibility to investigate a system in terms of higher-order correlation functions, which is equivalent to solving the many-body problem step by step [72]. In a strongly correlated system, each order of correlation function might contain new information that is not accessible via the lower order correlation functions and might therefore indicate interesting physics. We therefore now briefly introduce the basic concepts of measuring and analyzing correlation functions, in particular by distinguishing connected and disconnected correlations.

The n^{th} order correlation function of an arbitrary operator $\hat{\mathcal{O}}(x)$ is defined via

$$\xi^{(n)}(\vec{x}) = \langle \hat{\mathcal{O}}(x_1)\hat{\mathcal{O}}(x_2)...\hat{\mathcal{O}}(x_N) \rangle, \tag{7.18}$$

where $\langle \mathcal{A} \rangle$ denotes the mean over the operator $\mathcal{A}$. Experimentally the mean is typically realized by either averaging over many experimental realizations or by averaging over a large ensemble of atoms. Detecting a non-zero n^{th} order correlation function $\xi^{(n)}$ does not necessarily imply that the system features true n^{th} order correlations, since lower-order correlations can also cause structure in the n^{th} order correlation function. To investigate true higher-order correlations one therefore has to subtract all lower-order contributions. This is done by decomposing the correlation function into two parts, the connected and the disconnected correlation function,

$$\xi^{(n)} = \xi^{(n)}_{\text{con}} + \xi^{(n)}_{\text{dis}}. \tag{7.19}$$

The disconnected correlation function $\xi^{(n)}_{\text{dis}}$ contains all lower-order correlations up to order $n-1$. It is hence the connected correlation function $\xi^{(n)}_{\text{con}}$, that contains information about true n^{th} order correlations. $\xi^{(n)}_{\text{dis}}$ can be calculated as a sum over all lower-order correlation functions, weighted with combinatorial factors that can be

constructed by [72]

$$\xi_{\text{con}}^{(n)} = \sum_{\pi} \underbrace{(-1)^{|\pi|-1}\,(|\pi|-1)!}_{A(\pi)} \prod_{B\in\pi} \left\langle \prod_{i\in B} \hat{\mathcal{O}}(x_i) \right\rangle . \tag{7.20}$$

The sum runs over all possible partitions π of $\{1, 2, ...n\}$, the first product over all blocks B in π and the second product over all elements i in B. To better understand the formula, we explicitly give two examples for $n = 2$ and $n = 3$.

Example for $n = 2$

1. $n = 2 \rightarrow$ There are two partition: $\pi_1 = \{1, 2\}$ and $\pi_2 = \{1\}\{2\}$
2. $|\pi_1| = 1$, $|\pi_2| = 2$
3. $A(\pi_1) = 1$, $A(\pi_2) = -1$
4. There is one block in π_1 and two blocks in π_2, each with one element
5. $\xi_{\text{con}}^{(2)} = \langle\hat{\mathcal{O}}(x_1)\hat{\mathcal{O}}(x_2)\rangle - \underbrace{\langle\hat{\mathcal{O}}(x_1)\rangle\langle\hat{\mathcal{O}}(x_2)\rangle}_{\xi_{\text{dis}}}$

Example for $n = 3$

1. $n = 3 \rightarrow$ There are five partitions:
   $\{\pi_1; \pi_2; \pi_3; \pi_4; \pi_5\} = \{\{1, 2, 3\}; \{1, 2\}\{3\}; \{2, 3\}\{1\}; \{3, 1\}\{2\}; \{1\}\{2\}\{3\}\}$
2. $|\pi_1| = 1, |\pi_2| = 2, |\pi_3| = 2, |\pi_4| = 2, |\pi_5| = 3$
3. $A(\pi_1) = 1$, $A(\pi_2) = A(\pi_3) = A(\pi_4) = -1$, $A(\pi_5) = 2$
4. There is one block in π_1, two blocks in $\pi_{2,3,4}$ and three blocks in π_5
5. There are three elements in the block in π_1, two elements in the first block and one element in the second block in $\pi_{2,3,4}$, and one element in each block in π_5.
6. $$\left.\begin{aligned} \xi_{\text{con}}^{(3)} = {} & \langle\hat{\mathcal{O}}(x_1)\hat{\mathcal{O}}(x_2)\hat{\mathcal{O}}(x_3)\rangle \\ & -\langle\hat{\mathcal{O}}(x_1)\hat{\mathcal{O}}(x_2)\rangle\langle\hat{\mathcal{O}}(x_3)\rangle \\ & -\langle\hat{\mathcal{O}}(x_2)\hat{\mathcal{O}}(x_3)\rangle\langle\hat{\mathcal{O}}(x_1)\rangle \\ & -\langle\hat{\mathcal{O}}(x_3)\hat{\mathcal{O}}(x_1)\rangle\langle\hat{\mathcal{O}}(x_2)\rangle \\ & +2\langle\hat{\mathcal{O}}(x_1)\rangle\langle\hat{\mathcal{O}}(x_2)\rangle\langle\hat{\mathcal{O}}(x_3)\rangle \end{aligned}\right\} - \xi_{\text{dis}}^{(3)}$$

As will become clear in Chap. 8, the choice of the operator influences whether there are higher-order correlations or not and that even systems with pairwise exchange statistics can exhibit higher-order momentum-density correlations.

In order to illustrate the concept of connected and disconnected correlation functions, we look at the state of two non-interacting fermions in a balanced double-well potential, that we theoretically already discussed in Sec. 7.3,

$$|\Psi_0\rangle = \frac{1}{\sqrt{2}}(|L\rangle + |R\rangle) \otimes \frac{1}{\sqrt{2}}(|L\rangle + |R\rangle). \tag{7.21}$$

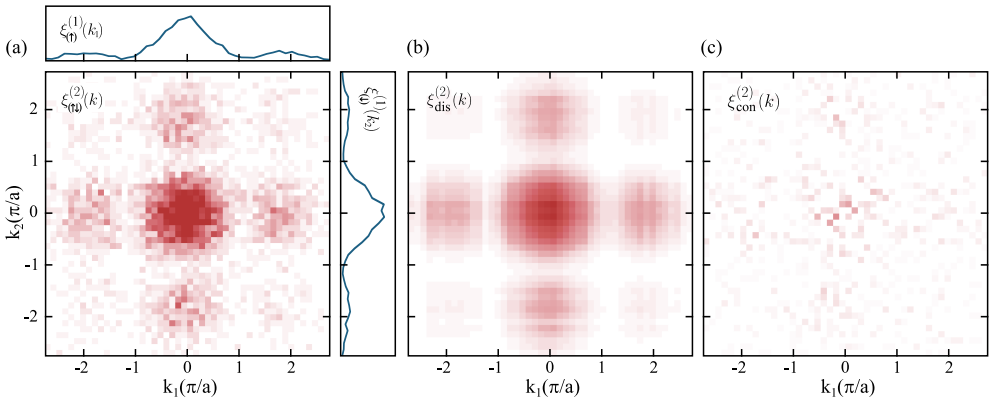

Figure 7.11: Connected and disconnected correlation functions. (a) Measured first and second-order correlation functions $\xi^{(1)}(k)$ and $\xi^{(2)}(k)$ of two non-interacting atoms in the ground state of a double-well potential. (b) Disconnected correlations function $\xi^{(2)}_{\mathrm{dis}}(k)$, computed from measured first-order correlation function $\xi^{(1)}(k)$. (c) Connected correlation function $\xi^{(2)}_{\mathrm{con}}(k)$, computed as the difference between the measured $\xi^{(2)}(k)$ (a) and $\xi^{(2)}_{\mathrm{dis}}(k)$. The connected correlation function vanishes since all correlations are purely caused by single-particle coherences.

As described in detail in [62, 85], we initialize this state in the laboratory as the non-interacting ground state of a tunnel-coupled double-well potential with well spacing a. We measure the spin-resolved single particle momenta $k_\uparrow$ and $k_\downarrow$ by expanding the system in our ODT for a quarter of the trap period, $t_{\mathrm{tof}} = T_{\mathrm{ODT}}/4$ before imaging. We postselect the data set to the correct atom number, $N_\uparrow = N_\downarrow = 1$ and calculate both the average momentum distributions $\xi^{(1)}_{(\uparrow)}(k) = \langle n_{k_\uparrow} \rangle$ and $\xi^{(1)}_{(\downarrow)}(k) = \langle n_{k_\downarrow} \rangle$ and the second-order momentum correlation function $\xi^{(2)}_{(\uparrow\downarrow)}(k) = \langle n_{k_\uparrow} n_{k_\downarrow} \rangle$. The plots in Fig. 7.11 (a) show the measured momentum densities $\xi^{(1)}_{(\uparrow/\downarrow)}(k)$ together with the computed momentum correlation function $\xi^{(2)}_{(\uparrow\downarrow)}(k)$. As explained in Sec. 7.4.1, $\xi^{(1)}_{(\uparrow/\downarrow)}(k)$ shows interference fringes that indicate single-particle coherences. According to Eq. (7.20) we define the disconnected and connected correlation functions as

$$\begin{aligned} \xi^{(2)}_{\mathrm{dis}}(k) &= \langle n_{k_\uparrow} \rangle \langle n_{k_\downarrow} \rangle \\ \xi^{(2)}_{\mathrm{con}}(k) &= \langle n_{k_\uparrow} n_{k_\downarrow} \rangle - \langle n_{k_\uparrow} \rangle \langle n_{k_\downarrow} \rangle, \end{aligned} \tag{7.22}$$

which we can both compute from the measured first and second-order momentum correlation functions. We plot the disconnected correlation function in Fig. 7.11 (b) and the connected correlation function in (c). This example nicely shows that even though there is a clear structure in the computed second order correlation function, these correlations are purely caused by single-particle coherences and no second-order correlations are present in the system. The connected correlation function hence vanishes and does not show any structure. Only if the n^{th} order connected correlation function does not vanish, the system exhibits true n^{th} order correlations. As we will discuss in the next chapter, such correlations depend on the operator that we choose to investigate and can be purely caused by quantum statistics.

Chapter 8

High-Contrast Interference of Ultracold Fermions

The analysis and measurement of correlation functions finds applications in almost all fields of physics. One of the most prominent examples thereof was the famous idea of Hanbury-Brown and Twiss (HBT) to measure the angular diameter of a bright star by correlating the intensity measured from two distant detectors [185, 186], see Fig. 8.1 (a) for illustration. They were able to show that intensity correlations of a bright star measured with two spatially separated detectors depend on their mutual distance and that the periodicity of the correlated signal was given by the angular spread of the star. By analyzing the correlation function as a function of the detector spacing, the angular diameter can be resolved even beyond the optical resolution of the two detectors. While this classical effect is caused by the wave nature of the electromagnetic field, there exists an analogous quantum mechanical effect, in which the same type of correlations can be observed.

Let us consider two absolutely identical fermions in a double-well potential, with one fermion per site. Furthermore, suppose that we have two detectors at variable positions x_1 and x_2, as illustrated in Fig. 8.1 (b). At $t = 0$ we release the two fermions from the double-well potential and monitor the coincidence events between the two detectors, i.e. the events in which we detect one particle in each detector at the same time. For those events, there are two possible paths the atoms can take from their initial position to the detectors. However, due to the indistinguishable nature of the atoms, the observer cannot tell, which of the two possible paths were taken. Hence quantum mechanics dictates that each atom takes both paths at the same time, which leads to correlations in the relative wave function of the two atoms. While the individual signals of the two detectors do not contain any signature of those correlations, they manifest themselves in the correlated signal of the two detectors. Indeed, as we will discuss in detail later in this chapter, the two paths interfere either constructively or destructively so that for some detector distances $d = x_1 - x_2$ no coincidences occur, while for others they are favored. One finds a sinusoidal dependence of those coincidences on d, where the frequency is solely given by the initial separation of the two atoms.

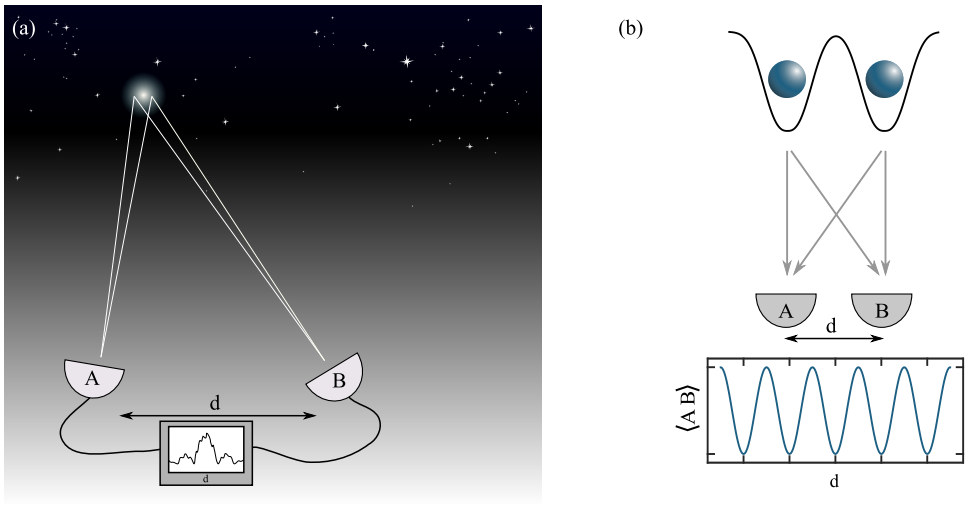

Figure 8.1: Hanbury-Brown Twiss effect. (a) The HBT effect was originally proposed in radio astronomy to resolve the angular diameter of a star beyond the optical resolution of a telescope by analyzing intensity correlations from two distant detectors. (b) In a quantum mechanical system, similar correlations occur when there is no *which-way* information and different paths interfere.

These correlations are caused by the exchange symmetry of the two fermions and they are a pure quantum-mechanical effect. In particular it is a prominent example, that shows how correlation functions can be used to extract information beyond single-particle observables, and, as in the case of radio astronomy, it does not suffer from a limited optical resolution of the detectors. The HBT effect is therefore also an important tool in other fields of physics, as for example in high-energy nuclear and particle physics [187]. Together with similar effects, such as Hong-Ou-Mandel interference [188], the HBT effect has been extensively studied in photonic systems [189–191] and finally led to the development of quantum optics [192]. More recently such correlations also became relevant for ultracold quantum gas experiments, operating with individual particles [60, 61, 63, 193–195] and have proven to be ideal tools for the charaterization of states but also for studying many-body interference effects and their influence on the dynamics and entanglement properties of many-body states.

In this chapter we present momentum-density correlation measurements on systems consisting of two or three identical, non-interacting fermions. In analogy to the HBT effect, we observe strong sinussoidal correlations in the second-order correlation function and show that three identical fermions can exhibit true third-order correlations in the momentum density. These experiments combine the on-demand preparation of highly indistinguishable particles with high-quality measurements of correlation functions and might enable the future study of quantum-optics experiments with massive particles such as fermionic ghost imaging or Bell tests [196–200]. Parts of this chapter have been published in [61].

8.1 HBT Effect between Identical Fermions

Quantum-mechanical correlations of the HBT type are caused by exchange statistics and therefore may arise between any two indistinguishable atoms. In order to observe the HBT effect in a quantum-mechanical setting, we experimentally prepare two identical fermions in a double-well potential. To this end we independently prepare two atoms in two spatially separated optical tweezers with large initial separation a_i. Even though the two identical fermions are strictly non-interacting, this ensures that the two particles are independently initialized and that observed correlations are purely caused by quantum statistics. After this preparation we approach the two tweezers to the final distance of $a_f < a_i$ from which we release the atoms into our optical dipole trap (ODT), serving as a one-dimensional wave guide potential as explained in Sec. 7.4. After a fixed time of flight of a quarter of the ODT trap period, $t_{\mathrm{tof}} = T_{\mathrm{ODT}}/4$, we detect the positions of the two atoms using our single-atom sensitive imaging scheme and post select the data set to the correct atom number, $N^{\uparrow} = 2$, with post-selection rates of about 80%. The positions x_1 and x_2 after time of flight correspond to the initial momenta k_1 and k_2. From this data set we compute the momentum correlation function $\xi^{(2)}(k) = \langle n_{k_1} n_{k_2} \rangle$, which we show in Fig. 8.2 (a). The momentum correlation function shows almost full-contrast oscillations in the relative coordinate $k_1 - k_2$.

To understand why we observe oscillations in the second-order correlation functions we choose for now to describe the state within the framework of first quantization. We therefore introduce labels $\{1, 2\}$ to identify the particles via $|X\rangle_1$ and $|X\rangle_2$, $X \in \{L, R\}$. We obtain the first-quantized wave function by antisymmetrizing over the degree of freedom in which the particles are distinguishable,

$$|\Psi\rangle = \frac{1}{\sqrt{2}} \left(|L\rangle_1 |R\rangle_2 - |R\rangle_1 |L\rangle_2 \right). \tag{8.1}$$

For fermions trapped in optical tweezers, we can explicitly write down the single-particle spatial wave function as $|X\rangle_i = \psi(x_i - x_X)$, with $X \in \{L, R\}$, $i \in \{1, 2\}$ and the onsite wave function $\psi(x)$. Using the harmonic oscillator ground state for $\psi(x)$ and plugging everything into Eq. (8.1), we illustrate the time evolution of the relative wave function $|\Psi(x_1, x_2)|^2 = \langle \Psi | \Psi \rangle$ between the two atoms in Fig. 8.2 (b). Note that x_1 and x_2 are not two orthogonal real-space dimensions but are the one-dimensional coordinates of particle 1 and 2, respectively. The atoms are initially localized within the two tweezers and start expanding at $t = 0$. During the expansion the relative wave function develops fringes in the relative coordinate $x_1 - x_2$. We will now explicitly perform this transformation and calculate the second-order momentum-density correlation function $\xi^{(2)}(k)$.
Using $\phi(k) = \int \psi(x) e^{ikx} \mathrm{d}x$ and basic rules of the Fourier transform we write the single-particle states in momentum space as

$$\begin{aligned} |L\rangle_i &\rightarrow g(k_i) e^{i k_i x_L} \\ |R\rangle_i &\rightarrow g(k_i) e^{i k_i x_R}, \end{aligned} \tag{8.2}$$

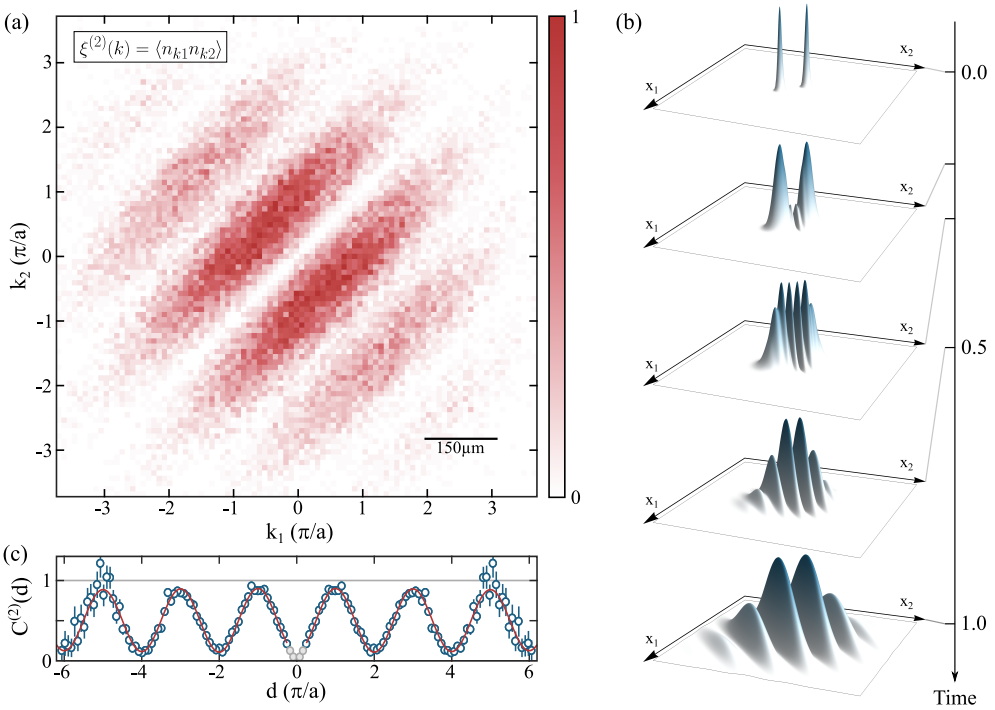

Figure 8.2: Fermionic Hanbury-Brown Twiss experiment. (a) Measured momentum-density correlation function $\xi^{(2)}(k)$ for a system of two identical fermions in two optical tweezers (Number of datapoints: 16600). Size bar indicates real-space dimension of appearing correlation features. (b) Simulated time evolution of fermionic wave function $|\Psi(x_1, x_2)|^2$ released from two tightly confined optical tweezers. (c) Normalized correlator $C^{(2)}(d)$ for correlation function shown in (a). Red solid line is a fit to the data points. Grey points around $d = 0$ are excluded from analysis because they are below the resolution of our imaging scheme.

with an envelope function $g(k) = \mathcal{F}[\psi(x)]$, i.e. the Fourier transform of the single-particle real-space wave function. We will from now on drop the particle subscripts in the state representation and write the states as $|X\rangle_1 |Y\rangle_2 \to |XY\rangle$, identifying the first entry as the first particle and the second entry as the second particle, respectively. Setting $x_L = -x_R = a/2$ and using $\hat{n}_{k'} = \sum_k \delta(k' - k)$, we can explicitly calculate the second-order momentum-density correlation function,

$$\begin{aligned}
\xi^{(2)}(k) &= \langle n_{k_1} n_{k_2} \rangle \\
&= \sum_{p,q} \langle \Psi | \, \delta(k_1 - p)\delta(k_2 - q) \, | \Psi \rangle \\
&= \frac{1}{4} \left(2g(k_1)^2 g(k_2)^2 - \langle LR|RL\rangle_{\to k} - \langle RL|LR\rangle_{\to k} \right) \\
&\overset{(8.2)}{=} \frac{g(k_1)^2 g(k_2)^2}{2} \left(1 - \cos\left((k_1 - k_2)/k_{\mathrm{lat}}\right)\right) \qquad (8.3)
\end{aligned}$$

with the lattice momentum $k_{\mathrm{lat}} = \pi/a$. One typically normalizes the correlation function by dividing out the envelope functions,

$$\xi_{\mathrm{n}}^{(2)}(k) = \frac{\langle n_{k_1} n_{k_2} \rangle}{g(k_1)^2 g(k_2)^2} = \frac{1}{2}\left(1 - \cos\left((k_1 - k_2)/k_{\mathrm{lat}}\right)\right). \tag{8.4}$$

Using Eq. (7.20), we can finally also write down the connected, normalized correlation function as

$$\xi_{\mathrm{con}}^{(2)}(k) \quad = \quad -\frac{1}{2}\cos\left((k_1 - k_2)/k_{\mathrm{lat}}\right). \tag{8.5}$$

The momentum-density correlation function hence exhibits true second-order correlations in the relative momentum of the particles, $k_1 - k_2$, multiplied by an envelope function, which is given by the Fourier transform of the single-particle real-space wave functions, exactly as we observe in Fig. 8.2 (a). This is completely analogous to the classical HBT effect. In the spirit of their initial ideas, one could even deduce the initial spacing between the two wells a, which cannot be resolved optically, by extracting the periodicity of the correlation function. One should note that the same resolution of the initial spacing can be achieved with first-order interference experiments. We presented such an experiment in Sec. 7.4.1, where we discussed single-particle coherences. However, interference experiments are typically technically much more demanding or even impossible in the case of stellar astronomy.

To quantify the oscillation in the relative momentum and to extract its contrast and periodicity we define the normalized correlator

$$C^{(2)}(d) = \int \frac{\langle n_k n_{k+d} \rangle}{\langle n_k \rangle \langle n_{k+d} \rangle} \mathrm{d}k. \tag{8.6}$$

This integration is performed along the center-of-mass momentum, i.e. along the diagonal $k_1 + k_2$ of the correlation function. Using Eq. (8.3), we find $C^{(2)}(d) = 1 - \cos(d/k_{\mathrm{lat}})$. We compute $C^{(2)}(d)$ from the experimentally measured correlation functions and show the result in Fig. 8.2 (c). The correlator exhibits almost full-contrast oscillations (limitations of contrast are discussed below). We exclude the points around $d = 0$ (grey points in the plot) from the further analysis because of the inability to detect two identical particles below the resolution of our imaging scheme [67]. We fit the correlator with a damped cosine of the form

$$C^{f}(d) = \frac{1}{2}\left(1 - \mathrm{erf}\left(\frac{|d| - s}{w}\right)\right)\left(y_0 - c e^{-\frac{d^2}{2\sigma^2}} \cos\left(\pi d/k_{\mathrm{lat}}\right)\right), \tag{8.7}$$

with s, w, y_0, σ, c and k_{lat} as free fit parameters. The error function takes the detection hole around $d = 0$ into account. The Gaussian envelope with width σ accounts for an eventual loss of contrast c for large particle separation d due to technical noise. From the fit to the correlator (solid red line in Fig. 8.2 (c)) we obtain a contrast of $c = 79(2)\%$.

As argued above, the observed correlations are purely caused by fermionic ex-

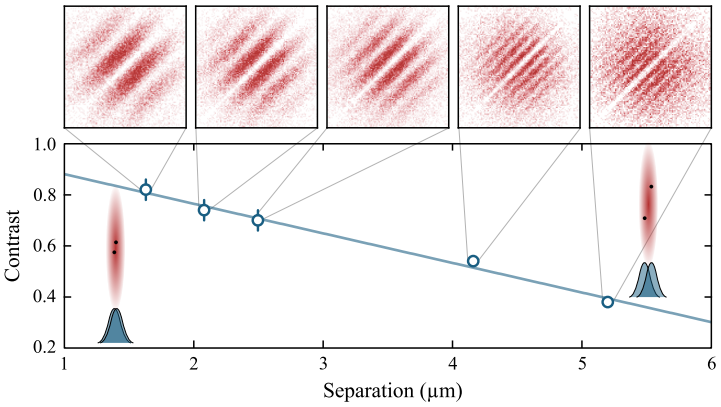

Figure 8.3: Reduction of measured contrast. We measure the contrast of the correlation function $\xi^{(2)}(k)$ for different separations between the optical tweezers. While the frequency of the modulation increases due to an increasing k_{lat}, the contrast of the modulation decreases for increasing separation. As illustrated in the insets, we attribute the reduced contrast to a reduced mode overlap along the expansion axis.

change statistics and are present between any two indistinguishable fermions. This is fundamentally different to the case where correlations arise due to the fact that the system is in a superposition state, as we discussed in Sec. 7.4.1, and as we will further discuss in Chap. 10. The observed correlations between identical fermions thus do not suffer from decoherence and perfectly indistinguishable fermions should yield a contrast of 100%. However, there are a few experimental reasons that can reduce the observed contrast:

1. **Detection:** We post select our images to the correct atom number $N = 2$. However, this also includes images where e.g. only one atom was prepared and a second was detected as a false-positive event due to imaging noise. For such events, the detected positions are uncorrelated and therefore reduce the contrast. This *second-order* effect is very small and we estimate it to be negligible since it involves e.g. a bad preparation, (typically on the order of 5-10%) and a false-positive detection (typically on the order of 1%) at the same time.

2. **Imaging Resolution:** The finite imaging resolution blurs the correlation function. As discussed in [67, 85], the position-uncertainty is on the order of 2 pixels and thus much smaller than the oscillatory feature of the correlation function. We hence exclude that this effect significantly reduces the measured contrast.

3. **Excitation to Higher Tweezer Levels:** For the case where one of the two atoms does not occupy the lowest level within its tweezer, no correlations arise after time of flight, since the particles are no longer indistinguishable. With a ground-state preparation fidelity of about 97 % we expect a reduction of the contrast of at most 5 %. This is a significant contribution, but cannot explain the reduction of the contrast by 20 %.

4. **Bad Mode Overlap:** Despite careful alignment of all optical components, there is a finite angle between the axis connecting the two tweezers and the axis

of the ODT, in which we perform the expansion. As illustrated in Fig. 8.3, this effectively induces some degree of distinguishability between the two particles, because of a reduced mode overlap along the expansion axis. The larger the initial separation between the atoms, the larger the loss of contrast, as we verify with a range of measurements. The contrast linearly decreases with increasing spacing. We fit the measurement with a linear function and extrapolate a contrast of $c_0 = 99\,(2)$ at $a = 0$. This extrapolation might overestimate the expected contrast but is in good agreement with the reduction of the contrast that we expect from the above mentioned effects.

Since both the tweezer axis and the angle of the dipole trap cannot be changed in the experiment, an improvement of the contrast is not straightforward. However, an expansion in a two-dimensional trap would remove this issue so that in the future we hope to be able to achieve even higher contrasts for arbitrary well spacings. Nevertheless, the presented system realizes a high-quality, on-demand single-fermion source and the high contrast of $c = 79(2)\%$ is sufficient to explore a range of quantum optics experiments with massive particles [199] or to address many-particle interference in fermionic systems [195].

In the next step we increase the systems size and study a system with three identical fermions in a triple-well potential. This allows us to investigate higher-order momentum correlations and the influence of exchange statistics on the third-order momentum correlation function.

8.2 Third-Order Momentum Correlations between Identical Fermions

We have seen that two indistinguishable fermions exhibit strong second-order correlations in the momentum density. These correlations are purely caused by the quantum statistics and by the antisymmetrization of the wave function and they even exist for two fermions that have been prepared in completely separate optical tweezers. Using our single-atom sensitive imaging scheme we are able to measure the second-order correlation function with very high quality. In this section we investigate correlations in a system of three identical fermions. We detect and discuss strong connected third-order correlations in their momentum density. This minimal example of fermionic many-particle interference shows that a many-body system of identical particles is more than just the sum over its constituents [195, 201].

Before starting to discuss the measurements we first evaluate the relevant correlation functions, for which we switch to the second quantization formalism. For the case of N fermions trapped in a one-dimensional array of N optical tweezers with

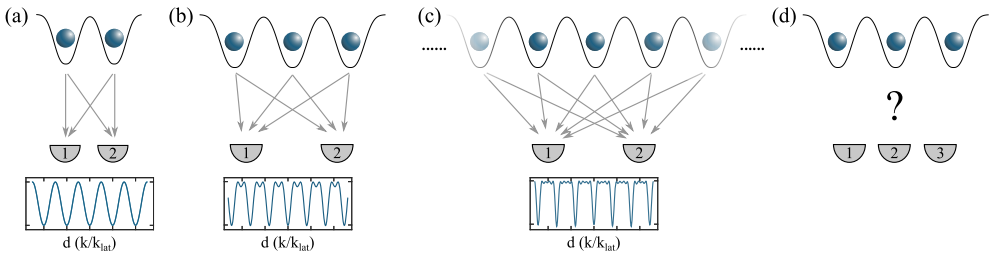

Figure 8.4: Interference between many fermions. (a) Two identical fermions released from individual traps feature a sinusoidal momentum correlation function due to interference of possible paths they can take to the detector. (b) and (c) For multiple sources, the measured second-order correlation function is a sum over all mutual correlation functions, resulting in sharp dips at the lattice momenta for large systems. (d) If a systems exhibits true third-order correlations, the correlation function contains more information than second-order correlation functions and cannot be constructed from lower-order correlation measurements.

positions x_i we define the real and momentum-space field operators as

$$\begin{aligned} \hat{\Psi}_\sigma^\dagger(x) &= \sum_{i=1}^{N} \Phi_x(x - x_i) c_{\sigma,i}^\dagger \\ \hat{\Psi}_\sigma^\dagger(k) &= \sum_{i=1}^{N} \Phi_k(k) e^{-ikx_i} c_{\sigma,i}^\dagger, \end{aligned} \tag{8.8}$$

with the onsite wave function $\Phi_x(x)$, its Fourier transform $\Phi_k = \mathcal{F}[\Phi_x](k)$ and fermionic creation operators $c_{\sigma,i}^\dagger$ on site i with spin σ. The sum is running over all wells i. Using the density operator $\hat{n} = \hat{\Psi}^\dagger \hat{\Psi}$ we can calculate all relevant correlation functions. Since we are considering identical fermions, we drop the spin label σ for the following calculations. The first moment of the momentum density is given by

$$\begin{aligned} \xi^{(1)}(k) &= \langle n_k \rangle \\ &= \langle \Psi^\dagger(k) \Psi(k) \rangle \\ &= |\Phi_k(k)|^2 \sum_{i,j} e^{ik(x_i - x_j)} \underbrace{\langle c_i^\dagger c_j \rangle}_{\delta_{ij}} \\ &= N \left|\Phi_k(k)\right|^2 . \end{aligned} \tag{8.9}$$

The normalization is such that

$$\int_{-\infty}^{\infty} \langle n_k \rangle \mathrm{d}k = N \int_{-\infty}^{\infty} \left|\Phi_k(k)\right|^2 = N. \tag{8.10}$$

The second-order correlation function is calculated in the same way,

$$\begin{aligned}
\xi^{(2)}(k) &= \langle n_{k_1} n_{k_2} \rangle \\
&= \langle \Psi^\dagger(k_1)\Psi^\dagger(k_2)\Psi(k_2)\Psi(k_1)\rangle \\
&= |\Phi_k(k_1)|^2 |\Phi_k(k_2)|^2 \\
&\quad \sum_{i,j,m,n} e^{ik_1(x_i-x_n)+ik_2(x_j-x_m)} \underbrace{\langle c_i^\dagger c_j^\dagger c_m c_n\rangle}_{\delta_{in}\delta_{jm}-\delta_{im}\delta_{jn}} \\
&= |\Phi_k(k_1)|^2 |\Phi_k(k_2)|^2 \\
&\quad \sum_{i,j} \left(1 - e^{i(k_1-k_2)(x_i-x_j)}\right) \\
&= |\Phi_k(k_1)|^2 |\Phi_k(k_2)|^2 \\
&\quad \sum_{\langle i,j\rangle} (2 - 2\cos\left((k_1-k_2)/k_{\mathrm{lat}}^{ij}\right), \qquad (8.11)
\end{aligned}$$

with the lattice momenta $k_{\mathrm{lat}}^{ij} = \pi/(x_i - x_j)$. The remaining sum runs over all combinations of wells $\langle i,j\rangle$ and is valid for any particle and well number N. Hence, as illustrated in Fig. 8.4 (a-c), in the case of non-interacting fermions, the full second-order correlation function is the sum over all mutual pairs of wells. E.g. for the commensurately spaced triple well there are three combinations, $\langle i,j\rangle \in \{\langle 1,2\rangle, \langle 2,3\rangle, \langle 1,3\rangle\}$ and each combination contributes with its own spatial frequency, given by the inverse of the respective well spacing $\pi/(x_i - x_j)$. The correlation function is hence the Fourier synthesis of all appearing well spacings. For a larger array of wells, the sum gets more terms and for a homogeneously spaced array ultimately results in distinct dips at the lattice momenta, as was observed via noise-correlation measurements in optical lattices [194].

The measurement of the second-order correlation function is analogous to the double-well case, that we discussed in the previous section. We start by preparing three identical fermions in three independent tweezers with large initial spacings and then approach the tweezers to the final configuration. We expand the atoms in our ODT for $t_{\mathrm{tof}} = T_{\mathrm{ODT}}/4$ and measure the single-particle momenta. We post select the data set to the correct atom number $N = 3$ with post-selection rates of about 60 %. We realize two different well configurations, namely the commensurate triple-well with equal spacing ($a_{12} = a_{23} = 2\,\mu$m) and an incommensurately spaced triple well with spacing $a_{12} = 1.6\,\mu$m, $a_{23} = 1.5a_{12} = 2.4\,\mu$m. These two configurations are illustrated in the upper insets in Fig. 8.5 (a) and (b). The same figure shows the measured second-order momentum correlation function and also the theoretically expected full-contrast calculations in the lower insets. We also compute the integrated correlator $C^{(2)}(d)$, which we plot below the correlation functions. Compared to the double-well case, the momentum correlation function of both configurations show additional structure, which is caused by the additional spatial frequencies from the additional pairs of wells. To verify the validity of Eq. (8.11), we also measure mutual second-order momentum correlation functions of all well combinations by preparing atoms only in two of the three wells (see Fig. 8.5 (c)), from which we extract contrast

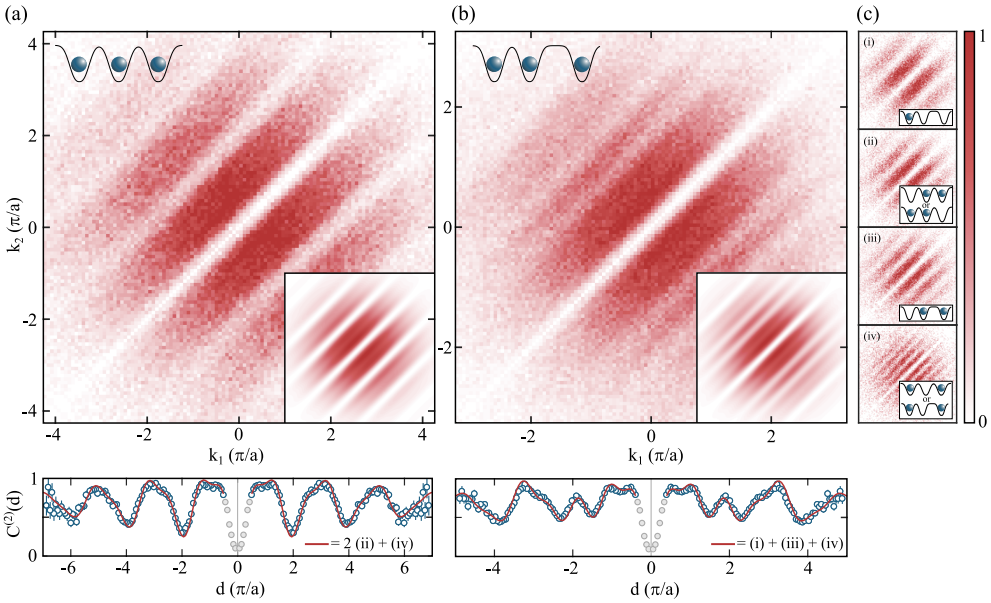

Figure 8.5: Second-order correlations in the triple well. (a-b) Measured and expected (inset) second-order correlation functions for three identical atoms in a triple well for two different spatial configurations. The plots below show the integrated correlator $C(d)$ together with a curve one would expect from measurements of mutual second-order correlations (the solid line in **not** a fit to the triple-well data). (c) Measurement of all mutual correlation functions for two atoms in a triple well.

and periodicity using Eq. (8.7). We feed the results into Eq. (8.11) and plot the resulting correlator as solid red line on top of the data points in the lower panels in Fig. 8.5 (a-b). We find excellent agreement between the data computed from the three-atom system and the sum over the data from the two-atom systems. This agreement indicates that indeed the main mechanism for the loss of contrast is the bad mode overlap for larger well spacings as we already discussed in the previous section and not a poor fidelity of the state preparation. The results also show that we can measure high-quality momentum-correlation functions also for larger systems and that the observed contrast is currently only limited by the alignment of the tweezer-axis with respect to our optical dipole trap. The presented methods are hence perfectly suited to detect microscopic ordering in small systems where the optical resolution is not sufficient to detect single atoms [181] or where ordering appears on sub-wavelength scales [202, 203].

The fact that the full second-order correlation function is only a sum over pairwise correlations, naively suggests that the third-order momentum correlation function does not contain additional information. This is however not the case, as we see will see in the following. We start by explicitly calculating the third-order momentum correlation function, analogously to the calculation of the second-order correlation function above,

$$\begin{aligned}
\xi^{(3)}(k) &= \langle n_{k_1} n_{k_2} n_{k_3} \rangle \\
&= \langle \Psi^\dagger(k_1)\Psi^\dagger(k_2)\Psi^\dagger(k_3)\Psi(k_3)\Psi(k_2)\Psi(k_1)\rangle \\
&= |\Phi_k(k_1)|^2 |\Phi_k(k_2)|^2 |\Phi_k(k_3)|^2 \\
&\quad \sum_{i,j,m,n,l,s} e^{ik_1(x_i-x_s)+ik_2(x_j-x_l)+ik_3(x_m-x_n)} \underbrace{\langle c_i^\dagger c_j^\dagger c_m^\dagger c_n c_l c_s\rangle}_{(*)} \\
&= |\Phi_k(k_1)|^2 |\Phi_k(k_2)|^2 |\Phi_k(k_3)|^2 \\
&\quad \sum_{i,j,m} \Big(1 + e^{ik_1(x_i-x_j)+ik_2(x_j-x_m)+ik_3(x_m-x_i)} \\
&\quad + e^{ik_1(x_i-x_m)+ik_2(x_j-x_i)+ik_3(x_m-x_j)} \\
&\quad - e^{ik_1(x_i-x_m)+ik_3(x_m-x_i)} \\
&\quad - e^{ik_1(x_i-x_j)+ik_2(x_j-x_i)} \\
&\quad - e^{ik_2(x_j-x_m)+ik_3(x_m-x_j)}\Big) \\
&= |\Phi_k(k_1)|^2 |\Phi_k(k_2)|^2 |\Phi_k(k_3)|^2 \\
&\quad \sum_{i,j,m} \Big(1 + e^{i(k_1-k_3)x_i+i(k_2-k_1)x_j+i(k_3-k_2)x_m} \\
&\quad + e^{i(k_1-k_2)x_i+i(k_2-k_3)x_j+i(k_3-k_1)x_m} \\
&\quad - e^{i(k_1-k_3)(x_i-x_m)} - e^{i(k_1-k_2)(x_i-x_j)} - e^{i(k_2-k_3)(x_j-x_m)}\Big). \qquad (8.12)
\end{aligned}$$

The expression $(*)$ in the third line is only non-zero, if the three creation operators cancel the effect of the three annihilation operators. One finds the expression

$$(*) = \delta_{is}\delta_{jl}\delta_{mn} + \delta_{in}\delta_{js}\delta_{ml} + \delta_{il}\delta_{jn}\delta_{ms} - \delta_{in}\delta_{jl}\delta_{ms} - \delta_{il}\delta_{js}\delta_{mn} - \delta_{is}\delta_{jn}\delta_{ml}. \quad (8.13)$$

The result of Eq. (8.12) depends on the precise shape of the triple-well potential. We explicitly write down the third-order correlation function for the two studied cases. For the commensurately spaced triple well we find

$$\begin{aligned}
\langle \hat{n}_{k_1}\hat{n}_{k_2}\hat{n}_{k_3}\rangle = &\frac{2n_{k_1}n_{k_2}n_{k_3}}{27}(3 \\
&- 2\cos(2\pi(k_1-k_2)) - \cos(4\pi(k_1-k_2)) \\
&- 2\cos(2\pi(k_1-k_3)) - \cos(4\pi(k_1-k_3)) \\
&- 2\cos(2\pi(k_2-k_3)) - \cos(4\pi(k_2-k_3)) \\
&+ 2\cos(2\pi(2k_1-k_2-k_3)) \\
&+ 2\cos(2\pi(2k_2-k_1-k_3)) \\
&+ 2\cos(2\pi(2k_3-k_1-k_2))). \qquad (8.14)
\end{aligned}$$

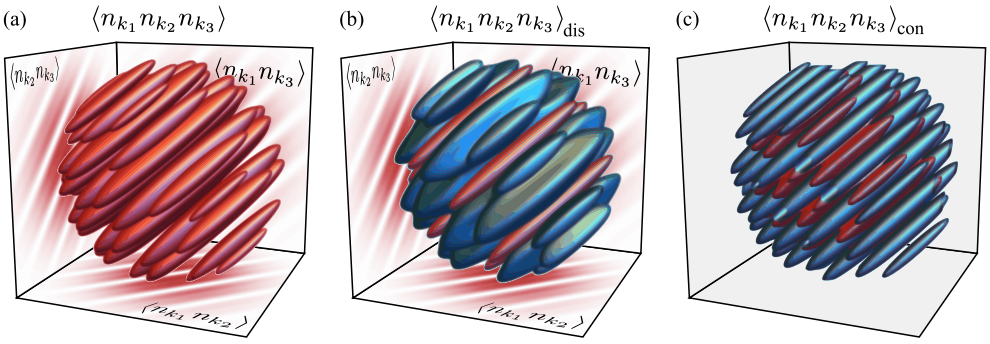

Figure 8.6: Calculated third-order momentum correlation function of commensurately spaced triple well. The contour plots show isosurfaces of the third-order momentum correlation function (red: positive, blue: negative). Integration over any of the three momenta of the full correlation function (a) or the disconnected correlation function (b) gives the second-order correlation function, as indicated with the projection on the three planes. The integral over any of the three momenta of the connected correlation function (c) vanishes, since n^{th} order connected correlations cannot be accessed from $n-1$ order correlations.

The correlation function of the incommensurately spaced triple well evaluates to

$$\begin{aligned}\langle \hat{n}_{k_1} \hat{n}_{k_2} \hat{n}_{k_3} \rangle =& \frac{2 n_{k_1} n_{k_2} n_{k_3}}{27} (3 \\ & - \cos(2\pi(k_1 - k_2)) - \cos(3\pi(k_1 - k_2)) - \cos(5\pi(k_1 - k_2)) \\ & - \cos(2\pi(k_1 - k_3)) - \cos(3\pi(k_1 - k_3)) - \cos(5\pi(k_1 - k_3)) \\ & - \cos(2\pi(k_2 - k_3)) - \cos(3\pi(k_2 - k_3)) - \cos(5\pi(k_2 - k_3)) \\ & + \cos(2\pi(3k_1 + 2k_2 - 5k_3)) \\ & + \cos(2\pi(2k_1 + 3k_2 - 5k_3)) \\ & + \cos(2\pi(-5k_1 + 2k_2 + 3k_3)) \\ & + \cos(2\pi(-5k_1 + 3k_2 + 2k_3)) \\ & + \cos(2\pi(3k_1 - 5k_2 + 2k_3)) \\ & + \cos(2\pi(2k_1 - 5k_2 + 3k_3)). \end{aligned} \tag{8.15}$$

To make the expression more readable and to keep the normalization from Eq. (8.10) we substituted $|\Phi_k(k_i)|^2$ by $\frac{n_{k_i}}{N}$ and rescaled the momenta by the lattice momentum $k_{\text{lat}} = \pi/a_{12}$, that we define in terms of the smallest well spacing.

The third-order correlation function depends on all three momenta and can hence not be plotted in a straightforward way. We illustrate the correlation function $\langle n_{k_1} n_{k_2} n_{k_3} \rangle$ for the commensurately spaced triple well in Fig. 8.6 (a) as a three dimensional contour plot. Integrating the third-order correlation function along any of the three momenta yields the second-order momentum correlation functions $\xi^{(2)}(k)$ as is indicated in the figure by the projection onto the three planes. Similar to the second-order cases, the contour plot indicates that there is no structure along the diagonal of the correlation

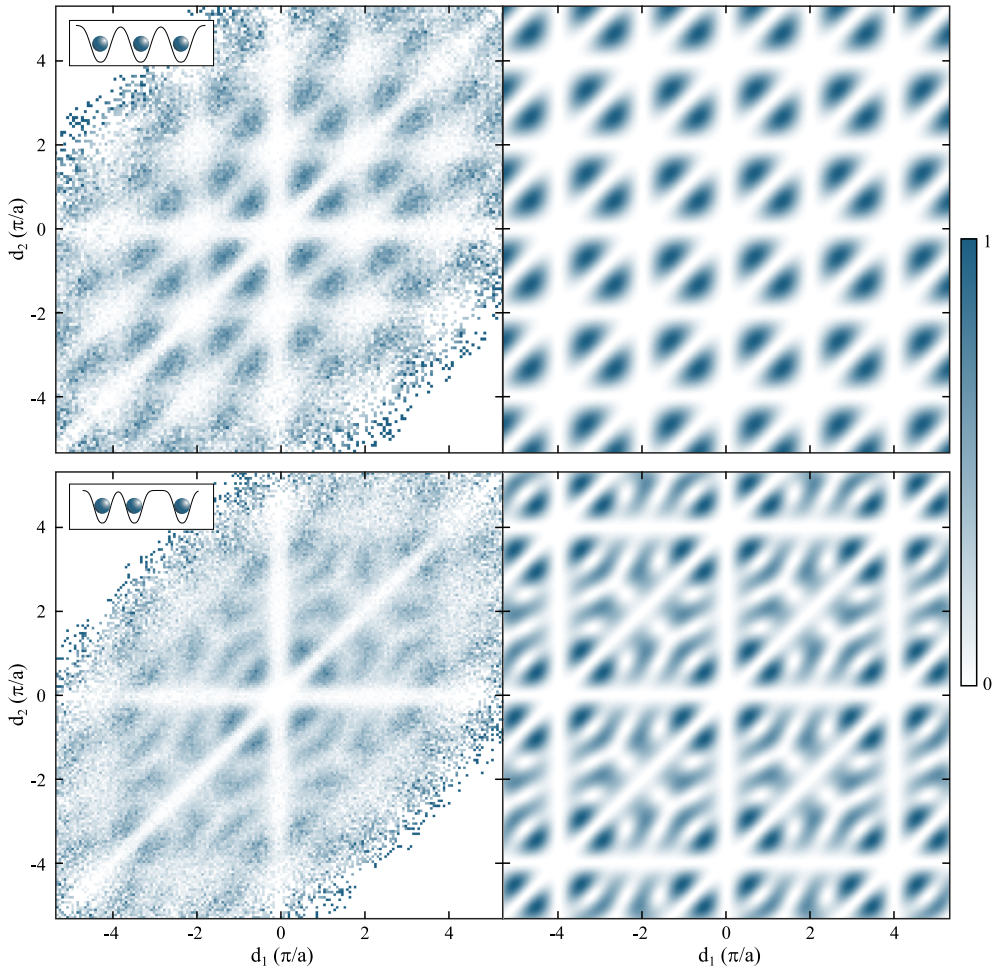

Figure 8.7: Measured and calculated correlator of the triple well. The figure shows the measured (left) and calculated (right) momentum correlator $C^{(3)}(d_1, d_2)$ for two triple-well configurations as illustrated in the insets. Number of data points for commensurately/incommensurately spaced triple well: 36100/55300

function. We hence define the normalized correlator as

$$C^{(3)}(d_1, d_2) = \int \frac{\langle n_k n_{k+d_1} n_{k+d_2} \rangle}{\langle n_k \rangle \langle n_{k+d_1} \rangle \langle n_{k+d_2} \rangle} \mathrm{d}k, \tag{8.16}$$

which again corresponds to an integral along the axis of the center-of-mass momentum $k_1 + k_2 + k_3$.

To compute the third-order correlator from experimental data we use the same data set as we used for the calculation of the plots shown in Fig. 8.5. Figure 8.7 shows both the measured and calculated $C^{(3)}(d_1, d_2)$ for both the commensurately-spaced (a) and the incommensurately-spaced (b) triple well. The correlator shows a very rich structure, in particular, the correlator for the incommensurately-spaced triple well clearly shows the presence of three distinct spatial frequencies. Besides the reduced contrast in the experimentally measured correlator, which we already discussed in the previous section, the agreement with the calculated correlator is very good.

As was already discussed in Sec. 7.5, for the investigation of true n^{th} order correlations we have to consider the connected correlation function and subtract all lower-order correlations from the full correlation function. Looking at Eq. (8.12) - Eq. (8.15) and using Eq. (7.20) for $n = 3$ as well as the calculation of the second-order correlation function we can rewrite the third-order correlation function as

$$\langle n_{k_1} n_{k_2} n_{k_3} \rangle = \langle n_{k_1} n_{k_2} n_{k_3} \rangle_{\mathrm{con}} + \langle n_{k_1} n_{k_2} n_{k_3} \rangle_{\mathrm{dis}}, \tag{8.17}$$

with the disconnected correlation function defined as

$$\begin{aligned} \langle n_{k_1} n_{k_2} n_{k_3} \rangle_{\mathrm{dis}} &= s(N)(2\langle n_{k_1} \rangle \langle n_{k_2} \rangle \langle n_{k_3} \rangle) \\ &+ p(N) \left(\langle n_{k_1} \rangle \langle n_{k_2} n_{k_3} \rangle + \langle n_{k_2} \rangle \langle n_{k_3} n_{k_1} \rangle + \langle n_{k_3} \rangle \langle n_{k_1} n_{k_2} \rangle \right). \end{aligned} \tag{8.18}$$

Here $s(N) = \frac{N(N-1)(N-2)}{N^3} = \frac{6}{27}$ and $p(N) = \frac{N(N-1)(N-2)}{N^2(N-1)} = \frac{1}{3}$ are scaling coefficients, that account for a proper normalization of the correlation function and ensure particle-number conservation (see below for additional information). The disconnected correlation function contains at most second-order correlations and can hence be calculated from experimental second-order measurements. The connected correlation function can then be calculated as the difference between the full and the disconnected correlation function, which explicitly evaluates to

$$\begin{aligned} \langle n_{k_1} n_{k_2} n_{k_3} \rangle_{\mathrm{con}} &= \frac{1}{2}(\cos(2\pi(2k_1 - k_2 - k_3)) + \cos(2\pi(2k_2 - k_3 - k_1)) \\ &+ \cos(2\pi(2k_3 - k_1 - k_2))) \end{aligned} \tag{8.19}$$

for the commensurate case and

$$\begin{aligned} \langle n_{k_1} n_{k_2} n_{k_3} \rangle_{\mathrm{con}} &= \frac{1}{4}(\cos(\pi(3k_1 + 2k_2 - 5k_3)) + \cos(\pi(2k_1 + 3k_2 - 5k_3)) \\ &+ \cos(\pi(5k_1 - 2k_2 - 3k_3)) + \cos(\pi(5k_1 - 3k_2 - 2k_3)) \\ &+ \cos(\pi(3k_1 - 5k_2 + 2k_3)) + \cos(\pi(2k_1 - 5k_2 + 3k_3))) \end{aligned} \tag{8.20}$$

for the incommensurate triple well.
The connected correlation function contains all cosine terms with three momenta in the argument. These are exactly the terms that do not show up in the lower-order correlation functions, as they involve the momenta of all three atoms. Similar to the full correlation function, we illustrate the disconnected and the connected correlation functions as a three dimensional contour plot in Fig. 8.6 (b) and (c), respectively. Integration over any of the three momenta of the disconnected correlator again yields the second-order correlation functions, whereas the integral vanishes for the connected correlator. It is hence exactly this three-dimensional structure that shows the correlations that are not accessible from second-order measurements. They should however show up in the connected correlator, which we define similar to Eq. (8.16) for the connected and the disconnected correlation functions. Figure 8.8 shows the measured and calculated correlators $C^{(3)}_{\mathrm{dis}}$ and $C^{(3)}_{\mathrm{con}}$ for the two well configurations. Apart from the

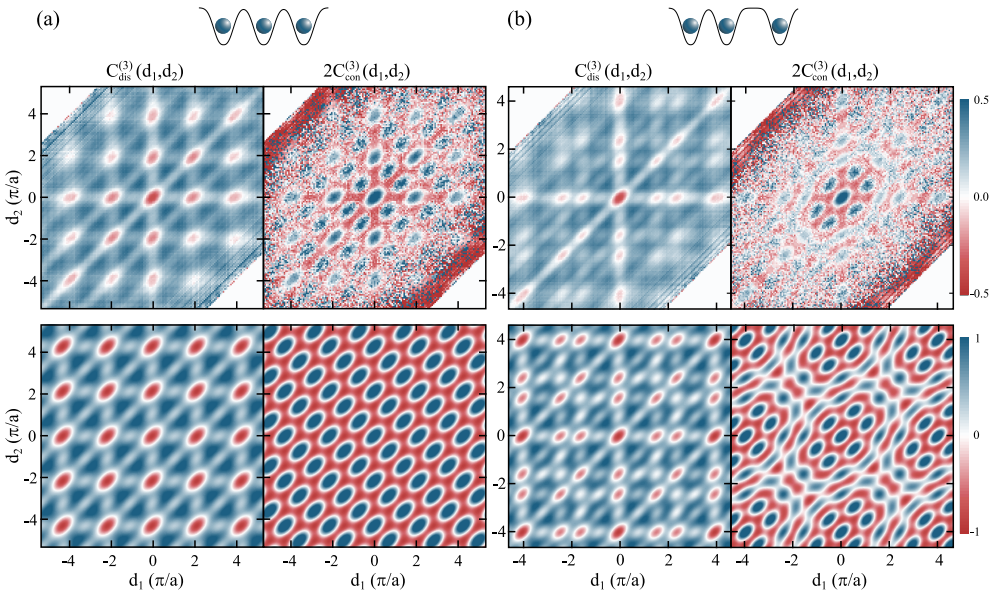

Figure 8.8: Disconnected and connected correlations in the triple well. The figure shows the measured (top) and calculated (bottom) disconnected and connected third-order correlators $C^{(3)}_{\mathrm{dis}}(d_1, d_2)$ and $C^{(3)}_{\mathrm{con}}(d_1, d_2)$ for the commensurately (a) and incommensurately (b) spaced triple well. For better visibility we plot $2C^{(3)}_{\mathrm{con}}(d_1, d_2)$ and adapt the colorscales of the measured correlation function as indicated by the different colorbars on the right.

reduced contrast, the measured correlators agree very well with the calculated correlators. The results show that three indistinguishable fermions exhibit true third-order correlations in the sense that the measured *combination* of two momenta has a direct impact on the momentum of the third atom. It is interesting to note, that the correlators $C^{(3)}(d_1, d_2)$ behave similar to the correlation functions $\xi^{(3)}(k)$ upon integration, i.e. integration over any of the two coordinates d_1 or d_2 results in the second-order correlator $C^{(2)}(d)$ for the full and the disconnected correlators but vanishes for the connected correlator.

Particle-Number Conservation

From the explicit calculations of the third-order momentum correlation functions in Eq. (8.14) and Eq. (8.15), it seems intuitive to define the connected correlation function as the sum over all cosine terms with all three momenta in the argument. However, this definition does not agree with the definition of the connected correlation function in Eq. (7.20). Indeed from that definition of the connected third-order correlation function, we would find significant connected third-order correlations only by the conservation of total particle number, cf. [204].
Intuitively speaking, detecting one out of N uncorrelated atoms at position x reduces the possibility of detecting another particle at position x' to $1 - \frac{1}{N}$. This effect vanishes for large particle number. In contrast, in systems of identical fermions, the Pauli-exclusion principle prohibits the detection of a second particle at position x. We hence include the two scaling coefficients $s(N)$ and $p(N)$ in Eq. (8.18), that ac-

count for particle-number conservation and a proper normalization of the correlation functions. Normalization of the correlation functions is such that

$$\begin{aligned} \int \langle \hat{n}_{k_1} \rangle \mathrm{d}k_1 &= N \\ \iint \langle \hat{n}_{k_1} \hat{n}_{k_2} \rangle \mathrm{d}k_1 \mathrm{d}k_2 &= N(N-1) \\ \iiint \langle \hat{n}_{k_1} \hat{n}_{k_2} \hat{n}_{k_3} \rangle \mathrm{d}k_1 \mathrm{d}k_2 \mathrm{d}k_3 &= N(N-1)(N-2). \end{aligned} \tag{8.21}$$

By choosing $s(N) = \frac{N(N-1)(N-2)}{N^3} \overset{\mathrm{N=3}}{=} \frac{6}{27}$ and $p(N) = \frac{N(N-1)(N-2)}{N^2(N-1)} \overset{\mathrm{N=3}}{=} \frac{1}{3}$ we ensure that correlations from number conservation are removed, such that uncorrelated particles give $C^{(3)}_{\mathrm{con}}(d_1, d_2) = 0$ for any N and our definition of the disconnected correlation functions agrees with the standard form for $N \to \infty$.

8.2.1 Wick's Theorem and Field Correlation Functions

It is important to mention that what was called n^{th} order momentum-correlation functions are n^{th} order correlations in the momentum-density operator $\hat{n} = \hat{\Psi}^\dagger \hat{\Psi}$ and therefore correlation functions of $(2n)^{th}$ order in the quantum-field operators $\hat{\Psi}$. Vacuum expectation values of field operators can always be decomposed into second-order correlation functions and hence no correlations beyond second order are expected to occur [205]. Using Wick's theorem [206], we can compute the momentum-density correlation functions in terms of the field operators as follows,

$$\langle \hat{n}_{k_1} \hat{n}_{k_2} \rangle = \langle n_{k_1} \rangle \langle n_{k_2} \rangle - G_{k_1,k_2} G_{k_2,k_1}, \tag{8.22}$$

where we used $\langle \hat{n}_{k_1} \rangle = \langle \hat{\Psi}^\dagger_{k_1} \hat{\Psi}_{k_1} \rangle$ and define the propagator $G_{k_1,k_2} = \langle \hat{\Psi}^\dagger_{k_1} \hat{\Psi}_{k_2} \rangle$, i.e. the diagonal and off-diagonal entries of the one-body density matrix, respectively. Since $G_{k_1,k_2} = G^*_{k_2,k_1}$, the connected second-order momentum-density correlation function reads as

$$\langle \hat{n}_{k_1} \hat{n}_{k_2} \rangle_{\mathrm{con}} = -G_{k_1,k_2} G_{k_2,k_1} = -\left| G_{k_1,k_2} \right|^2. \tag{8.23}$$

Hence we only measure the absolute value of the propagator and do not access its phase, which might be accessible by an additional first-order interference measurement.

With the above definitions we can expand the third-order momentum-density corre-

lation function as

$$\begin{aligned}
\langle \hat{n}_{k_1}\hat{n}_{k_2}\hat{n}_{k_3}\rangle &= \langle \hat{n}_{k_1}\rangle\langle \hat{n}_{k_2}\rangle\langle \hat{n}_{k_3}\rangle \\
&\quad -\langle \hat{n}_{k_1}\rangle G_{k_2,k_3}G_{k_3,k_2} - \langle \hat{n}_{k_2}\rangle G_{k_1,k_3}G_{k_3,k_1} - \langle \hat{n}_{k_3}\rangle G_{k_1,k_2}G_{k_2,k_1} \\
&\quad +G_{k_1,k_2}G_{k_2,k_3}G_{k_3,k_1} + G_{k_1,k_3}G_{k_3,k_2}G_{k_2,k_1} \\
&= \langle \hat{n}_{k_1}\rangle\langle \hat{n}_{k_2}\rangle\langle \hat{n}_{k_3}\rangle \\
&\quad -\langle \hat{n}_{k_1}\rangle |G_{k_2,k_3}|^2 - \langle \hat{n}_{k_2}\rangle |G_{k_1,k_3}|^2 - \langle \hat{n}_{k_3}\rangle |G_{k_1,k_2}|^2 \\
&\quad +G_{k_1,k_2}G_{k_2,k_3}G_{k_3,k_1} + G_{k_1,k_3}G_{k_3,k_2}G_{k_2,k_1} \\
&= -2\langle \hat{n}_{k_1}\rangle\langle \hat{n}_{k_2}\rangle\langle \hat{n}_{k_3}\rangle \\
&\quad +\langle \hat{n}_{k_1}\rangle\langle \hat{n}_{k_2}\hat{n}_{k_3}\rangle + \langle \hat{n}_{k_2}\rangle\langle \hat{n}_{k_1}\hat{n}_{k_3}\rangle + \langle \hat{n}_{k_3}\rangle\langle \hat{n}_{k_1}\hat{n}_{k_2}\rangle \\
&\quad +2\Re\{G_{k_1,k_2}G_{k_2,k_3}G_{k_3,k_1}\}. \qquad (8.24)
\end{aligned}$$

We recover the same structure that we obtained in Eq. (8.18) with the following definition of the connected correlation function

$$\langle \hat{n}_{k_1}\hat{n}_{k_2}\hat{n}_{k_3}\rangle_{\mathrm{con}} = 2\Re\{G_{k_1,k_2}G_{k_2,k_3}G_{k_3,k_1}\}. \qquad (8.25)$$

It is exactly this product of propagators that we cannot access in the experiment, since we are not sensitive to the phase of G_{k_i,k_j}. We therefore detect true third-order momentum-density correlations but emphasize that the third-order momentum-density correlation function would completely factorize into second-order field correlation functions, if we had access to the phase of the respective propagators.

Third-order connected correlations have recently also been studied in photonic systems [207, 208] in the context of multi-particle quantum interference. Following there ideas we can rewrite the propagator as $G_{k_i,k_j} = r_{ij}e^{i\phi_{ij}}$, where $r_{ij} \in [0,1]$ is zero for orthogonal states and one for perfectly indistinguishable states. In the measured second-order correlation functions, r_{ij} plays the role of the reduced contrast due to partial distinguishability, see Sec. 8.1. The phase ϕ_{ij} drops out in the above second-order formulas and does not play a role in second-order interference experiments. However, rewriting the connected third-order correlation function in the same way,

$$\langle \hat{n}_{k_1}\hat{n}_{k_2}\hat{n}_{k_3}\rangle_{\mathrm{con}} = 2\Re\{Re^{i\Phi}\} = R\cos\Phi, \qquad (8.26)$$

with $R = r_{12}r_{23}r_{31}$ and the so called *triad* phase $\Phi = \phi_{12} + \phi_{23} + \phi_{31}$, immediately makes clear that the phase ϕ_{ij} does play a role for the observed third-order correlations. A non-zero triad phase reduces the contrast of the connected third-order correlation function beyond the reduction that is caused by partial indistinguishability due to bad mode overlap.

In this chapter we presented momentum-correlation measurements on systems containing two or three identical particles trapped in an array of optical tweezers. The observed correlations are purely caused by fermionic exchange statistics. We have shown that the pairwise exchange symmetry induced true third-order correlations

in the momentum-density of three identical particles. The understanding of such correlations is crucial for the investigations of mesoscopic systems, where additional correlations may arise due to interactions. Our measurements prove that our methods can produce high-quality momentum-density correlation functions of small systems and that they are therefore perfectly suited to study complex correlations in strongly correlated systems, to detect ordering beyond the optical resolution of the imaging scheme or to study many-particle interference and quantum optics with systems of massive fermions.

Chapter 9

Density-Matrix Reconstruction

So far we investigated correlations between identical fermions in a double-well and triple-well potential and showed that fermionic statistics and the antisymmetrization of the wave function induce complex higher-order correlations in the momentum density. The obtained results also proved that we can apply our experimental tools to measure high-quality momentum-density correlation functions. In this chapter, we develop new methods to analyze momentum correlation functions in systems containing two or three mobile, interacting particles. We present a scheme to relate momentum correlation functions to off-diagonal entries of the density matrix and reconstruct physical density matrices based on Bayesian inference. We start by discussing the double-well case and then generalize the scheme to the triple well.

9.1 Momentum Correlations of the Interacting Double Well

In contrast to the measurements that we discussed in the previous chapter, we now consider the interacting double well. The basic physics and relevant states were already discussed in Sec. 7.3. As explained in [62, 85, 94, 163] and illustrated in Fig. 9.1, we experimentally prepare the ground state of the double well by deterministically loading a single tweezer with two atoms, followed by an adiabatic passage to the balanced ground state by ramping on the second tweezer. During this passage the two atoms are non-interacting and stay in the total ground state of the system, resulting in the state described by Eq. (7.7). We then exploit the interspin Feshbach resonance and ramp the magnetic offset field to tune the interaction to the desired value of U/J. In the chosen basis, the final state can be described by a 4×4 density matrix. As described in Sec. 7.4 we either probe the in-situ density or the single-particle momentum distribution by releasing the two atoms into our optical dipole trap, acting as a one-dimensional wave guide, and detect the position of the atoms after time of flight. After post selection to the correct atom number $N_\uparrow = N_\downarrow = 1$ with a post-selection

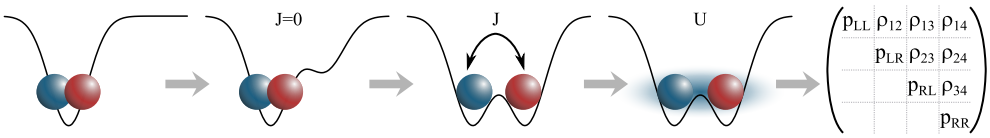

Figure 9.1: Ground-state preparation of the interacting double well. We start by preparing two non-interacting atoms in the ground state of a single optical tweezer. We adiabatically ramp on a second well to the balanced double well. We finally tune the interaction by ramping the magnetic offset field to the desired value of U/J. The two interacting atoms in the ground state of the double well are described by a 4×4 density matrix.

rate of about 80%, we compute the second-order in-situ and momentum space correlation function $\xi^{(2)}_{(\uparrow\downarrow)}(x) = \langle n_{x_\uparrow} n_{x_\downarrow} \rangle$ and $\xi^{(2)}_{(\uparrow\downarrow)}(k) = \langle n_{k_\uparrow} n_{k_\downarrow} \rangle$. Figure 9.2 presents both correlation functions for three selected interaction strengths: attractive interaction ($U/J = -5.87$), zero interaction ($U/J = 0$) and strong repulsive interaction ($U/J = 18.5$).

The in-situ measurements are presented in a spin-resolved way, i.e. in each run we measure one of the states $\Psi_i \in \{|LL\rangle, |RL\rangle, |LR\rangle, |RR\rangle\}$, where the first (second) entry is the location of the spin-up (spin-down) particle. Each quadrant in the upper panel in Fig. 9.2 represents one of those states. The shown data is the sampled in-situ distribution from around 1000 realizations. Summation of each quadrant yields the probability of projecting the state on the respective basis state $\langle \Psi_i | \Psi_{gs} \rangle \langle \Psi_{gs} | \Psi_i \rangle = p_i^2$, $i \in \{LL, LR, RL, RR\}$, as indicated in the figure. Those numbers directly give the diagonal entries of the density matrix ρ_{ii}. As discussed in Sec. 7.3, in particular in Fig. 7.5, the Hamiltonian favors (suppresses) doubly occupied sites for attractive (repulsive) interactions, which we observe in the in-situ data set by the induced asymmetry for the two interacting cases as compared to the non-interacting case (see [62] for more quantitative discussion of experimental results).

As argued in Sec. 7.4.1, diagonal entries of the density matrix do not contain information about coherence properties so that a pure state cannot be distinguished from a maximally mixed state without measuring off-diagonal entries of the density matrix. Following the proposals in [209, 210] we access information about the off-diagonal entries of the density matrix via the analysis of the momentum correlation functions. The key idea is to relate distinct pattern in the momentum correlation function to entries of the density matrix, which is achieved by expanding a general state to momentum space, as we will now work out in detail for the double-well case. Similar to the discussion around Eq. (8.11) we again start by defining the general real and momentum space wave functions of the two spin states as

$$\begin{aligned} \hat{\Psi}^\dagger_\sigma(x) &= \sum_i^N \Phi_x(x - x_i) c^\dagger_{\sigma,i} \\ \hat{\Psi}^\dagger_\sigma(k) &= \sum_i^N \Phi_k(k) e^{-ikx_i} c^\dagger_{\sigma,i}. \end{aligned} \tag{9.1}$$

Here $\Phi(x)$ is the onsite Wannier function, which is well approximated by a Gaussian within the experimental precision. We assume that the onsite wave functions on

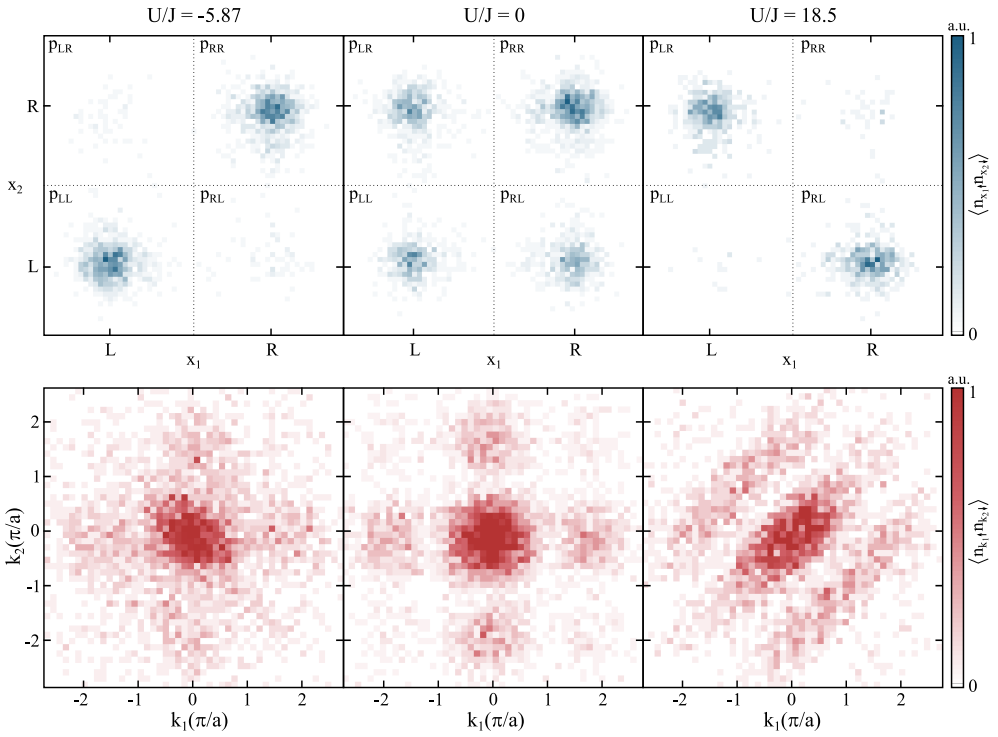

Figure 9.2: In-situ and momentum correlations of the interacting double well. The upper panel shows the measured spin-resolved insitu correlation functions for three different interaction strength $U/J = -5.87$ (left), 0 (center) and 18.5 (right). The lower plots show the spin-resolved momentum correlation function for the same U/J. For vanishing interactions the correlation functions factorize and no second-order correlations are present. For attractive (repulsive) interactions, double occupancies are favored (suppressed) and correlations in the absolute (relative) momenta arise.

different sites are orthogonal. $\Phi_k = \mathcal{F}[\Phi_x](k)$ is the Fourier transform of $\Phi(x)$ and $c^\dagger_{\sigma,i}$ are fermionic creation operators on site i with spin σ. The sum runs over all wells i. Neglecting the envelope Φ_x from now on, we can write down the opposite-spin second-order momentum-density correlation function as

$$\begin{aligned}\langle \hat{n}_{k_1\uparrow}\hat{n}_{k_2\downarrow}\rangle &= \langle \hat{\Psi}^\dagger_\uparrow(k_1)\hat{\Psi}_\uparrow(k_1)\hat{\Psi}^\dagger_\downarrow(k_2)\hat{\Psi}_\downarrow(k_2)\rangle \\ &= \sum_{k,l,m,n} e^{ik_1(x_l-x_k)+ik_2(x_n-x_m)}\langle c^\dagger_{\uparrow k}c_{\uparrow l}c^\dagger_{\downarrow m}c_{\downarrow n}\rangle \end{aligned} \tag{9.2}$$

with $k,l,m,n \in \{L,R\}$ for the double-well case. To relate the above expression to the density matrix, we will rewrite the expression in its matrix representation. To this end we evaluate the term in the brackets $\langle\cdot\rangle$ with respect to all combinations of basis states, using

$$\begin{aligned}\langle n_{k_1\uparrow}n_{k_2\downarrow}\rangle_{ij} &= \langle ii'|\, n_{k_1\uparrow}n_{k_2\downarrow}\,|jj'\rangle \\ &= \sum_{k,l,m,n} e^{ik_1(x_l-x_k)+ik_2(x_n-x_m)}\,\langle 0|\, c_{\uparrow i}c_{\downarrow i'}c^\dagger_{\uparrow k}c_{\uparrow l}c^\dagger_{\downarrow m}c_{\downarrow n}c^\dagger_{\uparrow j}c^\dagger_{\downarrow j'}\,|0\rangle \end{aligned} \tag{9.3}$$

with i, i', j, j' the respective entries of the four basis states $i, j \in \{LL, LR, RL, RR\}$. We exemplarily evaluate this expression for $\{ii', jj'\} = \{LR, LL\}$,

$$\begin{aligned}
\langle LR|\, \hat{n}_{k_1\uparrow}\hat{n}_{k_2\downarrow}\, |LL\rangle &= \sum_{k,l,m,n} e^{ik_1(x_l-x_k)+ik_2(x_n-x_m)}\, \langle 0|\, c_{\uparrow L}c_{\downarrow R}c^\dagger_{\uparrow k}c_{\uparrow l}c^\dagger_{\downarrow m}c_{\downarrow n}c^\dagger_{\uparrow L}c^\dagger_{\downarrow L}\, |0\rangle \\
&= \sum_{k,l,m,n} e^{ik_1(x_l-x_k)+ik_2(x_n-x_m)}\delta_{Ln}\delta_{Rm}\delta_{kl} \\
&= \sum_{k} e^{ik_1(x_k-x_k)+ik_2(x_L-x_R)} \\
&= 2e^{ik_2 a}, \qquad (9.4)
\end{aligned}$$

where the factor 2 in the last line is due to the normalization of the wave function. In the last line we furthermore used $a = x_L - x_R$ with the well spacing of the double-well potential a. We obtain the full momentum-density correlation operator in matrix form as

$$\widehat{(n_{k_1} n_{k_2})} = \begin{pmatrix} 1 & e^{-iak_2} & e^{-iak_1} & e^{-ia(k_1+k_2)} \\ & 1 & e^{-ia(k_1-k_2)} & e^{-iak_1} \\ & & 1 & e^{-iak_2} \\ h.c. & & & 1 \end{pmatrix}. \qquad (9.5)$$

From the operator expression above, we can calculate the momentum-density correlation function by taking the trace of the operator, multiplied by the density matrix,

$$\begin{aligned}
\langle n_{k_1} n_{k_2}\rangle = \mathrm{Tr}(\rho\widehat{(n_{k_1} n_{k_2})}) &= \sum_{i,j} \rho_{ji}\widehat{(n_{k_1} n_{k_2})}_{ij} \\
&= p_{LL} + p_{LR} + p_{RL} + p_{RR} \\
&\quad +2\Re\{(\rho_{13}+\rho_{24})e^{iak_1}\} \\
&\quad +2\Re\{(\rho_{12}+\rho_{34})e^{iak_2}\} \\
&\quad +2\Re\Big\{\rho_{14}e^{ia(k_1+k_2)}\Big\} \\
&\quad +2\Re\Big\{\rho_{23}e^{ia(k_1-k_2)}\Big\} \qquad (9.6)
\end{aligned}$$

For our analysis we rewrite this expression into the quadrature representation, which will also become useful for the generalization to larger systems,

$$\begin{aligned}
\langle n_{k_1} n_{k_2}\rangle = 1 & \\
&+ 2\Re(\rho_{13}+\rho_{24})\cos(ak_1) && +2\Im(\rho_{13}+\rho_{24})\sin(ak_1) \\
&+ 2\Re(\rho_{12}+\rho_{34})\cos(ak_2) && +2\Im(\rho_{12}+\rho_{34})\sin(ak_2) \\
&+ 2\Re(\rho_{14})\cos(a(k_1+k_2)) && +2\Im(\rho_{14})\sin(a(k_1+k_2)) \\
&+ 2\Re(\rho_{23})\cos(a(k_1-k_2)) && +2\Im(\rho_{23})\sin(a(k_1-k_2)). \qquad (9.7)
\end{aligned}$$

The four diagonal entries of in Eq. (9.6), p_{LL}, p_{LR}, p_{RL}, and p_{RR}, are the projection probabilities of the state onto the four basis states, that we get from the in-situ measurements and sum up to 1. ρ_{ij} are the off-diagonal entries according the basis states as defined above (see also Fig. 9.1). The result shows that each oscillatory pattern in the momentum-correlation function can be related to specific elements of the density

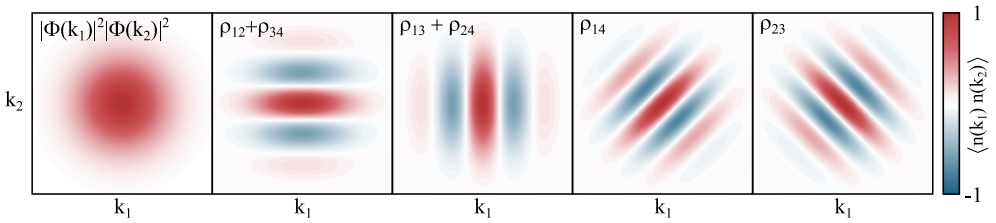

Figure 9.3: Illustration of fitting functions for momentum correlation functions. Each pattern can be related to an entry or a sum over two entries of the density matrix. Horizontal and vertical stripes correspond to single-particle coherences whereas diagonal stripes are caused by two-particle coherences.

matrix, e.g. the contrast of a cosinusoidal oscillation in the relative momentum $k_1 - k_2$ corresponds to the real part of ρ_{23} whereas a phase shifted oscillation indicates a non-zero imaginary part of ρ_{23}. Note that not all entries of the density matrix can be uniquely identified, because some of them only appear as a sum, such as $(\rho_{13} + \rho_{24})$. In total there are oscillatory patterns with four different frequencies, as we illustrate in Fig. 9.3, together with a Gaussian envelope that we omitted in the calculations. As mentioned before, this envelope is given as the Fourier transform of the real-space wave function (cf. Eq. (9.1)). By decomposing the measured momentum-density correlation function into the set of trigonometric functions according to Eq. (9.7), we extract a set of 8 equations for the 6 complex off-diagonal entries of the density matrix (i.e. 6 real and 6 imaginary coefficients). In particular, we can directly determine the anti-diagonal elements ρ_{14} and ρ_{23}. However, the two patterns with oscillations in k_1 or k_2 only appear with the sum of two entries so that only the sum of those entries can be constrained. Note that those patterns correspond to the single-particle coherences, that we already discussed in Sec. 7.4.1. A determination of those entries is possible e.g. via a rotation in the $\{L, R\}$ basis [209], or by performing correlation measurements in the near field [211]. However, we do not perform such additional measurements, but rather employ a Bayesian quantum state estimation [212]. This approach reconstructs a set of physical density matrices, based on the constraints that we obtain from the momentum-density correlation function. Before discussing this approach in Sec. 9.2, we generalize the analysis of the momentum-correlation function to the case of three interacting, mobile particles in a triple-well potential.

9.1.1 Three Interacting Fermions in a Triple Well

Before going into the technical details of how to analyze the triple-well correlation functions, we present a more intuitive way of how to relate the entries of the density matrix to trigonometric functions that appear in the momentum correlation function. As illustrated in Fig. 9.4 (a) for the double well and in (b) for the triple well, one can analyze how many tunnel events are necessary to transform one basis state Ψ_i into another basis state Ψ_j. For example for ρ_{24} of the 4×4 matrix of the double well, the state $\Psi_2 = |LR\rangle$ connects to $\Psi_4 = |RR\rangle$ via a single tunnel event of the first atom from left to right. This process contributes with $\cos(k_1 a)$ to the total momentum correlations function, since the first atom *moved* the distance a in positive direction.

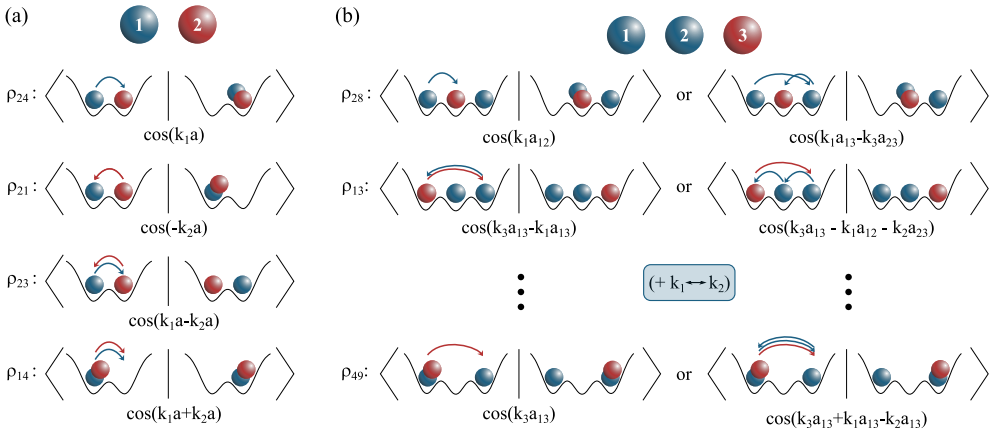

Figure 9.4: Density-matrix reconstruction. Instead of doing the maths to relate patterns in the momentum correlation function to entries of the density matrix, we can also analyze, which states contribute to the entry and by how many tunneling events they are connected. (a) Illustration of assignment scheme for the double well with spacing a. (b) Illustration of the assignment scheme for the triple well with spacings a_{12}, a_{23}, and $a_{13} = a_{12} + a_{23}$. Due to the indistinguishability of two atoms, there are always two possible tunneling configurations. Labeling the particles is crucial to associate the correlations to the correct momenta. However, also the antisymmetric correlations $k_1 \leftrightarrow k_2$ appear due to the indistinguishability of the two identical particles.

Similarly for ρ_{21}, the second atom hops to the left well and therefore contributes with $\cos(-k_2 a)$. The anti-diagonal entries of the density matrix correspond to processes, that involve the movement of both atoms, e.g. $\langle LR| \leftrightarrow |RL\rangle$ contributes with $\cos(k_1 a - k_2 a)$, since the first particle hops to the right ("$+k_1$") and the second to the left ("$-k_2$"), respectively. We can apply the same scheme to the triple-well case, but have to take care of the spacing between the wells, which might not be commensurate. Furthermore in the case of indistinguishable particles, one also has to take the antisymmetrized form into account. Based on that intuitive scheme we will define a set of trigonometric basis functions into which we decompose the highest-order momentum correlation function.

Suppose we have prepared three atoms in three optical tweezers in the laboratory and we want to characterize the exact state of the system. The only interacting configuration consists of two spin-up and one spin-down atom (or vice versa). As discussed in Sec. 7.3, there are hence nine different basis states, which we define as

$$\begin{aligned} |\Psi\rangle \quad \in \quad & \{|\uparrow,\uparrow,\downarrow\rangle\,;|\uparrow,\downarrow,\uparrow\rangle\,;|\downarrow,\uparrow,\uparrow\rangle\,; \\ & |\uparrow\downarrow,\uparrow,\cdot\rangle\,;|\uparrow\downarrow,\cdot,\uparrow\rangle\,; \\ & |\uparrow,\uparrow\downarrow,\cdot\rangle\,;|\cdot,\uparrow\downarrow,\uparrow\rangle\,; \\ & |\uparrow,\cdot,\uparrow\downarrow\rangle\,;|\cdot,\uparrow,\uparrow\downarrow\rangle\}, \end{aligned} \tag{9.8}$$

where the first, second and third entry describe the spin occupation of the left, center and right well, respectively. Within the lowest-band approximation of the Fermi-Hubbard model (see Sec. 7.3) fermions with opposite spin can occupy the same well

but two identical spins in the same well are forbidden by the Pauli-exclusion principle. Similar to the double-well case, we investigate the system in real space by repeatedly imaging the spin-resolved in-situ distribution. We directly extract the nine diagonal entries of the density matrix p_i, which are given by the probability of projecting the state onto each of the nine basis states.
We then measure the spin-resolved single-particle momenta from which we construct the third-order momentum-correlation function $\xi^{(3)}_{(\uparrow\uparrow\downarrow)}(k_1, k_2, k_3) = \langle n_{k_1\uparrow} n_{k_2\uparrow} n_{k_3\downarrow}\rangle$. As argued above, we know that each off-diagonal entry of the density matrix contributes to the correlation function with specific trigonometric patterns. Motivated by Eq. (9.7) and Fig. 9.4 we decompose $\xi^{(3)}_{(\uparrow\uparrow\downarrow)}$ into a general set of trigonometric basis functions

$$\xi^{(3)}_{(\uparrow\uparrow\downarrow)}(\vec{k}) = \sum_i c_i \cos(2\pi\vec{q}_i\vec{k}) + s_i \sin(2\pi\vec{q}_i\vec{k}), \tag{9.9}$$

where $\vec{k} = (k_1, k_2, k_3)^T$ and the different $\vec{q}_i$s are vectors that contain the appearing real space distances between spatial modes. In the general case of an incommensurately spaced triple well, with $a_{12} \neq a_{23}$, each of the three components in $\vec{q}_i$ can take any of the seven values $\{-a_{13}, -a_{12}, -a_{23}, 0, a_{23}, a_{12}, a_{13}\}$. In total this gives rise to $7^3 = 343$ different $\vec{q}_i$s, including the zero-vector (0,0,0), which does not generate any pattern. Due to the symmetry of the cosine and sine functions ($\cos(x) = \cos(-x)$ and $\sin(x) = -\sin(-x)$), half of the $\vec{q}_i$s are redundant, reducing the total set of possible $\vec{q}_i$ to $342/2 = 171$ (hence 171 c_i and 171 s_i).
Following the discussion around Eqs.(9.5 - 9.7) we expand the third-order momentum-density correlation operator $\hat{\xi}^{(3)}(\vec{k})$ and calculate the correlation function of a general density matrix ρ_g as $\mathrm{Tr}\left(\rho_g \hat{\xi}(\vec{k})\right)$ using Mathematica [213]. The full momentum-density correlation function can be written in a similar form as Eq. (9.9),

$$\xi^{(3)}_{(\uparrow\uparrow\downarrow)}(\vec{k}) = \sum_{i,j} K_{ij}\Re(\rho_j)\cos(2\pi\vec{q}_i\vec{k}) + N_{ij}\Im(\rho_j)\sin(2\pi\vec{q}_i\vec{k}). \tag{9.10}$$

Here $\mathbf{K}$ and $\mathbf{N}$ are coefficient matrices and $\vec{\rho}$ is a vectorized form of the density matrix. Equating the two equations (9.9) and (9.10), we obtain a set of coupled linear equations for the off-diagonal entries of the density matrix

$$\begin{aligned} \mathbf{K}\Re(\vec{\rho}) &= \vec{c} \\ \mathbf{N}\Im(\vec{\rho}) &= \vec{s}. \end{aligned} \tag{9.11}$$

The size and the rank of the two matrices $\mathbf{M}$ and $\mathbf{N}$ depend on the shape of the triple well. Let us consider the incommensurately spaced triple well with two spin-up and one spin-down particles. In the case where two of the three atoms are indistinguishable, the number of possible trigonometric pattern can be further reduced. We choose k_1 and k_2 for the atoms in $|\uparrow\rangle$ and k_3 for the atom in $|\downarrow\rangle$.
Pauli Exclusion: Due to the Pauli-exclusion principle, no states which involve two identical fermions on the same lattice site are involved. Combinations such as $\vec{q}_i = (-a_{13}, -a_{12}, X)$ or $\vec{q}_i = (-a_{12}, a_{23}, X)$ for any X are not allowed, because they are caused by processes where the two indistinguishable particles either hop to the

same well or start from the same well (cf. Fig. 9.4). This reduces the number of possible $\vec{q}_i$ to $171 - \frac{3\cdot6\cdot7}{2} = 108$. The factor 1/2 is due to the $\vec{q}_i$s that have already been removed as argued above.
Diagonal Entries: There are 3 $\vec{q}_i$s on the diagonal (such as $\langle\uparrow\uparrow\downarrow \mid \uparrow\uparrow\downarrow\rangle \rightarrow \cos((k_1 - k_2)a_{12})$, which do not contribute to the sine terms, because all diagonal entries are real. Since we constrain the diagonal entries with the in-situ measurements, we exclude them from the further analysis. There are hence 105 $\vec{q}_i$ for the off-diagonals.
Indistinguishable Duplicates: Within the $2 \cdot 105 = 210$ trigonometric pattern there are six of the form $(0, 0, X)$. The remaining 204 entries contain 102 duplicates due to the indistinguishability of the first two atoms in the sense that they can be obtained from each other by exchanging k_1 and k_2.

For the incommensurately spaced triple well we are finally left with 108 trigonometric pattern that constrain the off-diagonal entries of the density matrix and 9 constraints for the diagonal entries from the in-situ measurement. Combining the matrices $\mathbf{K}$ and $\mathbf{N}$ into a single block diagonal matrix $\mathbf{B}$ and the real and imaginary entries of the vectorized density matrix into a single vector of the form $\vec{b} = (\Re(\vec{\rho}), \Im(\vec{\rho}))^T$, we can write Eq. (9.11) as

$$\mathbf{B}\vec{b} = \begin{pmatrix} \vec{c} \\ \vec{s} \end{pmatrix}, \tag{9.12}$$

with $\dim(\mathbf{B})=117\times81$, $\dim(\vec{b}) = 81\times1$ and $\dim(\mathbf{B}\vec{b}) = 117\times1$. Obviously these 117 equations are not linearly independent. In fact we find that the matrix $\mathbf{B}$ has a rank of $\mathrm{rank}(\mathbf{B}) = 69$ and hence constrains 69 of 81 entries of the density matrix.
With similar arguments we can deduce the matrix $\mathbf{B}_c$ also for the commensurate triple well and find $\dim(\mathbf{B}_c) = 61 \times 81$ and $\mathrm{rank}(\mathbf{B}_c) = 37$. The reason for the lower rank of $\mathbf{B}_c$ compared to the incommensurate case is that there is one spatial frequency less in the commensurate case (since $a_{12} = a_{23}$) and therefore less unique constraints for the density matrix. However, the set of equations in Eq. 9.12 is based on experimental measurements and therefore also contains experimental noise so that the set of equations of Eq. 9.11 effectively has full rank. As we will explain later, we use the full set of equations for the further analysis.

The set of equations that we can extract from the momentum-density correlation function and the in-situ measurements are not sufficient to fully constrain the density matrix. This applies both to the double-well and the triple-well case. Even if we could constrain the full density matrix, the result would most likely not describe a physical state due to the density matrix being not positive semidefinite because of statistical uncertainties of all entries. Based on the reconstructed set of equations $\mathbf{B}$, we choose to reconstruct the full density matrix via a Bayesian quantum state estimation as we describe in the following section.

9.2 Bayesian Quantum State Estimation

Finding a density matrix that describes measurement outcomes is called a *quantum state estimation*. As nicely outlined in Ref. [212] there are two typical approaches to estimate a quantum state: *Maximum Likelihood Estimation* (MLE) and *Bayesian Mean Estimation* (BME). In both cases one wants to find a state ρ that would have produced the observed data $\mathcal{M}$. One therefore defines the likelihood $\mathcal{L}(\rho) = p(\mathcal{M}|\rho)$ as the probability of measuring $\mathcal{M}$ if the prepared state was ρ.
MLE finds the most likely state ρ_{MLE}, i.e. the state that simply maximizes the likelihood function $\mathcal{L}(\rho)$. However, this approach has serious flaws, in particular since it might predict rank-deficient states with zero eigenvalues (with no error bars), which can never be justified with a finite number of experiments. The idea of state estimation however is not only to explain the *obtained* measurements but to find a state from which one can also predict *future* measurements.
The approach of BME is different. Here, one does not only obtain the most likely state, but considers all states that are consistent with the observed measurements. Since there are many such states, it also naturally comes with error bars and therefore does not suffer from rank-deficiency. In this section we explain how we can perform a Bayesian mean estimation based on the previously discussed correlation measurements.

With the presented analysis of correlation functions there are two remaining issues:

1. We cannot constrain the full density matrix, since some patterns in the momentum correlation function cannot be unambiguously related to a single entry of the density matrix. A full state tomography would require additional measurements [209, 211], however, for larger systems these measurements might become technically impossible.

2. The decomposition of the correlation function into trigonometric basis functions, as we discussed in the previous section, determines each entry of the density matrix with its own statistical uncertainties. These statistical uncertainties might lead to unphysical properties of the density matrix, such as negative eigenvalues.

In order to obtain a physical density matrix that is most compatible with our measurements, we employ a Bayesian quantum state estimation. We follow the scheme outlined in Ref. [212] and divide the estimation into three major steps.

1. **Generate a Likelihood Function from Experimental Data, $\mathcal{L}(\rho)$**
   The likelihood function represents all the information about the system that we can extract in the experiment. From a Bayesian point of view, the likelihood function $\mathcal{L}(\rho) = p(M|\rho)$ is the probability of observing the outcome M, conditioned on the real density matrix ρ. Assuming Gaussian distributed errors, the likelihood function is given by

$$\mathcal{L}(\rho) = \prod_i \frac{1}{\sqrt{2\pi\sigma_i^2}} \exp\left(-\frac{(M_i - \text{Tr}(\hat{M}_i\rho))^2}{2\sigma_i^2}\right). \tag{9.13}$$

This function compares measured values M_i to the expectation values of the observables $\hat{M}_i$ for a given ρ, weighted by the experimental uncertainties σ_i.

2. **Prior and Posterior Distribution**
   We assume no prior knowledge about the states and therefore choose an uninformative prior $\pi(\rho)d\rho$. For d dimensional pure states a suitable measure is the Haar measure $d_d\rho$. Mixed states are taken care of by starting with the Haar measure in $d+n$ dimensions and tracing out the ancillary dimensions. $d_n\rho$ is hence the Haar measure while $d_d\rho$ is the Hilbert–Schmidt measure. Multiplying the prior with the likelihood function yields the posterior distribution $\mathcal{L}(\rho)\pi(\rho)d\rho$

3. **Mean Posterior Distribution**
   The best description of the knowledge of the state is the integral over the posterior distribution $\rho_{\mathrm{BME}} = \int \rho\mathcal{L}(\rho)\pi(\rho)d\rho$. In order to compute this function over our integral measure, we apply the Metropolis-Hastings (MH) algorithm, which calculates the average of a function ρ over the integration measure. Compared to other Monte-Carlo techniques, that randomly sample over the integration measure, the MH algorithm makes local, *biased* jumps: Before jumping from ρ to ρ', the likelihood ratio $r = \frac{\mathcal{L}(\rho)\pi(\rho)}{\mathcal{L}(\rho')\pi(\rho')}$ is computed. If $r > 1$, the algorithm jumps from ρ to ρ', but if $r < 1$ the algorithm jumps with probability r to the new state. This jumping rule ensures that the algorithm spends more time at regions with more likely states.

To apply the above algorithm to the reconstruction of density matrices of experimentally realized states, we use the constraints that we obtain from the analysis of the momentum-density correlation function (see Eq. (9.12)) to define the likelihood function. As described, we write the basis states in a vectorized form $\vec{\rho}$ with 10 real and 6 imaginary entries for the double well and 45 real and 36 imaginary entries for the triple well. We combine the two matrices $\mathbf{K}$ and $\mathbf{N}$ into a single matrix $\mathbf{B}$, and combine the constraints $\vec{c}$ and $\vec{s}$ into the vector $\vec{\chi} = \begin{pmatrix}\vec{c}\\ \vec{s}\end{pmatrix}$ together with their uncertainties $\delta\vec{\chi} = \begin{pmatrix}\vec{c}\\ \vec{s}\end{pmatrix}$. We obtain the likelihood function as

$$\mathcal{L}(\rho) = \prod_i \frac{1}{\sqrt{2\pi\delta\chi_i^2}} \exp\left(-\frac{(\chi_i - \sum_i B_{ij}\rho_j)^2}{2\delta\chi_i^2}\right). \tag{9.14}$$

The MH algorithm step by step samples the posterior distribution $\mathcal{L}(\rho)\pi(\rho)d\rho$ over the integration measure and in each step generates a physical density matrix. While the mean over all those states ρ_{BME} is the best description of the state based on the experimental observations, the full posterior distribution of density matrices can be used for further analysis and especially for the calculation of uncertainties. In the next section we apply the Bayesian quantum state estimation to all states that we realized in the laboratory.

9.3 State Reconstruction

We are now ready to apply the reconstruction scheme to experimental data. In total we investigate three different classes of states to which we apply the described schemes; a polarized, *spin-rotated triplet* state in the double well (i), a set of *interacting singlet states* in the double well with different interaction strengths (ii), and two *three-particle states* in the triple well (iii). In this section we separately describe and discuss the density-matrix reconstruction of each investigated state. The explicit form of the reconstructed density matrices of each state and the uncertainties are given in Appendix A. In the next chapter we will use the obtained density matrices to investigate entanglement properties in systems containing indistinguishable particles.

9.3.1 Spin-Rotated Triplet State in a Double Well

The first state that we investigate is a non-interacting state of identical, polarized fermions. As we will see, this state features strong second order momentum correlations in each spin configuration and will be relevant for the discussion of particle-particle entanglement in the next chapter. Since the basis states are different from the interacting double well, it has to be treated in a slightly different way. However, we choose to start with the discussion of that state because it is nicely suited to illustrate the working principle of the Bayesian reconstruction. To initialize the state, we start with the spin-polarized state $|\uparrow,\uparrow\rangle$, which we discussed in Chapter 8, and which is illustrated again in Fig. 9.5 (a). By applying a resonant radio-frequency (rf) pulse, we rotate the spin of each atom into the equatorial plane of the Bloch sphere, i.e. we rotate each of the two atoms into the coherent superposition $|\uparrow\rangle \xrightarrow{\pi} |\rightarrow\rangle = {}^1\!/\!\sqrt{2}\,(|\uparrow\rangle + |\downarrow\rangle)$. This procedure realizes the state

$$\Psi = \frac{1}{2}\left(|\uparrow\rangle_L + |\downarrow\rangle_L\right) \otimes \left(|\uparrow\rangle_R + |\downarrow\rangle_R\right), \tag{9.15}$$

where we omitted to explicitly write out the antisymmetrized form for better readability. If we keep measuring in the σ_z basis, the state shows spin fluctuations and the density matrix becomes a 4×4 matrix with the four basis states $\{|\uparrow,\uparrow\rangle, |\uparrow,\downarrow\rangle, |\downarrow,\uparrow\rangle, |\downarrow,\downarrow\rangle\}$, see Fig. 9.5 (a).

We investigate this state only in momentum space and do not explicitly measure the in-situ density. Instead we constrain the diagonal entries of the density matrix from the occurrences of spin combinations in the momentum measurements. As described before, to compute momentum-density correlation functions, we release the atoms into the ODT and measure the single-particle momentum distributions after time-of-flight. Upon imaging the two atoms get equally projected onto one of the four spin combinations. The occurence of each configuration directly gives the diagonal entries of the density matrix. While the measurement of $|\uparrow,\uparrow\rangle$ and $|\downarrow,\downarrow\rangle$ is uniquely related to one diagonal entry, we cannot uniquely assign the appearance of different-spin combinations to any of the states $|\uparrow,\downarrow\rangle$ and $|\downarrow,\uparrow\rangle$, and therefore only extract the sum of the two entries $p_{\uparrow\downarrow} + p_{\downarrow\uparrow}$.
Figure 9.5 (b) shows all measured momentum correlation functions between all possi-

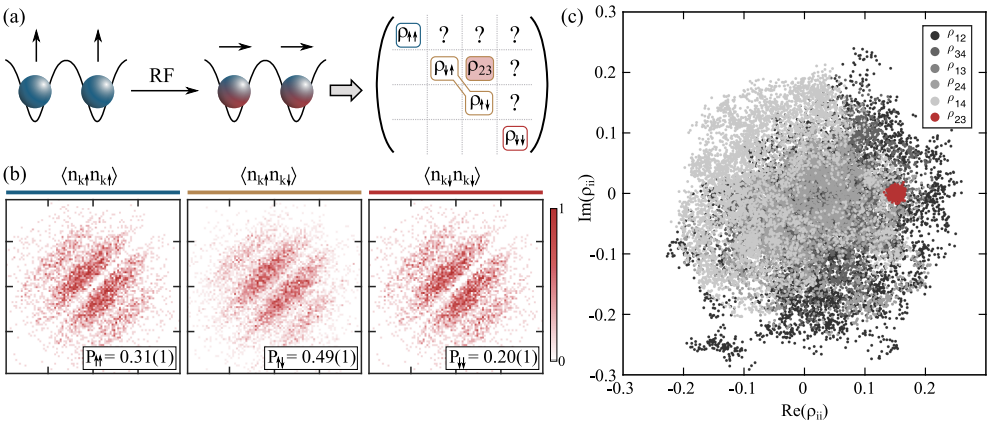

Figure 9.5: Reconstruction of spin-rotated state. (a) Initialization of state via radio-frequency rotation. We start with the state $|\uparrow,\uparrow\rangle$ and apply a radio frequency π pulse. In the σ_z basis this enlarges the density matrix to a 4×4 matrix. (b) Measured momentum correlation functions with occurrences of spin combinations (inset) from which we infer $\rho_{\uparrow\uparrow}$, $\rho_{\uparrow\downarrow}+\rho_{\downarrow\uparrow}$, and $\rho_{\downarrow\downarrow}$. ρ_{23} is given by by the contrast of $\langle n_{k\uparrow}n_{k\downarrow}\rangle$, which we obtain by fitting the correlator with a cosine function. Total number of datapoints for all three correlation functions: 14500 (c) Sampled posterior distribution of off-diagonal entries. The unconstrained entries explore the full space, while the constrained entry ρ_{23} (red points) only navigates within the experimental uncertainties.

ble spin combinations, $\langle n_{k\uparrow}n_{k\uparrow}\rangle$, $\langle n_{k\uparrow}n_{k\downarrow}\rangle$, and $\langle n_{k\downarrow}n_{k\downarrow}\rangle$. The state features identical momentum correlations within each spin combination. As we discussed in Chapter 8 for the state $|\uparrow,\uparrow\rangle$, these correlations are only due to the exchange symmetry of two identical fermions. To determine the contrast of the modulation of the correlation functions we fit the correlator $C^{(2)}(d)$ with a damped cosine function (see Eq. (8.6) and Eq. (8.7)). Within the statistical uncertainty all correlation functions show an identical contrast of 62(2) %. As illustrated in Fig. 9.5 (a), the contrast of the fit to $\langle n_{k\uparrow}n_{k\downarrow}\rangle$ constrains the entry ρ_{23} of the density matrix. All remaining off-diagonal entries cannot be constrained. Although we have very limited constraints on the density matrix in this case, we apply the Bayesian quantum state estimation as outlined in the previous section. The likelihood function, that we define as given in Eq. (9.14), hence only constrains the diagonal entries and ρ_{23}, all remaining off-diagonal entries do not appear in the likelihood function and are therefore not constrained at all.
Figure 9.5 (c) shows the sampled posterior distribution of all off-diagonal entries with $\Re(\rho_{ij})$ on the x-axis and $\Im(\rho_{ij})$ on the y-axis, respectively (5000 steps of the Metropolis-Hastings algorithm). While all unconstrained entries (grey points) freely navigate around and randomly explore the full physical Hilbert space, ρ_{23} only explores the Hilbert space within the experimental uncertainties. The diagonal entries are not plotted in the same graph since they are real numbers and therefore only explore the real axis. Instead we plot the the posterior distribution of the diagonal entries as histograms in Fig. 9.6 (a). The plot in (b) of the same figure shows exemplary histograms of the posterior distribution of the real part of four off-diagonal entries, including $\Re(\rho_{23})$. The histograms nicely show that all entries that are directly constrained by the likelihood function are Gaussian distributed, i.e. ρ_{11}, ρ_{44}, ρ_{23}, and

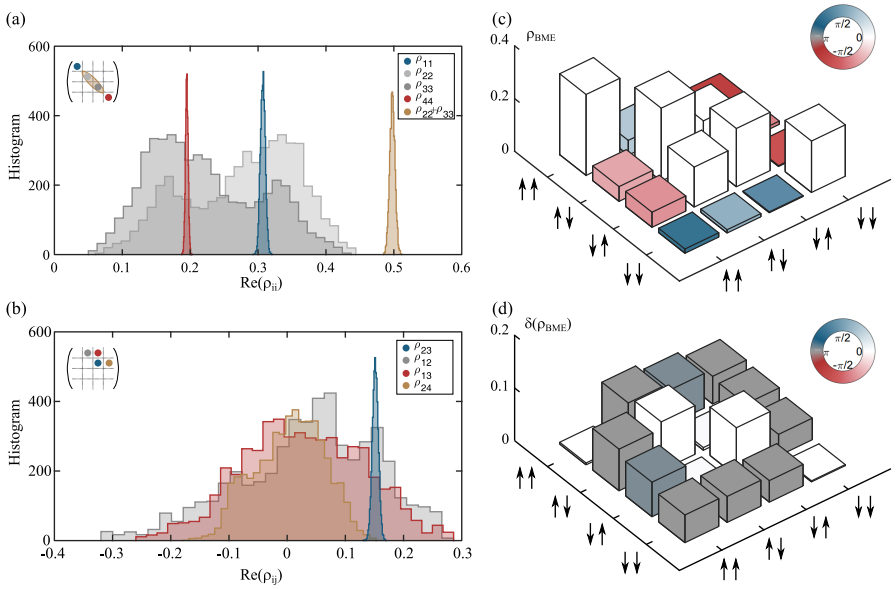

Figure 9.6: Posterior distribution of Bayesian state estimation. (a) Posterior distribution of all diagonal entries and of the sum $\rho_{22} + \rho_{33}$, which is directly constrained by the likelihood function. (b) Posterior distribution of the real part of four exemplary off-diagonal entries, including ρ_{23}. All quantities that are directly constrained by the likeklihood function are Gaussian distributed and sharply peaked. (c) ρ_{BME} for the rotated triplet state. The height of the bars is given by $|\rho_{\mathrm{BME}}|$ and the phase of each entry is encoded in the color. (d) 68% credible interval of the posterior distribution of all entries.

$\rho_{22} + \rho_{33}$. Entries that are not directly constrained, such as ρ_{22} and ρ_{33}, have a large spread, but explore the Hilbert space in a correlated way, as their sum is constrained. All unconstrained off-diagonal entries spread across the whole allowed Hilbert space. The mean over the posterior distribution ρ_{BME} represents the best knowledge of the experimentally realized state. However, note that the full information about uncertainties is encoded in the posterior distribution of states, that are sampled by the Bayesian estimation. We show ρ_{BME} for the discussed state in Fig. 9.6 (c) and the 68% credible interval of each entry in (d). The height of the bars gives the absolute value of each entry $|\rho_{\mathrm{BME}}|$ and the color encodes the phase $\phi(\rho_{\mathrm{BME}})$ as indicated by the phase wheel in the figure. The density matrix shows that all unconstrained entries have large uncertainties, as is expected from the posterior distribution.

9.3.2 Interacting Singlet State in a Double Well

We now turn to the discussion of states involving two interacting atoms in a the ground state of a double-well potential. The measurements of the correlation functions were in parts already shown in Sec. 9.1 and discussed in detail in Ref. [62]. As also discussed in Sec. 9.1, we extract 12 values from the analysis of the experimental data: 4 real numbers from insitu measurements that constrain the diagonal entries and 8 numbers that constrain real and imaginary party of all off-diagonal entries, of which two are only given as the sum of two off-diagonal entries. Note that even though this does

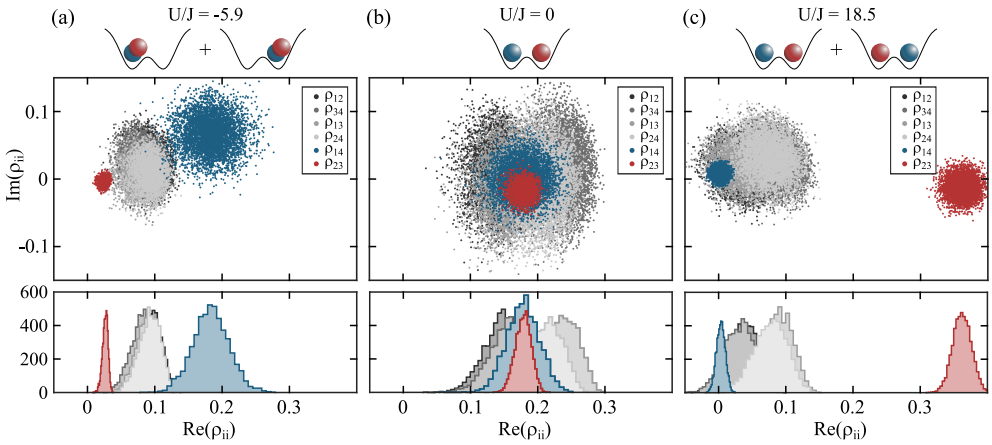

Figure 9.7: Posterior distribution of interacting double well. The upper plots show the sampled posterior distribution of all off-diagonal entries for the interacting double well for three different interaction strengths, $U/J = -5.9$ (a), $U/J = 0$ (b), and $U/J = 18.5$ (c). The histograms below show the distribution of the real part of all off-diagonal entries. Colored entries are directly constrained by likelihood function.

not fully constrain the density matrix, all entries appear in the likelihood function and are therefore constrained in some way. This is qualitatively different from the state that we discussed before, since we now expect the posterior distribution of each entry to be a peaked function. In total we apply the Bayesian state estimation to 8 different data sets with interaction strength $U/J \in \{-5.9, -2.9, 0, 2.5, 5, 8, 11.6, 18.5\}$. However, we will only discuss the three cases of $U/J \in \{-5.9, -0, 18.5\}$ in this section. We will nevertheless use the reconstructed states of all interaction strengths in the next chapter.

Fig. 9.7 shows the sampled posterior distribution of all off-diagonal entries together with histograms over the real part of all off-diagonal entries for all three interaction strengths. The colored entries are the anti-diagonal entries of the diagonal entries, which are directly constrained by the measurements. The posterior distribution of the diagonal entries is not plotted. We sampled the posterior distribution with 5000 steps of the Metropolis-Hastings algorithm. Both the posterior distribution and the histograms show that all entries are peaked functions and indeed, all constrained quantities (i.e. ρ_{23}, ρ_{14}, $\rho_{12} + \rho_{34}$, and $\rho_{13} + \rho_{24}$) are Gaussian distributed. The spread of each entry is given by experimental uncertainties. The mean estimate ρ_{BME} for all three interaction strengths is shown in Fig. 9.8 (a) together with the standard deviation of all entries in (b). The shown density matrices show exactly the structure, which we discussed in Sec. 7.3, i.e. on the attractive side, $U/J < 0$, doubly occupied wells are favored, whereas on the repulsive side, $U/J > 0$, doubly occupied sites are suppressed. In the non-interacting state, $U/J = 0$, all entries of the density matrix are equally high. For detailed discussion of the obtained density matrices, see Ref. [62]. As mentioned above, we also reconstruct density matrices for the five remaining interaction strengths, that are not shown here. However, we will use the results in the next chapter for the investigation of entanglement properties in identical-particle states.

As a consistency check of the reconstructed density matrices, we calculate the cor-

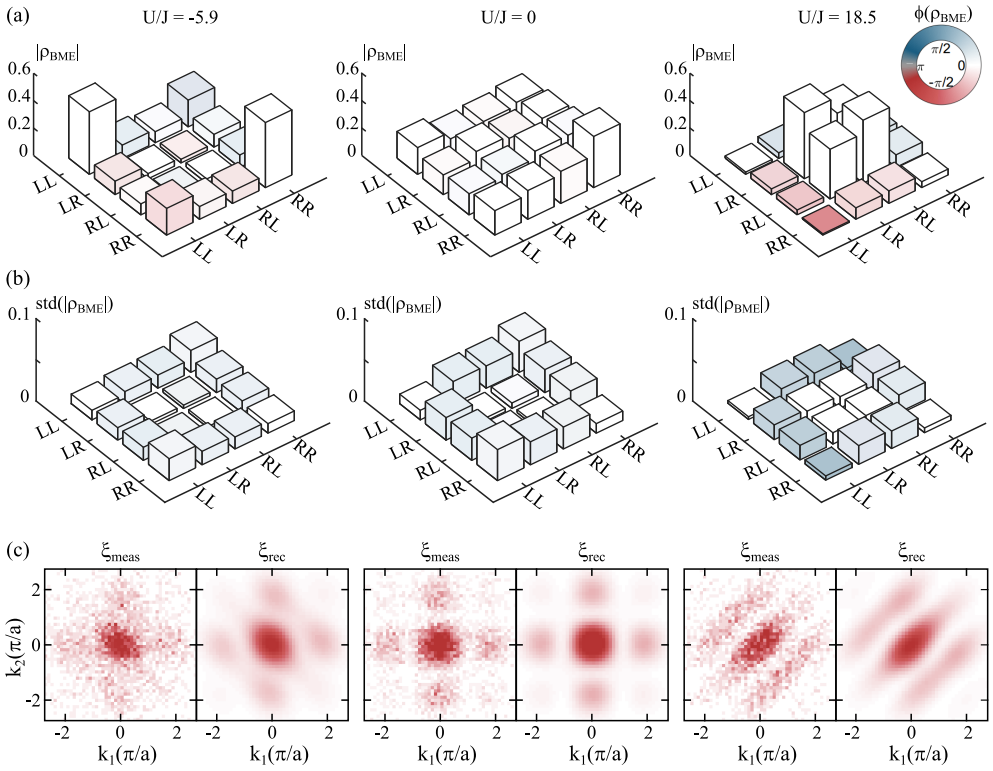

Figure 9.8: Reconstructed density matrices of interacting double well. (a)-(b) ρ_{BME} and standard deviation of each entry for three different interaction strengths, $U/J = -5.9$ (left column), $U/J = 0$ (middle column), and $U/J = 18.5$ (right column). Height indicates the absolute value $|\rho_{\mathrm{BME}}|$ and color indicates the phase, according to the color wheel. Note the different z-scales for the mean value and the standard deviations. (c) Comparison of the measured correlation functions to the correlation function that we reconstruct from ρ_{BME}.

relation functions that one would measure of a state described by the density matrix ρ_{BME}. To this end we use Eq. (9.7) and plug in the entries of ρ_{BME} and the lattice momentum k_{lat} that we obtained by fitting the correlation functions. Figure 9.8 (c) shows the measured and the reconstructed momentum-density correlation functions for the same states as above. We find very good agreement.

9.3.3 Interacting Triple Well

We finally realize two interacting three-particle states consisting of two spin-up and one spin-down particle. The first state that we investigate is a state with a biseparable structure consisting of a spin singlet in a double well and a third independent particle in a distant tweezer. Starting from that state we tried to realize the ground state of a commensurately spaced triple well by approaching the third well towards the double well. We separately discuss the realization and analysis of these two states.

A Biseparable State in the Triple Well

We so far discussed two different origins of momentum correlations: fermionic exchange symmetry, as extensively discussed in Chapter 8, and interaction as discussed in the previous section. Comparing the structure of observed momentum-density correlation functions, one sees that these two effects cause almost identical patterns. In order to analyze those different types of contributions to the momentum correlation functions and their influence on entanglement properties (as we will discuss in detail in the next chapter), an interesting candidate involving three particles is a state consisting of two interacting atoms in the ground state of a double well and an additional third atom in an independent tweezer. If there is no tunnel coupling between this independent third well and the double well, the third particle only contributes to the correlation function via its exchange symmetry and indistinguishability to the other spin-up particle.

As illustrated in Fig. 9.9 (a), we experimentally realize such a state by preparing two atoms in one well and a single atom in a separate third well. Exactly as for the preparation of the double-well ground state (cf Fig. 9.1), we adiabatically ramp on the central well to obtain a balanced double well with a third distant tweezer, i.e. a state of the form $|\psi\rangle = |\uparrow\rangle \otimes |DW\rangle$. We ensure a negligible tunnel coupling to the third well by choosing an incommensurate well spacing $a_{12} = 1.5a_{23}$ (see figure) and by deliberately detuning the depth of the third well away from the tunnel resonance to the central well. We do not observe any tunneling on experimental time scales and estimate a residual tunnel coupling of at most 0.1 Hz. After ramping to the balanced double well we induce interactions by tuning the magnetic offset field to 630 G. At that magnetic field we measure the interaction to be $U/J \simeq 16$.

To investigate the state we proceed exactly in the same way as we did for the double-well measurements, i.e. we measure both the single-particle and spin resolved in-situ populations and momentum density. We post select the data to the correct atom number of $N^{\uparrow} = 2$, $N^{\downarrow} = 1$ with post-selection rates on the order of 70%. For the presented data set we retain about 19400 shots. We extract the diagonal entries from the in-situ measurements and compute the third-order momentum-density correlation function $\xi^{(3)}_{(\uparrow\uparrow\downarrow)} = \langle n_{k_1\uparrow} n_{k_2\uparrow} n_{k_3\downarrow} \rangle$. We plot the measured momentum-density correlator $C^{(3)}(d_1, d_2)$ in Fig. 9.9 (b) (see Eq. (8.16) for definition of C). $C^{(3)}$ shows complex structure with many different spatial frequencies.

As explained in Sec. 9.1.1, we decompose the correlation function $\xi^{(3)}_{(\uparrow\uparrow\downarrow)}$ into a set of trigonometric basis functions and obtain a 117×81 matrix $\mathbf{B}$ that constrains the entries of the density matrix. These 117 equations are not linearly independent. In fact $\mathbf{B}$ has a rank of $\mathrm{rank}(\mathbf{B}) = 69$. We nevertheless define the likelihood function using the full matrix $\mathbf{B}$ and apply the Bayesian state estimate. We sample the posterior distribution with 50000 steps. This is a factor of 10 more compared to the double-well data due to the significantly larger density matrix.

Figure 9.9 (c) shows the posterior distribution of all off-diagonal entries. Only the major six entries are colored, while the remaining 30 entries concentrate around zero and are shown in grey. Note that the distributions for ρ_{28} and ρ_{16} (blue points), as well as the distributions for ρ_{26} and ρ_{18} (red points) are almost identical and lie

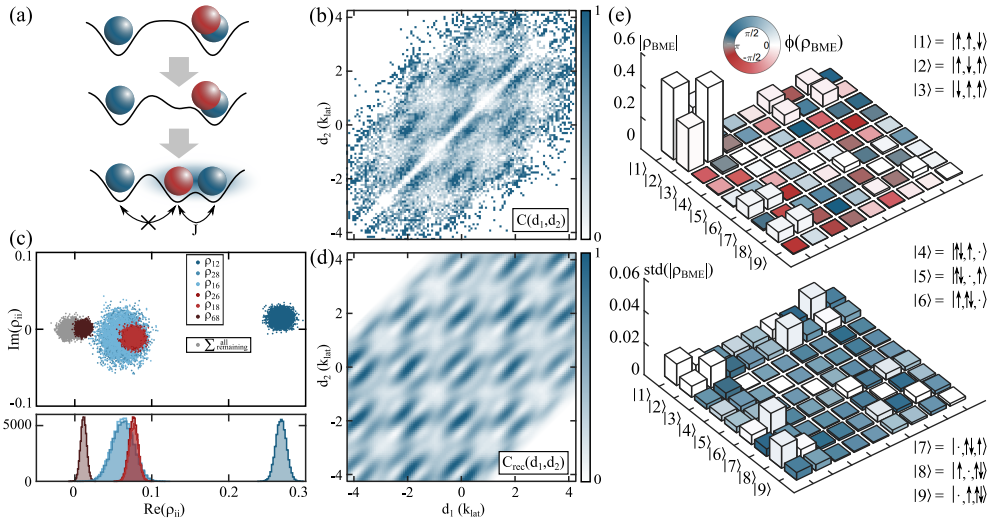

Figure 9.9: Reconstruction of incommensurately spaced triple well. (a) Illustration of preparation of biseparable three-atom state in which we entirely decouple the third well from the double well. (b) Measured momentum-density correlator $C^{(3)}(d_1, d_2)$. Number of data points: 19400 (c) Sampled posterior distribution of all 36 off-diagonal entries. Only major six entries are colored. Distributions for remaining 30 entries scatter around zero and are shown in grey. Note that the distributions for ρ_{28} and ρ_{16} (blue points), as well as for ρ_{26} and ρ_{18} (red points) lie almost on top of each other. (d) Reconstructed momentum-density correlator. (e) Bayesian mean estimate ρ_{BME} (upper row) and standard deviations of all entries (lower row).

on top of each other. Due to the rather complicated structure of $\mathbf{B}$, all entries of the density matrix appear in the likelihood function and are therefore constrained to some degree. All constrained quantities are Gaussian distributed and, despite the reduced rank of $\mathbf{B}$, all entries of the density matrix are sharply peaked with relatively small standard deviations. The resulting mean estimate ρ_{BME} is shown in Fig. 9.9 (e) together with the standard deviation of all entries. Note the different z-scales of the mean and standard deviation. We again check the resulting density matrix by computing the momentum correlator we would expect from a state described by ρ_{BME}. We show the result in Fig. 9.9 and again find very good agreement. The reconstructed density matrix ρ_{BME} has one major off-diagonal entry ρ_{12}, which is given by the two-particle coherence within the double well. The four small entries at ρ_{16}, ρ_{18}, ρ_{26} and ρ_{28} are single particle coherences within the double well, which are suppressed due to the large repulsive interaction (see previous sections and chapter for discussion of double well coherences). We illustrate the theoretically expected density matrix in the lower left panel of Fig. 9.10 (lowest energy state at $J_{12} = 0$). Apart from the reduced magnitude of ρ_{12} the agreement between experimental and theoretical density matrices is very satisfying. We find the purity of the reconstructed state to be $p_{\mathrm{exp}} = \mathrm{Tr}(\rho^2_{\mathrm{BME}}) = 0.61(1)$, which we mainly attribute to a bad mode overlap along the axis of expansion (as discussed in Sec. 8.1). Indeed if we include the measured loss of contrast for large distances between the tweezers (see Fig. 8.3) into our analysis, we find almost perfect agreement between the measured and the expected coefficients in $\mathbf{B}$. Hence also for the interacting states, we assume the purity to be much higher

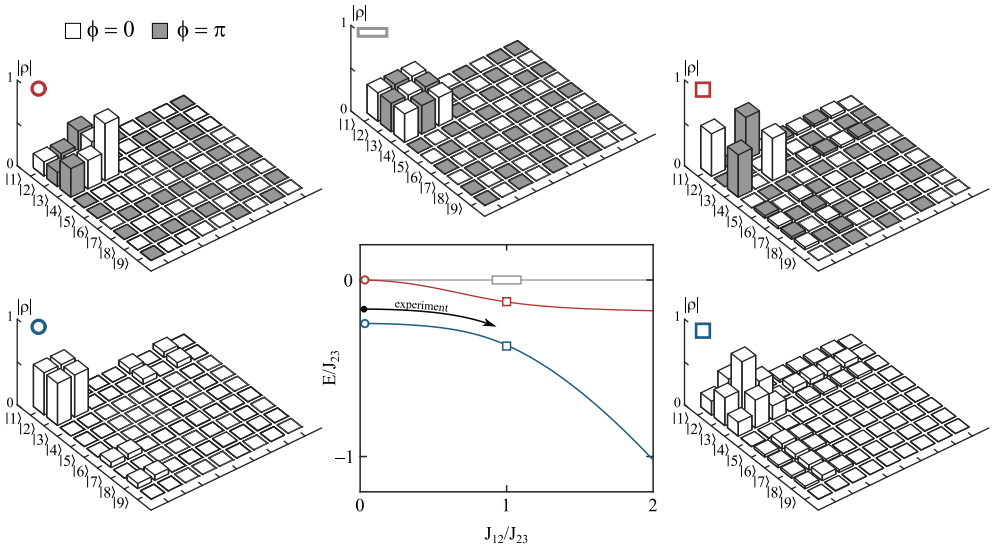

Figure 9.10: Lowest states of interacting triple well. The plot shows the energy of the three lowest eigenstates as a function of the tunnel coupling J_{12} between the first and the second well at $U/J \simeq 16$. The energy splitting between the lowest state is on the order of the super exchange energy $4J^2/U$. The five density matrices are the corresponding eigenstates as indicated by the different markers. In the experiment we first realized the lowest state at $J_{12} = 0$ and for the second state we ramped the tunnel coupling from zero to $J_{12} = J_{23}$.

and currently only limited by the expansion in the ODT.

Ground State of the Commensurately Spaced Triple Well

The plot in Fig. 9.10 shows the energies of the three lowest eigenstates of the triple well as a function of the ratio of tunnel couplings J_{12}/J_{23} at an interaction strength of $U/J \simeq 16$. We exemplarily show theoretical density matrices of the three states at different tunneling strengths. The bi-separable state that we discussed above is the ground-state of the triple well with $J_{12} = 0$ as indicated with the blue circle. It is hence adiabatically connected to the ground state of the homogeneous triple well with $J_{12}/J_{23} = 1$ (blue square). In a final measurement we made an attempt to realize such a state by approaching the third well towards the central well. As indicated in the figure, this effectively ramps the tunnel coupling J_{12} from zero to the homogeneous triple well, $J_{12} = J_{23}$. The excitation gap between the lowest states is only on the order of the super exchange interaction energy $4J^2/U$. For $U/J = 16$ and typical tunneling rates around 100 Hz in our experiment, the splitting is only a few Hz, such that the purity of the experimental state might suffer a lot from too fast changes of the optical potentials.

To initialize the system we start from the biseparable state that we discussed above and approach the third well. For the analysis we proceed as before by measuring both the in situ populations and the momentum-density correlation function $\xi^{(3)}_{(\uparrow\uparrow\downarrow)}$. We show the measured momentum-density correlator $C^{(3)}(d_1, d_2)$ in Fig. 9.11(b). We decompose the momentum correlation function $\xi^{(3)}_{(\uparrow,\uparrow,\downarrow)}$ and obtain a 61×81 matrix $\mathbf{B}$

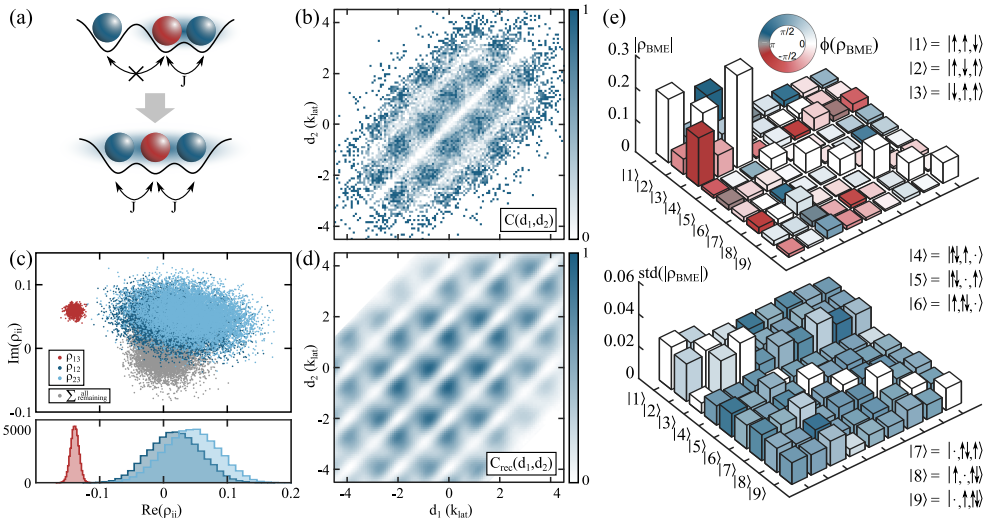

Figure 9.11: Reconstruction of commensurately spaced triple well. (a) Illustration of preparation of homogeneous triple well. (b) Measured momentum-density correlator $C^{(3)}(d_1, d_2)$. Number of data points: 10300 (c) Sampled posterior distribution of all 36 off-diagonal entries. Only the major three entries are colored. Distributions for remaining 33 entries scatter around zero and are shown in grey. (d) Reconstructed momentum-density correlator. (e) Bayesian mean estimate ρ_{BME} (upper row) and standard deviations of all entries (lower row).

with rank($\mathbf{B}$) = 37. As discussed in the previous chapter, the reduction of rank($\mathbf{B}$) as compared to the incommensurately spaced triple well is due to the fact that there are less possible lattice momenta (since $a_{12} = a_{23} = a$). We define the likelihood function as above by using the full matrix $\mathbf{B}$ as constraints and perform the Bayesian state estimation. We again sample the posterior distribution with 50000 steps. The sampled posterior distribution of all off-diagonal entries is presented in Fig. 9.11 (c). Only the major three entries are colored, ρ_{13} (red points), ρ_{12} (dark blue points), and ρ_{23} (light blue points). All remaining entries scatter around zero and are shown in grey. The histograms below confirm that all constrained values are Gaussian distributed. The posterior distribution shows that the three major off-diagonal entries have a significant imaginary part, which can also be seen in the mean density matrix ρ_{BME} in (e). In combination with the relatively high amount of doubly-occupied sites ($\rho_{44} - \rho_{99}$), and a computed purity of $p = \mathrm{Tr}(\rho^2) = 0.29(2)$ this indicates that the ramp to the final state was not performed in an adiabatic way. Indeed the chosen timing for the ramp of 125 ms from $J = 0$ to the final configuration is fast compared to timescales given by the super exchange energy. Such a *quench* results in a superposition state of the lowest states, causing off-diagonal entries of the density matrix to become imaginary. Dephasing and random excitations to higher states due to technical noise lead to a substantial reduction of the purity of ρ_{BME}. The comparatively large uncertainties on ρ_{BME} are mainly caused by the reduced rank of $\mathbf{B}$ but also by too little statistics of about 10300 shots after post selection (71% post-selection rate). Nevertheless we again verify the validity of the reconstructed density matrix by computing the momentum correlator that one would expect from the state ρ_{BME}. We show the result

in Fig. 9.11 (d) and find very good agreement.

Despite the very low purity of the reconstructed density matrix, this example shows that our reconstruction scheme can readily be applied both to states involving technical noise or poor statistics and in particular to mixed states. This is particularly relevant for the characterization of experimental states since they always suffer from decoherence and reduced purity.
The density matrix contains the full information of a state. For instance its purity characterizes the *quality* of the state in the sense of how mixed it is. Being able to reconstruct the density matrix of experimentally realized states is not only a valuable tool to characterize the performance of an experiment, it also enables direct calculation of any observable including entanglement. In the next chapter we will use the experimentally obtained density matrices to investigate entanglement properties in identical-particle states. We are particularly interested in the entanglement between particles rather than spatial mode entanglement, as we will motivate and discuss throughout the chapter.

Chapter 10

Identical-Particle Entanglement

Entanglement is one of the most fundamental properties of quantum mechanics. In fact E. Schrödinger already considered entanglement to be *'the characteristic trait of quantum mechanics, the one that enforces its entire departure from classical lines of thought'* [214]. Initially causing many conceptual problems [215] such as the violation of locality and causality, entanglement turned out to be so fundamental that it can be used to fundamentally test quantum mechanics by ruling out any local hidden variable theories via the violation of Bell's inequalities [216]. On a more practical level, entanglement is seen as a major resource for quantum enhanced sensing and metrology [21, 217, 218], for quantum computation, but also for identifying and studying phase transitions [74, 75] or identifying topological states [219–222]. Despite its usefulness and wide range of applications, entanglement still seems to raise many conceptual questions. One reason for the mysterious nature of entanglement might be the fact that entanglement is not only a property of a quantum state but entirely depends on the choice of partitioning for which in turn there are various types one can choose from.

A particularly useful choice of partitioning is to divide the system into spatial modes [223, 224] and to ask for entanglement between different spatial regions of the system. Scaling analysis of such entanglement has brought together many seemingly unrelated physical systems such as black holes, quantum information science, and quantum many-body physics [75]. Furthermore the study of spatial mode entanglement helps to understand ground-state properties of the Hubbard model [59, 224–226] and enables entanglement steering in spatially separated Bose-Einstein condensates [227–229]. However, this is clearly not the only choice to partition a system and has pathological limits in terms of extracting useful entanglement as a single particle delocalized in free space provides entanglement beween infinitely many spatial modes.

Another intuitive choice of subsystems is to consider individual particles. This obviously can cause conceptual problems, in particular when it comes to states of indistinguishable particles. The fact that particles are indistinguishable raises the question whether they are all entangled with each other, which has led to a long discussion in

the literature on the role of fermionic exchange symmetry on measured entanglement properties [230–240].
In this chapter we use the reconstructed density matrices that we presented in the previous chapter to investigate entanglement properties in states with indistinguishable particles. We are particularly interested in entanglement between particles rather than spatial modes. We will discuss, that special care has to be taken for fermionic antisymmetrized wave-functions and introduce the simple notion of an antisymmetric negativity for quantifying particle-particle entanglement of fermionic density matrices. We start by reviewing the basic concept of entanglement and its quantification. The content of this chapter has been published in [241].

10.1 A Brief Introduction to Entanglement

In this section we try to give an intuition of how an entangled state looks like and try to highlight where conceptual problems may arise. We do not rigorously discuss all facets of entanglement, for which we refer the reader to the literature [242, 243].
In simple words, when two atoms are entangled with each other, they can no longer be described as individual constituents of the whole system. They rather have to be considered together since any action on one atom immediately affects the state of the remaining atom. More formally, for two subsystems A and B with Hilbert spaces $\mathcal{H}_A$ and $\mathcal{H}_B$, respectively, a quantum state $|\Psi\rangle_{AB}$ is called entangled with respect to the partitioning $A|B$ if it is not separable with respect to the tensor factorization $\mathcal{H}_A \otimes \mathcal{H}_B$, i.e. if it cannot be written as a product state of the form $|\Psi\rangle_{AB} \neq |\psi\rangle_A \otimes |\psi\rangle_B$.
It is instructive to consider the following simple example of two atoms, which we can both initialize in an arbitrary superposition of two internal states. Labeling those two states as $|\uparrow\rangle$ and $|\downarrow\rangle$, we can write down the normalized general single-particle wave function as

$$\begin{aligned} |\Psi_1\rangle &= \alpha\,|\uparrow\rangle + \underbrace{\sqrt{1-\alpha^2}}_{\alpha'}\,|\downarrow\rangle \\ |\Psi_2\rangle &= \beta\,|\uparrow\rangle + \underbrace{\sqrt{1-\beta^2}}_{\beta'}\,|\downarrow\rangle\,. \end{aligned} \tag{10.1}$$

With the two above states we obtain a general two-atom wave function by tensor multiplying the two states,

$$|\Psi_{\mathrm{sep}}\rangle = |\Psi_1\rangle \otimes |\Psi_2\rangle = (\alpha\beta\,|\uparrow\uparrow\rangle + \alpha\beta'\,|\uparrow\downarrow\rangle + \alpha'\beta\,|\downarrow\uparrow\rangle + \alpha'\beta'\,|\downarrow\downarrow\rangle)\,. \tag{10.2}$$

This state is fully described by the two parameters α and β. However, it immediately becomes clear that this wave function cannot describe all states that are allowed by quantum mechanics, for which one needs four parameters:

$$|\Psi_G\rangle = (a\,|\uparrow\uparrow\rangle + b\,|\uparrow\downarrow\rangle + c\,|\downarrow\uparrow\rangle + d\,|\downarrow\downarrow\rangle)\,. \tag{10.3}$$

As illustrated in Fig. 10.1 (a), all two-particle states of the form $|\Psi_G\rangle$, that cannot be written in the form of a separable state $|\Psi_{\mathrm{sep}}\rangle = |\Psi\rangle_A \otimes |\Psi\rangle_B$ are called entangled

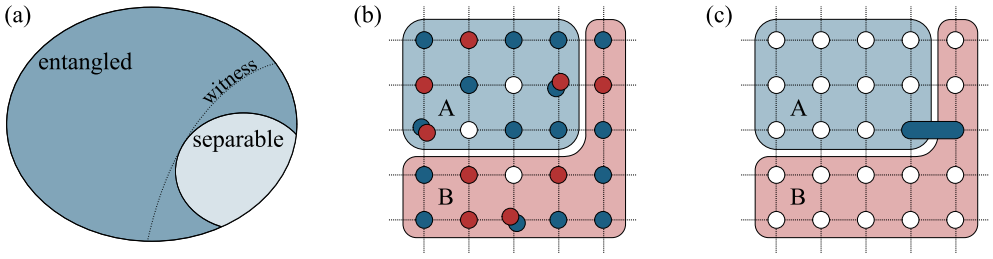

Figure 10.1: Entanglement detection. (a) A state that cannot be factorized into its subsystems is called entangled. An entanglement witness is a sufficient but not necessary criterion for entanglement. (b) Illustration of spatial mode entanglement, which is used to characterize many-body systems by dividing a system into spatial modes and asking for entanglement between these subsystems. (c) A single particle delocalized across the boundary of the subsystems induces mode entanglement between systems A and B.

states.

A simple example of an entangled wave function based on the above example is the spin wave function of two atoms in a spin-singlet configuration,

$$|\Psi_S\rangle = \frac{1}{\sqrt{2}}\left(|\uparrow\downarrow\rangle - |\downarrow\uparrow\rangle\right). \tag{10.4}$$

In order to write $|\Psi_S\rangle$ as a separable state in the form of Eq. (10.2), we need $\alpha\beta = \alpha'\beta' = 0$ but at the same time also $\alpha\beta' = \alpha'\beta = \frac{1}{\sqrt{2}}$, which is impossible. For the state $|\Psi_S\rangle$, a projective measurement on one atom can have both outcomes $|\uparrow\rangle$ or $|\downarrow\rangle$, but would immediately affect the spin of the other atom, i.e. detecting the first atom in the $|\uparrow\rangle$ state, immediately projects the second atom into the $|\downarrow\rangle$ state. The definition of entanglement via the non-separability of the wave function is very general and does not only apply to internal modes of two atoms. There is obviously a range of choices of how to characterize entanglement. This leads to many different notions of entanglement such as mode entanglement or particle-particle entanglement [223], but also entanglement between different systems such as atom-photon, photon-phonon or magnon-photon-phonon entanglement is possible [17, 244, 245].

As already mentioned above, a very useful choice for the characterization of ultracold atom experiments is entanglement between spatial modes [59, 224, 229, 246]. The basic idea of mode entanglement is illustrated in Fig. 10.1 (b). An ensemble of atoms trapped e.g. in a two-dimensional optical lattice is spatially divided into two subsystems A and B. By looking for example at atom number fluctuations within the two subsystems, entanglement can be detected by the violation of entanglement witnesses, a sufficient but not a necessary condition for entanglement (see Fig. 10.1 (a)). However, the detected mode entanglement entirely depends on the chosen boundary and even a single atom, delocalized across two wells might induce mode entanglement, if it is delocalized across the boundary of the subsystems, see Fig. 10.1 (c). In that sense a *single* atom in the ground state of a balanced double-well potential, as we discussed

in Sec. 7.4.1, where the wave function in mode representation is given by

$$|\Psi\rangle = \frac{1}{\sqrt{2}} \left(|10\rangle + |01\rangle \right), \tag{10.5}$$

with the atom being either in the first ($|10\rangle$) or the second ($|01\rangle$) well, induces spatial mode entanglement between the two wells. Hence a single atom delocalized across many wells can in principle induce entanglement between arbitrarily many spatial modes. Mode entanglement does not only exist between spatial modes. The momentum-space wave function of a single atom localized in space ($\sum_i c^\dagger_{k_i} |000...0\rangle$) is a superposition state of infinitely many momentum modes and can hence also be interpreted as a mode-entangled state, where all momentum modes are entangled.
An alternative possibility is to consider entanglement between particles rather than modes. Obviously in the case of identical particles special care must be taken and conceptual difficulties arise when particles are fully indistinguishable.

10.2 Particle-Particle Entanglement

Entanglement between particles and the role of exchange symmetry has been extensively discussed in the literature [230–239, 242]. Taking individual atoms as subsystems immediately causes conceptual problems when two or more particles are indistinguishable. In order to uniquely identify single atoms as subsystems, particles have to be labeled $\{1...N\}$ and a first-quantized formalism has to be adopted. The conceptual problems already become apparent by considering two identical fermions localized in two spatial modes, such as the state that we extensively discussed in Chap. 8. Due to fermionic exchange symmetry, the first-quantized wave function of such a state has to be antisymmetrized over the spatial degree of freedom,

$$|\Psi\rangle = \frac{1}{\sqrt{2}} \left(|L\rangle_1 |R\rangle_2 - |R\rangle_1 |L\rangle_2 \right), \tag{10.6}$$

where the subscripts are particle labels and L and R the left and the right mode, respectively. This state is not a separable state since it cannot be written as the product of two single-particle wave functions. It even resembles the maximally entangled Bell-state and is formally an entangled state. However, this type of entanglement only arises from antisymmetrizing the wave function and hence exists between any two identical fermions. Although it might be argued that such entanglement is a mere artefact of the formalism of first quantization, it is still under debate whether it can actually be used for quantum information processing [247–249]. With the advent of experiments operating with individually controllable, indistinguishable particles [59–63, 224–226] the debate on the role of exchange symmetry on measured entanglement properties has gained new urgency. In fact as we have demonstrated in Chap. 8 and Chap. 9, fermionic exchange statistics can induce strong correlations in experimental observables that look very similar to correlations in strongly interacting systems. It is hence desirable to analyze experimental measurements in a way that entanglement induced by (anti)symmetrization can be separated from other forms of entanglement.

Before discussing how to quantify entanglement and how to isolate the different contributions to the detected entanglement, we need to introduce a few more concepts such as mixed-state entanglement, separability and genuine multipartite entanglement.

10.3 Generalization of Entanglement

In this section we briefly comment on how to extend the concepts that we introduced in the previous section to mixed states and to larger systems that can be partitioned into more than just two subsystems.

Mixed-State Entanglement

So far we only considered pure quantum states, i.e. states with a purity $p = \mathrm{Tr}(\rho^2)$ of one. However, experimentally characterized quantum states usually suffer from experimental noise and hence a reduced purity $p < 1$. In order to characterize experimental density matrices, the definition of entanglement has to be generalized to mixed quantum states. A mixed quantum state is called separable with respect to the partitioning $A|B$ if its density matrix can be written as a probabilistic mixture of separable pure states [250],

$$\rho_{\mathrm{sep}}^{\mathrm{mix}} = \sum_i p_i \rho_{\mathrm{sep,i}}^{A|B}, \tag{10.7}$$

with $\sum p_i = 1$ and the density matrix of a pure separable state $\rho_{\mathrm{sep,i}}^{A|B}$, which can be written as

$$\rho_{\mathrm{sep,i}}^{A|B} = |\psi_i\rangle\langle\psi_i|_A \otimes |\phi_i\rangle\langle\phi_i|_B \,. \tag{10.8}$$

If the density matrix cannot be written in the form of Eq. (10.7), the state is called entangled. For a general mixed density matrix there are of course infinitely many decompositions into a probabilistic mixture of pure states and ruling out that there is any decomposition of the form of Eq. (10.7) is a non-deterministic polynomial-time (NP)-hard problem [251].

Separability

The notion of entanglement becomes richer for systems that can be divided into multiple subsystems. In such cases, there are different choices for the boundary between two subsystems and both the detection but also the amount of detected entanglement depends on the chosen boundary. Furthermore, partitioning the system into more than two subsystems leads to the notion of multipartite entanglement (see below). To better understand the structure of possible states, one introduces the concept of partial separability [252]. Let us consider a state with N modes and split the system $\{1, ..., N\}$ into $k \leq N$ subsystems. As illustrated in Fig. 10.2, we call the state k-separable with respect to the split α_k, if it can be written as a factorized state over the partitioning α_k, i.e.

$$|\Psi\rangle = |\psi\rangle\langle\psi|_{\alpha_1} \otimes |\phi\rangle\langle\phi|_{\alpha_2} \otimes ... |\chi\rangle\langle\chi|_{\alpha_k} \,. \tag{10.9}$$

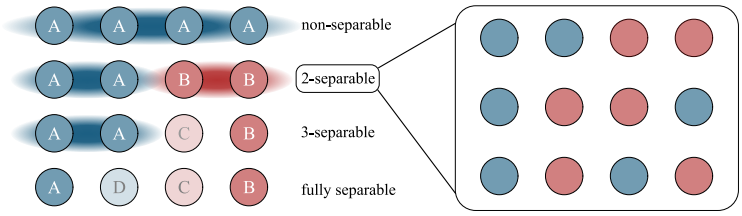

Figure 10.2: Separability of quantum states. A state that can be factorized over the k-fold partitioning α_k is called k-separable. For each k with $1 < k < N$ there are multiple possible partitionings as indicated on the right side for the case of $N = 4$ and $k = 2$.

For a given k with $1 < k < N$ there are multiple possible partitionings α_k. Note that a k-separable state is always $k-1$ separable while the opposite is not generally true. For $k = N$ we call the state fully separable. Since entanglement is defined via the contrapositive of separability, the hierarchy of entanglement is inverted with respect to separability. A fully separable state is not entangled at all whereas in a non-separable state all possible bipartitions are entangled. Such a state is called a genuinely multipartite entangled state.

Genuine Multipartite Entanglement

To better understand genuine multipartite entanglement let us consider the following state of three spins

$$\begin{aligned} |\Psi\rangle &= \frac{1}{\sqrt{2}}\left(|\uparrow\uparrow\downarrow\rangle + |\uparrow\downarrow\uparrow\rangle\right) \\ &= \frac{1}{\sqrt{2}}\left(|\uparrow\rangle \otimes \left(|\uparrow\downarrow\rangle + |\downarrow\uparrow\rangle\right)\right). \end{aligned} \tag{10.10}$$

This state is separable with respect to the partitioning $|\cdot|\cdot\cdot\rangle$ but not with respect to the partitioning $|\cdot\cdot|\cdot\rangle$. The state is hence biseparable and not genuinely multipartite entangled. However it is also not fully separable and therefore features *bipartite* entanglement within the partitioning $|\cdot\cdot|\cdot\rangle$. A famous example of a genuinely multipartite entangled state is the GHZ-state [253, 254],

$$|\Psi_{\mathrm{GHZ}}\rangle = \frac{1}{\sqrt{2}}\left(|\uparrow\uparrow\uparrow\rangle + |\downarrow\downarrow\downarrow\rangle\right). \tag{10.11}$$

or the W-state [255],

$$|\Psi_{\mathrm{W}}\rangle = \frac{1}{\sqrt{3}}\left(|\uparrow\uparrow\downarrow\rangle + |\uparrow\downarrow\uparrow\rangle + |\downarrow\uparrow\uparrow\rangle\right). \tag{10.12}$$

These state are not separable with respect to any possible bipartition and can therefore not be factorized. They are therefore called genuinely multipartite entangled. In a similar way as above, we call a mixed state genuinely multipartite entangled, if it can neither be written as a biseparable state with respect to any bipartition $\mathrm{A}|\bar{\mathrm{A}}$ [256]

nor as a probabilitics mixture thereof

$$\rho^{\mathrm{bs}} = \sum_i p_i \rho_{\mathrm{A}_i|\bar{\mathrm{A}}_i}, \tag{10.13}$$

with $\sum p_i = 1$ and separable states $\rho_{\mathrm{A}_i|\bar{\mathrm{A}}_i}$.

10.4 Entanglement Quantification

So far we only defined an entangled state as being a state that is not separable. However, for the general two-particle state of the form of Eq. (10.3) it seems to be intuitive to find states that are *more* entangled than others. In order to understand how entanglement can be quantified, we follow Ref. [257] and first introduce the concept of *Local Operations and Classical Communication* (LOCC).

Suppose we have prepared a quantum system that we partition into two subsystems A and B, which we transport into two distant laboratories. The two laboratories can perform local operations on their part of the system and communicate via a classical link with each other. The set of all operations on the systems that only involve local operations on the two subsystems and classical communication between the two laboratories is referred to as LOCC. If the two subsystems have not been entangled before, LOCC cannot create any entanglement between them. Consequently, entanglement is not allowed to increase under any LOCC operation. These two fundamental laws of quantum information processing [258, 259] can be used to implement a hierarchy of entanglement.

If a state ρ can be transformed into state σ only by LOCC, ρ is at least as entangled as σ. If the transformation is not possible, ρ is less entangled as σ [257]. However, care must be taken when comparing different classes of entangled states. E.g. in a system of three atoms it is not possible to compare the entanglement of a GHZ state to the entanglement of a W-state. The states cannot be converted into one another by LOCC but are both maximally entangled states [255].

In order to generalize this idea and to make it applicable to mixed states, one might ask the question: how many copies of a state ρ are necessary to find an equal amount of entanglement in m copies of a different state σ, i.e. for which n can $\rho^{\otimes n}$ be transformed into $\sigma^{\otimes m}$ only with LOCC. The ratio n/m is used for ordering the amount of entanglement in the two states ρ and σ. Based on these ideas important entanglement measures can be defined such as the *Entanglement Cost* [260, 261], the *Distillable Entanglement* [262, 263] or the *Entropy of Entanglement* [264, 265].

In contrast to this operationally motivated approach to quantifying entanglement there is also an axiomatic approach to entanglement measures. Based on the above considerations certain requirements for a proper entanglement measure can be formulated [257, 264, 266]:

1. An entanglement measure $E(\rho)$ is a mapping from density matrices to real positive numbers, $\rho \mapsto E(\rho)$

2. $E(\rho) = 0$ for any separable state ρ.

3. E does not increase on average under LOCC.

4. For a pure state $\rho = |\psi\rangle\langle\psi|$, E reduces to the entropy of entanglement.

Apart from many others, a very useful axiomatically motivated entanglement measure is the (logarithmic) Negativity [267]. Since we will be using the Negativity on the experimentally obtained density matrices, we briefly summarize its main properties.

Negativity

For a state, described by the density matrix ρ, the Negativity is defined as

$$\mathcal{N}(\rho) = \frac{||\rho^{\Gamma_A}|| - 1}{2} \tag{10.14}$$

where ρ^{Γ_A} is the partial transpose of ρ with respect to subsystem A, and $||\cdot||$ denotes the trace norm. Equivalently the negativity can be calculated as the sum of the absolute values of all negative eigenvalues of ρ^{Γ_A}, $\sum_{i,\lambda_i<0} |\lambda_i|$. The negativity is a convex function, $\mathcal{N}(\sum p_i\rho_i) \leq \sum p_i\mathcal{N}(\rho_i)$ and does not increase under LOCC operations. For a separable state $\rho_s = \rho_A \otimes \rho_B$, one finds $\rho_s^{\Gamma_A} = \rho_A^T \otimes \rho_B = \rho_A \otimes \rho_B = \rho_s$ and consequently a negativity of 0. For 2×2 and 2×3 systems (i.e. systems of two qubits or two qutrits), $\mathcal{N} > 0$ is a sufficient and necessary condition for entanglement [268, 269]. For any larger system a finite negativity is only a sufficient but not a necessary condition for entanglement. The negativity is an entanglement measure, that is easy to compute because it reduces to calculating the eigenvalues of a density matrix. As we will see in the next section, when applied to states where we choose particles as subsystems, the negativity detects entanglement due to the antisymmetrization of the fermionic wave function.

PPT-mixtures

The negativity relies on the fact that separable states have a positive partial transpose (PPT) [268, 269]. While this condition is only sufficient and necessary for 2×2 or 2×3 systems, it is still a sufficient condition for larger systems. Separable states have a positive partial transpose, so whenever a state does not have a positive partial transpose, it is an entangled state. For later purposes we define a general mixed PPT state as a state that can be obtained as a probabilistic mixture of pure PPT states [256],

$$\rho_{\text{ppt}}^{\text{mix}} = \sum_i p_i \rho_{\text{ppt}}. \tag{10.15}$$

10.5 Particle-Particle Negativity

Let us again address the state of two identical fermions in a double-well potential, $\Psi = \frac{1}{\sqrt{2}}(|L_1R_2\rangle - |R_1L_2\rangle)$ and apply the above definition of the negativity. We mentioned already, that the state cannot be factorized due to antisymmetrization of the wave function. In the first-quantized formalism, its density matrix $\rho = |\Psi\rangle\langle\Psi|$ is

given by

$$\rho = |\Psi\rangle\langle\Psi| = \frac{1}{2}\begin{pmatrix} 0 & 0 & 0 & 0 \\ 0 & 1 & 1 & 0 \\ 0 & 1 & 1 & 0 \\ 0 & 0 & 0 & 0 \end{pmatrix}, \tag{10.16}$$

where we used the basis $(|L_1L_2\rangle, |L_1R_2\rangle, |R_1L_2\rangle, |R_1R_2\rangle)$. We perform the partial transpose on one of the two atoms and get

$$\rho^{\Gamma} = |\Psi\rangle\langle\Psi| = \frac{1}{2}\begin{pmatrix} 0 & 0 & 0 & 1 \\ 0 & 1 & 0 & 0 \\ 0 & 0 & 1 & 0 \\ 1 & 0 & 0 & 0 \end{pmatrix}, \tag{10.17}$$

with the four eigenvalues $\lambda_1 = -1/2$, and $\lambda_{2,3,4} = 1/2$. We calculate the Negativity to be $\mathcal{N}(\rho) = 0.5 > 0$. The negativity hence detects the state as non-separable and therefore as an entangled state. This result suggests that any two identical fermions are entangled because of their exchange symmetry. How should this result be interpreted?

According to Ghirardi, Marinatto, and Weber (GMW) [242] an antisymmetrized state should not be regarded as entangled if it can be obtained from antisymmetrizing a separable state. In their work they define entanglement between two subsystems of a composite system via the possession of a *complete set of properties*. This means that if the two subsystems possess definite physical properties that are independent of the existence of the other part, the two subsystems are non-entangled. While also with this definition some conceptual problems arise for the case of identical particles, they rigorously show that two identical fermions that are described by a pure normalized state $|\Psi\rangle$ are non-entangled, if and only if $|\Psi\rangle$ can be obtained by antisymmetrizing a factorized state.
For the wave function of two identical fermions discussed above, this immediately implies that we should not consider the state as an entangled state, because it is obtained by antisymmetrizing the separable state,

$$|\Psi\rangle = |L_1R_2\rangle \xrightarrow{\mathcal{P}_A} \frac{1}{\sqrt{2}}\left(|L_1R_2\rangle - |R_1L_2\rangle\right), \tag{10.18}$$

where $\mathcal{P}_A$ denotes the antisymmetrization operator. Note that the state before antisymmetrization is not unique, as also the state $|R_1L_2\rangle$ yields the same antisymmetric state. While this trivial example nicely illustrates the idea of GMW, finding such a state e.g. for a mixed state consisting of three interacting particles is not a straightforward task. Hence, for the calculation of particle-particle entanglement special care has to be taken in order to separate contributions to entanglement from antisymmetrization from other origins of entanglement such as interaction. In the next section we therefore introduce the notion of an *Antisymmetric Negativity*, which is able to separate those two different origins of entanglement.

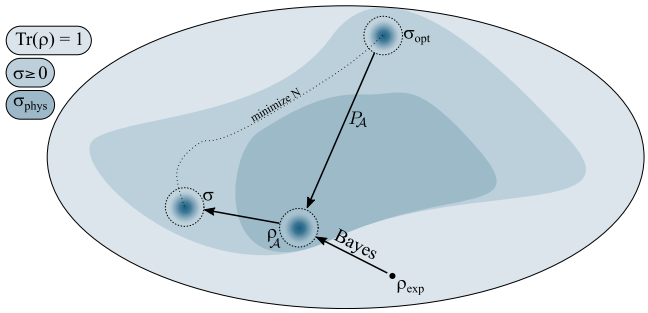

Figure 10.3: Schematic illustration of Antisymmetric Negativity. From the experimental results we obtain a normalized density matrix, which might not by physical and contain negative eigenvalues due to systematical uncertainties. The Bayesian inference method provides us with a representative set of physical density matrices that is compatible with our experimental uncertainties. The $\mathcal{AN}$ searches for the optimal state $\sigma_{\rm opt}$ by minimizing the negativity of the optimization variable σ under the constraint that the projection on the antisymmetric subspace retrieves the initial state $\rho_{\mathcal{A}}$. We call the negativity of $\sigma_{\rm opt}$ the antisymmetric negativity of $\rho_{\mathcal{A}}$.

10.6 Antisymmetric Negativity

As described in the previous section, according to the GMW criteria [242] an antisymmetric state that is obtained from antisymmetrizing a factorized state should be considered as a separable, non-entangled state. This suggests that entanglement properties of identical-particle states should be addressed before antisymmetrization. Based on this intuition we introduce the simple notion of an *Antisymmetric Negativity*, $\mathcal{N}_{\mathcal{A}}$ [241, 270], which determines the smallest entanglement that must already exist in a state before (anti)symmetrization. For the mathematical details of the antisymmetric negativity, please see Ref. [270].

For an antisymmetrized, fermionic wave function $\rho_{\mathcal{A}}$ we consider the functional

$$E_{\mathcal{A}}(\rho_{\mathcal{A}}) = \min_{\sigma \geq 0} \{E(\sigma) : P_{\mathcal{A}} \sigma P_{\mathcal{A}} = c\rho_{\mathcal{A}}\}, \tag{10.19}$$

for any entanglement measure E. $P_{\mathcal{A}}$ is the projection onto the antisymmetric subspace and the factor $c = \max\{\mathrm{Tr}(P_{\mathcal{A}}\sigma) : \sigma = \sigma_{\mathrm{PPTm}}\}$ is the maximal projection probability of σ such that $\rho_{\mathcal{A}}$ may not be obtained by antisymmetrizing a PPT-mixed state [270]. As derived in [270], $c = 1/2$ for the bipartite case with same local dimensions such as our double-well states. Instead, $c = 1/3$ for the triple well, as shown in [271]. We choose $c = 1/2$ for the discussion here. As illustrated in Fig. 10.3 the optimization variable σ is a normalized, positive-semidefinite quantum state that does not obey any specific exchange symmetry and exists in a larger Hilbert space than the antisymmetric, physical state $\rho_{\mathcal{A}}$. The optimization searches for the state $\sigma_{\rm opt}$ with the smallest entanglement $E(\sigma_{\rm opt})$ under the constraint that its antisymmetric projection is $\frac{1}{2}\rho_{\mathcal{A}}$.
Thus, for a given fermionic state $\rho_{\mathcal{A}}$, if there exists a factorized state σ such that $P_{\mathcal{A}}\sigma P_{\mathcal{A}} = \frac{1}{2}\rho_{\mathcal{A}}$, then $E_{\mathcal{A}}(\rho_{\mathcal{A}}) = 0$. If there is no such state, then $E_{\mathcal{A}}(\rho_{\mathcal{A}}) > 0$ and the

identical-particle state is considered to be entangled. If we apply this formalism to the state of two identical fermions, Eq. (10.18) immediately implies that $E_{\mathcal{A}}(\rho) = 0$ and therefore identifies the state as non-entangled.
This idea can be applied to any entanglement measure E but in the case of E being the standard negativity $\mathcal{N}$ it can be explicitly calculated in the form of a semidefinite program (SDP). We define the *Antisymmetric Negativity* ($\mathcal{AN}$) as

$$\mathcal{N}_{\mathcal{A}}(\rho_{\mathcal{A}}) = \min_{\sigma \geq 0} \left\{ \mathcal{N}(\sigma) : P_{\mathcal{A}} \sigma P_{\mathcal{A}} = \frac{1}{2} \rho_{\mathcal{A}} \right\}. \tag{10.20}$$

Semi Definite Programming

Semi Definite Programming is a field of convex optimization and finds numerous applications in quantum information theory [272, 273]. For Φ being a hermitian-preserving map between two complex Euclidean spaces $\mathcal{A}$ and $\mathcal{B}$, with A and B hermitian operators $A \in \mathrm{Herm}(\mathcal{A})$ and $B \in \mathrm{Herm}(\mathcal{B})$, a semidefinite program (SDP) consists of the triple (Φ, A, B) associated with the following optimization problem,

$$\begin{aligned} \text{minimize} \quad & \langle A, X \rangle \\ \text{such that} \quad & \Phi(X) = B \\ & X \geq 0, \end{aligned} \tag{10.21}$$

where $\langle ., . \rangle$ is a linear function that is minimized under the constraints $\Phi(X) = B$ and X being positive semidefinite, $X \geq 0$. Following [270, 272], we can rewrite the trace norm of a matrix as a SDP, which we can immediately extend to the negativity. We find that the negativity of a matrix ρ is given by the optimal value of the SDP

$$\begin{aligned} \text{minimize} \quad & (\mathrm{Tr}(M) - 1)/2 \\ \text{such that} \quad & -M \leq \rho^{\Gamma} \leq M. \\ & M \geq 0, \end{aligned} \tag{10.22}$$

where ρ^{Γ} is the partial transpose of the partitioning for which the negativity is calculated. By adding further constraints to the above SDP we can ultimately formulate the antisymmetric negativity as a SDP. For an antisymmetric fermionic state $\rho_{\mathcal{A}}$ we call the bipartite antisymmetric negativity $\mathcal{AN}_2$ the optimal value of the following optimization,

$$\begin{aligned} \text{minimize} \quad & (\mathrm{Tr}(M) - 1)/2 \\ \text{such that} \quad & -M \leq X^{\Gamma} \leq M \\ & M \geq 0 \\ & X \geq 0 \\ & \mathrm{Tr}(X) = 1 \\ & P_{\mathcal{A}} X P_{\mathcal{A}} = \mathrm{Tr}(P_{\mathcal{A}} X) \rho_{\mathcal{A}} \\ & \mathrm{Tr}(P_{\mathcal{A}} X) = c. \end{aligned} \tag{10.23}$$

This SDP minimizes the negativity of a positive-semidefinite, normalized state X, whose projection on the antisymmetric subspace is $c\rho_{\mathcal{A}}$. Following [256, 274] we generalize the $\mathcal{AN}$ to detect genuine multipartite entanglement. To this end we first extend the standard negativity to the tripartite case. For a three-atom state we call the genuine tripartite negativity $\mathcal{N}_3$ of a state ρ the optimal value of the following SDP,

$$\begin{aligned}
\text{minimize} \quad & (\mathrm{Tr}(M_{A|BC} + M_{B|AC} + M_{C|AB}) - 1)/2 \\
\text{such that} \quad & M_{A|BC}, M_{B|AC}, M_{C|AB} \geq 0 \\
& \tilde{\rho}_{A|BC}, \tilde{\rho}_{B|AC}, \tilde{\rho}_{C|AB} \geq 0 \\
& -M_{A|BC} \leq \tilde{\rho}^{\Gamma}_{A|BC} \leq M_{A|BC} \\
& -M_{B|AC} \leq \tilde{\rho}^{\Gamma}_{B|AC} \leq M_{B|AC} \\
& -M_{C|AB} \leq \tilde{\rho}^{\Gamma}_{C|AB} \leq M_{C|AB} \\
& \rho = \tilde{\rho}_{A|BC} + \tilde{\rho}_{B|AC} + \tilde{\rho}_{C|AB}, \qquad (10.24)
\end{aligned}$$

where the indices denote the partitioning of the system, i.e. $A|BC$ means that the partial transposition operation is carried out on subsystem A. We finally extend $\mathcal{N}_3$ to the genuine tripartite antisymmetric negativity $\mathcal{AN}_3$ via the optimal value of the SDP,

$$\begin{aligned}
\text{minimize} \quad & (\mathrm{Tr}(M_{A|BC} + M_{B|AC} + M_{C|AB}) - 1)/2 \\
\text{such that} \quad & M_{A|BC}, M_{B|AC}, M_{C|AB} \geq 0 \\
& \tilde{\rho}_{A|BC}, \tilde{\rho}_{B|AC}, \tilde{\rho}_{C|AB} \geq 0 \\
& -M_{A|BC} \leq \tilde{\rho}^{\Gamma}_{A|BC} \leq M_{A|BC} \\
& -M_{B|AC} \leq \tilde{\rho}^{\Gamma}_{B|AC} \leq M_{B|AC} \\
& -M_{C|AB} \leq \tilde{\rho}^{\Gamma}_{C|AB} \leq M_{C|AB} \\
& \tilde{\rho} = \tilde{\rho}_{A|BC} + \tilde{\rho}_{B|AC} + \tilde{\rho}_{C|AB} \\
& P_{\mathcal{A}}\tilde{\rho}P_{\mathcal{A}} = \mathrm{Tr}(P_{\mathcal{A}}\tilde{\rho})\rho_{\mathcal{A}} \\
& \mathrm{Tr}(P_{\mathcal{A}}\tilde{\rho}) = c. \qquad (10.25)
\end{aligned}$$

The latter equation can be readily extended to the N-partite case.
For the calculation of the $\mathcal{AN}$ we perform all optimizations using Qetlab [275] and CVX, a package for specifying and solving convex programs [276, 277].

10.7 Application of AN to Experimental States

In order to benchmark the usefulness of the $\mathcal{AN}$ we investigate the experimentally realized states that we discussed in Sec. 9.3. In particular we will demonstrate that (i) the $\mathcal{AN}$ can be computed from experimental data including noise; (ii) it identifies states which exhibit correlations only due to quantum statistics as unentangled; (iii) it identifies interaction-driven entanglement in two-particle systems, and (iv) it can be extended to multipartite scenarios.

As already mentioned, we adopt a first-quantized formalism that allows us to treat particles as subsystems. To this end we label the particles $\{1, ..., N\}$ and convert all density matrices into their first-quantized representation. For the double-well data this is achieved by mapping the 4×4 density matrices onto the 16-dimensional basis $\{|X\sigma\rangle |Y\tau\rangle\}$, for $X, Y \in \{L, R\}$ and $\sigma, \tau \in \{\uparrow, \downarrow\}$. The 9×9 density matrices of the triple well are mapped onto the 216-dimensional basis $\{|X\sigma\rangle |Y\tau\rangle |Z\kappa\rangle\}$, for $X, Y, Z \in \{L, C, R\}$ and $\sigma, \tau, \kappa \in \{\uparrow, \downarrow\}$. This is done using the substitution rule according to the slater determinant, i.e. $|X\rangle_\uparrow |Y\rangle_\downarrow \to \frac{1}{\sqrt{2}}(|X\uparrow\rangle |Y\downarrow\rangle - |Y\downarrow\rangle |X\uparrow\rangle)$ for the double-well case and analogously for the triple-well case.

The states that we investigate can be grouped into three different classes. We start by discussing all spin-polarized states $|\uparrow,\uparrow\rangle$, $|\uparrow,\uparrow,\uparrow\rangle$ and $|\rightarrow,\rightarrow\rangle$, which we discussed in Chap. 8 and Sec. 9.3.1, respectively. We then continue with the discussion of two interacting atoms in the ground state of a double well, see Sec. 9.3.2, and finally investigate the two triple-well states, which we discussed in Sec. 9.3.3. For the double-well states, we will try to give some explicit examples in order to better illustrate the calculations. Expressions and density matrices for the triple well are typically too large to be explicitly shown.

Separable States

The first class of states that we investigate are spin-polarized states. Since they consist of identical fermions, these are all strictly non-interacting states and hence correlations are purely caused by exchange symmetry. We discussed the three different states $|\Psi_1\rangle = |\uparrow,\uparrow\rangle$, $|\Psi_2\rangle = |\uparrow,\uparrow,\uparrow\rangle$, and $|\Psi_3\rangle = |\rightarrow,\rightarrow\rangle$.
We explicitly performed the calculation of the negativity of the first state in Sec. 10.5 and showed that the negativity evaluates to $\mathcal{N}(\rho_1) = 0.5$. We also discussed that the $\mathcal{AN}$ correctly identifies the state as non-entangled, $\mathcal{AN}(\rho_1) = 0$ (Eq. (10.18)). The calculation of the second state is analogous. We first write down the first quantized, antisymmetrized wavefunction,

$$\begin{aligned} |\Psi_2^{\mathcal{A}}\rangle \quad = \quad & \frac{1}{\sqrt{6}} \left(|L\uparrow, C\uparrow, R\uparrow\rangle + |R\uparrow, L\uparrow, C\uparrow\rangle + |C\uparrow, R\uparrow, L\uparrow\rangle \right. \\ & \left. - |R\uparrow, C\uparrow, L\uparrow\rangle - |L\uparrow, R\uparrow, C\uparrow\rangle - |C\uparrow, L\uparrow, R\uparrow\rangle\right), \end{aligned} \tag{10.26}$$

and obtain the 36×36 first-quantized density matrix by calculating $\rho_3^{\mathcal{A}} = |\Psi_3^{\mathcal{A}}\rangle \langle\Psi_3^{\mathcal{A}}|$ in the basis $\{|X\uparrow\rangle |Y\uparrow\rangle |Z\uparrow\rangle\}$, with $X, Y, Z \in \{L, C, R\}$. For this state we explicitly calculate the negativity to be $\mathcal{N}$=1 for all possible partitionings due to the exchange symmetry. The $\mathcal{AN}$ identifies this state as separable, $\mathcal{AN}(\rho_2) = 0$, since it is obviously obtained by antisymmetrizing a separable state.
As we discussed in Sec. 9.3.1, the third state $|\psi_3\rangle$, which was obtained by rf-rotation of the first state $|\psi_1\rangle$ into the equatorial plane of the Bloch sphere, shows spin fluctuations upon measuring and momentum correlations in all three possible spin combinations. These spin fluctuations are only induced by the rotation of the basis states and do not change the structure of the state. However, the reconstructed density matrix suffers from technical noise and therefore a reduced purity, so that the state

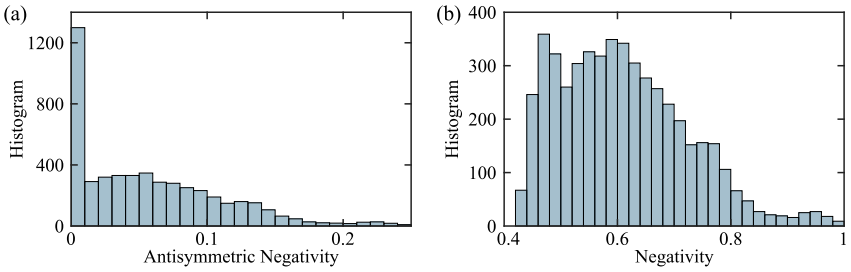

Figure 10.4: Calculated negativities of rotated-triplet state. Histograms of calculated $\mathcal{AN}$ (a) and $\mathcal{N}$ (b) over the posterior distribution of density matrices (5000 states) of the rf-rotated state $|\Psi_3\rangle$. We find a median of $\mathcal{AN}(\rho_3) = 0.048^{+0.064}_{-0.048}$ and $\mathcal{N}(\rho_3) = 0.6^{+0.13}_{-0.11}$, where the errors indicate the 68% credible interval. The large spread of the negativites is caused by the large experimental uncertainties and the missing constraints for 5 of the 6 off-diagonal entries (see Fig. 9.5).

is well suited to test the AN on separable mixed states. Generally, a reduced purity also reduces the detected entanglement due to the convexity of entanglement measures ($E(\sum(p_i\rho_i)) \leq \sum p_i E(\rho_i)$). As described in the previous chapter, the Bayesian reconstruction scheme provides us with a posterior distribution of physical density matrices, consisting of 5000 states, that represent the experimental measurements. We convert each of these density matrices into their first-quantized representation and calculate both $\mathcal{N}$ and $\mathcal{AN}$ for each state. Figure 10.4 shows histograms of the calculated negativities. The standard negativity is centered around 0.6 with a median of $\mathcal{N}(\rho_3) = 0.6^{+0.13}_{-0.11}$ where the errors indicate the 68% credible interval. In contrast, the $\mathcal{AN}$ is peaked at zero with a median and credible interval of $\mathcal{AN}(\rho_3) = 0.048^{+0.064}_{-0.048}$, compatible with zero. The large spread of the calculated negativities is caused by the poor reconstruction of that particular state, as we discussed in Sec. 9.3.1. Nevertheless, the $\mathcal{AN}$ removes the contribution of antisymmetrizing the wave function and identifies the spin-rotated state as being compatible with a non-entangled state. These three examples show that the AN identifies both pure and mixed separable states as non-entangled.

Interaction-Induced Entanglement

To test the $\mathcal{AN}$ on states where entanglement is induced by interaction we investigate the interacting singlet state in the double-well potential (see Sec. 9.3.2). We proceed in a similar way as above: for each interaction strength we calculate both $\mathcal{N}$ and $\mathcal{AN}$ for the whole posterior distribution that we obtain from the Bayesian quantum state estimation, consisting of a representative set of 5000 density matrices each. In addition we also calculate $\mathcal{N}$ and $\mathcal{AN}$ for theoretical density matrices for pure ground states of the balanced two-well Fermi-Hubbard model, obtained by diagonalizing the Hamiltonian in Eq. (7.4).

In Fig. 10.5 we illustrate the optimization of the SDP and the search of the $\mathcal{AN}$ with a single exemplary density matrix. We randomly chose a state of the posterior distribution from the Bayesian state estimation at an interaction strength of $U/J = 18.5$. The state in (a) shows the 4×4 density matrix obtained by the state reconstruction.

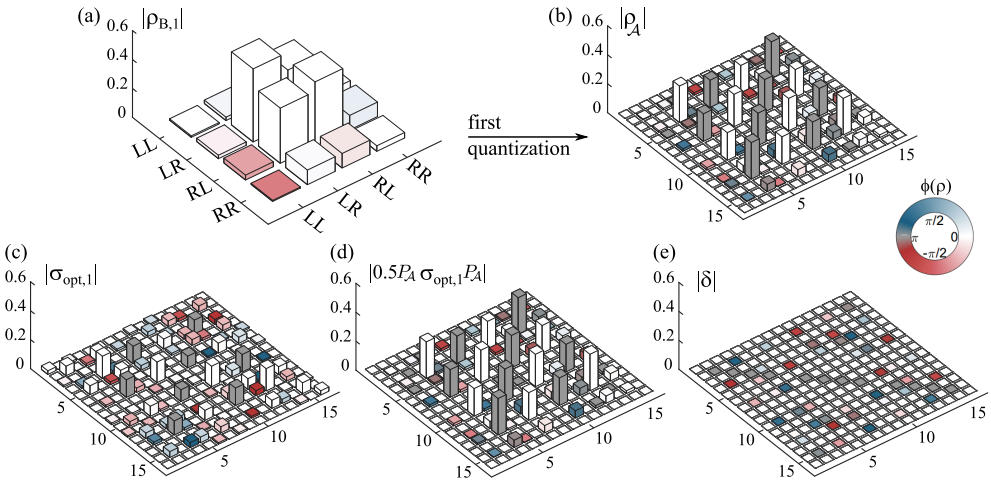

Figure 10.5: Example of optimization. (a) Density matrix of a randomly chosen matrix from the posterior distribution of the Bayesian state estimation of the interacting double well with $U/J = 18.5$. (b) First-quantized density matrix for state in (a). For a clearer view, the basis states are only labeled from 1...16. (c) Density matrix of the optimal state σ_{opt}, of which the negativity $\mathcal{N}(\sigma_{\text{opt}})$ is the antisymmetric negativity of $\rho_{\mathcal{A}}$. (d) Antisymmetric projection of the optimal state. (e) Difference between antisymmetrized state in (b) and antisymmetrized optimal state in (d).

Using the substitution rule as explained above, we convert the 4×4 density matrix into its 16×16 first-quantized representation $\rho_{\mathcal{A}}$, which we show in (b). $\rho_{\mathcal{A}}$ is the state of which we want to compute the $\mathcal{AN}$. The result of the optimization, σ_{opt}, is shown in (c). Although this state is normalized, i.e. $\text{Tr}(\sigma_{\text{opt}}) = 1$, it is not a physical state since it does not necessarily satisfy fermionic exchange symmetry and therefore allows the occupation of states that are forbidden by the Pauli-exclusion principle. For instance the first entry ρ_{11} (which is non-zero in σ_{opt}) is a state where two spin-up particles occupy the same spatial mode. Antisymmetrizing σ_{opt} yields a physical state that satisfies fermionic exchange symmetry. The state $\rho_{\mathcal{A}}^{\text{opt}} = \mathcal{P}_{\mathcal{A}}\sigma_{\text{opt}}\mathcal{P}_{\mathcal{A}}$ is shown in (d). We finally compute the difference between the states in (d) and (b) and show the result in (e). This difference is basically zero, whereas the residual noise on the individual entries is determined by the convergence parameters during the optimization. For the double-well case, the optimization only takes a few seconds per density matrix.

Figure 10.6 presents the calculated negativities as a function of the interaction strength U/J. All shown experimental values are the median with a 68% credible interval. In addition we also show one exemplary posterior distribution of $\mathcal{N}$ and $\mathcal{AN}$ for an interaction strength of $U/J = 18.5$ in (b) of the same figure. For all interaction strengths the experimental values are reduced compared to the theoretic curves due to a reduced purity of the experimental density matrices. The solid lines are the calculated negativities of the pure ground states. Both negativities show the same qualitative behaviour, i.e. the states become stronger entangled for stronger interaction and are symmetric around the non-interacting state at $U/J = 0$. However, the standard negativity is always larger than the antisymmetric negativity and even

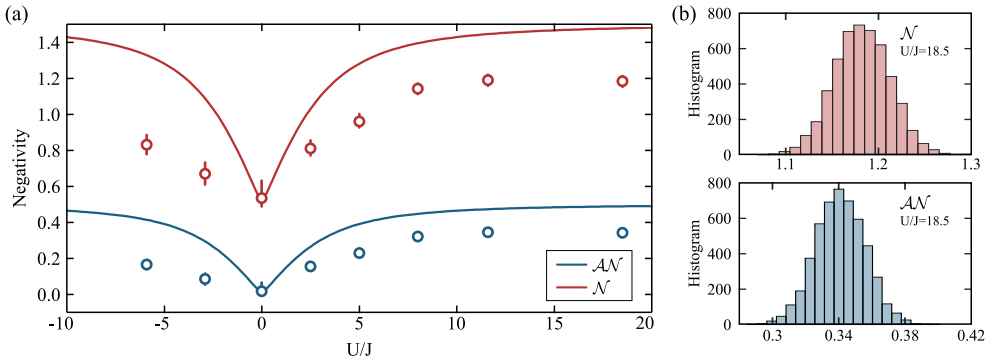

Figure 10.6: Negativities of the interacting double well. (a) Calculated $\mathcal{N}$ (red) and $\mathcal{AN}$ (blue) for an interaction strength U/J ranging from -10 to 20. Solid lines are the results from theoretical density matrices obtained from diagonalization of the Hamiltonian, data points are median and 68% credible interval of the negativities over the posterior distribution of the BME. (b) One example of the posterior distribution of $\mathcal{N}$ and $\mathcal{AN}$ for a repulsively interacting state with $U/J = 18.5$.

$\mathcal{N} = 0.5$ at $U/J = 0$, where the the theoretical and experimental $\mathcal{AN}$ both identify the state as separable. Indeed the difference between both negativities is caused by the antisymmetrizion of the density matrix over the spin degree of freedom. The $\mathcal{AN}$ successfully removes this contribution to the negativity and only detects entanglement due to interaction. It is interesting to note that the $\mathcal{AN}$ takes exactly the same values as the spin-mode negativity [62], since the two atoms could be uniquely identified by their spin state.

Three-particle states

To generalize the concept of the antisymmetric negativity to genuine multipartite entanglement we consider three particles in a triple-well configuration. As presented in Sec. 9.3.3, we consider the two experimentally realized states at $U/J = 16$ that we illustrate again in the top panel of Fig. 10.7. The first state is the incommensurately spaced triple well where we prepared an interacting singlet in a double well and added a third independent atom in the third tweezer. The second state is the ground state of the homogeneous triple well with $J_{12} = J_{23} = J$. We also theoretically investigate the same pure states for variable interaction strengths U/J from -20 to 20.

As we argued in Sec. 9.3.3, the first state with $J_{12} = 0$ has a clear bi-separable structure and features complex momentum correlations that are substantially modified both by interactions and antisymmetrization over the third independent particle. The second state is in principle expected to show genuine multipartite entanglement but due to a very low experimental purity of the state (see Sec. 9.3.3) we might not be able to detect it.

The evaluation of the data is similar to the double-well case. However, in addition to $\mathcal{N}$ and $\mathcal{AN}$ we also calculate the tripartite negativity $\mathcal{N}_3$ and the tripartite antisymmetric negativity $\mathcal{AN}_3$ as we defined in the previous sections. Due to the significantly larger first-quantized density matrices (216×216), each calculation of

$\mathcal{AN}_2$ and $\mathcal{AN}_3$ takes about 15-30min. Instead of calculating the antisymmetric negativity over the whole posterior distribution (containing 50.000 states), we choose a randomly sampled, representative subset of 1000 density matrices for the calculation of the experimental $\mathcal{AN}_{2/3}$.
Figure 10.7 summarizes all negativities for both states. We note that the calculation of the bipartite and tripartite negativity (solid line and light-colored dots in (a) of the figure) yield exactly the same results due to the antisymmetrized structure of the states. As a first characterization of the entanglement in the system, we can use the standard negativity (plotted in (a)) as an entanglement witness, but we will see that it requires the $\mathcal{AN}$ to provide a complete picture of multipartite entanglement. As indicated in the graph by the colored areas, there are three different regions, in which the negativity reveals information about the entanglement structure of the state. These three regions are based on the following two statements (see Appendix B for proofs):

1. *The maximum negativity that can be obtained by antisymmetrizing a fully separable three-particle state is one.*

2. *The maximum negativity that can be obtained by antisymmetrizing a biseparable state is 1.9428*

Hence any state with a negativity above one cannot be obtained from antisymmetrizing a fully-separable state and therefore exhibits at most a bi-separable structure. Any state with a negativity above 1.9428 is necessarily tripartite entangled, since it cannot be obtained by antisymmetrizing a bi-separable state. Indeed, as shown by the solid red line in Fig. 10.7 (a), the first state saturates these bounds for $U/J = 0$ and for $U/J \to \pm\infty$. The two histograms in Fig. 10.7 (a) show the results of the calculation of the negativity over the posterior distribution for both experimental states. We detect a negativity of $\mathcal{N} = 1.39 \pm 0.02$ for the first and $\mathcal{N} = 1.14^{+0.05}_{+0.04}$ for the second state, respectively. We conclude that none of the states is fully separable and both exhibit at least bipartite entanglement.
As we plot in Fig. 10.7 (b) the $\mathcal{AN}$ of the first state evaluates to zero both for the theoretical and the experimental state despite the fact that the state is not fully separable. This result is independent of the chosen partitioning. For each of the three possible partitionings, i.e. 1|23, 2|31, or 3|12, the minimization finds a state where a single atom can be factorized out. For instance for the partitioning 3|12 and $U/J \to \infty$ the optimization finds the state $\Psi_{\text{opt}} = (|C\uparrow\rangle_1 |R\downarrow\rangle_2 + |R\downarrow\rangle_1 |C\uparrow\rangle_2) |L\uparrow\rangle_3$. This state factorizes in the chosen partitioning and therefore features a negativity of zero. However, if we choose to investigate the partitioning 1|23, the optimization finds the state $\Psi_{\text{opt}} = |L\uparrow\rangle_1 (|C\uparrow\rangle_2 |R\downarrow\rangle_3 + |R\downarrow\rangle_2 |C\uparrow\rangle_3)$ and returns an $\mathcal{AN}$ of zero. Not that one cannot fine a state, that is separable in both partitioning at the same time, which projects onto the antisymmetrized state. This factorization of the optimal state is independent of the interaction strength so that we detect an $\mathcal{AN}$ of zero for all values of U/J. Indeed the $\mathcal{AN}$ is zero whenever the dimensions of the partitioning coincides with dimensions of the partitioning in which the state is biseparable.
The ground state of the homogeneous triple well (solid blue line in (a)) even exceeds the bound for biseparability for strong attractive and repulsive interactions. While

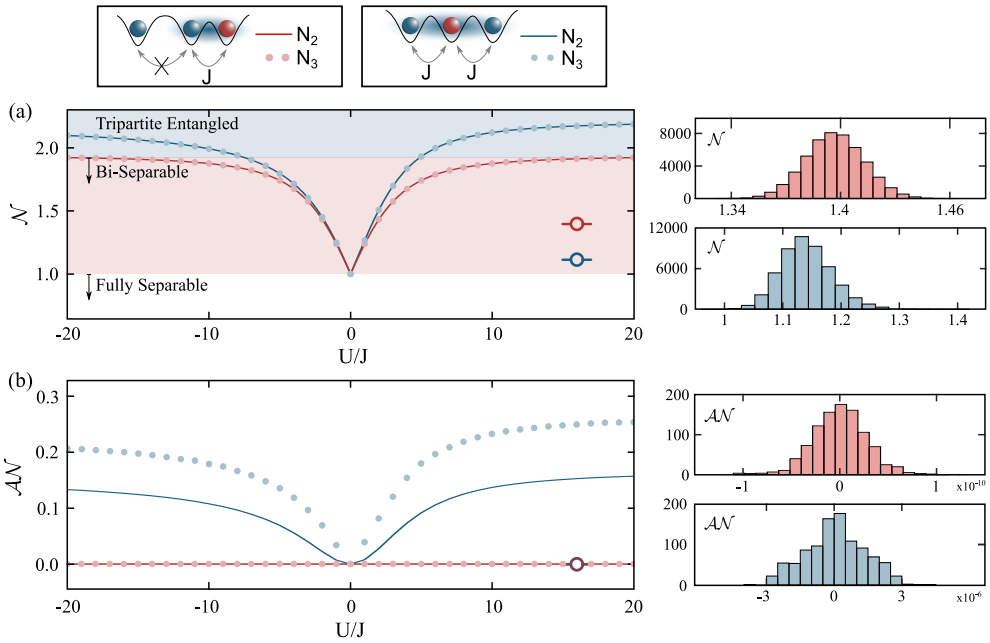

Figure 10.7: Bi- and tripartite antisymmetric negativity in the triple well. (a) Calculated standard negativity for both illustrated states. The histograms show the negativity of the posterior distribution of both experimentally realized states. Both experimental states exceed the bound for fully-separable states. The calculation of the bipartite and tripartite negativity yield the same values for each state due to the antisymmetrized structure of the density matrix. (b) Calculated antisymmetric negativity. The ground state of the homogeneous triple well shows finite values for any finite interaction strength, certifying the presence of genuine tripartite particle-particle entanglement. $\mathcal{AN}$ of experimental states is consistent with zero due to low purity of the experimental density matrices.

this is a signature of genuine multipartite entanglement, the standard negativity does not reveal anything about the entanglement structure for weaker interactions. However, both the bipartite and tripartite antisymmetric negativity $\mathcal{AN}_{2/3}$ of the same state (solid blue line and light blue dots in Fig. 10.7 (b)) show that the state exhibits genuine tripartite entanglement for any finite interaction strengths. Only at $U/J = 0$ the state can be obtained by antisymmetrizing a fully-separable state, so that we detect an $\mathcal{AN}$ of zero. Unfortunately the $\mathcal{AN}$ of the experimentally realized state is also 0, as shown in the histograms in Fig. 10.7 (b) due to the poor purity of the reconstructed density matrix.

To assess the relevance of the $\mathcal{AN}$ for experimental investigations, we analyze the robustness of the tripartite antisymmetric negativity $\mathcal{AN}_3$ against white noise. To this end we consider the ground state of the homogeneous triple well at an interaction of $U/J = 16$, $|\Psi\rangle$, an gradually add white noise, $\rho_{\text{noise}} = (1-r)\mathbb{1} + r\,|\Psi\rangle\langle\Psi|$, with $r \in [0, 1]$. We find a finite tripartite antisymmetric negativity $\mathcal{AN}_3$ down to $r = 0.75$, which corresponds to a purity of $p = 0.61$. This is significantly higher than the purity that we achieved with the second experimental three-particle state, but can be reasonably expected in experiments.

In this chapter we introduced a new notion of entanglement to quantify particle-particle entanglement for fermionic density matrices, called Antisymmetric Negativity. We applied the $\mathcal{AN}$ both to theoretical and experimental states and showed that it identifies separable states as non-entangled and that it can be used to separate entanglement originating from exchange symmetry from entanglement induced by interaction. The $\mathcal{AN}$ can also detect genuine multipartite entanglement, in particular, it can be used to reveal the entanglement structure of a multipartite entangled states, which is not accessible via the standard negativity alone. Our results enable the quantitative study of entanglement and exchange antisymmetry in experimental settings and help to provide further insight into the entanglement of indistinguishable particles.

Chapter 11

Summary and Outlook

In the second part of this thesis I explored the analysis of momentum correlation functions for the characterization of small, strongly correlated fermionic systems. This approach to characterizing a many-body quantum state is complementary to traditional tomography methods and does not require complex measurement protocols. We benchmark the applicability of our approach on a range of different states that we realize in the laboratory, including non-interacting systems, where correlations arise purely by fermionic exchange symmetry, and systems, where additional correlations may arise due to strong interactions.

In systems of non-interacting, indistinguishable particles we measure strong connected second and third-order momentum-density correlations. The contrast of the measured correlation functions indicates a high degree of indistinguishability of the individual particles, which we think is currently only limited by the expansion in the ODT. The measurements show both that our system realizes an on-demand source of highly indistinguishable fermions and that momentum correlations are perfectly suited to detect ordering in mesoscopic fermionic systems. This enables the future study of many-body interference or quantum optics experiments with massive particles.

In systems of distinguishable particles, correlations do not only arise due to exchange statistics but also due to interaction. These two contributions to the momentum correlation function are fundamentally different and have to be separated from each other. By decomposing momentum correlation functions into a set of trigonometric basis functions, we develop a scheme to constrain large parts of the density matrix and to fully reconstruct physical states via a Bayesian quantum state estimation. We reconstruct density matrices of various different states and discuss the contribution of antisymmetrization and interactions to measured correlation functions.

The reconstructed density matrices contain the full information about the states. In the final chapter, we use these density matrices to address particle-particle entanglement in identical-particle states. When treating particles as subsystems, standard entanglement measures lead to conceptual problems and detect entanglement due to the antisymmetrized structure of the fermionic wave function. To remedy these problems we employ the notion of an *Antisymmetric Negativity* that searches for the smallest entanglement that must already exist before antisymmetrization. We show

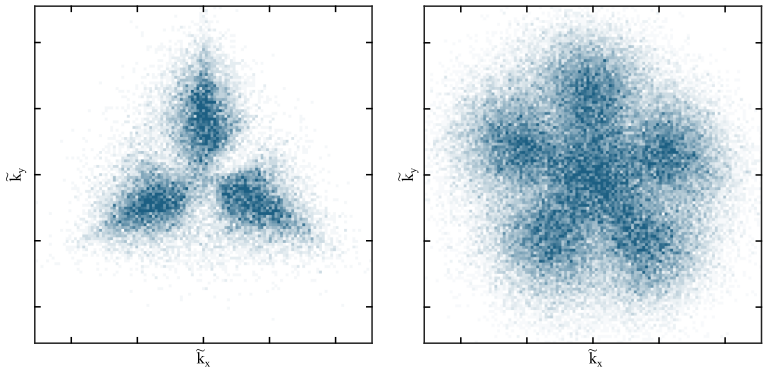

Figure 11.1: Measurement of Pauli Crystal. The plots show the measurement of the configurational probability in a non-interacting Fermi gas of $N = 3$ (left) and $N = 6$ (right) atoms [278]. Angular correlations are induced by Pauli-exclusion principle.

that the antisymmetric negativity reveals multipartite entanglement structure that is not accessible via the standard negativity alone.

Outlook

Throughout the cause of this thesis, we developed new techniques and concepts to characterize strongly correlated fermionic systems via momentum correlation measurements. While we focused on the full reconstruction of density matrices, we anticipate that the presented ideas also find application for the characterization of larger systems and the detection of many-body ordering or pairing in mesoscopic, fermionic systems.

We recently upgraded our experimental apparatus to be able to generate two dimensional optical potentials [279]. This allows the expansion of states in the 2D plane and is expected to substantially enhance the measured contrast of momentum correlation functions. Such an improvement enables to extend the study of Fermi-Hubbard-like states to larger one-dimensional systems with higher purity but also to address problems related to many-body interference in arrays of fermionic atoms [280].

A two-dimensional optical potential furthermore extends the range of possible states that we can realize in the laboratory. Using similar preparation schemes as before we can deterministically initialize mesoscopic systems in closed-shell configurations. While such a system already provides interesting physics to explore on its own [281, 282], we plan to investigate mesoscopic, interacting 2D systems via single-particle resolved momentum-density correlations [182, 283]. Figure 11.1 shows the measurement of the configurational probability in a non-interacting Fermi gas of 3 and 6 atoms (cf. Ref. [283]), a beautiful example, where fermionic exchange statistics induces ordering, which can only be revealed by sing-particle resolved momentum measurements. In particular by adding interaction and investigating such systems across the BEC-BCS crossover we hope to see signatures of many-body pairing in the strongly correlated regime [284]. Such signatures do not require a full tomography of the quantum state but should be apparent in higher-order correlation functions.

While deep in the BEC or BCS regime, the system is expected to show only second-order correlations in the in-situ or the momentum density, respectively, the signature should change drastically in the strongly correlated regime and might also be visible in higher-order correlation functions.
Due to the high degree of controllability in our setup, we can readily increase the particle number of the two-dimensional system to bridge the gap from microscopic to macroscopic Fermi systems. In future measurements we will investigate very dilute, yet strongly correlated, low entropy states of a few 100 atoms. In this mesoscopic regime the system is expected to show rich many-body behavior while both in-situ and momentum correlation measurements on the single-particle level are still within reach.
In addition we plan to further upgrade our experimental setup with a spatial light modulator (SLM). An SLM can be used to shape complex optical potentials and will enable the investigation of two-dimensional Fermi-Hubbard systems, including the study of Nagaoka magnetism on a 2×2 plaquette [285] or to explore fractional quantum hall physics using rotating traps [286].

Chapter 12

Bibliography

[1] J. J. Balmer. Notiz über die Spectrallinien des Wasserstoffs. *Annalen der Physik*, **261**:80–87, 1885.

[2] H. Hertz. Ueber einen Einfluss des ultravioletten Lichtes auf die electrische Entladung. *Annalen der Physik*, **267**:983–1000, 1887.

[3] P. Zeeman. The Effect of Magnetisation on the Nature of Light Emitted by a Substance. *Nature*, **55**:347, 1897.

[4] B. Lubsandorzhiev. On the history of photomultiplier tube invention. *Nuclear Instruments and Methods in Physics Research Section A: Accelerators, Spectrometers, Detectors and Associated Equipment*, **567**:236 – 238, 2006. Proceedings of the 4th International Conference on New Developments in Photodetection.

[5] J. Bardeen and W. H. Brattain. The transistor, a semi-conductor triode. *Physical Review*, **74**(2):230, 1948.

[6] A. J. Gross and T. R. Herrmann. History of lasers. *World journal of urology*, **25**(3):217–220, 2007.

[7] D. Goodstein and J. Goodstein. Richard Feynman and the history of superconductivity. *Physics in Perspective*, **2**:30–47, 2000.

[8] R. P. Feynman. Simulating physics with computers. *International Journal of Theoretical Physics*, **21**:467–488, 1982.

[9] C. Gross and I. Bloch. Quantum simulations with ultracold atoms in optical lattices. **357**:995–1001, 2017.

[10] M. J. Hartmann. Quantum simulation with interacting photons. *Journal of Optics*, **18**:104005, 2016.

[11] R. Blatt and C. F. Roos. Quantum simulations with trapped ions. *Nature Physics*, **8**:277–284, 2012.

[12] T. Bothwell, D. Kedar, E. Oelker, J. M. Robinson, S. L. Bromley, W. L. Tew, J. Ye, and C. J. Kennedy. JILA SrI optical lattice clock with uncertainty of 2.0×10^{-18}. *Metrologia*, **56**:065004, oct 2019.

[13] L. von der Wense, B. Seiferle, and P. G. Thirolf. Towards a 229Th-Based Nuclear Clock. *Measurement Techniques*, **60**:1178–1192, 2018.

[14] R. Barends, J. Kelly, A. Megrant, A. Veitia, D. Sank, E. Jeffrey, T. C. White, J. Mutus, A. G. Fowler, B. Campbell, et al. Superconducting quantum circuits at the surface code threshold for fault tolerance. *Nature*, **508**:500–503, 2014.

[15] T. Byrnes, N. Y. Kim, and Y. Yamamoto. Exciton–polariton condensates. *Nature Physics*, **10**:803–813, 2014.

[16] D. Hempston, J. Vovrosh, M. Toroš, G. Winstone, M. Rashid, and H. Ulbricht. Force sensing with an optically levitated charged nanoparticle. *Applied Physics Letters*, **111**:133111, 2017.

[17] M. Aspelmeyer, T. J. Kippenberg, and F. Marquardt. Cavity optomechanics. *Rev. Mod. Phys.*, **86**:1391–1452, 2014.

[18] B. Hensen, H. Bernien, A. E. Dréau, A. Reiserer, N. Kalb, M. S. Blok, J. Ruitenberg, R. F. Vermeulen, R. N. Schouten, C. Abellán, et al. Loophole-free Bell inequality violation using electron spins separated by 1.3 kilometres. *Nature*, **526**:682–686, 2015.

[19] V. Andreev and N. Hutzler. Improved limit on the electric dipole moment of the electron. *Nature*, **562**:355–360, 2018.

[20] A. D. Rider, D. C. Moore, C. P. Blakemore, M. Louis, M. Lu, and G. Gratta. Search for Screened Interactions Associated with Dark Energy below the 100 μm Length Scale. *Phys. Rev. Lett.*, **117**:101101, 2016.

[21] L. Pezzè, A. Smerzi, M. K. Oberthaler, R. Schmied, and P. Treutlein. Quantum metrology with nonclassical states of atomic ensembles. *Rev. Mod. Phys.*, **90**: 035005, 2018.

[22] M. H. Anderson, J. R. Ensher, M. R. Matthews, C. E. Wieman, and E. A. Cornell. Observation of Bose-Einstein Condensation in a Dilute Atomic Vapor. *Science*, **269**:198–201, 1995.

[23] K. B. Davis, M. O. Mewes, M. R. Andrews, N. J. van Druten, D. S. Durfee, D. M. Kurn, and W. Ketterle. Bose-Einstein Condensation in a Gas of Sodium Atoms. *Phys. Rev. Lett.*, **75**:3969–3973, Nov 1995.

[24] B. DeMarco and D. S. Jin. Onset of Fermi Degeneracy in a Trapped Atomic Gas. *Science*, **285**:1703–1706, 1999.

[25] I. Bloch, J. Dalibard, and S. Nascimbene. Quantum simulations with ultracold quantum gases. *Nature Physics*, **8**:267–276, 2012.

[26] K. Viebahn, M. Sbroscia, E. Carter, J.-C. Yu, and U. Schneider. Matter-Wave Diffraction from a Quasicrystalline Optical Lattice. *Phys. Rev. Lett.*, **122**:110404, Mar 2019.

[27] D. Barredo, V. Lienhard, S. De Leseleuc, T. Lahaye, and A. Browaeys. Synthetic three-dimensional atomic structures assembled atom by atom. *Nature*, **561**:79–82, 2018.

[28] C. Chin, R. Grimm, P. Julienne, and E. Tiesinga. Feshbach resonances in ultracold gases. *Rev. Mod. Phys.*, **82**:1225–1286, 2010.

[29] M. Höfer, L. Riegger, F. Scazza, C. Hofrichter, D. R. Fernandes, M. M. Parish, J. Levinsen, I. Bloch, and S. Fölling. Observation of an Orbital Interaction-Induced Feshbach Resonance in ^{173}Yb. *Phys. Rev. Lett.*, **115**:265302, Dec 2015.

[30] S. Kuhr. Quantum-gas microscopes: a new tool for cold-atom quantum simulators. *National Science Review*, **3**:170–172, 04 2016.

[31] A. Omran, H. Levine, A. Keesling, G. Semeghini, T. T. Wang, S. Ebadi, H. Bernien, A. S. Zibrov, H. Pichler, S. Choi, J. Cui, M. Rossignolo, P. Rembold, S. Montangero, T. Calarco, M. Endres, M. Greiner, V. Vuletić, and M. D. Lukin. Generation and manipulation of Schrödinger cat states in Rydberg atom arrays. *Science*, **365**:570–574, 2019. doi:10.1126/science.aax9743.

[32] A. Bohrdt, C. S. Chiu, G. Ji, M. Xu, D. Greif, M. Greiner, E. Demler, F. Grusdt, and M. Knap. Classifying snapshots of the doped Hubbard model with machine learning. *Nature Physics*, **15**:921–924, 2019.

[33] L. Tanzi, E. Lucioni, F. Famà, J. Catani, A. Fioretti, C. Gabbanini, R. N. Bisset, L. Santos, and G. Modugno. Observation of a Dipolar Quantum Gas with Metastable Supersolid Properties. *Phys. Rev. Lett.*, **122**:130405, 2019.

[34] L. Chomaz, D. Petter, P. Ilzhöfer, G. Natale, A. Trautmann, C. Politi, G. Durastante, R. M. W. van Bijnen, A. Patscheider, M. Sohmen, M. J. Mark, and F. Ferlaino. Long-Lived and Transient Supersolid Behaviors in Dipolar Quantum Gases. *Phys. Rev. X*, **9**:021012, 2019.

[35] F. Böttcher, J.-N. Schmidt, M. Wenzel, J. Hertkorn, M. Guo, T. Langen, and T. Pfau. Transient Supersolid Properties in an Array of Dipolar Quantum Droplets. *Phys. Rev. X*, **9**:011051, 2019.

[36] M. A. Norcia, A. W. Young, W. J. Eckner, E. Oelker, J. Ye, and A. M. Kaufman. Seconds-scale coherence on an optical clock transition in a tweezer array. *Science*, **366**:93–97, 2019.

[37] A. Griesmaier, J. Werner, S. Hensler, J. Stuhler, and T. Pfau. Bose-Einstein Condensation of Chromium. *Phys. Rev. Lett.*, **94**:160401, Apr 2005.

[38] T. Lahaye, T. Koch, B. Fröhlich, M. Fattori, J. Metz, A. Griesmaier, S. Giovanazzi, and T. Pfau. Strong dipolar effects in a quantum ferrofluid. *Nature*, **448**:672–675, 2007.

[39] T. Lahaye, J. Metz, B. Fröhlich, T. Koch, M. Meister, A. Griesmaier, T. Pfau, H. Saito, Y. Kawaguchi, and M. Ueda. *d*-Wave Collapse and Explosion of a Dipolar Bose-Einstein Condensate. *Phys. Rev. Lett.*, **101**:080401, 2008.

[40] B. Pasquiou, E. Maréchal, G. Bismut, P. Pedri, L. Vernac, O. Gorceix, and B. Laburthe-Tolra. Spontaneous Demagnetization of a Dipolar Spinor Bose Gas in an Ultralow Magnetic Field. *Phys. Rev. Lett.*, **106**:255303, 2011.

[41] M. Lu, N. Q. Burdick, S. H. Youn, and B. L. Lev. Strongly Dipolar Bose-Einstein Condensate of Dysprosium. *Phys. Rev. Lett.*, **107**:190401, 2011.

[42] K. Aikawa, A. Frisch, M. Mark, S. Baier, A. Rietzler, R. Grimm, and F. Ferlaino. Bose-Einstein Condensation of Erbium. *Phys. Rev. Lett.*, **108**:210401, 2012.

[43] H. Kadau, M. Schmitt, M. Wenzel, C. Wink, T. Maier, I. Ferrier-Barbut, and T. Pfau. Observing the Rosensweig instability of a quantum ferrofluid. *Nature*, **530**:194–197, 2016.

[44] D. S. Petrov. Quantum Mechanical Stabilization of a Collapsing Bose-Bose Mixture. *Phys. Rev. Lett.*, **115**:155302, Oct 2015.

[45] F. Wächtler and L. Santos. Quantum filaments in dipolar Bose-Einstein condensates. *Phys. Rev. A*, **93**:061603, Jun 2016.

[46] L. Chomaz, R. M. van Bijnen, D. Petter, G. Faraoni, S. Baier, J. H. Becher, M. J. Mark, F. Waechtler, L. Santos, and F. Ferlaino. Observation of roton mode population in a dipolar quantum gas. *Nature physics*, **14**:442–446, 2018.

[47] M. Lu, N. Q. Burdick, and B. L. Lev. Quantum Degenerate Dipolar Fermi Gas. *Phys. Rev. Lett.*, **108**:215301, 2012.

[48] K. Aikawa, A. Frisch, M. Mark, S. Baier, R. Grimm, and F. Ferlaino. Reaching Fermi Degeneracy via Universal Dipolar Scattering. *Phys. Rev. Lett.*, **112**: 010404, 2014.

[49] B. Naylor, A. Reigue, E. Maréchal, O. Gorceix, B. Laburthe-Tolra, and L. Vernac. Chromium dipolar Fermi sea. *Phys. Rev. A*, **91**:011603, Jan 2015.

[50] J. Quintanilla, S. T. Carr, and J. J. Betouras. Metanematic, smectic, and crystalline phases of dipolar fermions in an optical lattice. *Phys. Rev. A*, **79**: 031601, 2009.

[51] M. A. Baranov, M. S. Mar'enko, V. S. Rychkov, and G. V. Shlyapnikov. Superfluid pairing in a polarized dipolar Fermi gas. *Phys. Rev. A*, **66**:013606, 2002.

[52] J. Levinsen, N. R. Cooper, and G. V. Shlyapnikov. Topological $p_x + ip_y$ superfluid phase of fermionic polar molecules. *Phys. Rev. A*, **84**:013603, 2011.

[53] M. A. Baranov, L. Dobrek, and M. Lewenstein. Superfluidity of Trapped Dipolar Fermi Gases. *Phys. Rev. Lett.*, **92**:250403, 2004.

[54] D. Peter, S. Müller, S. Wessel, and H. P. Büchler. Anomalous Behavior of Spin Systems with Dipolar Interactions. *Phys. Rev. Lett.*, **109**:025303, 2012.

[55] A. Celi, P. Massignan, J. Ruseckas, N. Goldman, I. B. Spielman, G. Juzeliūnas, and M. Lewenstein. Synthetic Gauge Fields in Synthetic Dimensions. *Phys. Rev. Lett.*, **112**:043001, 2014.

[56] L. F. Livi, G. Cappellini, M. Diem, L. Franchi, C. Clivati, M. Frittelli, F. Levi, D. Calonico, J. Catani, M. Inguscio, and L. Fallani. Synthetic Dimensions and Spin-Orbit Coupling with an Optical Clock Transition. *Phys. Rev. Lett.*, **117**: 220401, 2016.

[57] G. C. Strinati, P. Pieri, G. Röpke, P. Schuck, and M. Urban. The BCS–BEC crossover: From ultra-cold Fermi gases to nuclear systems. *Physics Reports*, **738**:1–76, 2018.

[58] G. M. Bruun and E. Taylor. Quantum Phases of a Two-Dimensional Dipolar Fermi Gas. *Phys. Rev. Lett.*, **101**:245301, Dec 2008.

[59] R. Islam, R. Ma, P. Preiss, M. Tai, A. Lukin, M. Rispoli, and M. Greiner. Measuring entanglement entropy in a quantum many-body system. *Nature*, **528**:77 – 83, 2015.

[60] P. M. Preiss, R. Ma, M. E. Tai, A. Lukin, M. Rispoli, P. Zupancic, Y. Lahini, R. Islam, and M. Greiner. Strongly correlated quantum walks in optical lattices. *Science*, **347**:1229–1233, 2015.

[61] P. M. Preiss, J. H. Becher, R. Klemt, V. Klinkhamer, A. Bergschneider, N. Defenu, and S. Jochim. High-Contrast Interference of Ultracold Fermions. *Phys. Rev. Lett.*, **122**:143602, 2019.

[62] A. Bergschneider, V. M. Klinkhamer, J. H. Becher, R. Klemt, L. Palm, G. Zürn, S. Jochim, and P. M. Preiss. Experimental characterization of two-particle entanglement through position and momentum correlations. *Nature Physics*, **15**:640 – 644, 2019.

[63] T. Jeltes, J. M. McNamara, W. Hogervorst, W. Vassen, V. Krachmalnicoff, M. Schellekens, A. Perrin, H. Chang, D. Boiron, A. Aspect, and C. I. Westbrook. Comparison of the Hanbury Brown–Twiss effect for bosons and fermions. *Nature*, **445**:402 –405, 2007.

[64] R. Bücker, A. Perrin, S. Manz, T. Betz, C. Koller, T. Plisson, J. Rottmann, T. Schumm, and J. Schmiedmayer. Single-particle-sensitive imaging of freely propagating ultracold atoms. *New Journal of Physics*, **11**:103039, 2009.

[65] M. Boll, T. A. Hilker, G. Salomon, A. Omran, J. Nespolo, L. Pollet, I. Bloch, and C. Gross. Spin- and density-resolved microscopy of antiferromagnetic correlations in Fermi-Hubbard chains. *Science*, **353**:1257–1260, 2016.

[66] P. M. Preiss, R. Ma, M. E. Tai, J. Simon, and M. Greiner. Quantum gas microscopy with spin, atom-number, and multilayer readout. *Phys. Rev. A*, **91**: 041602, 2015.

[67] A. Bergschneider, V. M. Klinkhamer, J. H. Becher, R. Klemt, G. Zürn, P. M. Preiss, and S. Jochim. Spin-resolved single-atom imaging of ^{6}Li in free space. *Phys. Rev. A*, **97**:063613, 2018.

[68] M. Cramer, M. B. Plenio, S. T. Flammia, R. Somma, D. Gross, S. D. Bartlett, O. Landon-Cardinal, D. Poulin, and Y.-K. Liu. Efficient quantum state tomography. *Nature communications*, **1**:1–7, 2010.

[69] G. Tóth, W. Wieczorek, D. Gross, R. Krischek, C. Schwemmer, and H. Weinfurter. Permutationally Invariant Quantum Tomography. *Phys. Rev. Lett.*, **105**:250403, 2010.

[70] C. Riofrío, D. Gross, S. T. Flammia, T. Monz, D. Nigg, R. Blatt, and J. Eisert. Experimental quantum compressed sensing for a seven-qubit system. *Nature communications*, **8**:1–8, 2017.

[71] B. Lanyon, C. Maier, M. Holzäpfel, T. Baumgratz, C. Hempel, P. Jurcevic, I. Dhand, A. Buyskikh, A. Daley, M. Cramer, et al. Efficient tomography of a quantum many-body system. *Nature Physics*, **13**:1158–1162, 2017.

[72] T. Schweigler, V. Kasper, S. Erne, I. Mazets, B. Rauer, F. Cataldini, T. Langen, T. Gasenzer, J. Berges, and J. Schmiedmayer. Experimental characterization of a quantum many-body system via higher-order correlations. *Nature*, **545**: 323–326, 2017.

[73] M. Rispoli, A. Lukin, R. Schittko, S. Kim, M. Tai, J. Léonard, and M. Greiner. Quantum critical behaviour at the many-body localization transition. *Nature*, **573**:385 – 389, 2019.

[74] L. Amico, R. Fazio, A. Osterloh, and V. Vedral. Entanglement in many-body systems. *Rev. Mod. Phys.*, **80**:517–576, 2008.

[75] J. Eisert, M. Cramer, and M. B. Plenio. Colloquium: Area laws for the entanglement entropy. *Rev. Mod. Phys.*, **82**:277–306, 2010.

[76] M. Ohliger, V. Nesme, and J. Eisert. Efficient and feasible state tomography of quantum many-body systems. *New Journal of Physics*, **15**:015024, jan 2013.

[77] A. Elben, B. Vermersch, C. F. Roos, and P. Zoller. Statistical correlations between locally randomized measurements: A toolbox for probing entanglement in many-body quantum states. *Phys. Rev. A*, **99**:052323, 2019.

[78] E. Khatami, E. Guardado-Sanchez, B. M. Spar, B. M. Carrasquilla, W. S. Bakr, and R. T. Scalettar. Visualizing Correlations in the 2D Fermi-Hubbard Model with AI. *arXiv preprint arXiv:2002.12310*, 2020.

[79] G. Torlai, B. Timar, E. P. L. van Nieuwenburg, H. Levine, A. Omran, A. Keesling, H. Bernien, M. Greiner, V. Vuletić, M. D. Lukin, R. G. Melko, and M. Endres. Integrating Neural Networks with a Quantum Simulator for State Reconstruction. *Phys. Rev. Lett.*, **123**:230504, Dec 2019.

[80] W. Ketterle and M. W. Zwierlein. Making, probing and understanding ultracold Fermi gases. *arXiv preprint arXiv:0801.2500*, 2008.

[81] A. Frisch. Dipolar Quantum Gases of Erbium. *PhD Thesis*, 2014.

[82] S. Baier. *Ultracold Dipolar Erbium Atoms: From Scattering Phenomena to Quantum Simulations.* PhD thesis, Universität Innsbruck, 2018.

[83] F. Serwane. *Deterministic preparation of a tunable few-fermion system.* PhD thesis, Heidelberg University, 2011.

[84] G. Zürn. *Few-fermion systems in one dimension.* PhD thesis, Heidelberg University, 2012.

[85] A. Bergschneider. *Strong correlations in few-fermion systems.* PhD thesis, Heidelberg University, 2017.

[86] M. E. Gehm. *Preparation of an optically-trapped degenerate Fermi gas of 6Li: Finding the route to degeneracy.* Duke University, 2003.

[87] P. Ilzhöfer, G. Durastante, A. Patscheider, A. Trautmann, M. J. Mark, and F. Ferlaino. Two-species five-beam magneto-optical trap for erbium and dysprosium. *Phys. Rev. A*, **97**:023633, Feb 2018.

[88] H. J. Metcalf and P. Van der Straten. Laser cooling and trapping of neutral atoms. *The Optics Encyclopedia: Basic Foundations and Practical Applications*, 2007.

[89] A. Frisch, K. Aikawa, M. Mark, A. Rietzler, J. Schindler, E. Zupanič, R. Grimm, and F. Ferlaino. Narrow-line magneto-optical trap for erbium. *Phys. Rev. A*, **85**:051401, May 2012.

[90] R. Grimm, M. Weidemüller, and Y. B. Ovchinnikov. Optical dipole traps for neutral atoms. In *Advances in atomic, molecular, and optical physics*, volume 42, pages 95–170. Elsevier, 2000.

[91] J. Mitroy, M. S. Safronova, and C. W. Clark. Theory and applications of atomic and ionic polarizabilities. *Journal of Physics B: Atomic, Molecular and Optical Physics*, **43**:202001, 2010.

[92] W. Ketterle, D. S. Durfee, and D. Stamper-Kurn. Making, probing and understanding Bose-Einstein condensates. *arXiv preprint cond-mat/9904034*, 1999.

[93] H. Friedrich. *Scattering Theory. Lecture Notes in Physics.* Springer, 2013. ISBN 978-3-642-38281-9.

[94] V. M. Klinkhamer. *Few-Fermion Systems under a Matterwave Microscope*. PhD thesis, Heidelberg University, 2018.

[95] S. Kotochigova. Controlling interactions between highly magnetic atoms with Feshbach resonances. *Reports on Progress in Physics*, **77**:093901, 2014.

[96] H. Li, J.-F. Wyart, O. Dulieu, S. Nascimbène, and M. Lepers. Optical trapping of ultracold dysprosium atoms: transition probabilities, dynamic dipole polarizabilities and van der WaalsC6coefficients. *Journal of Physics B: Atomic, Molecular and Optical Physics*, **50**:014005, 2016.

[97] T. Maier, H. Kadau, M. Schmitt, M. Wenzel, I. Ferrier-Barbut, T. Pfau, A. Frisch, S. Baier, K. Aikawa, L. Chomaz, M. J. Mark, F. Ferlaino, C. Makrides, E. Tiesinga, A. Petrov, and S. Kotochigova. Emergence of Chaotic Scattering in Ultracold Er and Dy. *Phys. Rev. X*, **5**:041029, 2015.

[98] A. Frisch, M. Mark, K. Aikawa, F. Ferlaino, J. Bohn, C. Makrides, A. Petroc, and S. Kotochigova. Quantum chaos in ultracold collisions of gas-phase erbium atoms. *Nature*, **504**:475–479, 2014.

[99] L. Chomaz, S. Baier, D. Petter, M. J. Mark, F. Wächtler, L. Santos, and F. Ferlaino. Quantum-Fluctuation-Driven Crossover from a Dilute Bose-Einstein Condensate to a Macrodroplet in a Dipolar Quantum Fluid. *Phys. Rev. X*, **6**:041039, 2016.

[100] C. Ticknor. Collisional Control of Ground State Polar Molecules and Universal Dipolar Scattering. *Phys. Rev. Lett.*, **100**:133202, 2008.

[101] J. L. Bohn, M. Cavagnero, and C. Ticknor. Quasi-universal dipolar scattering in cold and ultracold gases. *New Journal of Physics*, **11**:055039, 2009.

[102] S. Baier, D. Petter, J. H. Becher, A. Patscheider, G. Natale, L. Chomaz, M. J. Mark, and F. Ferlaino. Realization of a Strongly Interacting Fermi Gas of Dipolar Atoms. *Phys. Rev. Lett.*, **121**:093602, 2018.

[103] M. Randeria and E. Taylor. Crossover from Bardeen-Cooper-Schrieffer to Bose-Einstein Condensation and the Unitary Fermi Gas. *Annual Review of Condensed Matter Physics*, **5**:209–232, 2014.

[104] T. Maier, H. Kadau, M. Schmitt, M. Wenzel, I. Ferrier-Barbut, T. Pfau, A. Frisch, S. Baier, K. Aikawa, L. Chomaz, M. J. Mark, F. Ferlaino, C. Makrides, E. Tiesinga, A. Petrov, and S. Kotochigova. Emergence of Chaotic Scattering in Ultracold Er and Dy. *Phys. Rev. X*, **5**:041029, 2015.

[105] R. J. Mears, L. Reekie, I. Jauncey, and D. N. Payne. Low-noise erbium-doped fibre amplifier operating at 1.54 μm. *Electronics Letters*, **23**:1026–1028, 1987.

[106] X. W. Zhang, T. Lin, P. Zhang, H. C. Song, H. Jin, J. Xu, J. Xu, P. J. Wang, K. Y. Niu, and K. J. Chen. Tunable quantum dot arrays as efficient sensitizers for enhanced near-infrared electroluminescence of erbium ions. *Nanoscale*, **10**: 4138–4146, 2018.

[107] H. Sun, L. Yin, Z. Liu, Y. Zheng, F. Fan, S. Zhao, X. Feng, Y. Li, and C. Z. Ning. Giant optical gain in a single-crystal erbium chloride silicate nanowire. *Nature Photonics*, **11**:4138–4146, 2017.

[108] J. J. McClelland and J. L. Hanssen. Laser Cooling without Repumping: A Magneto-Optical Trap for Erbium Atoms. *Phys. Rev. Lett.*, **96**:143005, 2006.

[109] W. C. Martin, R. Zalubas, and L. Hagan. Atomic Energy Levels-The Rare-Earth Elements. The Spectra of Lanthanum, Cerium, Praseodymium, Neodymium, Promethium, Samarium, Europium, Gadolinium, Terbium, Dysprosium, Holmium, Erbium, Thulium, Ytterbium, and Lutetium. Technical report, NATIONAL STANDARD REFERENCE DATA SYSTEM, 1978.

[110] J. Reader, C. H. Corliss, W. L. Wiese, and G. Martin. Wavelengths and Transition Probabilities for Atoms and Atomic Ions. Part I. Wavelengths. Part II. Transition Probabilities. Technical report, NATIONAL STANDARD REFERENCE DATA SYSTEM, 1980.

[111] M. Lepers, J.-F. Wyart, and O. Dulieu. Anisotropic optical trapping of ultracold erbium atoms. *Phys. Rev. A*, **89**:022505, 2014.

[112] H. Y. Ban, M. Jacka, J. L. Hanssen, J. Reader, and J. J. McClelland. Laser cooling transitions in atomic erbium. *Opt. Express*, **13**:3185–3195, 2005.

[113] J. J. McClelland and J. L. Hanssen. Laser Cooling without Repumping: A Magneto-Optical Trap for Erbium Atoms. *Phys. Rev. Lett.*, **96**:143005, 2006.

[114] J. E. Lawler, J.-F. Wyart, and E. A. D. Hartog. Atomic transition probabilities of Er i. *Journal of Physics B: Atomic, Molecular and Optical Physics*, **43**: 235001, 2010.

[115] E. A. D. Hartog, J. P. Chisholm, and J. E. Lawler. Radiative lifetimes of neutral erbium. *Journal of Physics B: Atomic, Molecular and Optical Physics*, **43**:155004, 2010.

[116] S. Baier. An optical dipole trap for erbium with tunable geometry. Master's thesis, Universität Innsbruck, 2012.

[117] S. Baier, M. J. Mark, D. Petter, K. Aikawa, L. Chomaz, Z. Cai, M. Baranov, P. Zoller, and F. Ferlaino. Extended Bose-Hubbard models with ultracold magnetic atoms. *Science*, **352**:201–205, 2016.

[118] J. G. Conway and B. G. Wybourne. Low-Lying Energy Levels of Lanthanide Atoms and Intermediate Coupling. *Phys. Rev.*, **130**:2325–2332, 1963.

[119] R. Grimm, M. Weidemüller, and Y. B. Ovchinnikov. Optical Dipole Traps for Neutral Atoms. volume 42 of *Advances In Atomic, Molecular, and Optical Physics*, pages 95 – 170. Academic Press, 2000.

[120] R. D. Cowan. *The theory of atomic structure and spectra*. Univ of California Press, 1981.

[121] H. Li, J.-F. m. c. Wyart, O. Dulieu, and M. Lepers. Anisotropic optical trapping as a manifestation of the complex electronic structure of ultracold lanthanide atoms: The example of holmium. *Phys. Rev. A*, **95**:062508, 2017.

[122] P.-L. Liu, Y. Huang, W. Bian, H. Shao, H. Guan, Y.-B. Tang, C.-B. Li, J. Mitroy, and K.-L. Gao. Measurement of Magic Wavelengths for the $^{40}Ca^{+}$ Clock Transition. *Phys. Rev. Lett.*, **114**:223001, 2015.

[123] H. Katori, M. Takamoto, V. G. Pal'chikov, and V. D. Ovsiannikov. Ultrastable Optical Clock with Neutral Atoms in an Engineered Light Shift Trap. *Phys. Rev. Lett.*, **91**:173005, 2003.

[124] B. Arora, M. S. Safronova, and C. W. Clark. Tune-out wavelengths of alkali-metal atoms and their applications. *Phys. Rev. A*, **84**:043401, 2011.

[125] W. Kao, Y. Tang, N. Q. Burdick, and B. L. Lev. Anisotropic dependence of tune-out wavelength near Dy 741-nm transition. *Opt. Express*, **25**:3411–3419, 2017.

[126] E. Copenhaver, K. Cassella, R. Berghaus, and H. Müller. Measurement of a ^{7}Li tune-out wavelength by phase-patterned atom interferometry. *Phys. Rev. A*, **100**:063603, 2019.

[127] W.-W. Yu, R.-M. Yu, and Y.-J. Cheng. Tune-Out Wavelengths for the Rb Atom. *Chinese Physics Letters*, **32**:123102, 2015.

[128] O. Mandel, M. Greiner, A. Widera, T. Rom, T. W. Hänsch, and I. Bloch. Coherent Transport of Neutral Atoms in Spin-Dependent Optical Lattice Potentials. *Phys. Rev. Lett.*, **91**:010407, 2003.

[129] B. Yang, H.-N. Dai, H. Sun, A. Reingruber, Z.-S. Yuan, and J.-W. Pan. Spin-dependent optical superlattice. *Phys. Rev. A*, **96**:011602, 2017.

[130] I. Kuzmenko, T. Kuzmenko, Y. Avishai, and G.-B. Jo. Multipolar Kondo effect in a $^{1}S_0 - ^{3}P_2$ mixture of ^{173}Yb atoms. *Phys. Rev. B*, **97**:075124, 2018.

[131] A. J. Daley, M. M. Boyd, J. Ye, and P. Zoller. Quantum Computing with Alkaline-Earth-Metal Atoms. *Phys. Rev. Lett.*, **101**:170504, 2008.

[132] R. Chamakhi, H. Ahlers, M. Telmini, C. Schubert, E. M. Rasel, and N. Gaaloul. Species-selective lattice launch for precision atom interferometry. *New Journal of Physics*, **17**:123002, 2015.

[133] J. H. Becher, S. Baier, K. Aikawa, M. Lepers, J.-F. Wyart, O. Dulieu, and F. Ferlaino. Anisotropic polarizability of erbium atoms. *Phys. Rev. A*, **97**: 012509, 2018.

[134] F. Le Kien, P. Schneeweiss, and A. Rauschenbeutel. Dynamical polarizability of atoms in arbitrary light fields: general theory and application to cesium. *The European Physical Journal D*, **67**:92, 2013.

[135] R. Vexiau, D. Borsalino, M. Lepers, A. Orbán, M. Aymar, O. Dulieu, and N. Bouloufa-Maafa. Dynamic dipole polarizabilities of heteronuclear alkali dimers: optical response, trapping and control of ultracold molecules. *International Reviews in Physical Chemistry*, **36**:709–750, 2017.

[136] A. Messiah. Quantum mechanics, volume II. *Appendix C (Section IV)(North-Holland Publishing Company, Amsterdam, 1969)*, pages 1061–1065, 1962.

[137] L. Corman, P. Fabritius, S. Häusler, J. Mohan, L. H. Dogra, D. Husmann, M. Lebrat, and T. Esslinger. Quantized conductance through a dissipative atomic point contact. *Phys. Rev. A*, **100**:053605, 2019.

[138] A. Kramida, Yu. Ralchenko, J. Reader, and and NIST ASD Team. NIST Atomic Spectra Database (ver. 5.7.1), [Online]. Available: `https://physics.nist.gov/asd` [2020, January 16]. National Institute of Standards and Technology, Gaithersburg, MD., 2019.

[139] N. Q. Burdick, Y. Tang, and B. L. Lev. Long-Lived Spin-Orbit-Coupled Degenerate Dipolar Fermi Gas. *Phys. Rev. X*, **6**:031022, 2016.

[140] A. Heinz, A. Park, N. Šantić, J. Trautmann, S. Porsev, M. Safronova, I. Bloch, and S. Blatt. State-dependent optical lattices for the strontium optical qubit. *arXiv preprint arXiv:1912.10350*, 2019.

[141] A. Mazloom, B. Vermersch, M. A. Baranov, and M. Dalmonte. Adiabatic state preparation of stripe phases with strongly magnetic atoms. *Phys. Rev. A*, **96**: 033602, 2017.

[142] J. M. Khosrofian and B. A. Garetz. Measurement of a Gaussian laser beam diameter through the direct inversion of knife-edge data. *Appl. Opt.*, **22**:3406–3410, 1983.

[143] C. Ravensbergen, V. Corre, E. Soave, M. Kreyer, S. Tzanova, E. Kirilov, and R. Grimm. Accurate Determination of the Dynamical Polarizability of Dysprosium. *Phys. Rev. Lett.*, **120**:223001, 2018.

[144] A. Patscheider, B. Zhu, L. Chomaz, D. Petter, S. Baier, A. Rey, F. Ferlaino, and M. Mark. Controlling Dipolar Exchange Interactions in a Dense 3D Array of Large Spin Fermions. *arXiv preprint arXiv:1904.08262*, 2019.

[145] Q. Beaufils, R. Chicireanu, T. Zanon, B. Laburthe-Tolra, E. Maréchal, L. Vernac, J.-C. Keller, and O. Gorceix. All-optical production of chromium Bose-Einstein condensates. *Phys. Rev. A*, **77**:061601, 2008.

[146] J. Ulitzsch, D. Babik, R. Roell, and M. Weitz. Bose-Einstein condensation of erbium atoms in a quasielectrostatic optical dipole trap. *Phys. Rev. A*, **95**: 043614, 2017.

[147] E. Lucioni, L. Tanzi, A. Fregosi, J. Catani, S. Gozzini, M. Inguscio, A. Fioretti, C. Gabbanini, and G. Modugno. Dysprosium dipolar Bose-Einstein condensate with broad Feshbach resonances. *Phys. Rev. A*, **97**:060701, 2018.

[148] N. Q. Burdick, K. Baumann, Y. Tang, M. Lu, and B. L. Lev. Fermionic Suppression of Dipolar Relaxation. *Phys. Rev. Lett.*, **114**:023201, 2015.

[149] K. Aikawa, S. Baier, A. Frisch, M. Mark, C. Ravensbergen, and F. Ferlaino. Observation of Fermi surface deformation in a dipolar quantum gas. *Science*, **345**:1484–1487, 2014.

[150] K. Aikawa, A. Frisch, M. Mark, S. Baier, R. Grimm, J. L. Bohn, D. S. Jin, G. M. Bruun, and F. Ferlaino. Anisotropic Relaxation Dynamics in a Dipolar Fermi Gas Driven Out of Equilibrium. *Phys. Rev. Lett.*, **113**:263201, Dec 2014.

[151] M. Mayle, B. P. Ruzic, and J. L. Bohn. Statistical aspects of ultracold resonant scattering. *Phys. Rev. A*, **85**:062712, 2012.

[152] Y. Kawaguchi, H. Saito, and M. Ueda. [**?**]Einstein–de Haas Effect in Dipolar Bose-Einstein Condensates. *Phys. Rev. Lett.*, **96**:080405, Mar 2006.

[153] M. Köhl, H. Moritz, T. Stöferle, K. Günter, and T. Esslinger. Fermionic Atoms in a Three Dimensional Optical Lattice: Observing Fermi Surfaces, Dynamics, and Interactions. *Phys. Rev. Lett.*, **94**:080403, 2005.

[154] K. Günter, T. Stöferle, H. Moritz, M. Köhl, and T. Esslinger. p-Wave Interactions in Low-Dimensional Fermionic Gases. *Phys. Rev. Lett.*, **95**:230401, 2005.

[155] A. J. Moerdijk, B. J. Verhaar, and A. Axelsson. Resonances in ultracold collisions of ^{6}Li, ^{7}Li, and ^{23}Na. *Phys. Rev. A*, **51**:4852–4861, 1995.

[156] A. Frisch, M. Mark, K. Aikawa, S. Baier, R. Grimm, A. Petrov, S. Kotochigova, G. Quéméner, M. Lepers, O. Dulieu, and F. Ferlaino. Ultracold Dipolar Molecules Composed of Strongly Magnetic Atoms. *Phys. Rev. Lett.*, **115**:203201, 2015.

[157] V. Gurarie and L. Radzihovsky. Resonantly paired fermionic superfluids. *Annals of Physics*, **322**:2 – 119, 2007. January Special Issue 2007.

[158] D. S. Petrov. Three-body problem in Fermi gases with short-range interparticle interaction. *Phys. Rev. A*, **67**:010703, 2003.

[159] M. Mancini, G. Pagano, G. Cappellini, L. Livi, M. Rider, J. Catani, C. Sias, P. Zoller, M. Inguscio, M. Dalmonte, and L. Fallani. Observation of chiral edge states with neutral fermions in synthetic Hall ribbons. *Science*, **349**:1510–1513, 2015.

[160] W. Li, A. Dhar, X. Deng, K. Kasamatsu, L. Barbiero, and L. Santos. Disorderless quasi-localization of polar gases in one-dimensional lattices. *Physical review letters*, **124**:010404, 2020.

[161] U. Schneider, L. Hackermüller, J. P. Ronzheimer, S. Will, S. Braun, T. Best, I. Bloch, E. Demler, S. Mandt, D. Rasch, et al. Fermionic transport and out-of-equilibrium dynamics in a homogeneous Hubbard model with ultracold atoms. *Nature Physics*, **8**:213–218, 2012.

[162] F. Serwane, G. Zürn, T. Lompe, T. B. Ottenstein, A. N. Wenz, and S. Jochim. Deterministic Preparation of a Tunable Few-Fermion System. *Science*, **332**: 336–338, 2011.

[163] S. Murmann, A. Bergschneider, V. M. Klinkhamer, G. Zürn, T. Lompe, and S. Jochim. Two Fermions in a Double Well: Exploring a Fundamental Building Block of the Hubbard Model. *Phys. Rev. Lett.*, **114**:080402, 2015.

[164] R. C. Weast, M. J. Astle, W. H. Beyer, et al. *CRC handbook of chemistry and physics*, volume 69. CRC press Boca Raton, FL, 1988.

[165] C. L. Satter, S. Tan, and K. Dieckmann. Comparison of an efficient implementation of gray molasses to narrow-line cooling for the all-optical production of a lithium quantum gas. *Phys. Rev. A*, **98**:023422, 2018.

[166] R. Wei and E. J. Mueller. Magnetic-field dependence of Raman coupling in alkali-metal atoms. *Phys. Rev. A*, **87**:042514, 2013.

[167] E. Arimondo, M. Inguscio, and P. Violino. Experimental determinations of the hyperfine structure in the alkali atoms. *Rev. Mod. Phys.*, **49**:31–75, 1977.

[168] J. H. Becher. Towards Spin and Site-Resolved, Single-Atom Imaging of 6Li Atoms in a Multiwell Potential. Master's thesis, Heidelberg University, 2016.

[169] S. Murmann. *Few-particle quantum magnetism with ultracold atoms*. PhD thesis, Heidelberg University, 2015.

[170] V. M. Klinkhamer. An apparatus for few-fermion systems in multiple well potentials. Master's thesis, Heidelberg University, 2012.

[171] A. Bergschneider. Ultracold few-fermion systems in multiwell potentials. Master's thesis, Heidelberg University, 2013.

[172] A. N. Wenz, G. Zürn, S. Murmann, I. Brouzos, T. Lompe, and S. Jochim. From Few to Many: Observing the Formation of a Fermi Sea One Atom at a Time. *Science*, **342**:457–460, 2013.

[173] G. Zürn, A. N. Wenz, S. Murmann, A. Bergschneider, T. Lompe, and S. Jochim. Pairing in Few-Fermion Systems with Attractive Interactions. *Phys. Rev. Lett.*, **111**:175302, 2013.

[174] S. Murmann, F. Deuretzbacher, G. Zürn, J. Bjerlin, S. M. Reimann, L. Santos, T. Lompe, and S. Jochim. Antiferromagnetic Heisenberg Spin Chain of a Few Cold Atoms in a One-Dimensional Trap. *Phys. Rev. Lett.*, **115**:215301, 2015.

[175] J. Hubbard. Electron correlations in narrow energy bands. *Proceedings of the Royal Society of London. Series A. Mathematical and Physical Sciences*, **276**: 238–257, 1963.

[176] D. Jaksch and P. Zoller. The cold atom Hubbard toolbox. *Annals of Physics*, **315**:52 – 79, 2005. Special Issue.

[177] T. Esslinger. Fermi-Hubbard Physics with Atoms in an Optical Lattice. *Annual Review of Condensed Matter Physics*, **1**:129–152, 2010.

[178] L. Tarruell and L. Sanchez-Palencia. Quantum simulation of the Hubbard model with ultracold fermions in optical lattices. *Comptes Rendus Physique*, **19**:365 – 393, 2018.

[179] O. Daigle, J. Turcotte, É. Artigau, and R. Doyon. Preliminary characterization results of a large format 4k x 4k emccd. In *High Energy, Optical, and Infrared Detectors for Astronomy VIII*, volume 10709, page 107090A. International Society for Optics and Photonics, 2018.

[180] P. A. Murthy, D. Kedar, T. Lompe, M. Neidig, M. G. Ries, A. N. Wenz, G. Zürn, and S. Jochim. Matter-wave Fourier optics with a strongly interacting two-dimensional Fermi gas. *Phys. Rev. A*, **90**:043611, 2014.

[181] S. Fölling, F. Gerbier, A. Widera, O. Mandel, T. Gericke, and I. Bloch. Spatial quantum noise interferometry in expanding ultracold atom clouds. *Nature*, **434**: 481–484, 2005.

[182] M. Greiner, C. A. Regal, J. T. Stewart, and D. S. Jin. Probing Pair-Correlated Fermionic Atoms through Correlations in Atom Shot Noise. *Phys. Rev. Lett.*, **94**:110401, 2005.

[183] R. Dall, A. Manning, S. Hodgman, W. Rugway, K. Kheruntsyan, and A. Truscoll. Ideal n-body correlations with massive particles. *Nature Physics*, **9**: 341–344, 2005.

[184] S. S. Hodgman, R. I. Khakimov, R. J. Lewis-Swan, A. G. Truscott, and K. V. Kheruntsyan. Solving the Quantum Many-Body Problem via Correlations Measured with a Momentum Microscope. *Phys. Rev. Lett.*, **118**:240402, 2017.

[185] R. H. Brown and R. Q. Twiss. Correlation between photons in two coherent beams of light. *Nature*, **177**:27–29, 1956.

[186] R. H. Brown and R. Q. Twiss. A test of a new type of stellar interferometer on Sirius. *Nature*, **178**:1046–1048, 1956.

[187] T. Csörgö. Review of HBT or Bose-Einstein correlations in high energy heavy ion collisions. *Journal of Physics: Conference Series*, **50**:259–270, 2006.

[188] C. K. Hong, Z. Y. Ou, and L. Mandel. Measurement of subpicosecond time intervals between two photons by interference. *Phys. Rev. Lett.*, **59**:2044–2046, 1987.

[189] R. Ghosh and L. Mandel. Observation of nonclassical effects in the interference of two photons. *Phys. Rev. Lett.*, **59**:1903–1905, 1987.

[190] R. J. Glauber. Coherent and Incoherent States of the Radiation Field. *Phys. Rev.*, **131**:2766–2788, 1963.

[191] F. Arecchi, E. Gatti, and A. Sona. Time distribution of photons from coherent and Gaussian sources. *Physics Letters*, **20**:27 – 29, 1966.

[192] M. O. Scully and M. S. Zubairy. *Quantum Optics*. Cambridge University Press, Cambridge, 1997.

[193] M. Schellekens, R. Hoppeler, A. Perrin, J. V. Gomes, D. Boiron, A. Aspect, and C. I. Westbrook. Hanbury Brown Twiss Effect for Ultracold Quantum Gases. *Science*, **310**:648–651, 2005.

[194] T. Rom, T. Best, D. von Oosten, U. Schneider, S. Fölling, B. Paredes, and I. Bloch. Free fermion antibunching in a degenerate atomic Fermi gas released from an optical lattice. *Nature*, **444**:733–736, 2006.

[195] M. C. Tichy. Interference of identical particles from entanglement to boson-sampling. *Journal of Physics B: Atomic, Molecular and Optical Physics*, **47**: 103001, 2014.

[196] H.-C. Liu. High-order correlation of chaotic bosons and fermions. *Phys. Rev. A*, **94**:023827, Aug 2016.

[197] R. I. Khakimov, B. Henson, D. Shin, S. Hodgman, R. Dall, K. Baldwin, and A. Truscott. Ghost imaging with atoms. *Nature*, **540**:100–103, 2016.

[198] S. S. Hodgman, W. Bu, S. B. Mann, R. I. Khakimov, and A. G. Truscott. Higher-Order Quantum Ghost Imaging with Ultracold Atoms. *Phys. Rev. Lett.*, **122**:233601, Jun 2019.

[199] R. J. Lewis-Swan and K. V. Kheruntsyan. Proposal for a motional-state Bell inequality test with ultracold atoms. *Phys. Rev. A*, **91**:052114, 2015.

[200] D. Shin, B. Henson, S. Hodgman, T. Wasak, J. Chwedeńczuk, and A. Truscott. Bell correlations between spatially separated pairs of atoms. *Nature communications*, **10**:1–7, 2019.

[201] M. Walschaers. Signatures of many-particle interference. *Journal of Physics B: Atomic, Molecular and Optical Physics*, **53**:043001, jan 2020.

[202] W. Yi, A. J. Daley, G. Pupillo, and P. Zoller. State-dependent, addressable subwavelength lattices with cold atoms. *New Journal of Physics*, **10**:073015, jul 2008.

[203] Y. Wang, S. Subhankar, P. Bienias, M. Łacki, T.-C. Tsui, M. A. Baranov, A. V. Gorshkov, P. Zoller, J. V. Porto, and S. L. Rolston. Dark State Optical Lattice with a Subwavelength Spatial Structure. *Phys. Rev. Lett.*, **120**:083601, Feb 2018.

[204] S. Fölling. Quantum Noise Correlation Experiments with Ultracold Atoms. In *Quantum Gas Experiments: Exploring Many-Body States*, chapter 8, pages 145–177. World Scientific, 2015.

[205] M. E. Peskin. *An introduction to quantum field theory*. CRC press, 2018.

[206] G. C. Wick. The Evaluation of the Collision Matrix. *Phys. Rev.*, **80**:268–272, 1950.

[207] S. Agne, T. Kauten, J. Jin, E. Meyer-Scott, J. Z. Salvail, D. R. Hamel, K. J. Resch, G. Weihs, and T. Jennewein. Observation of Genuine Three-Photon Interference. *Phys. Rev. Lett.*, **118**:153602, 2017.

[208] A. J. Menssen, A. E. Jones, B. J. Metcalf, M. C. Tichy, S. Barz, W. S. Kolthammer, and I. A. Walmsley. Distinguishability and Many-Particle Interference. *Phys. Rev. Lett.*, **118**:153603, 2017.

[209] M. Bonneau, W. J. Munro, K. Nemoto, and J. Schmiedmayer. Characterizing twin-particle entanglement in double-well potentials. *Phys. Rev. A*, **98**:033608, 2018.

[210] C. Yannouleas, B. B. Brandt, and U. Landman. Interference, spectral momentum correlations, entanglement, and Bell inequality for a trapped interacting ultracold atomic dimer: Analogies with biphoton interferometry. *Phys. Rev. A*, **99**:013616, 2019.

[211] G. Taguchi, T. Dougakiuchi, N. Yoshimoto, K. Kasai, M. Iinuma, H. F. Hofmann, and Y. Kadoya. Measurement and control of spatial qubits generated by passing photons through double slits. *Phys. Rev. A*, **78**:012307, 2008.

[212] R. Blume-Kohout. Optimal, reliable estimation of quantum states. *New Journal of Physics*, **12**:043034, 2010.

[213] W. R. Inc. Mathematica, Version 12.0. Champaign, IL, 2019.

[214] E. Schrödinger. Discussion of probability relations between separated systems. In *Mathematical Proceedings of the Cambridge Philosophical Society*, volume 31, pages 555–563. Cambridge University Press, 1935.

[215] A. Einstein, B. Podolsky, and N. Rosen. Can Quantum-Mechanical Description of Physical Reality Be Considered Complete? *Phys. Rev.*, **47**:777–780, 1935.

[216] J. S. Bell. On the einstein podolsky rosen paradox. *Physics Physique Fizika*, **1**: 195, 1964.

[217] H. Strobel, W. Muessel, D. Linnemann, T. Zibold, D. B. Hume, L. Pezzè, A. Smerzi, and M. K. Oberthaler. Fisher information and entanglement of non-Gaussian spin states. *Science*, **345**:424–427, 2014.

[218] F. Benatti, R. Floreanini, and U. Marzolino. Entanglement in fermion systems and quantum metrology. *Phys. Rev. A*, **89**:032326, 2014.

[219] A. Kitaev and J. Preskill. Topological Entanglement Entropy. *Phys. Rev. Lett.*, **96**:110404, 2006.

[220] H. Li and F. D. M. Haldane. Entanglement Spectrum as a Generalization of Entanglement Entropy: Identification of Topological Order in Non-Abelian Fractional Quantum Hall Effect States. *Phys. Rev. Lett.*, **101**:010504, 2008.

[221] B. Zeng, X. Chen, D.-L. Zhou, and X.-G. Wen. *Quantum Information Meets Quantum Matter*. Springer New York, 2019.

[222] P. Fromholz, G. Magnifico, V. Vitale, T. Mendes-Santos, and M. Dalmonte. Entanglement topological invariants for one-dimensional topological superconductors. *Phys. Rev. B*, **101**:085136, 2020.

[223] M. C. Tichy, F. Mintert, and A. Buchleitner. Essential entanglement for atomic and molecular physics. *Journal of Physics B: Atomic, Molecular and Optical Physics*, **44**:192001, 2011.

[224] M. Cramer, A. Bernard, N. Fabbri, L. Fallani, C. Fort, S. Rosi, F. Caruso, M. Inguscio, and M. Plenio. Spatial entanglement of bosons in optical lattices. *Nature*, **4**:2161, 2013.

[225] C. Moura Alves and D. Jaksch. Multipartite Entanglement Detection in Bosons. *Phys. Rev. Lett.*, **93**:110501, 2004.

[226] A. J. Daley, H. Pichler, J. Schachenmayer, and P. Zoller. Measuring Entanglement Growth in Quench Dynamics of Bosons in an Optical Lattice. *Phys. Rev. Lett.*, **109**:020505, 2012.

[227] M. Fadel, T. Zibold, B. Décamps, and P. Treutlein. Spatial entanglement patterns and Einstein-Podolsky-Rosen steering in Bose-Einstein condensates. *Science*, **360**:409–413, 2018.

[228] K. Lange, J. Peise, B. Lücke, I. Kruse, G. Vitagliano, I. Apellaniz, M. Kleinmann, G. Tóth, and C. Klempt. Entanglement between two spatially separated atomic modes. *Science*, **360**:416–418, 2018.

[229] P. Kunkel, M. Prüfer, H. Strobel, D. Linnemann, A. Frölian, T. Gasenzer, M. Gärttner, and M. K. Oberthaler. Spatially distributed multipartite entanglement enables EPR steering of atomic clouds. *Science*, **360**:413–416, 2018.

[230] J. Schliemann, J. I. Cirac, M. Kuś, M. Lewenstein, and D. Loss. Quantum correlations in two-fermion systems. *Phys. Rev. A*, **64**:022303, 2001.

[231] P. Zanardi. Quantum entanglement in fermionic lattices. *Phys. Rev. A*, **65**: 042101, 2002.

[232] M. R. Dowling, A. C. Doherty, and H. M. Wiseman. Entanglement of indistinguishable particles in condensed-matter physics. *Phys. Rev. A*, **73**:052323, 2006.

[233] K. Eckert, J. Schliemann, D. Bruß, and M. Lewenstein. Quantum Correlations in Systems of Indistinguishable Particles. *Annals of Physics*, **299**:88 – 127, 2002.

[234] H. M. Wiseman and J. A. Vaccaro. Entanglement of Indistinguishable Particles Shared between Two Parties. *Phys. Rev. Lett.*, **91**:097902, 2003.

[235] G. Ghirardi and L. Marinatto. General criterion for the entanglement of two indistinguishable particles. *Phys. Rev. A*, **70**:012109, 2004.

[236] A. P. Balachandran, T. R. Govindarajan, A. R. de Queiroz, and A. F. Reyes-Lega. Entanglement and Particle Identity: A Unifying Approach. *Phys. Rev. Lett.*, **110**:080503, 2013.

[237] Y. Shi. Quantum entanglement of identical particles. *Phys. Rev. A*, **67**:024301, 2003.

[238] Y. S. Li, B. Zeng, X. S. Liu, and G. L. Long. Entanglement in a two-identical-particle system. *Phys. Rev. A*, **64**:054302, 2001.

[239] N. Killoran, M. Cramer, and M. B. Plenio. Extracting Entanglement from Identical Particles. *Phys. Rev. Lett.*, **112**:150501, 2014.

[240] F. Benatti, R. Floreanini, F. Franchini, and U. Marzolino. Remarks on entanglement and identical particles. *Open Systems & Information Dynamics*, **24** (03):1740004, 2017.

[241] J. H. Becher, E. Sindici, R. Klemt, S. Jochim, A. J. Daley, and P. M. Preiss. Measurement of Identical Particle Entanglement and the Influence of Antisymmetrisation. *arXiv preprint arXiv:2002.11207*, 2020.

[242] G. Ghirardi, L. Marinatto, and T. Weber. Entanglement and Properties of Composite Quantum Systems: A Conceptual and Mathematical Analysis. *Journal of Statistical Physics*, **108**:49–122, 2002.

[243] R. Horodecki, P. Horodecki, M. Horodecki, and K. Horodecki. Quantum entanglement. *Rev. Mod. Phys.*, **81**:865–942, 2009.

[244] J. M. Raimond, M. Brune, and S. Haroche. Manipulating quantum entanglement with atoms and photons in a cavity. *Rev. Mod. Phys.*, **73**:565–582, 2001.

[245] J. Li, S.-Y. Zhu, and G. S. Agarwal. Magnon-Photon-Phonon Entanglement in Cavity Magnomechanics. *Phys. Rev. Lett.*, **121**:203601, 2018.

[246] A. M. Kaufman, M. E. Tai, A. Lukin, M. Rispoli, R. Schittko, P. M. Preiss, and M. Greiner. Quantum thermalization through entanglement in an isolated many-body system. *Science*, **353**:794–800, 2016.

[247] R. Lo Franco and G. Compagno. Indistinguishability of Elementary Systems as a Resource for Quantum Information Processing. *Phys. Rev. Lett.*, **120**:240403, 2018.

[248] R. L. Franco and G. Compagno. Quantum entanglement of identical particles by standard information-theoretic notions. *Scientific reports*, **6**:20603, 2016.

[249] B. Morris, B. Yadin, M. Fadel, T. Zibold, P. Treutlein, and G. Adesso. Entanglement between identical particles is a useful and consistent resource. *arXiv preprint arXiv:1908.11735*, 2019.

[250] N. Friis, G. Vitagliano, M. Malik, and M. Huber. Entanglement certification from theory to experiment. *Nature Reviews Physics*, **1**:72–87, 2019.

[251] L. Gurvits. Classical complexity and quantum entanglement. *Journal of Computer and System Sciences*, **69**:448 – 484, 2004. Special Issue on STOC 2003.

[252] W. Dür and J. I. Cirac. Classification of multiqubit mixed states: Separability and distillability properties. *Phys. Rev. A*, **61**:042314, 2000.

[253] D. M. Greenberger, M. A. Horne, and A. Zeilinger. Going beyond bell's theorem. In *Bell's theorem, quantum theory and conceptions of the universe*, pages 69–72. Springer, 1989.

[254] D. Bouwmeester, J.-W. Pan, M. Daniell, H. Weinfurter, and A. Zeilinger. Observation of Three-Photon Greenberger-Horne-Zeilinger Entanglement. *Phys. Rev. Lett.*, **82**:1345–1349, 1999.

[255] W. Dür, G. Vidal, and J. I. Cirac. Three qubits can be entangled in two inequivalent ways. *Phys. Rev. A*, **62**:062314, 2000.

[256] B. Jungnitsch, T. Moroder, and O. Gühne. Taming Multiparticle Entanglement. *Phys. Rev. Lett.*, **106**:190502, 2011.

[257] M. B. Plenio and S. S. Virmani. An introduction to entanglement theory. In *Quantum Information and Coherence*, pages 173–209. Springer, 2014.

[258] C. H. Bennett, H. J. Bernstein, S. Popescu, and B. Schumacher. Concentrating partial entanglement by local operations. *Phys. Rev. A*, **53**:2046–2052, 1996.

[259] M. B. Plenio and V. Vedral. Teleportation, entanglement and thermodynamics in the quantum world. *Contemporary Physics*, **39**:431–446, 1998.

[260] P. M. Hayden, M. Horodecki, and B. M. Terhal. The asymptotic entanglement cost of preparing a quantum state. *Journal of Physics A: Mathematical and General*, **34**:6891–6898, aug 2001.

[261] G. Vidal, W. Dür, and J. I. Cirac. Entanglement Cost of Bipartite Mixed States. *Phys. Rev. Lett.*, **89**:027901, Jun 2002.

[262] E. M. Rains. Rigorous treatment of distillable entanglement. *Phys. Rev. A*, **60**: 173–178, Jul 1999.

[263] C. H. Bennett, D. P. DiVincenzo, J. A. Smolin, and W. K. Wootters. Mixed-state entanglement and quantum error correction. *Phys. Rev. A*, **54**:3824–3851, Nov 1996.

[264] V. Vedral and M. B. Plenio. Entanglement measures and purification procedures. *Phys. Rev. A*, **57**:1619–1633, 1998.

[265] K. Audenaert, J. Eisert, E. Jané, M. B. Plenio, S. Virmani, and B. De Moor. Asymptotic Relative Entropy of Entanglement. *Phys. Rev. Lett.*, **87**:217902, Nov 2001.

[266] M. J. Donald, M. Horodecki, and O. Rudolph. The uniqueness theorem for entanglement measures. *Journal of Mathematical Physics*, **43**:4252–4272, 2002.

[267] G. Vidal and R. F. Werner. Computable measure of entanglement. *Phys. Rev. A*, **65**:032314, Feb 2002.

[268] M. Horodecki, P. Horodecki, and R. Horodecki. Separability of mixed states: necessary and sufficient conditions. *Physics Letters A*, **223**:1 – 8, 1996.

[269] A. Peres. Separability Criterion for Density Matrices. *Phys. Rev. Lett.*, **77**: 1413–1415, 1996.

[270] E. Sindici. *Quantum Correlations and Exchange Symmetry*. PhD thesis, Strathclyde University, 2019.

[271] T. Eggeling and R. F. Werner. Separability properties of tripartite states with $U \bigotimes U \bigotimes U$ symmetry. *Phys. Rev. A*, **63**:042111, 2001.

[272] J. Watrous. *The Theory of Quantum Information*. Cambridge University Press, 2018.

[273] S. Boyd and L. Vandenberghe. *Convex optimization*. Cambridge university press, 2004.

[274] M. Hofmann, T. Moroder, and O. Gühne. Analytical characterization of the genuine multiparticle negativity. *Journal of Physics A: Mathematical and Theoretical*, **47**:155301, 2014.

[275] N. Johnston. QETLAB: A MATLAB toolbox for quantum entanglement, version 0.9, 2016.

[276] M. Grant and S. Boyd. CVX: Matlab software for disciplined convex programming, version 2.1. `http://cvxr.com/cvx`, March 2014.

[277] M. Grant and S. Boyd. Graph implementations for nonsmooth convex programs. In V. Blondel, S. Boyd, and H. Kimura, editors, *Recent Advances in Learning and Control*, Lecture Notes in Control and Information Sciences, pages 95–110. Springer-Verlag Limited, 2008. `http://stanford.edu/~boyd/graph_dcp.html`.

[278] M. Holten et al. Observation of Pauli crystals in an ultracold Fermi gas. *In preparation*.

[279] R.-J. Petzold. Few ultracold fermions in a two-dimensional trap. Master's thesis, Universität Heidelberg, 2020.

[280] M. C. Tichy, M. Tiersch, F. Mintert, and A. Buchleitner. Many-particle interference beyond many-boson and many-fermion statistics. *New Journal of Physics*, **14**:093015, 2012.

[281] J. Bjerlin, S. M. Reimann, and G. M. Bruun. Few-Body Precursor of the Higgs Mode in a Fermi Gas. *Phys. Rev. Lett.*, **116**:155302, Apr 2016.

[282] M. Rontani, J. R. Armstrong, Y. Yu, S. Åberg, and S. M. Reimann. Cold Fermionic Atoms in Two-Dimensional Traps: Pairing versus Hund's Rule. *Phys. Rev. Lett.*, **102**:060401, Feb 2009.

[283] D. Rakshit, J. Mostowski, T. Sowiński, M. Załuska-Kotur, and M. Gajda. On the observability of Pauli crystals in experiments with ultracold trapped Fermi gases. *Scientific reports*, **7**:1–11, 2017.

[284] P. A. Murthy, M. Neidig, R. Klemt, L. Bayha, I. Boettcher, T. Enss, M. Holten, G. Zürn, P. M. Preiss, and S. Jochim. High-temperature pairing in a strongly interacting two-dimensional Fermi gas. *Science*, **359**:452–455, 2018.

[285] J. von Stecher, E. Demler, M. D. Lukin, and A. M. Rey. Probing interaction-induced ferromagnetism in optical superlattices. *New Journal of Physics*, **12**: 055009, 2010.

[286] L. Palm. Exploring fractional quantum hall physics using ultracold fermions in rotating traps. Master's thesis, Universität Heidelberg, 2018.

Appendices

Appendix A

Reconstructed Density Matrices

In this chapter we list the reconstructed density matrices of all states that were used in this thesis. We also mention the number of steps of the Metropolis-Hastings (MH) algorithm, which is the number of states of the sampled posterior distribution. We give the median of each entry together with the 68% credible interval.

Rotated Triplet State

Number of MH steps: 5000
Basis states: $\{|\uparrow\uparrow\rangle, |\uparrow\downarrow\rangle, |\downarrow\uparrow\rangle, |\downarrow\downarrow\rangle\}$

$$\Re(\rho) = \begin{pmatrix} 0.307 & 0.002 & 0.123 & 0.087 \\ & 0.290 & 0.152 & 0.080 \\ & & 0.208 & 0.081 \\ h.c. & & & 0.195 \end{pmatrix}, \Im(\rho) = \begin{pmatrix} 0 & -0.143 & -0.036 & -0.094 \\ & 0 & -0.001 & -0.047 \\ & & 0 & 0.044 \\ h.c. & & & 0 \end{pmatrix}, \tag{A.1}$$

with 68% credible interval

$$\delta\Re(\rho) = \begin{pmatrix} 0.007 & 0.111 & 0.220 & 0.091 \\ & 0.185 & 0.010 & 0.009 \\ & & 0.184 & 0.022 \\ h.c. & & & 0.004 \end{pmatrix}, \delta\Im(\rho) = \begin{pmatrix} 0 & 0.116 & 0.015 & 0.221 \\ & 0 & 0.010 & 0.119 \\ & & 0 & 0.173 \\ h.c. & & & 0 \end{pmatrix}. \tag{A.2}$$

Interacting Double Well

Number of MH steps for each interaction strength: 5000
Basis states: $\{|LL\rangle, |LR\rangle, |RL\rangle, |RR\rangle\}$

U/J = -5.9

$$\Re(\rho) = \begin{pmatrix} 0.456 & 0.102 & 0.077 & 0.191 \\ & 0.038 & 0.028 & 0.093 \\ & & 0.031 & 0.094 \\ h.c. & & & 0.0475 \end{pmatrix}, \Im(\rho) = \begin{pmatrix} 0 & -0.001 & 0.011 & 0.045 \\ & 0 & 0.001 & 0.027 \\ & & 0 & 0.006 \\ h.c. & & & 0 \end{pmatrix}, \tag{A.3}$$

with 68% credible interval

$$\delta\Re(\rho) = \begin{pmatrix} 0.023 & 0.029 & 0.035 & 0.037 \\ & 0.008 & 0.008 & 0.034 \\ & & 0.007 & 0.037 \\ h.c. & & & 0.023 \end{pmatrix}, \delta\Im(\rho) = \begin{pmatrix} 0 & 0.039 & 0.005 & 0.050 \\ & 0 & 0.004 & 0.013 \\ & & 0 & 0.004 \\ h.c. & & & 0 \end{pmatrix}. \tag{A.4}$$

U/J = -2.9

$$\Re(\rho) = \begin{pmatrix} 0.389 & 0.129 & 0.129 & 0.161 \\ & 0.095 & 0.073 & 0.138 \\ & & 0.086 & 0.133 \\ h.c. & & & 0.4290 \end{pmatrix}, \Im(\rho) = \begin{pmatrix} 0 & 0.048 & 0.027 & 0.025 \\ & 0 & -0.013 & -0.056 \\ & & 0 & 0.006 \\ h.c. & & & 0 \end{pmatrix}, \tag{A.5}$$

with 68% credible interval

$$\delta\Re(\rho) = \begin{pmatrix} 0.035 & 0.043 & 0.045 & 0.054 \\ & 0.019 & 0.019 & 0.05 \\ & & 0.018 & 0.03 \\ h.c. & & & 0.036 \end{pmatrix}, \delta\Im(\rho) = \begin{pmatrix} 0 & 0.034 & 0.037 & 0.084 \\ & 0 & 0.001 & 0.021 \\ & & 0 & 0.05 \\ h.c. & & & 0 \end{pmatrix}. \tag{A.6}$$

U/J = 0

$$\Re(\rho) = \begin{pmatrix} 0.195 & 0.152 & 0.162 & 0.177 \\ & 0.199 & 0.177 & 0.211 \\ & & 0.233 & 0.241 \\ h.c. & & & 0.373 \end{pmatrix}, \Im(\rho) = \begin{pmatrix} 0 & 0.01 & -0.013 & -0.031 \\ & 0 & -0.036 & 0.051 \\ & & 0 & -0.019 \\ h.c. & & & 0 \end{pmatrix}, \tag{A.7}$$

with 68% credible interval

$$\delta\Re(\rho) = \begin{pmatrix} 0.016 & 0.045 & 0.054 & 0.049 \\ & 0.016 & 0.022 & 0.058 \\ & & 0.016 & 0.026 \\ h.c. & & & 0.019 \end{pmatrix}, \delta\Im(\rho) = \begin{pmatrix} 0 & 0.035 & 0.002 & 0.043 \\ & 0 & 0.01 & 0.05 \\ & & 0 & 0.0146 \\ h.c. & & & 0 \end{pmatrix}. \tag{A.8}$$

$\underline{U/J = 2.5}$

$$\Re(\rho) = \begin{pmatrix} 0.142 & 0.165 & 0.168 & 0.110 \\ & 0.364 & 0.288 & 0.190 \\ & & 0.340 & 0.187 \\ h.c. & & & 0.154 \end{pmatrix}, \Im(\rho) = \begin{pmatrix} 0 & -0.094 & -0.048 & -0.009 \\ & 0 & -0.007 & 0.003 \\ & & 0 & 0.046 \\ h.c. & & & 0 \end{pmatrix}, \tag{A.9}$$

with 68% credible interval

$$\delta\Re(\rho) = \begin{pmatrix} 0.021 & 0.038 & 0.054 & 0.025 \\ & 0.031 & 0.030 & 0.050 \\ & & 0.029 & 0.042 \\ h.c. & & & 0.022 \end{pmatrix}, \delta\Im(\rho) = \begin{pmatrix} 0 & 0.022 & 0.040 & 0.024 \\ & 0 & 0.004 & 0.128 \\ & & 0 & 0.068 \\ h.c. & & & 0 \end{pmatrix}. \tag{A.10}$$

$\underline{U/J = 5.0}$

$$\Re(\rho) = \begin{pmatrix} 0.068 & 0.136 & 0.129 & 0.053 \\ & 0.433 & 0.299 & 0.149 \\ & & 0.416 & 0.140 \\ h.c. & & & 0.084 \end{pmatrix}, \Im(\rho) = \begin{pmatrix} 0 & 0.004 & -0.004 & -0.004 \\ & 0 & -0.007 & -0.009 \\ & & 0 & 0.054 \\ h.c. & & & 0 \end{pmatrix}, \tag{A.11}$$

with 68% credible interval

$$\delta\Re(\rho) = \begin{pmatrix} 0.015 & 0.045 & 0.047 & 0.019 \\ & 0.034 & 0.034 & 0.045 \\ & & 0.033 & 0.035 \\ h.c. & & & 0.017 \end{pmatrix}, \delta\Im(\rho) = \begin{pmatrix} 0 & 0.043 & 0.052 & 0.001 \\ & 0 & 0.042 & 0.047 \\ & & 0 & 0.030 \\ h.c. & & & 0 \end{pmatrix}. \tag{A.12}$$

$\underline{U/J = 8.0}$

$$\Re(\rho) = \begin{pmatrix} 0.033 & 0.086 & 0.079 & 0.025 \\ & 0.467 & 0.36 & 0.136 \\ & & 0.436 & 0.126 \\ h.c. & & & 0.065 \end{pmatrix}, \Im(\rho) = \begin{pmatrix} 0 & -0.033 & -0.040 & 0.020 \\ & 0 & -0.037 & -0.004 \\ & & 0 & 0.045 \\ h.c. & & & 0 \end{pmatrix}, \tag{A.13}$$

with 68% credible interval

$$\delta\Re(\rho) = \begin{pmatrix} 0.010 & 0.030 & 0.038 & 0.013 \\ & 0.032 & 0.027 & 0.019 \\ & & 0.032 & 0.033 \\ h.c. & & & 0.014 \end{pmatrix}, \delta\Im(\rho) = \begin{pmatrix} 0 & 0.015 & 0.046 & 0.002 \\ & 0 & 0.021 & 0.070 \\ & & 0 & 0.031 \\ h.c. & & & 0 \end{pmatrix}. \tag{A.14}$$

$U/J = 11.6$

$$\Re(\rho) = \begin{pmatrix} 0.023 & 0.068 & 0.068 & 0.019 \\ & 0.486 & 0.370 & 0.105 \\ & & 0.448 & 0.092 \\ h.c. & & & 0.043 \end{pmatrix}, \Im(\rho) = \begin{pmatrix} 0 & -0.030 & 0.015 & -0.005 \\ & 0 & -0.037 & -0.016 \\ & & 0 & 0.049 \\ h.c. & & & 0 \end{pmatrix}, \tag{A.15}$$

with 68% credible interval

$$\delta\Re(\rho) = \begin{pmatrix} 0.007 & 0.035 & 0.030 & 0.014 \\ & 0.025 & 0.029 & 0.027 \\ & & 0.024 & 0.032 \\ h.c. & & & 0.009 \end{pmatrix}, \delta\Im(\rho) = \begin{pmatrix} 0 & 0.028 & 0.024 & 0.008 \\ & 0 & 0.010 & 0.006 \\ & & 0 & 0.053 \\ h.c. & & & 0 \end{pmatrix}. \tag{A.16}$$

$U/J = 18.5$

$$\Re(\rho) = \begin{pmatrix} 0.016 & 0.028 & 0.040 & -0.004 \\ & 0.482 & 0.362 & 0.084 \\ & & 0.459 & 0.066 \\ h.c. & & & 0.043 \end{pmatrix}, \Im(\rho) = \begin{pmatrix} 0 & 0.041 & 0.020 & 0.011 \\ & 0 & -0.014 & 0.029 \\ & & 0 & 0.072 \\ h.c. & & & 0 \end{pmatrix}, \tag{A.17}$$

with 68% credible interval

$$\delta\Re(\rho) = \begin{pmatrix} 0.007 & 0.056 & 0.055 & 0.019 \\ & 0.031 & 0.028 & 0.045 \\ & & 0.031 & 0.054 \\ h.c. & & & 0.011 \end{pmatrix}, \delta\Im(\rho) = \begin{pmatrix} 0 & 0.049 & 0.027 & 0.001 \\ & 0 & 0.013 & 0.031 \\ & & 0 & 0.034 \\ h.c. & & & 0 \end{pmatrix}. \tag{A.18}$$

Incommensurately Spaced Triple Well

Number of MH steps: 50000

Basis states:

$\{|\uparrow,\uparrow,\downarrow\rangle, |\uparrow,\downarrow,\uparrow\rangle, |\downarrow,\uparrow,\uparrow\rangle, |\uparrow\downarrow,\uparrow,\cdot\rangle, |\uparrow\downarrow,\cdot,\uparrow\rangle, |\uparrow,\uparrow\downarrow,\cdot\rangle, |\cdot,\uparrow\downarrow,\uparrow\rangle, |\uparrow,\cdot,\uparrow\downarrow\rangle, |\cdot,\uparrow,\uparrow\downarrow\rangle\}$

$$\Re(\rho) = \begin{pmatrix} 0.446 & 0.268 & -0.005 & 0.005 & 0.005 & 0.076 & -0.009 & 0.065 & -0.005 \\ & 0.465 & -0.014 & 0.004 & 0.002 & 0.062 & 0.001 & 0.077 & 0.007 \\ & & 0.002 & 0.001 & 0 & 0.002 & 0.001 & -0.002 & 0 \\ & & & 0.002 & 0 & 0.001 & -0.001 & 0.001 & -0.001 \\ & & & & 0.002 & 0.001 & -0.001 & 0 & 0.001 \\ & & & & & 0.034 & -0.001 & 0.010 & 0.003 \\ & & & & & & 0.006 & -0.001 & 0.001 \\ & & & & & & & 0.034 & 0.003 \\ h.c. & & & & & & & & 0.009 \end{pmatrix}$$

$$\Im(\rho) = \begin{pmatrix} 0 & 0.013 & 0.002 & 0.006 & 0.005 & -0.013 & -0.005 & -0.010 & 0.007 \\ & 0 & 0 & -0.004 & -0.006 & -0.021 & 0.008 & 0.001 & 0.001 \\ & & 0 & 0 & -0.001 & -0.001 & 0 & -0.002 & 0.001 \\ & & & 0 & -0.001 & 0.002 & 0 & 0.002 & 0 \\ & & & & 0 & -0.002 & 0 & 0.002 & 0 \\ & & & & & 0 & -0.003 & -0.007 & 0.004 \\ & & & & & & 0 & 0.004 & 0.002 \\ & & & & & & & 0 & -0.002 \\ h.c. & & & & & & & & 0 \end{pmatrix}$$

with 68% credible interval

$$\delta\Re(\rho) = \begin{pmatrix} 0.027 & 0.014 & 0.008 & 0.004 & 0.007 & 0.009 & 0.012 & 0.019 & 0.004 \\ & 0.027 & 0.009 & 0.001 & 0.009 & 0.029 & 0.005 & 0.010 & 0.007 \\ & & 0.001 & 0.001 & 0.001 & 0 & 0.002 & 0.003 & 0.002 \\ & & & 0.001 & 0 & 0.003 & 0.002 & 0.001 & 0.001 \\ & & & & 0.001 & 0 & 0 & 0.003 & 0.002 \\ & & & & & 0.008 & 0.001 & 0.007 & 0.001 \\ & & & & & & 0.002 & 0.004 & 0.002 \\ & & & & & & & 0.008 & 0.005 \\ h.c. & & & & & & & & 0.003 \end{pmatrix}$$

$$\delta\Im(\rho) = \begin{pmatrix} 0 & 0.003 & 0.005 & 0.007 & 0.002 & 0.015 & 0.002 & 0.027 & 0.014 \\ & 0 & 0.002 & 0.007 & 0.005 & 0.009 & 0.008 & 0.021 & 0.010 \\ & & 0 & 0 & 0.001 & 0.004 & 0 & 0.002 & 0.002 \\ & & & 0 & 0.001 & 0.002 & 0.001 & 0.003 & 0.001 \\ & & & & 0 & 0.003 & 0.002 & 0.002 & 0.002 \\ & & & & & 0 & 0.005 & 0.002 & 0.005 \\ & & & & & & 0 & 0.001 & 0.004 \\ & & & & & & & 0 & 0.005 \\ h.c. & & & & & & & & 0 \end{pmatrix}.$$

Commensurately Spaced (Homogeneous) Triple Well

Number of MH steps: 50000
Basis states:
$\{|\uparrow,\uparrow,\downarrow\rangle, |\uparrow,\downarrow,\uparrow\rangle, |\downarrow,\uparrow,\uparrow\rangle, |\uparrow\downarrow,\uparrow,\cdot\rangle, |\uparrow\downarrow,\cdot,\uparrow\rangle, |\uparrow,\uparrow\downarrow,\cdot\rangle, |\cdot,\uparrow\downarrow,\uparrow\rangle, |\uparrow,\cdot,\uparrow\downarrow\rangle, |\cdot,\uparrow,\uparrow\downarrow\rangle\}$

$$\Re(\rho) = \begin{pmatrix} 0.197 & 0.010 & -0.139 & 0.010 & -0.025 & 0.016 & -0.009 & 0.003 & 0.023 \\ & 0.162 & 0.041 & -0.016 & -0.017 & 0.023 & 0.031 & 0.020 & 0.021 \\ & & 0.288 & 0.005 & 0.035 & 0.002 & 0.033 & -0.027 & 0.005 \\ & & & 0.035 & 0.010 & -0.008 & 0.012 & 0.011 & -0.003 \\ & & & & 0.060 & 0.015 & 0.010 & -0.001 & 0.012 \\ & & & & & 0.050 & 0.013 & 0.012 & -0.004 \\ & & & & & & 0.087 & 0.013 & -0.015 \\ & & & & & & & 0.055 & -0.002 \\ h.c. & & & & & & & & 0.063 \end{pmatrix}$$

$$\Im(\rho) = \begin{pmatrix} 0 & 0.060 & 0.060 & -0.020 & -0.012 & -0.022 & 0.029 & -0.028 & 0.010 \\ & 0 & 0.066 & 0.012 & 0.015 & 0.006 & 0.001 & -0.008 & 0.009 \\ & & 0 & -0.023 & -0.008 & -0.027 & -0.034 & 0.010 & -0.031 \\ & & & 0 & 0.009 & -0.009 & -0.003 & -0.003 & 0.012 \\ & & & & 0 & 0.005 & 0.015 & 0.013 & 0.007 \\ & & & & & 0 & 0.011 & 0.007 & -0.012 \\ & & & & & & 0 & -0.015 & -0.015 \\ & & & & & & & 0 & 0.017 \\ h.c. & & & & & & & & 0 \end{pmatrix}$$

with 68% credible interval

$$\delta\Re(\rho) = \begin{pmatrix} 0.053 & 0.080 & 0.010 & 0.030 & 0.034 & 0.050 & 0.034 & 0.048 & 0.030 \\ & 0.051 & 0.075 & 0.023 & 0.014 & 0.030 & 0.038 & 0.003 & 0.006 \\ & & 0.064 & 0.019 & 0.040 & 0.024 & 0.044 & 0 & 0.017 \\ & & & 0.016 & 0.022 & 0.012 & 0.015 & 0.023 & 0.004 \\ & & & & 0.026 & 0.022 & 0.014 & 0.016 & 0.006 \\ & & & & & 0.022 & 0.008 & 0.020 & 0.021 \\ & & & & & & 0.035 & 0.011 & 0.021 \\ & & & & & & & 0.024 & 0.010 \\ h.c. & & & & & & & & 0.027 \end{pmatrix}$$

$$\delta\Im(\rho) = \begin{pmatrix} 0 & 0.001 & 0.010 & 0.023 & 0.012 & 0.016 & 0.038 & 0.018 & 0.003 \\ & 0 & 0.001 & 0.034 & 0.022 & 0.034 & 0.007 & 0.024 & 0.049 \\ & & 0 & 0.042 & 0.057 & 0.035 & 0.001 & 0.034 & 0.052 \\ & & & 0 & 0.003 & 0.010 & 0.022 & 0.003 & 0.009 \\ & & & & 0 & 0.022 & 0.018 & 0.011 & 0.023 \\ & & & & & 0 & 0.017 & 0.022 & 0.001 \\ & & & & & & 0 & 0.028 & 0.016 \\ & & & & & & & 0 & 0.028 \\ h.c. & & & & & & & & 0 \end{pmatrix}.$$

Appendix B

Negativity Bounds

We briefly proof the bounds of the negativity, which we used in the discussion around Fig. 10.7.

1. *The maximum negativity that can be obtained by antisymmetrizing a fully separable three-particle state is one.*
   A pure separable state can be written in the form

$$|\Psi^{\mathrm{p}}_{\mathrm{sep}}\rangle = |\phi_1\rangle \otimes |\phi_2\rangle \otimes |\phi_3\rangle \,, \tag{B.1}$$

   with single-particle pure states $|\phi_i\rangle$. We obtain its normalized, antisymmetrized density matrix as

$$\rho^{\mathcal{A}}_{\mathrm{sep}} = \frac{P_{\mathcal{A}} \, |\psi^p_{\mathrm{sep}}\rangle \, \langle\psi^p_{\mathrm{sep}}| \, P_{\mathcal{A}}}{\mathrm{Tr}(P_{\mathcal{A}} \, |\psi^p_{\mathrm{sep}}\rangle \, \langle\psi^p_{\mathrm{sep}}| \, P_{\mathcal{A}})}, \tag{B.2}$$

   and verify numerically that for any random single-particle state $|\phi_i\rangle$ the negativity of the antisymmetrized wavefunction evaluates to $\mathcal{N}(\rho^{\mathcal{A}}_{\mathrm{sep}}) = 1$ along any possible bipartition due to the exchange symmetry of the first-quantized density matrix. A general mixed fully-separable state can be obtained as the probabilistic sum of pure fully-separable states,

$$\tilde{\rho}^{\mathcal{A}}_{\mathrm{sep}} = \sum_i p_i \rho^{\mathcal{A}}_{\mathrm{sep,i}}. \tag{B.3}$$

   Due to the convexity of the negativity, we find the inequality

$$\mathcal{N}(\tilde{\rho}^{\mathcal{A}}_{\mathrm{sep}}) \leq \sum_i p_i \mathcal{N}\left(\rho^{\mathcal{A}}_{\mathrm{sep,i}}\right) = 1. \tag{B.4}$$

   We therefore find the upper bound for the bipartite negativity of an antisymmetrized fully-separable state,

$$\mathcal{N}^{\max}_{\mathrm{sep}} = 1. \tag{B.5}$$

2. *The maximum negativity that can be obtained by antisymmetrizing a biseparable state is 1.9428*

We can write down a general biseparable state as

$$|\psi_{\mathrm{bs}}^{p}\rangle = |\phi\rangle_1 \otimes |\phi\rangle_{23}\,, \tag{B.6}$$

with any pure two-particle state ϕ_{23} between atoms with label 2 and 3. For a maximally entangled two-particle state of the form

$$|\phi\rangle_{23} = \frac{1}{\sqrt{2}}\left(|X\sigma\rangle\,|Y\tau\rangle + e^{i\theta}\,|Y\tau\rangle\,|X\sigma\rangle\right), \tag{B.7}$$

we explicitly calculate the negativity of its antisymmetrized density matrix $\rho_{\mathcal{A}}^{\mathrm{bs}}$ to be $\mathcal{N}(\rho_{\mathcal{A}}^{\mathrm{bs}}) \sim 1.9428$. Based on the same arguments as above, we find an upper bound of the negativity for any mixed, biseparable state of

$$\mathcal{N}_{\mathrm{bs}}^{\mathrm{max}} = 1.9428. \tag{B.8}$$